UNIVERSITY OF TURIN

PhD School in Life and Health Sciences

Molecular Medicine

NEW MOLECULAR TARGETS AND THERAPEUTIC APPROACHES TO REVERSE CHEMORESISTANCE AND IMMUNOEVASION IN MALIGNANT PLEURAL MESOTHELIOMA

PREETA ANANTHANARAYANAN

UNIVERSITY OF TURIN

PhD School in Life and Health Sciences

Molecular Medicine

XXXII Cycle

Academic Years: 2016-2020

NEW MOLECULAR TARGETS AND THERAPEUTIC APPROACHES TO REVERSE CHEMORESISTANCE AND IMMUNOEVASION IN MALIGNANT PLEURAL MESOTHELIOMA

Tutor: Prof. Dr. Chiara Riganti Candidate: Preeta Ananthanarayanan

Coordinator: Prof. Francesco Novelli

This Thesis is dedicated to

my late grandfather

P. S. Arunachalam

who taught me the value of knowledge

ACKNOWLEDGEMENTS

I would like to express my deepest of gratitude, first and foremost, to my supervisor Dr. Chiara Riganti for her constant support and patient guidance through all the years of my doctoral journey. Always ready to help with her kind words of encouragement, she provided me the opportunity to work autonomously and motivated me to push forward and help me realise my goals.

I would like to also thank all the members of our lab at the Department of Oncology – the support from our post-doctoral researchers Dr. Joanna Kopecka for guiding me through my initial year on the project, Dr. Carolina Dimas Belisario for her support and cheer, Dr. Iris Chiara Salaroglio and Dr. Elena Gazzano.

I would also like to extend my thanks to all the past and present PhD and master students for their enormous support and round the clock assistance, especially to Dr. Vladan Milosevic, Dr. Gamal-Eldein Fathy Abd-Ellatef, Ahmad Abdullrahman, Dario Anobile, Muhlis Akman, Martina Godel and Sofia La Vecchia. We have not just built a strong research team over the years but also undeniable friendships. I would also like to acknowledge the continuous assistance and timely help by Costanzo Costamagna and all other members of the department whom I might have missed to mention for making this experience very memorable.

Furthermore, I am very grateful for my extended research period at the AO Research Institute, Davos, Switzerland under the guidance of Dr. Tiziano Serra. My thanks to him and to the entire team of Biomedical Engineering – Dr. Geraldine Geux, Dr. Mauro Alini, Dr. David Eiglin and Nicola DiMarzio for initiating a strong collaboration on our works for drug discovery. Their collective enthusiasm, ambition, and determination to achieve our research objectives within a short timeframe despite a global pandemic was infectious. To the COST-ACTION Stratagem, I owe a debt of gratitude for financing this challenging period.

Most essentially, I would also like to express my sincere gratitude to Elena Isaevska, for being by my side through thick and thin and inspiring me to always do better, to Rana Dash, for being the friend who helped me find my happiness, strength, and identity and to Guilherme Ferreira for being my light and rock.

To the wonderful people that I have met during my years in Turin, Adriana Zarovska, Francisca Lima, Milena Manasievska, Johnny Karam, Caterina Avenati, Cesar Olivera, Lia Millecamps, Carolina Branco, Slavica Trajkova, João Vieira and Giacomo Frassineti - having you in my life has not only shaped me but also made every day in Turin truly memorable.

Lastly and most importantly I express a profound sense of gratitude to my entire family and to my beloved parents, P A Ananthanarayanan and Prabha Ananthanarayanan. I am eternally indebted to them for their constant encouragement, infinite patience and innumerable sacrifices. They are my greatest strength, everlasting love and unyielding support and I will continue to carry these through all my endeavours in the future.

Preeta Ananthanarayanan

TABLE OF CONTENTS

TABLE OF ABBREVIATIONS

3D	3-Dimensional
ABR	Active Breakpoint Cluster Region-Related Protein
AD	Anno Domini
ADI	Arginine deiminase
ADM2	Adrenomedullin 2
ADP	Adenosine diphosphate
AKT	AKT Serine/Threonine Kinase
AKT3	AKT Serine/Threonine Kinase 3
ALOX12B	Arachidonate 12-Lipoxygenase 12R Type
ANNOVA	Analysis of Variance
AP-1	Activator Protein 1
ARF	Alternate Reading Frame
ARID1B	AT-Rich Interaction Domain 1B
ATCC	American Type Cell Culture
ATF6	Activating Transcription Factor 6
ATM	Ataxia Telangiectasia Mutated
ATP	Adenosine triphosphate
ATR	Ataxia Telangiectasia and Rad3-Related
AURKA	Aurora Kinase A
BAM	Binary Alignment Map
BAP1	BRCA1 Associated Protein 1
BAX	BCL2 Associated X
BCA	Bicinchoninic Acid
BEV	Bevacizumab
BEX	Bexarotene
BEX2	Brain Expressed X-Linked 2
bHLH	Basic Helix Loop Helix
BIP	Biphasic
BLM	Bloom Syndrome RecQ Like Helicase
BQR	Base Quality Recalibration
BQSR	Base Quality Score Recalibration
BRCA1	Breast Cancer 1
BRCA2	Breast Cancer Type 2
BRD4	Bromodomain Containing 4
BSA	Bovine Serum Albumin
C/EBP-β	CCAAT Enhancer Binding Protein Beta
CAF	Cancer Associated Fibroblasts
CA-IX	Carbonic Anhydrase 9
CAR	Chimeric Antigen Receptor
CCL2	C-C Motif Chemokine Ligand 2

CCL5	C-C Motif Chemokine Ligand 5
CCND2	Cyclin D2
CCR2	C-C Motif Chemokine Receptor 2
CCR4	C-C Motif Chemokine Receptor 4
CCR5	C-C Motif Chemokine Receptor 5
CCR6	C-C Motif Chemokine Receptor 6
CD	Cluster of Differentiation
CDH1	Cadherin 1
CDK12	Cyclin Dependent Kinase 12
CDK4	Cyclin Dependent Kinase 4
CDKN2A	Cyclin Dependent Kinase Inhibitor 2A
Cdt2	Denticleless Protein Homolog
CEA	Carcinoembryonic Antigen
CEBPA	CCAAT Enhancer Binding Protein Alpha
CHD3	Chromodomain Helicase DNA Binding Protein 3
CHOP	C/EBP Homologous Protein
CI	Confidence Interval
CIC	Capicua Transcriptional Repressor
CISPT	Cisplatin
COP1	Constitutive Photomorphogenesis Protein 1
CPT-11	Irinotecan
CREB3L3	CAMP Responsive Element Binding Protein 3 Like 3
CREBBP	CREB Binding Protein
CRL	Cullin Ring Ligase
CSF2	Colony Stimulating Factor 2
CT	Computed Tomography
CTLA	Cytotoxic T-Lymphocyte Antigen 4
CUL1	Cullin 1
CUL4A	Cullin 4A
CXCL12	C-X-C Motif Chemokine Ligand 12
CXCR4	C-X-C Motif Chemokine Receptor 4
DAB	3,3′-Diaminobenzidine
DAPI	4′,6-diamidino-2-phenylindole
dbNSFP	Database of Non-Synonymous Functional Prediction
DC	Dendritic Cell
DDIT3	DNA Damage Inducible Transcript 3
DET1	De-Etiolated Homolog 1
DMEM	Dulbecco’s Modified Eagle Medium
DMM	Diffuse Malignant Mesothelioma
DNA	Deoxyribonucleic acid
DNAJB9	DNAJ Heat Shock Protein Family (Hsp40) Member B9
DOT1L	DOT1 Like Histone Lysine Methyltransferase

E2F1	E2F Transcription Factor 1
EBI	European Bioinformatics Institute
EBM	Endothelial Cell Basal Medium
EC50	Half maximal effective concentration
ECF	Extracellular Factor
ECM	Extracellular Matrix
EDTA	Ethylene diamine tetraacetic acid
EGFR	Epidermal Growth Factor Receptor
EGM	Endothelial Cell Growth Medium
EGTA	Ethylene glycol-bis(2-aminoethylether) tetraacetic acid
EIF2α	Eukaryotic Translation Initiation Factor 2A
ELISA	Enzyme-Linked Immunosorbent Assay
EMBL	European Molecular Biology Laboratory
EMP	Elongated Mineral Particle
EMT	Epithelial-Mesenchymal Transition
EP300	E1A Binding Protein P300
EPI	Epithelioid
EPP	Extrapleural Pneumonectomy
ER	Endoplasmic Reticulum
ERBB2	Erb-B2 Receptor Tyrosine Kinase 2
ERBB4	Erb-B2 Receptor Tyrosine Kinase 4
ERG	ETS Transcription Factor ERG
ERK	Extracellular Signal-Regulated Kinase
ESC	Embryonic Stem Cell
EZH2	Enhancer of Zeste Homolog 2
FAK	Focal Adhesion Kinase
FAT1	FAT Atypical Cadherin 1
FBS	Fetal Bovine Serum
Fbw5	F-Box/WD Repeat Containing Protein 5
FBXW7	F-Box/WD Repeat Domain Containing 7
FDA	Food and Drug Administration
FDG	Fluorodeoxyglucose
FDR	False Discovery Rate
FGF-2	Fibroblast Growth Factor 2
FGF4	Fibroblast Growth Factor 4
FI	Functional Interaction
FISH	Fluorescence in-situ Hybridization
FITC	Fluorescein isothiocyanate
FLCN	Folliculin
FLJ37644	SOX9 Antisense RNA 1
FOXP1	Forkhead Box P1
FUBP1	Far Upstream Element Binding Protein 1

GALNT12	Polypeptide N-Acetylgalactosaminyltransferase 12
GAPDH	Glyceraldehyde 3-phosphate dehydrogenase
GATA2	GATA Binding Protein 2
GATK	Genome Analysis Toolkit
GEO	Gene Expression Omnibus
GFP	Green Fluorescent Protein
GINS2	GINS Complex Subunit 2
GLUT1	Glucose Transporter Type 1
GM-CSF	Granulocyte-Macrophage Colony-Stimulating Factor
GO	Gene Ontology
GOA	Gene Ontology Annotation
GPC3	Glypican 3
GRID	Global Research Identifier Database
GRP78	Glucose-Regulated Protein 78
GUSB	Glucuronidase Beta
H&E	Hematoxylin and Eosin
H4	Histone 4
HDAC	Histone Deacetylase
HDAC1	Histone Deacetylase 1
HDAC2	Histone Deacetylase 2
HGF	Hepatocyte Growth Factor
HIF	Hypoxia-Inducible Factor
HIST1H4	Histone Cluster 1 H4 Family
HIST1H4I	Histone Cluster 1 H4 Family Member I
HIST3H3	Histone Cluster 3 H3
HIST4H4	Histone Cluster 4 H4
HMGB1	High Mobility Group Box 1
HRP	Horseradish Peroxidase
HSPA4L	Heat Shock Protein Family A (Hsp70) Member 4 Like
HSV	Herpes Simplex Virus
HT	High Throughput
HTS	High Throughput System
HUVEC	Human Umbilical Vein Endothelial Cells
I2D	Interologous Interaction Database
IC50	Half maximal Inhibitory Concentration
ICAM1	Intercellular Adhesion Molecule 1
ICD	Immunogenic Cell Death
IF2	Interferon 2
IFN-α	Interferon Alpha
IGF	Insulin Like Growth Factor
IGF-1R	Insulin Like Growth Factor 1 Receptor
IHC	Immunohistochemistry

IL	Interleukin
IL7R	Interleukin 7 Receptor
IMIG	International Mesothelioma Interest Group
IMRT	Intensity-modulated radiation therapy
INHBE	Inhibin Subunit Beta E
INK4	Inhibitor of CDK4
iPSC	Induced Pluripotent Stem Cell
IRE1	Inositol-requiring enzyme 1
IRF7	Interferon Regulatory Factor 7
IRF8	Interferon Regulatory Factor 8
IU	International Unit
JAK3	Janus Kinase 3
KD	Dissociation Constant
KDM5A	Lysine Demethylase 5A
KDM5C	Lysine Demethylase 5C
KDR	Kinase Insert Domain Receptor
KI	Inhibitory Constant
KLF4	Kruppel Like Factor 4
KMT2C	Lysine Methyltransferase 2C
KMT2D	Lysine Methyltransferase 2D
LAG-3	Lymphocyte Activating 3
LAMP-1	Lysosomal Associated Membrane Protein 1
LATS2	Large Tumour Suppressor Kinase 2
LC	Liquid Chromatography
LDH	Lactate Dehydrogenase
LMM	Localized Malignant Mesothelioma
LY96	Lymphocyte Antigen 96
LYZ	Lysozyme
MAPK	Mitogen-Activated Protein Kinase
MAPK1	Mitogen-Activated Protein Kinase 1
MAPS	Mesothelioma Avastin Cisplatin Pemetrexed Study
MBV	Multi Base Variant
MDM2	Mouse Double Minute 2 Homolog
MDSC	Myeloid-Derived Suppressor Cell
MEF2B	Myocyte Enhancer Factor 2B
MEN1	Menin 1
MET	Mesenchymal Epithelial Transition
MFI	Mean Fluorescence Intensity
MGI	Mouse Genome Informatics
MHC	Major Histocompatibility Complex
MIF	Macrophage Migration Inhibitory Factor
MLH1	MutL Homolog 1

MLN	MLN4924/Pevonedistat
MMP	Matrix Metalloproteinases
MNC	Mononuclear Cell
MPM	Malignant Pleural Mesothelioma
MRC5	Medical Research Council Cell Strain 5
MRF	Modulator Recognition Factor
MRI	Magnetic Resonance Imaging
MS	Mass Spectrometry
MSH2	MutS Homolog 2
MSLN	Mesothelin
MTA1	Metastasis Associated 1
MTA2	Metastasis Associated 2
MTAP	Methylthioadenosine Phosphorylase
MTOR	Mechanistic Target of Rapamycin Kinase
MYC	MYC Proto-Oncogene
MYD88	Myeloid Differentiation Primary Response 88
NAE	NEDD8-activating enzyme
NCBI	National Center for Biotechnology Information
NCOR1	Nuclear Receptor Corepressor 1
NEDD8	Neural Precursor Cell Expressed, Developmentally Down-Regulated 8
NF2	Neurofibromin 2
NFKB1	Nuclear Factor Kappa B Subunit 1
NF-κB	Nuclear Factor Kappa B
NGS	Next-Generation Sequencing
NOTCH2	Notch Receptor 2
NOTCH3	Notch Receptor 3
NOTCH4	Notch Receptor 4
NPM1	Nucleophosmin 1
NR	Non-Responder
OLA	Olaparib
P/D	Pleurectomy or Decortication
PAGE	Polyacrylamide Gel Electrophoresis
PAN	Panobinostat
PARK2	Parkin RBR E3 Ubiquitin Protein Ligase
PARP1	Poly(ADP-Ribose) Polymerase 1
PAX5	Paired Box 5
PBMC	Peripheral Blood Mononuclear Cell
PBS	Phosphate-Buffered Saline
PCL	Pseudomesotheliomatous Carcinoma of The Lung
PCNA	Proliferating Cell Nuclear Antigen
PCR	Polymerase Chain Reaction
PD1	Programmed Cell Death Protein 1

PDGF	Platelet Derived Growth Factor
PDGF-A	Platelet Derived Growth Factor Subunit A
PDGFR	Platelet Derived Growth Factor Receptor
PDGFRA	Platelet Derived Growth Factor Receptor Alpha
PD-L1	Programmed Death Ligand 1
PDMS	Polydimethylsiloxane
PE	Phycoerythrin
PEG	Polyethylene glycol
PERK	Protein Kinase R-like ER kinase
PET	Positron Emission Tomography
Pfam	Protein Families
PFS	Progression-Free Survival
PI3K	Phosphoinositide-3-Kinase
PIK3C2G	Phosphatidylinositol-4-Phosphate 3-Kinase Catalytic Subunit Type 2 Gamma
PIK3CD	Phosphatidylinositol-4,5-Bisphosphate 3-Kinase Catalytic Subunit Delta
PKH2	PKB-Activating Kinase Homolog 2
PMAIP1	Phorbol-12-Myristate-13-Acetate-Induced Protein 1
PMS1	Postmeiotic Segregation Increased 1
PMSF	Phenylmethylsulfonyl Fluoride
POLE	DNA Polymerase Epsilon
PP1R15A	Protein Phosphatase 1 Regulatory Subunit 15A
PPAR-α	Peroxisome Proliferator Activated Receptor Alpha
PRDM1	PR/SET Domain 1
PRMT5	Protein Arginine Methyltransferase 5
PT	Cisplatin
PTEN	Phosphatase and Tensin Homolog
PTPN11	Protein Tyrosine Phosphatase Non-Receptor Type 11
PTPRT	Protein Tyrosine Phosphatase Receptor Type T
QC	Quality Control
qRT	Quantitative Reverse Transcription
R	Responder
RAD50	RAD50 Double Strand Break Repair Protein
RAD51	DNA Repair Protein RAD51 Homolog 1
RAD51B	RAD51 Paralog B
RAD52	RAD52 Homolog, DNA Repair Protein
RARA	Retinoic Acid Receptor Alpha
RARB	Retinoic Acid Receptor Beta
RET	Rearranged During Transfection
RGD	Arginylglycylaspartic acid
RIPA	Radioimmunoprecipitation assay
RLU	Relative Luminescence Units

RNA	Ribonucleic Acid
RNF43	Ring Finger Protein 43
RNS	Reactive Nitrogen Species
ROS	Reactive Oxygen Species
RPMI	Roswell Park Memorial Institute
RPS6KA4	Ribosomal Protein S6 Kinase A4
RRM2	Ribonucleotide Reductase Regulatory Subunit M2
RUNX1	Runt-Related Transcription Factor 1
SAR	Sarcomatous
SAW	Surface Acoustic Wave
SBV	Single Base Variant
SCF	SKP1-CUL1-F-box
SDHA	Succinate Dehydrogenase Complex Flavoprotein Subunit A
SDS	Sodium Dodecyl Sulfate
SEER	Surveillance, Epidemiology, and End Results Program
SEM	Scanning Electron Microscopy
SEM	Standard Error of Mean
SETBP1	SET Binding Protein 1
SETD2	SET Domain Containing 2
SETDB1	SET Domain Bifurcated 1
SIM	Sound Induced Morphogenesis
SKP1	S-Phase Kinase Associated Protein 1
SMAD2	Mothers Against Decapentaplegic Homolog 2
SMAD3	Mothers Against Decapentaplegic Homolog 3
SMARCA4	SWI/SNF Related, Matrix Associated, Actin Dependent Regulator Of Chromatin, Subfamily A, Member 4
SMARCB1	SWI/SNF Related, Matrix Associated, Actin Dependent Regulator Of Chromatin, Subfamily B, Member 1
SNP	single nucleotide polymorphism
SOX9	SRY-Box Transcription Factor 9
SRR	Split Read Realignment
SUZ12	Suppressor of Zeste 12 Protein Homolog
SV	Structural Variant
SV40	Simian Virus 40
TAA	Tumour Associated Antigen
TAM	Tumour Associated Macrophage
TBS	Tris-Buffered Saline
TCGA	The Cancer Genome Atlas
TET2	Tet Methylcytosine Dioxygenase 2
TGF	Transforming Growth Factor
TIF-1	Transcriptional Intermediary Factor 1
TIL	Tumour-infiltrating lymphocyte

TIM-3	T-Cell Immunoglobulin and Mucin Domain-Containing Protein 3
TLR5	Toll Like Receptor 5
TLR9	Toll Like Receptor 9
TME	Tumour Microenvironment
TNF	Tumour Necrosis Factor
TNF-R1	Tumour Necrosis Factor Receptor Type 1
TP53	Tumour Protein P53
TP63	Tumour Protein P63
TRAF7	TNF Receptor Associated Factor 7
TSC1	Tuberous Sclerosis 1
TTF-1	Thyroid Transcription Factor-1
UCSC	University of California, Santa Cruz
UHRF1	Ubiquitin Like with PHD And Ring Finger Domains 1
UK	United Kingdom
ULA	Ultra-Low Attachment
UPR	Unfolded Protein Response
USA	United States of America
UTR	Untranslated Region
UV	Ultraviolet
VATS	Video-Assisted Thoracoscopic Surgery
VCM	Vascularised Cancer Model
VEGF	Vascular Endothelial Growth Factor
VEGFR	Vascular Endothelial Growth Factor Receptor
VHL	Von Hippel-Lindau Tumour Suppressor
VISTA	V-domain Immunoglobulin Suppressor of T cell Activation
VTCN1	V-Set Domain Containing T Cell Activation Inhibitor 1
VTM	Vascularised Tumour Model
WDPM	Well-Differentiated Papillary Mesothelioma
WHO	World Health Organization
WT1	Wilms Tumour 1
XBP1	X-Box Binding Protein 1
YAP1	Yes1 Associated Transcriptional Regulator
α-SMA	Alpha-Smooth Muscle Actin
βTrCP	F-box/WD repeat-containing protein 1A

LIST OF FIGURES

LIST OF TABLES

REVIEW OF LITERATURE

1 INTRODUCTION

Malignant Pleural Mesothelioma (MPM) is a highly aggressive cancer having diverse pathologies and mechanistic origins [1]. Mesothelioma develops primarily from the pleura and peritoneum [2]. This type of cancer develops mostly because of asbestos exposure in Europe, Australia and Japan and also in USA, India where asbestos continues to be used, with a latency between 10 and 50 years from the exposure [3]. According to the WHO classification, MPM is either classified as epithelioid (mostly composed of epithelial-shaped cells), sarcomatous (mostly composed of spindle-shaped cells), or biphasic (composed of both types of cells) [3]. Most of the time the tumour is detected only at late-stages as radiological diagnostic tools are not effective and serum biomarkers for early detection have not yet been established [2]. The prognosis is generally poor with a reported median survival from presentation of 9–12 months in either untreated or treated (surgery, radiotherapy, or chemotherapy) patients [4]. The common consensus is that novel molecular targets should be identified by elucidating molecular defects and pathways involved in MPM pathogenesis and progression, to achieve better disease control and therapeutic options in the near future [1–4].

2 ASBESTOS AND DISEASE

2.1 ETIOLOGY AND HISTORY OF ASBESTOS USE

Asbestos, from the Greek word "ἄσβεστος" meaning "inextinguishable" or "unquenchable", is a family of naturally occurring minerals that have been used in various industries over hundreds of years. Mined from the mountains of Arcadia, asbestos crystals were first recorded in ancient Rome by Pliny the Elder (23–79 AD) as a material that could be easily woven into different shapes to make bucket shaped pottery and was used for cooking and storing of food. These pots have been estimated to contain over 70% asbestos and were used predominantly due to their high heat-resistive capacities [5]. Industrialisation, increasing demand and mining which dramatically expanded since the early 20th century saw increasing prevalence of MPM [5] while the use and manufacture of asbestos products peaked in 1970s globally. As of 2006, the largest producers were Russia, China, Canada, Kazakhstan, Brazil, and Zimbabwe with Canada engaging in trade of 300,000 tons of crude asbestos [6].

2.2 ASBESTOS AND ERIONITE – PUTATIVE ONCOGENIC AGENTS

Asbestos initially comprised of a group of 6 different silicate minerals primarily composed of long chains of silicon and oxygen that gives its unique long and fibrous nature. These fibres include actinolite, amosite, anthophyllite, crocidolite, tremolite that are amphiboles and chrysotile, which is a serpentine group of silicate mineral [7, 8] (Figure I). These are very thin irregular 'fibrils' having dimensions of 0.01 to 0.5 µm and a silky lustre, that are quite brittle and readily pliable by hand affecting their 'mesotheliomagenicity' [7] .

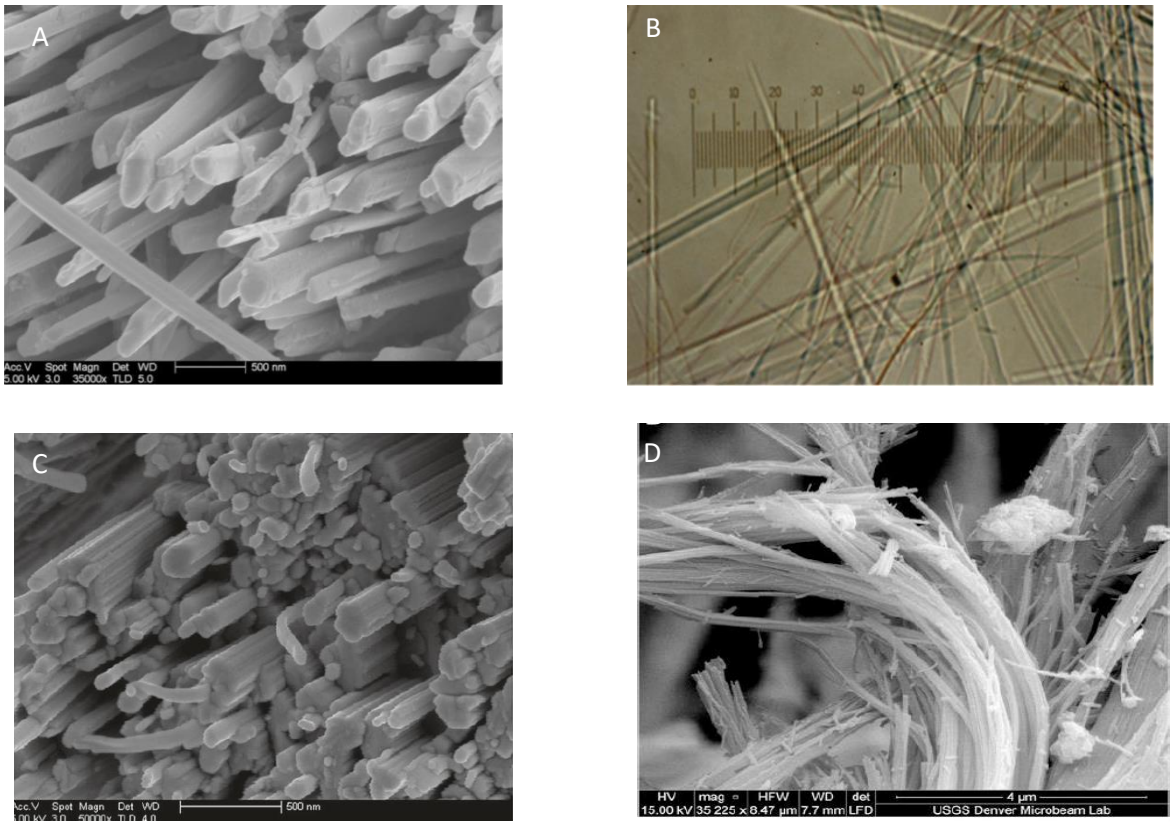

Figure I: Field Emission Scanning Electron Micrograph (SEM) of A) tremolite asbestos fibres B) actinolitic byssolite fibres (2 microns width). C) Crocidolite fibres and D) fibrous erionite. Source: Wylie, 2017.

Asbestos' unique properties include fire resistance, high tensile strength, flexibility and affordability among countless others [9]. These advantages allowed widespread use of asbestos over the years for a number of commercial applications with 85% of asbestos cement being used for low-cost building materials, piping and sheet roofs. Other applications included tiling,

gaskets, insulation boarding, automobile braking, military gas masks, hospital ventilators and certain textiles making it extremely invaluable. When mixed with rubber, tar and plastics they were used as steam engine components, roofing, ship panelling and electrical boards and wiring [9–13]. As its value rose, the catastrophic nature of the mineral became apparent.

Although the carcinogenicity of asbestos is now well established, there are numerous asbestos-like fibres that have been discovered since the establishment of different regulatory bans, where ambiguity still exists on their definition of 'asbestos' or 'fibrous minerals' based on context, industrial use, regulatory and physical and chemical properties and impact on disease. Apart from the previously discussed six different commercially available fibres, about over 400 naturally occurring fibrous minerals exist that potentially cause mesotheliomas and carcinomas following human exposure, listed in Figure II.

	Regulated fibrous minerals	Non-regulated fibrous minerals
Serpentine	Chrysotile ..	Antigorite Lizardite
Amphiboles	Actinolite Amosite (grunerite) Anthophyllite Crocidolite (riebeckite) Tremolite ..	Arfvedsonite Cummingtonite Fluoro-edenite Magnesio-hornblende Richterite Winchite
Gageite	..	Balangeroite
Wollastonite	..	Wollastonite
Zeolites	.. ..	Erionite Mordenite
Palygorskite-sepiolite	.. ..	Palygorskite Sepiolite
Carlosturite	.. ..	Carlosturite About 375 other fibrous minerals[3]

Figure II: Regulated and non-regulated fibrous minerals with carcinogenic properties. Source: Baumann et al., 2013.

Asbestos related toxicity is primarily due to its dimensions and bio-persistence leading to fibrosis, while the disease causing nature of these other fibrous minerals is still up for debate due to lack of funding and scientific consensus [8]. The regulatory definition for airborne particles to be classified as 'fibres' or Elongated Mineral Particles (EMPs) are that they be

longer than 5 microns, be visible by optical microscopy and have an aspect ratio of at least 3:1. While most asbestos fit these rules, there are plenty of unregulated fibres listed above that are below the resolution of light microscopy and <5 microns in length [7]. For example, erionite has been considered one of the most carcinogenic form of fibre but continues to be unregulated while chrysotile, reportedly less carcinogenic than erionite, is regulated [14]. Chrysotile continues to be mined "controllably" and sold worldwide particularly in low-income countries exponentially accounting to >95% of global asbestos use. [15]. Vermiculite contaminated with asbestiform winchite and richterite in Montana, USA and antigorite contamination among nickel miners in Poland continue to cause asbestosis and related diseases [8], while New Caledonia saw increased MPM cases due to the distribution of serpentinite tainted antigorite fibres to pave roads [16]. One of the largest MPM 'pandemics' to be witnessed is in certain Cappadocian villages in Turkey where erionite is being used to build houses and roads causing extreme forms of the disease [14].

As incidences of lung disease grew, various countries slowly decreased production and use of crocidolite and amosite, like South Africa in 1990 [17]. The European Union initially banned the use, import and export of 5 primary types of asbestos in 1999 but still allowed the use of white chrysotile asbestos for certain un-substituted applications. A total ban on all asbestos products was then placed into effect in 2005 [18]. Partial and complete bans soon followed in other countries in compliance with national and international trade laws according to the WHO. To date, there are only 53 countries worldwide that have called for bans on the use of asbestos [15].

With millions of workers worldwide being exposed to various forms of asbestos during the life cycle of the product from extraction, manufacture, use and disposal, it poses a massive threat to their health, with many individuals still developing the disease in 2020 following years of continuous exposure [7]. Over the past 20 years, there has been a conscious bid to rapidly phase out and replace any asbestos containing materials still in use to move towards an asbestos free and MPM free era.

3 EPIDMIOLOGY AND PREVALENCE OF MALIGNANT PLEURAL MESOTHELIOMA

The first definite link to diffuse pleural mesothelioma and asbestos exposure was reported in 1960 in the North Western cape province of South Africa where 32 out of 33 men and women had prior exposure to crocidolite asbestos [19]. Up to 20,000 asbestos-related lung cancers and 10,000 mesotheliomas occur annually across the population of Western Europe, Scandinavia, North America, Japan, and Australia [6, 20] and account for 3200 deaths in North America and 5000 deaths in Western Europe. A surge in disease is expected in nations like India, China, Russia, Zambia, Colombia, and Kazakhstan where production and use is expanding without adequate protection of those being exposed to asbestos [5]. Although the mortality of MPM is strongly dependent on the history of the country's population, around 107,000 people die annually from MPM and other asbestos-related diseases. The incidence in men is several folds higher than women. The long latency of the disease indicates that the incidence is expected to peak between 2020-2030 globally [21] despite measures implemented since 1970s and 1980s to regulate and eliminate use of asbestos in industrial nations. [13]. MPM is more common compared to peritoneal mesotheliomas. In a study conducted by Suzuki in 2000 showed pleural sites in 73.1% of the 1517 cases studied while secondary peritoneal mesothelioma was presented in 23.7% of certain asbestos insulation workers [22]. While pericardial mesothelioma is extremely rare, only 5 cases were recorded in this study. Globally, only 200 cases of pericardial mesothelioma have been recorded of date accounting for 2-3% of all cardial and pericardial malignancies [23, 24].

Although most MPM cases are attributed to occupational asbestos exposure, environmental exposure also has been found to be significant player in the disease. Environmental exposure included those individuals living in proximity to industries, domestic exposure from home projects and familial exposures. According to the SEER database (Surveillance, Epidemiology and End Results) recording all cases belonging to the United States, describe MPM peaking during the 1980s and 1990s with an incidence rate of 1.8 per 100,000 and 0.4 per 100,000 in men and women respectively [21]. An extensive review on 44 studies from 18 different countries shows the distribution, heterogeneity, measure of exposure and disease outcomes in both men and women [25]. The highest incidence rate in the world is being seen in Australia with 35 million cases per year [6]. These nations included industrial and mining zones in Wittenoom in Western Australia; Piemonte, Veneto, Liguria and Lombardy regions in Italy;

Thetford Mines in Canada, and hotspots of naturally occurring asbestos sites like Sivas, Turkey; New Caledonia; Biancavilla in Sicily, Italy and North Dakota, USA (Figure III). These studies have not been performed in developing countries, where further foci could be found.

	Mesothelioma Incidence			Use of Asbestos		
Country	Cases/Year	Cases/ Million/Year	Tons/Year	Kg/Capita/ Year	Tons/ Mesothelioma	References*
Australia	490 (2000)	35	70,000 (1970)	5.5	140	13,14
Finland	74 (1999)	18	11,000 (1970)	2.4	150	15,16,17
France	750 (1996)	16	143,000 (1970)	2.7	190	30,31,32
Germany	1,007 (1997)	15	230,000 (1975)	2.9	230	18,19,35
Great Britain	1,595 (1999)	33	170,000 (1970)	3.1	110	20,21,22
Italy	930 (1995)	19	140,000 (1975)	2.5	150	33,35
Netherlands	377 (1997)	30	49,000 (1976)	3.6	130	23,24,25
New Zealand	50 (1996)	18	8,000 (1970)	2.8	160	26
Norway	48 (1995)	14	8,000 (1970)	2.0	170	27
Sweden	105 (1996)	15	20,000 (1970)	2.5	190	28,29
United States	2,800 (2000)	14	552,000 (1975)	2.6	200	3,34
ALL COUNTRIES	8,236	18	1,401,000	2.8	170	

*See the reference list.

Figure III: Global mesothelioma index and asbestos consumption as of 2004. Source: Tossavainen, 2004.

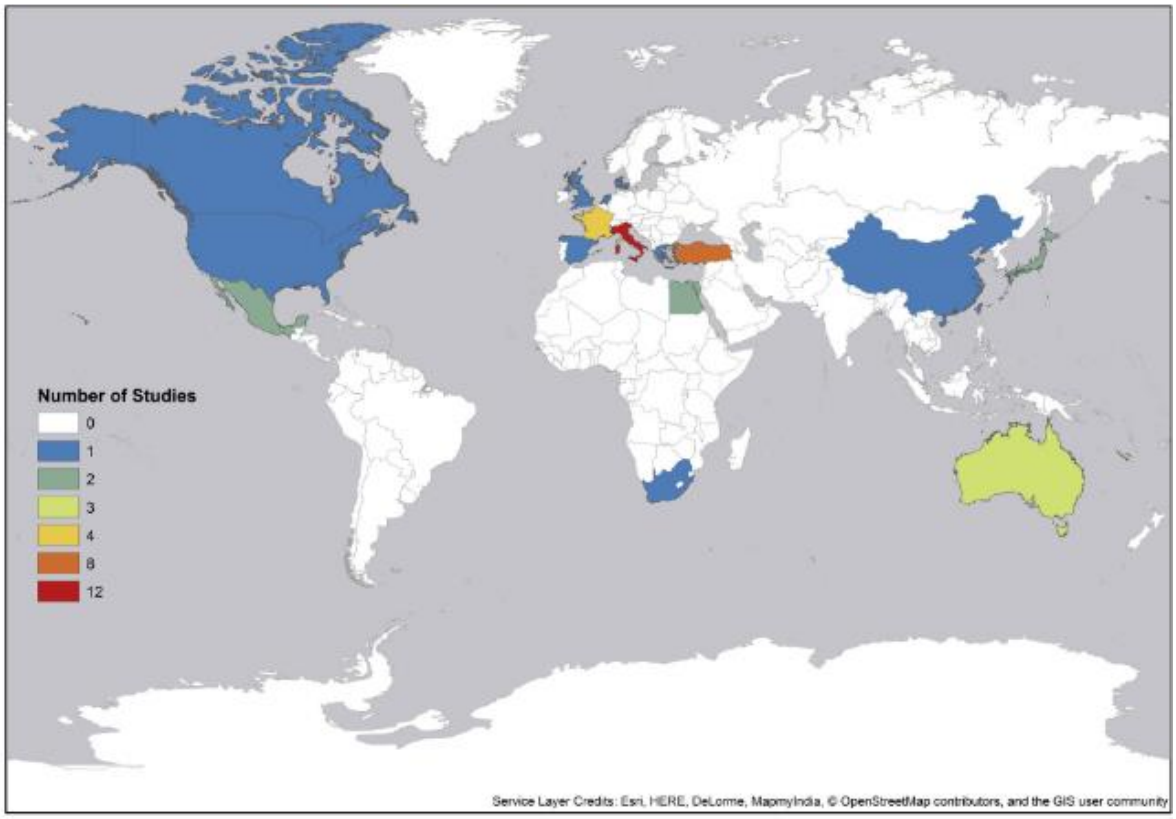

Figure IV: Global distribution of MPM on environmental exposure to asbestos. Source: Liu et al., 2017.

New Caledonia has a high incidence of MPM in the Houailou area with 128.7 cases per 100,000 people mainly due to the high serpentinite exposure from road surfaces, while people living near vegetation had a protective effect from the exposure [16]. In the UK, 3500 deaths are seen each year and it is expected to rise to 5000 deaths annually in the following years accounting for more than half of all the cancer related deaths in the UK [15]. In Europe (Figure IV), a review conducted between 2000 and 2015 identified multiple hotspots defined by specific occupational exposures such as proximity to shipyards (16 different studies) and asbestos cement manufacturing factories (10 studies) where a high incidence of MPM evolved over time [26]. One such classical example is the asbestos manufacturing town of Casale Monferrato in Italy which is infamous for causing disease among its workers and residents. The highest incidence rate was seen in the regions of Trieste, where asbestos is manufactured. Italy has incidences of 17.2 and 14.4 cases per 100,000 in men and women respectively; among males, Scotland and England has 8.8 and 8 cases per 100,000 persons, Netherlands 7.4 cases per 100,000 male persons. Other European nations like Spain, Germany, Belgium and France saw a wide range of occurrence from 0.6 to 4.24 per 100,000 persons [20] (Figure V). Similar rankings were seen for women in all countries albeit with lower values in relation to the men. The affected individuals were all found to work as dockyard workers, sea farers, asbestos textile, steel and iron, petrochemical and furniture manufacturing industry labourers. Most of this information is limited by the lack of extensive and thorough maintenance of data libraries particularly in developing and developed countries. For instance, in France, only 26 of the 96 districts have records on Mesothelioma surveillance that could lead to a gross underestimation of disease within the population distribution.

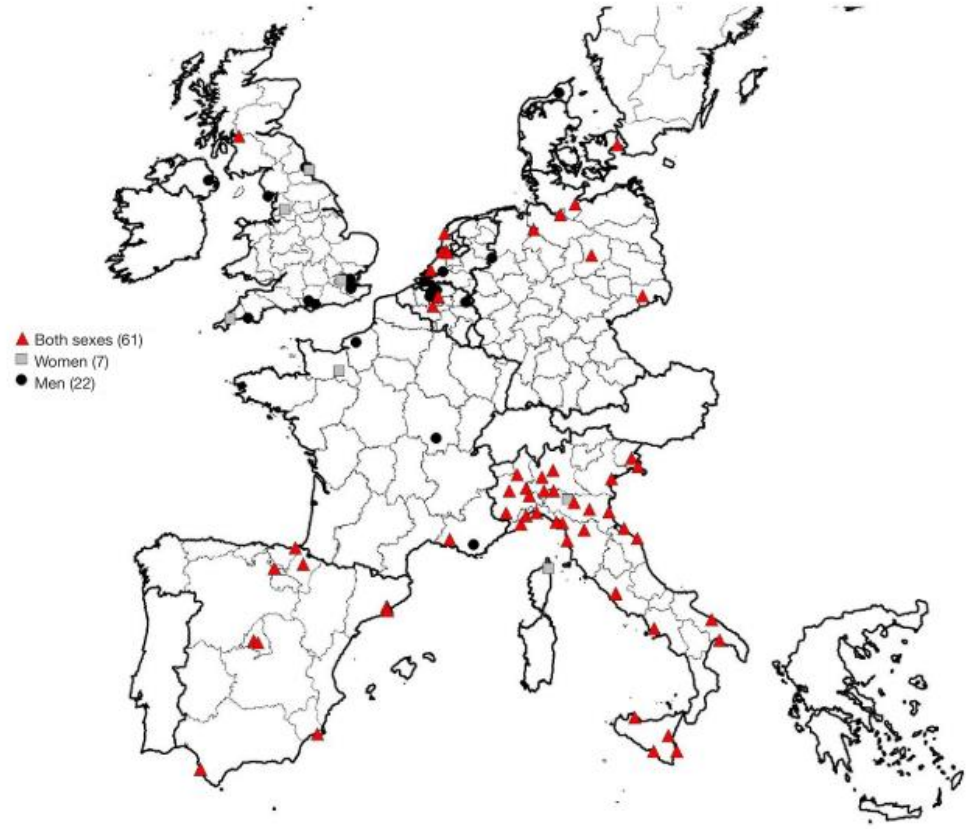

Figure V: Identification of MPM hotspots in Europe. Source: Nuyts et al., 2018.

4 PATHOGENESIS OF MESOTHELIOMA

4.1 PATHOPHYSIOLGY

The mesothelium, first identified by Bichat in 1837 and coined by Minot in 1880, refers to the epithelial lining of mesodermal cavities. It comprises of a monolayer of flattened cells covering the entire lining of three different serosal cavities – pleural, pericardial and peritoneal, including the organs within these cavities [27]. Mesothelial cells reside over a thin basement membrane and are supported by different kinds of stromal connective tissues. These cells are flat, squamous cells 25 microns in diameter with a central round or oval nucleus containing microtubules, vesicles, sparse mitochondria and poor Golgi and endoplasmic reticular network. Cells are often found with well-developed microvilli on the surface and strong cell-cell adherent junctions. Mesothelial cells have a strong role in maintaining the integrity of internal organs and providing protection against physical abrasions and invading pathogens. They have been found to secrete inflammatory cytokines, participate in antigen presentation and prevent

tumour cell adhesion [28] (Figure VI). These cells also undergo Epithelial Mesenchymal Transition (EMT), which has implications in both normal cellular repair and wound healing along with diseased mesothelioma.

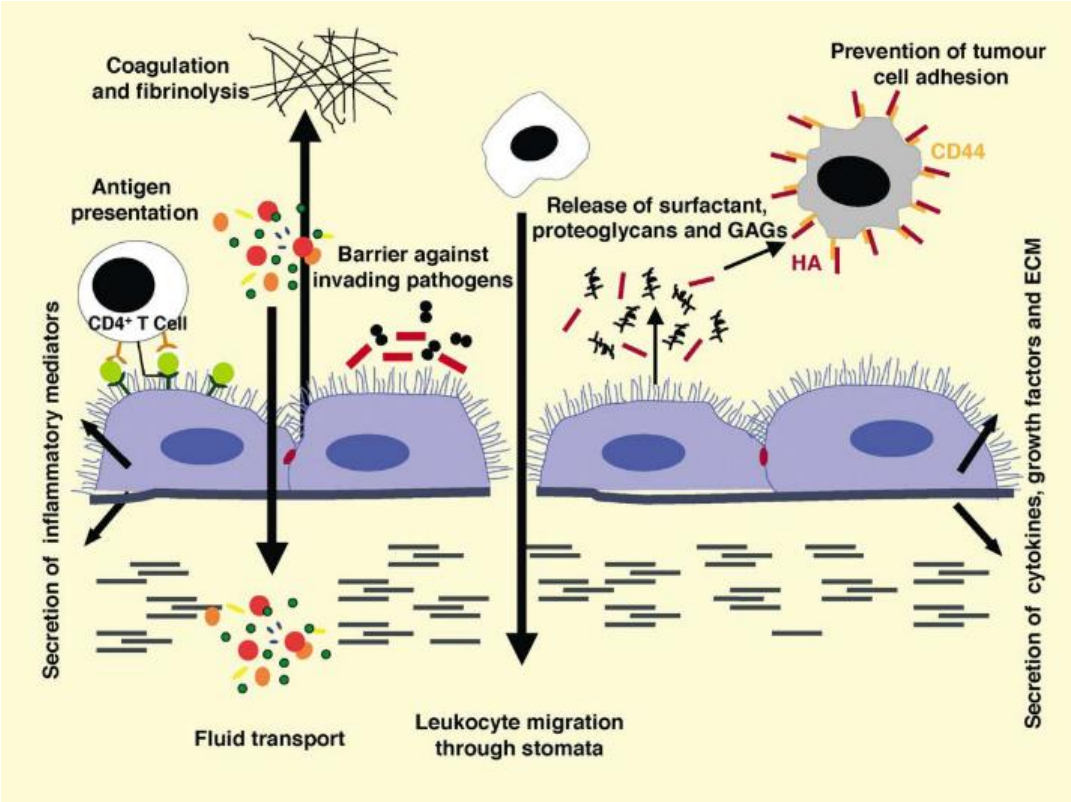

Figure VI: Overview of the functions of normal mesothelium Source: Mutsaers, 2004.

MPM are diffuse neoplasms that have a characteristic thick and confluent growth within the serosal membranes often resulting in associated effusions within the cavities and a decrease of pleural or peritoneal spaces [23, 29].

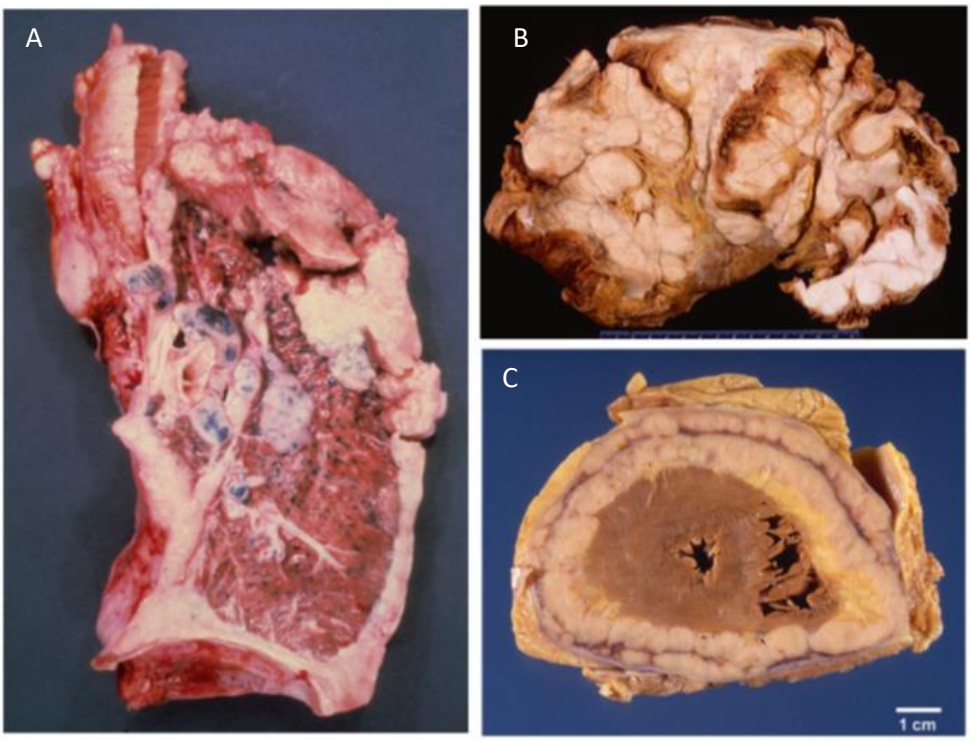

Figure VII: A) Pleural mesothelioma coronal slice of right lung showing the entire lung surrounded by white rind of tumour. B) Coronal slice of abdomen showing malignant peritoneal mesothelioma encompassing compressed bowels C) Transverse section of heart encased by malignant pericardial mesothelioma. Source: Pavlisko et al., 2017.

4.2 BASIS OF TRANSFORMATION

4.2.1 PRIMARY ASBESTOS ESPOSURE

Amphibole asbestos has been well established as a causative agent of MPM, specifically crocidolite fibres that are >=8µm in length due to longer bio-persistence. These fibres are able to penetrate the lung tissue and repeatedly cause tissue damage and repair and increased localised inflammation [30]. Amphibolic fibres react to lung fluids by leeching various minerals such as Ca, Na, Mg, K, Fe and Si by slow dissolution and fibres tend to persist in the lung after many years following exposure, while serpentine chrysotile is very soluble in lung fluid. Additionally, presence of talc further decreases its solubility [31] (Figure VIII).

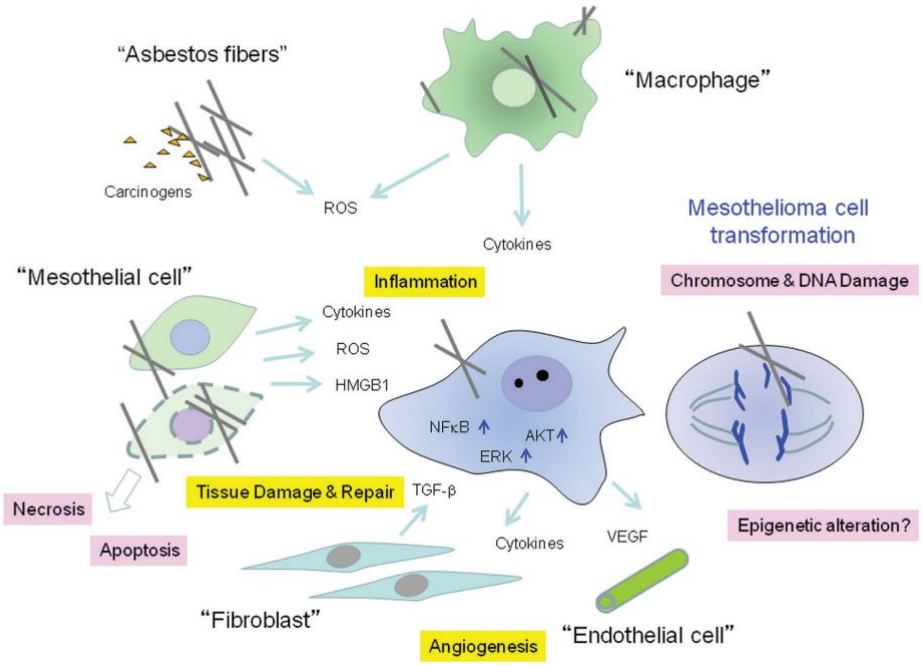

Figure VIII: Proposed mechanism of asbestos induced mesothelioma transformation. Source: Sekido, 2013.

The mechanisms of asbestos induced carcinogenicity have been extensively studied and there are multiple theories on how mesothelial cell transformation occurs to develop MPM over time. Following inhalation of the long and thin asbestos fibres into the lung, these fibres rest rather in the parietal pleural space than in the visceral pleura and trigger multiple cascades and cell-cell interactions through direct and indirect means. This could be explained by the fact that human mesothelial cells have been shown to be more sensitive to amosite asbestos toxicity in a dose depended manner by 10 to 100 times in comparison to human bronchial epithelial cells or fibroblasts [32]. Uptake of these fibres by the mesothelial and inflammatory cells triggers cell damage and repair pathways along with localised inflammation. Prolonged exposure ultimately leads to carcinogenesis although the exact mechanism of transformation still remains unclear [2, 30, 33, 34].

Classically four different mechanisms have been described.

- First, DNA damage induced by reactive oxygen species (ROS) and reactive nitrogen species (RNS) released by macrophages unable to digest the fibres leads to a spectrum of mutations within the genome causing malignancy [35, 36].

- Second, engulfment of the fibres by the mesothelial cells can physically interfere with cellular mitosis and spindle formation causing chromosomal abnormalities.
- Third, these fibres leach toxins and heavy metals bound to their surfaces and bind to proteins that interfere with normal cell function [2].
- Finally, cytokine signalling pathways including Tumour Necrosis Factor-α (TNF-α), Nuclear Factor kB (NF-κB) pathway [37–39] and Macrophage Migration Inhibitory factor (MIF-CD74) signalling [3] have been implicated in tumourigenesis. *In-vivo*, following asbestos exposure, pro-inflammatory reactions trigger macrophage differentiation of mononuclear phagocytes. Phagocytosis by the macrophages follows subsequent release of TNF-α and upregulation of TNF-R1 via paracrine and autocrine pathways and downstream activation of NF-κB, promoting cell survival. These surviving mesothelial cells accumulate DNA damage often caused by free radicals catalysed by iron leeched into peritoneal spaces by asbestos. Asbestos can further trigger multiple regulatory pro-survival signalling like the Epithelial Growth Factor Receptor (EGFR) dependent Extracellular Regulated Kinase 1/2 (ERK1/2) pathway, or cytokines such as Transforming Growth Factor-β (TGF-β), Interleukin-1 β (IL-1β) and Platelet-derived Growth Factor (PDGF) that induce inflammation, promote cell survival and mitosis [35, 36].

4.2.2 SV40 AND MESOTHELIOMA

SV40 or Simian Virus 40 is DNA virus commonly seen in primates that has been linked to MPM on multiple instances but not without its controversies. SV40 contaminated polio vaccines produced in 1955-78 was responsible for the species jump from monkeys to humans. Unlike permissive (i.e., condition where cells are lysed following infection and SV40 DNA replication) monkey cells and non-permissive (i.e., condition where SV40 DNA is not replicated and cells are transformed instead of lysis) rodent cells, human cells are semi-permissive to SV40 transformation which is rare event. Many significant positive correlations to MPM have now been re-evaluated as false positives attributing to plasmid PCR contaminations and lack of proper controls. Despite this, many carefully designed studies have indeed shown presence of SV40 in human MPM samples but not in adjacent normal tissues [30, 40]. SV40 has been seen as a causative agent of MPM as mesothelial cells are sensitive to transformation by SV40 both *in-vitro* and in *in-vivo* studies producing mesotheliomas in 100%

intrapleural and 60% intracardial injections in hamsters [27]. Two proteins coded by SV40 - the large T-antigen (Tag) and the small T-antigen (tag) – have been found to be oncogenic because of their ability to inactivate p53 and pRb tumour suppressor proteins [27, 30]. Tag has also been found to induce Insulin-like Growth Factor-1 (IGF-1) and IGF-1R while tag enhances Tag functions and thereby the direct mutagenicity via IGF-1 signalling cascade [27, 32, 41]. Furthermore, *in-vitro* experiments showed that human mesothelial cells in the presence of asbestos and SV40 developed more mutant foci in comparison to controls without asbestos exposure or asbestos only, suggesting presence of Tag and tag SV40 sequences and asbestos act as co-carcinogens [32]. Small t-antigen has been found to trigger carcinogenesis by activating Mitogen Activated Kinase protein (MAPK) signalling and Activator Protein-1 (AP-1) transcription factor, inducing cell invasiveness, telomerase activity and Notch-1 activation in human mesothelial and MPM cells [30].

4.2.3 ERIONITE EXPOSURE

Erionite, another fibrous mineral belonging to the zeolite group has also been recorded to cause MPM with highest potency. Although not inherently hazardous when undisturbed in rocks or soil, these fibres when present in surface soils, gravel and indoor dust built up by various activities can be potentially dangerous [7, 30]. Erionite is used to build homes and roads in the villages of Cappadocia, Turkey where over 50% of deaths are due to MPM. Evidence of hotspots of exposure have also been detected in Dunn County, North Dakota in the United States [14, 42]. Furthermore, a study conducted by Carbone et al., 2011, showed that the erionite fibres from North Dakota was structurally and chemically similar to the fibres isolated from Turkey. They appeared to be more potent in their ability to form tumourigenic foci in the presence of co-factors like high mobility group box-1 (HMGB-1) protein and TNF-α as part of the chronic inflammatory process triggering transformation [14].

4.2.4 GENETICS

Genetic predisposition to MPM has been a subject of debate and few evidences exist showing familial inheritance of the disease [5]. Here we discuss one such evidence of familial inheritance in the villages of 'Old' Sarihidir in Turkey in a study conducted by Yang et al., 2008 where MPM showed patterns of autosomal dominant presence in different families. High

risk members marrying into families with no familial history had their descendants developing MPM (Figure XI). This was however dependent strongly also on erionite exposure [30].

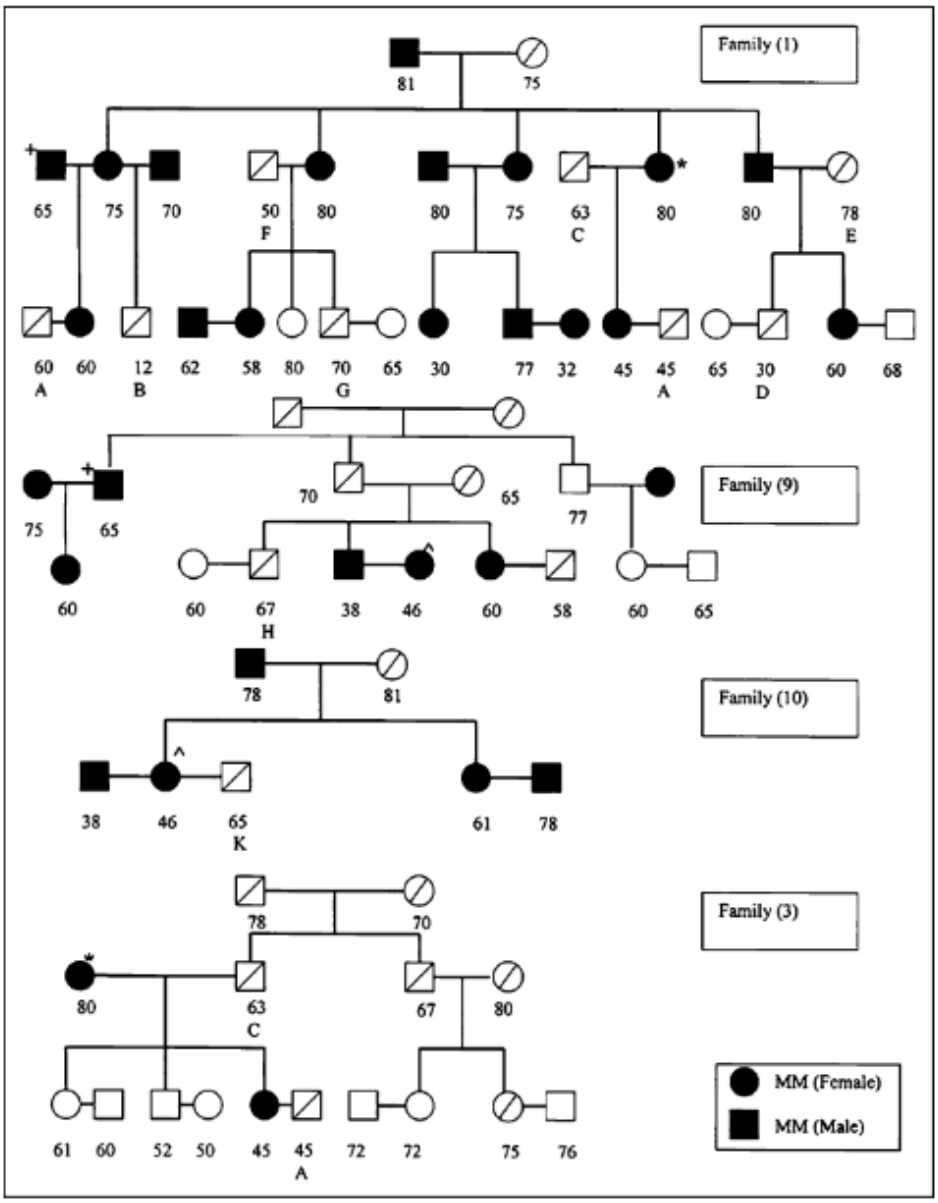

Figure IX: Pedigree of family of 30 from "Old" Sarihidir showing pattern of disease inheritance. Source: Yang et al., 2008.

4.2.5 RADIATION

Ionising radiation has also been etiologically linked to MPM in a small number of individuals receiving Thorotrast contrast agents emitting alpha particles [30, 43]. Further evidence linked patients who received prior radiotherapy for testicular cancer and Hodgkin's lymphoma, with the development of secondary mesothelioma tumours after an average of 21 years [44, 45]. Advanced knowledge of secondary tumours on radiation exposures are improving and it is possible that a stronger correlation between MPM and radiation will be found [5].

4.3 HISTOPATHOLOGY

Currently there are three basic histotypes of MPM recognised by the World Health Organisation – epithelioid, sarcomatous and biphasic [46–48]. One early study conducted in 1987 identified a prevalence of 50% epithelioid, 30% sarcomatous and 20% biphasic among all cases [23]. A more recent study by Suzuki in 2000 identified 61.1% epithelioid, 22.1% biphasic and lower 16.4% sarcomatous tumours [22]. These different forms demonstrate varying degrees of growth patterns and histological appearances [42].

4.3.1 EPITHELIOID HISTOTYPE

The most common epithelioid MPM has different heterogenous growth patterns including trabecular, tubule-papillary (branching tubules and short papillary networks) and solid variants [49]. The cells are oval, cuboidal or polygonal in shape with abundant cytoplasm, a paracentric prominent nuclei and occasional atypical mitosis. The presence of cytological atypia with anaplastic or highly pleomorphic cells often results in challenging distinction from PCL [23]. The pleomorphic variant with greater than 10% nuclear pleomorphisms has been shown to have a very poor survival, similar to that of sarcomatous neoplasms [46, 49]. Persons with epithelioid MPM have usually a median survival of 14 months, that is increased to 19 months if the MPM is resectable, according to the SEER database [47]. Mesothelin, which is normally expressed by the mesothelium having a role in cell adhesion, migration and invasion, is overexpressed in 75-100% of epithelioid MPM [48].

4.3.2 SARCOMATOUS HISTOTYPE

In sarcomatous MPM, cells are elongated, and spindle shaped. They are also heterogenous, mitotic, show pleomorphism and are arranged haphazardly or in 'fascicles' [28, 49]. Like the epithelioid subtype the sarcomatous MPM also exhibits multiple morphological subtypes identified as pleomorphic, lympho-histiocytoid, transitional and desmoplastic mesothelioma [23]. This form usually presents without much pleural effusions and metastasis occurs in over 60% of the cases and lacks mesothelin expression [50]. The reason of mesothelin loss remains unknown [48]. It has also been hypothesised that the sarcomatous type evolves from the epithelioid type directing towards further malignancy, but the morphological differentiation can be potentially reversible [48]. The median overall survival is least favourable of 13.1 months [51].

4.3.3 BIPHASIC HISTOTYPE

This subtype consists of both epithelial and sarcomatous cells inside the neoplasm, each constituting at least 10% of the tumour area [23, 49]. The extent of epithelioid and sarcomatous tissue presence therefore is responsible for the patient's survival and outcome. It has been observed that patients with less than 50% of epithelial components have a poor survival of 6.6 months in comparison to patients with greater than 50% epithelioid cells characterized by a survival of 20.1 months. Identification of the spindle components make it difficult to classify such a biphasic malignancy and in such instances, identification using specific predictive biomarkers such as BAP1 loss and CDKN2A/p16 homozygous deletion, discussed in detail in the following section, is necessary to discriminate biphasic from sarcomatous MPM [50].

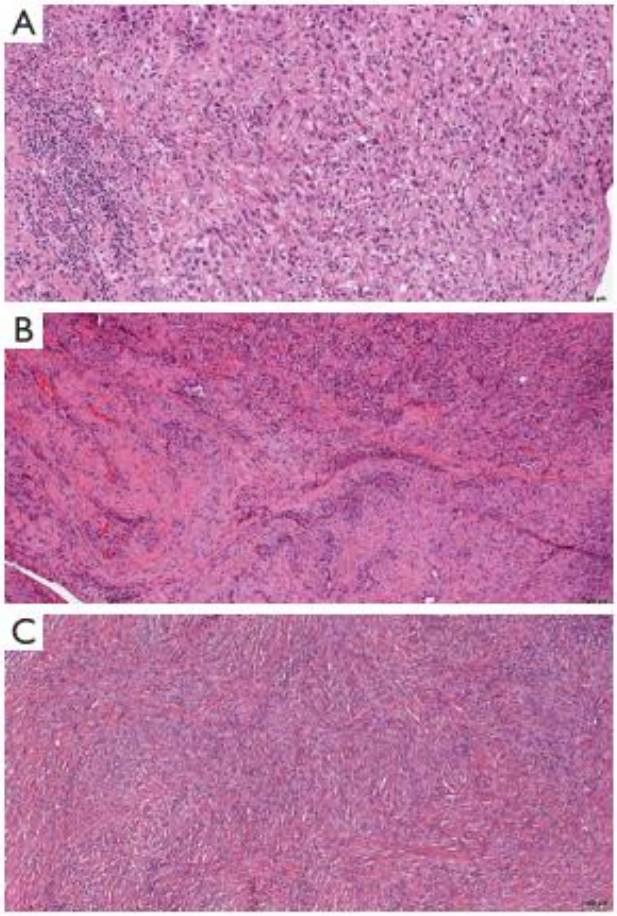

Figure X: H&E histological representative image showing A) epithelioid (10x) B) biphasic (5X) and C) sarcomatous (5X). Source: Brcic & Kern, 2020

5 PLEURAL MESOTHELIOMA DIAGNOSIS

MPM presents as multiple small nodules or macules of pleural surfaces usually parallel to the lymphatic system. In advanced form of MPM, patients present with dyspnoea, fatigue, chest pain, weight loss, insomnia and cough [29, 52]. Three different forms of MPM exist called well-differentiated papillary mesothelioma (WDPM), localised malignant mesothelioma (LMM) and diffuse malignant mesothelioma (DMM) [29, 50, 51]. WDPM is extremely rare form of the disease which is often associated with peritoneal disease. Multiple sets of deletions and mutations have been identified such as Nuclear Factor 2 (NF2) deletion, E2F1 point mutation along with normal BRCA1-associated Protein 1 (BAP1) expression and Cyclin Dependent Kinase Inhibitor 2A (CDKN2A/p16) that is useful in the differential diagnosis of WDPM [50, 51]. LMM presents with solitary localised nodules without involvement of the serosal surface, making is easily curable with surgery [23]. LMMs can be epithelioid, biphasic

and sarcomatous and some of them present with BAP1 and TNF Receptor Associated Factor 7 (TRAF7) mutations [50, 51]. DMM which is the most common form of the disease with diffused nodules and invasion possessing multiple challenges in its diagnosis and treatment [53]. Patients will typically complain of dypsnea and chest pain coupled with large pleural effusions into the pleural spaces which is visible on chest x-rays and Computed Tomography (CT) which is the radiological standard [23, 51, 54]. As the disease progresses, there is fusion of smaller nodules and cohesion of the visceral and parietal pleura. Tumours present unilaterally in 95% of all cases and in the right chest in 60% of cases. Oftentimes, the lung can get encased entirely by MPM and grow into the fissures and interlobular septae [29, 52]. Occasionally the tumour spreads to the bone, soft tissues of the chest wall, diaphragm, pericardium and mediastinal structures that can be more clearly elucidated using contrast Magnetic Resonance Imaging (MRI) and Positron Emission Tomography (PET) [23, 55]. Other Psuedomesotheliomatous Adenocarcinoma of the lung (PCL) has been observed in cases of primary lung adenocarcinomas which can also spread into the pleural cavity when it originates in the extreme periphery of the lung and can get mistaken at times for MPM. These have a very poor prognosis with multiple extra-pulmonary involvement [51]. Secondary tumours metastasised from extra-thoracic sites like the genitourinary tract, pancreas and salivary glands can also produce pleural involvement [35, 56, 57] making it difficult for differential diagnosis from MPM or PCL.

MPM most commonly metastasises into the lymphatic system to the hilar and mediastinal lymph nodes. In such cases, fluorodeoxyglucose-positron emission tomography or FDG-PET is more sensitive for providing a more accurate read on the staging of the disease and differentiating early MPM from a far advanced tumour [29, 51, 55]. Pleural fluid cytology and pathological analysis of pleural tissue can assist in MPM diagnosis in 20-33% of the patients. 87% of all cases are diagnosed using CT guided core needle biopsy [1, 42, 54]. Accuracy can be further enhanced by 90% using video-assisted thoracoscopy (VATS), which can also assist in draining a loculated effusion and providing adequate tissue samples for cytological and microscopic diagnosis. Minor disadvantage of such a technique is that it can result in tumour growth along the chest wall in 20% of cases due to the surgical incision which can be avoided by sampling along the site of future resections [35, 53, 58]. Conducting immunocytochemistry such as fluorescent in-situ hybridisation (FISH) for p16 increases diagnosis accuracy between benign and malignant pleural lesions [49].

MPM diagnostic markers, based on immunohistochemistry, are: calretinin, which is highly specific for MPM along with cytokeratin 5/6 [29, 35, 55, 59], pancytokeratin, Wilms Tumour Antigen 1 (WT1), Podoplanin (D2-40), Transcriptional Intermediary Factor 1 (TIF-1), Carcinoembryonic Antigen (CEA) and mesothelin that are part of a immunocytochemistry panel implemented by the IMIG for positive diagnosis [23, 49, 60]. These markers can be used to differentiate MPM from adenosarcoma which has additional markers like Thyroid Transcription Factor-1 (TTF-1) or Napsin A [29, 61].

Proper staging of the disease is necessary for providing rational and adequate treatment and information on the patient's outcome [62]. The International Mesothelioma Interest Group (IMIG) have a widely accepted TNM-type system for staging [29, 52–54].

1. Stage I includes MPMs with no lymph node involvement with minimal tumour in the parietal pleura (Ia) or minimal visceral pleural involvement (Ib).
2. Stage II includes MPMs with no lymph involvement but having a highly confluent tumour found on all surfaces of the pleura, with possible involvement of the diaphragm or lung parenchyma which can be resectable.
3. Stage III, the most common stage of MPM, includes MPMs with metastasis to hilar (N1) and mediastinal (N2) lymph nodes, or extensions to soft tissues in the chest cavity, endothoracic fascia, mediastinal fat or pericardium (T3).
4. Stage IV includes MPMs invading the spine, ribs, chest wall, transdiaphragmatic or contralateral pleural, contra-lateral or supraclavicular lymph nodes (N3) and with distant metastasis.

6 MOLECULAR LANDSCAPE AND PROGNOSTIC BIOMARKERS

Currently MPM does not have any definite predictive biomarkers for prognosis and early diagnosis of the disease [2, 50, 61, 63]. A recent extensive and integrated genomic study by Hmeljak et al., on 74 MPM samples part of The Cancer Genome Atlas (TCGA) showed that MPM had a much lower rate of somatic mutations compared to other cancers. Other genetic alterations resulted in loss of heterozygosity with multiple deletions and somatic alterations in chromosomes including 1p, 3p, 4p, 4q, 6q, 9p, 13q, 14q, 15q, and 22q [64]. These recurrent losses of chromosomes in regions containing tumour suppressor genes contribute to the disease progression. Frequent genetic alterations in genes like BAP1, NF2, CDKN2A, TP53, Large Tumour Suppressor Kinase 2 (LATS2) and SET Domain Containing 2 (SETD2) have been

identified but none of these have been uniquely targeted for therapy [51, 65, 66]. Distinctively, 3% of the cases with TP53 and SET Domain Bifurcated Histone Lysine Methyltransferase 1 (SETDB1) haploid mutations which allows for mitotic errors and chromosomal loss leading to catastrophic haploidy and reduced tumour suppression, were seen predominantly in younger females [67]. Interestingly, none of these samples contained viral genome markers for SV40 and focal deletions were found in tumour suppressor genes rather than in oncogenic drivers. Although the transcriptome and metabolic profiles have been found to be highly variable, several miRNAs like miR-15/16/17 that regulate the expression of TP53 and CDKN2A are downregulated in a subset of Mouse Double Minute 2 homolog (MDM2) positive MPM, an evidence that is suggestive of growth and proliferation [1, 68]. A high level of miR-29c is an independent diagnostic marker for epithelioid MPM [1, 65].

6.1 BAP1

Recurring deletion and inactivation of the nuclear deubiquitinase BAP1 could explain the increased recruitment of pro-proliferative transcription factors and in activation of Interferon Regulatory Factor 8 (IRF8) [23, 65]. BAP1 mutations have been also linked to changes in methylation status [64, 69, 70]. BAP1 loss is seen in 60-70% of epithelioid and biphasic MPM while no loss is observed in sarcomatous MPM.

6.2 CDKN2A

Another driver of MPM progression that has been identified is the CDKN2A deletions (locus 9p21), along with co-deletion of Methylthioadenosine Phosphorylase (MTAP) [65, 71]. The deletion of the 9p21 locus has been reported in 33-100% of MPM cases with a greater incidence in the sarcomatous tumours [72, 73]. Such deletion affect downstream effector proteins such as inhibitor of CDK4 (INK4a/p16) and Alternate Reading Frame (ARF/p14) that can impair the control of the cell cycle by Rb and TP53 [40, 66].

6.3 NF2

NF2 deletions at 22q12 occurs in 40-55% of MPM and it has been shown to alter the activity of Merlin resulting in upregulation of Cyclin-D1 and cell cycle progression along with inhibition of Focal Adhesion Kinase (FAK) signalling that can cause increased migration and invasion [40, 64, 74].

6.4 MONONUCLEAR CELL INFILTRATES

Mononuclear Cell (MNC) infiltration, Tumour Associated Macrophages (TAM) and Tumour Infiltrating Lymphocytes (TILs) have been considered as other prognostic markers in MPM, albeit with many controversial opinions. Sarcomatous MPM has been shown to have greater number of TILs and M2 TAMs along with higher PD-L1 expression and this pattern is considered to contribute reduced overall survival [75].

6.5 PD-L1

Programmed Death-Ligand 1 (PD-L1) been used as a predictive marker for many solid tumours and including MPM [76]. It is a ligand for the PD-1 receptor that is present on activated T-cells, where it mediates immune anergy. The activation of this signal leads to the suppression of anti-tumour response and promotes apoptosis of antigen specific T-cell clones [66]. PD-L1 can be expressed by both the tumour cells and TILs. PD-L1 overexpression is directly correlated to poor prognosis in patients having biphasic and sarcomatous MPMs [50, 68, 77]. PD-L1-positive patients have a lower survival by 3 months compared to negative groups, although they may potentially benefit from anti-PD-1/anti-PD-L1 immunotherapy. A contradicting randomised Phase III study of 214 MPM samples showed that despite PD-L1 positivity in 35% of the samples, overall survival was not statistically significant in these patients who received anti-PD-1 pembrolizumab treatment [50]. Other studies and clinical trials have shown successes of immunotherapy against MPM regardless of PD-L1 status. Another novel negative immune checkpoint marker typical of epithelioid MPM and MPM-related TAMs is V-set Immunoglobulin Domain Suppressor of T-cell Activation (VISTA), which represses T-cell activation and promotes resistance to therapy [65].

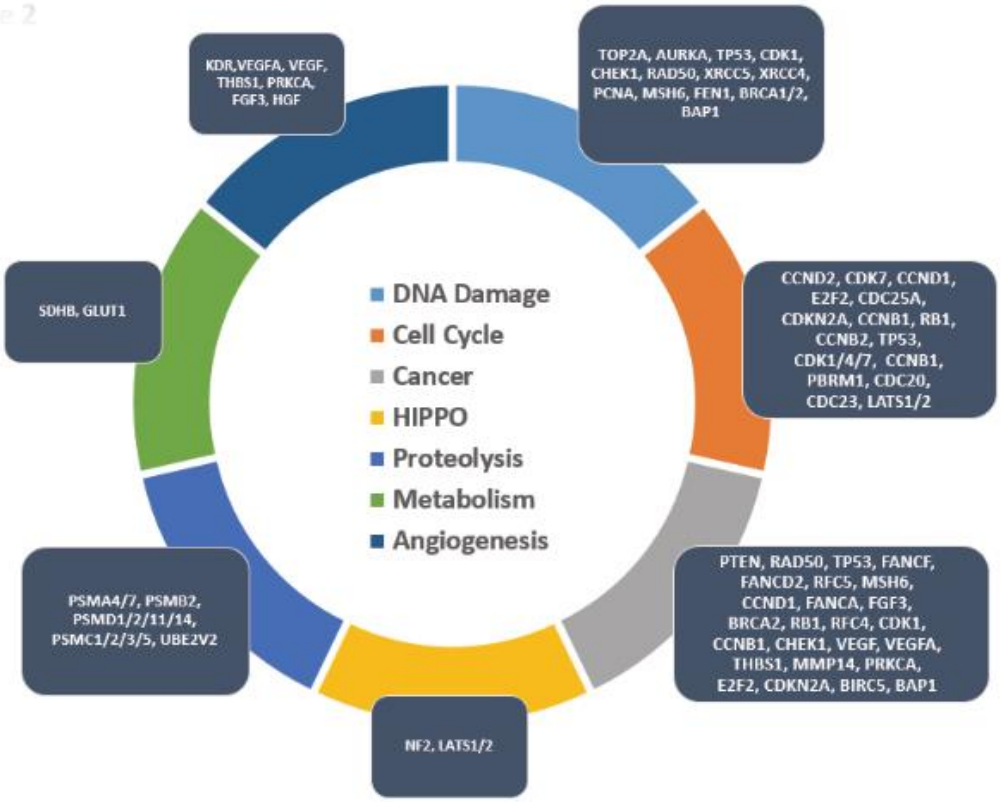

Figure XI: Collection of all reported gene alterations and their respective signalling pathways. Source: Nabavi et al., 2016.

7 TREATMENT OF MESOTHELIOMA

7.1 SURGERY

Treatment for MPM has not altered much over the years. The most effective form of treatment would be complete removal of the masses through surgical resection but as the nature of MPM is to diffuse entirely through the hemithorax this is rarely achieved [54, 78]. Since the treatment is directly dependent on the staging of the disease, it is recommended by the National Comprehensive Cancer Network guidelines that Stage I/I/III tumours of epithelioid and biphasic histotypes undergo multimodal therapy with surgery, while Stage IV patients and sarcomatous histotypes can benefit from chemotherapy alone [47]. The three most common forms of surgical interventions are discussed below.

7.1.1 VIDEO-ASSISTED THORACOSCOPY (VATS)

As mentioned earlier, VATS can play an important role in the diagnosis of the tumour by facilitating biopsies as a video guided tool and improves diagnosis in 25% of patients who previously failed other diagnostic tests [51, 79]. Simultaneously, this technique can also offer pain relief to the patient by removal of recurrent pleural effusions, lyses of the loculations and pleurodesis although without obvious reduction of the tumour volume [29]. VATS is most commonly followed by extrapleural pneumonectomy [54].

7.1.2 PLEURECTOMY OR DECORTICATION (P/D)

P/D is a technique that is performed by reducing tumour burden radically through the direct removal of the affected parietal pleural tissue along with part of the diaphragm [29]. Residual visible tumour tissues are often found within the lung 80% of the time. The main disadvantages are: air leaks, empyema, haemorrhage and local recurrence [52, 54]. P/D shows evidence of likely relapse in the hemithorax in terminal patients due to residual tumour presence [78, 79]. As there is not sufficient information from randomised clinical trials, it is very hard to say if P/D or extrapleural pneumonectomy are performed as part of palliative care or as a cytoreductive treatment and if one form offers any advantage over the other [29, 47, 51, 79].

7.1.3 EXTRAPLEURAL PNEUMONECTOMY (EPP)

EPP is the most aggressive form of surgical intervention that can be performed with complete removal of parietal and the visceral pleura ‘en-bloc’ along with the removal of mediastinal lymph nodes, diaphragm, and pericardium [52, 79, 80]. This is followed by reconstruction of part of the resected tissues of the diaphragm and the pericardium using a Gortex or Marlex mesh. Patients in Stage I or II, and rarely in Stage III, showing epithelioid subtype are considered for this form of surgical intervention. Patients must also have adequate lung function and no prior heart surgery [29, 54]. This procedure has been controversially shown to have a higher 30-day mortality and morbidity with a slightly lower recurrence rate without direct survival benefits [51, 79].

7.2 RADIOTHERAPY

Radiotherapy is widely used as palliative care for alleviating pain and as a prophylaxis to prevent future relapse in early disease [81]. Retrospective studies on patients treated with 40 Gy or more demonstrated substantial relief for dyspnoea, superior vena cava obstruction and dysphagia in 65% of the cases [29, 51, 82]. Delivering radiotherapy to MPM poses quite a major limitation as the tumour enveloped lung would require at least 60 Gy of radiation but the limiting doses of surrounding tissue (lung 20 Gy, liver 30 Gy, spinal cord 45 Gy, heart 45 Gy and oesophagus 45-50 Gy) prevent adequate delivery [52, 54]. Quite often, radiotherapy is administered as an adjuvant after EPP as a high dose hemithoracic radiotherapy of over 40 Gy. This approach showed limited local recurrence which was observed in only 13% of case in Phase II trials [83].

When radiotherapy is given prophylactically, it is unable to alter disease progression and is not recommended for patients after pleural interventions [29], but it can prevent sub-cutaneous metastasis along past surgical tracts due to tumour seeding [51]. A more recent technique called intensity-modulated radiotherapy (IMRT) has shown promise in the treatment of residual and unresected masses through targeted dose delivery and provides protection to surrounding risky organs with a 95% chance of disease control [54, 79]. This technique facilitates the delivery of high dose hemithoracic radiation by the modulation of multiple rough beams but few instances have reported fatal pneumonitis in 46% of cases in patients post-EPP, suggesting that patients with one lung have a lower tolerance to the treatment [83].

7.3 MULTIMODAL THERAPY

Most chemotherapeutic options involve a multimodal approach as single treatments have shown an abysmal response in patients. Multimodal or trimodal therapy involves a combination of surgery, radiation and chemotherapy [29, 55]. The success of multimodal therapy is evidenced by prospective studies on a case-to-case basis where P/D or EPP followed by hemithoracic radiotherapy and chemotherapy can improve local control [79, 81]. The most effective form of treatment studied in 137 patients in the UK over a 17 year period involved EPP in combination with chemotherapy and radiation (30-40 Gy) that increased the patient median survival to 19 months [54]. In epithelioid subset of patients, the 5-year survival was increased to 45% [52]. Other methods of surgical interventions have been tested in conjunction with Photodynamic Therapy where irradiation with laser along with the systemic

administration of a photosensitiser is done to induce tumour cell death [53]. This technique has been found to increase severe complications like bronchopleural fistulae, infections, cardiac arrest, perforations and empyema in over 49% of patients with considerable mortality and morbidity [52].

Globally, MPM continues to pose significant difficulties to treat with positive outcomes and several new drugs are being investigated. Also, a lack of adequate randomised clinical trials with large enough sample size prevents updates on outdated treatment opportunities [62].

7.4 CHEMOTHERAPY

7.4.1 CURRENT TREATMENT MODALITIES

Chemotherapy is the most widely used and well-established form of treatment. Chemotherapy has been shown to provide positive response in the maintenance and reduction of tumours but the response in MPM is a partial response or a stable disease in 15-20% cases, with very rare complete remissions [29, 52, 79, 84]. Currently, the treatment of MPM with a combination of cisplatin with pemetrexed demonstrates an improved survival by almost 3 months compared to singular treatment and is now widely considered as the first line treatment with a 41.3% response rate [29, 42, 68, 80]. Pemetrexed is often given to patients as maintenance therapy or as a second line treatment along with best supportive care and has been shown to be effective in epithelioid MPM [52, 79]. Patients demonstrate decreased pain, improved lung function and decreased dyspnoea in 41% of the cases. Studies have shown that treatment with other platinum drugs for first line treatment such as carboplatin are only recommended if the patient is unable to tolerate cisplatin since they have shown to have similar efficacy [29, 80, 84].

Second line drugs used are carboplatin, gemcitabine, vinorelbine, doxorubicin and CPT-11 that are provided singly or in combination with cisplatin, with response rates ranging from 12-48% [81, 85]. Gemcitabine plus vinorelbine used a second line treatment has shown a response rate of 7.4% with stabilisation of the disease in 37% of patients and delaying progression by 2.8 months [79]. Phase II trials of vinorelbine demonstrate an improved survival of 9.6 months. Various studies have investigated intrapleural administration of chemotherapy in place of traditional systemic administration after P/D. In these cases, combinations of cisplatin with mitomycin, cisplatin and cytosine arabinoside, observed a median survival ranging from 12-18

months with occasional nephrotoxicity [52]. Other drugs have been suggested for treatment but with limited response rates (Figure XII).

Drug	Total No. of Patients	No. of Studies	Response Rate
Doxorubicin	69	2	12%
Liposomal doxorubicin	109	3	5%
Epirubicin	69	2	12%
Gemcitabine	60	3	12%
Cisplatin	73	3	18%
Carboplatin	88	3	11%
Vinorelbine	29	1	24%
Paclitaxel	60	2	5%
Ifosfamide	83	3	8%
Docetaxel	41	2	15%
Methotrexate	78	3	41%
Trimetrexate	52	1	12%
Edatrexate	20	1	25%
Edatrexate/leucovorin	40	1	16%
Pemetrexed	64	1	14%

Figure XII: List of small molecule drugs and their efficacy in treatment of MPM. Source: Brcic., et al 2020.

7.4.2 INVESTIGATIVE TREATMENT MODALITIES – PERSONALISED MEDICINE & TARGETED THERAPY:

Since the efficacy of approved multimodal therapy is low, pre-clinical and clinical trials are continuing to provide insight into the possible mechanisms and targeted treatment opportunities (Figure XIII and Table I).

7.4.2.1 Targeted therapy

MPM has been shown to express a substantial amount of Vascular Endothelial Growth Factor (VEGF) that promotes its malignant and invasive nature. The novel recombinant monoclonal antibody Bevacizumab/Avastin targeting VEGF has shown promise in several clinical trials and is being included as part of a combinatorial treatment with cisplatin and pemetrexed in Phase II/III clinical trials [79, 86]. The MAPS study (Mesothelioma Avastin Cisplatin Pemetrexed Study) showed significant increase in the median progression free survival (PFS) by 2 months when patients were treated with bevacizumab in addition to the standard first line

chemotherapy [87]. A few patients demonstrated toxic effects like hypertension and thrombotic events which limits patient recruitment. So far, the treatment with Bevacizumab is limited to clinical trials [66].

Ranpirnase inhibiting tumour tRNA, which affects protein synthesis and cell cycle arrest at G1, has been shown to be effective as a single agent, showing a 43% stable disease rate in Phase II trials and increased 2-month survival in a subset of patients, in combination with doxorubicin. The treatment with Aurora Kinase A (AURKA) inhibitor Alisertib is currently in Phase II clinical trials. [65]. The Enhancer of Zeste Homolog 2 (EZH2) inhibitor tazemetostat is being used in a clinical trial to treat BAP null MPM. Another inhibitor of Protein Arginine Methyltransferase 5 (PRMT5) is being used in Phase 1 clinical investigation targeting downstream modifications due to the CDKN2A deletion [86]. Proteasome inhibitor bortezomib is under study as part of a large scale European clinical trial, as well as Histone Deacetylase (HDAC) inhibitors such as belinostat and vorinostat [84, 86]. For all these agents, the results of Phase II/Phase III clinical trials are still not known.

7.4.2.2 Oncolytic viruses and cell-based vaccines

Gene therapy based approaches are being investigated, using adenovirus mediated transfer of p14(ARF) in MPM cell lines to induce G1 phase cell cycle arrest and promote apoptosis [40]. Another oncolytic adenovirus-based treatment is the Ad-HSVtk, which involves the vector carrying Herpes Simplex Virus thymidine kinase gene where it is administered intrapleurally in combination with ganciclovir. Thymidine kinase is transduced into the tumour cell thereby allowing ganciclovir to discreetly destroy them. Positive results have been obtained in 2 patients with long term survival of 6.5 years [79, 80]. Another adenoviral vaccine encoding IFN-α-2b (AdenoV – IFN-α), administered along with gemcitabine and celecoxib is being investigated in ongoing Phase III trials, after a positive response in terms of safety [88, 89].

Vaccine based therapies have been investigated as novel therapies also to boost the immune system that is highly involved in the MPM disease evolution. WT-1 synthetic peptide vaccine Galinpepimut-S has been proven safe in Phase II clinical trials along with the immune checkpoint inhibitor Nivolumab, by re-sensitising immune cells against WT-1 and promote tumour cell destruction [89]. Other dendritic cell (DC)-based therapies include loading the DCs with allogenic tumour associated antigens (TAAs). Such phase II/III trials are underway and

have shown growing promise with increased PFS of 8.8 months [89]. Cell based therapies like Chimeric antigen receptor (CAR)-T cell targeting the MSLN gene coding for mesothelin, co-stimulating CD28 in MPM, showed over 50% decrease in serum MSLN protein suggestive of a positive anti-tumour response in a Phase I trial [88]. An additional form of immune stimulatory viral-based treatment includes transducing IFN-β with an adenoviral vector for targeting tumour cells that is currently in Phase I trials [79].

7.4.2.3 Immune Checkpoint Inhibitors

MPM has demonstrated to be one of the handful of cancers to have a strong immune presence and reaction in patients, characterized by a large number of immune infiltrates that are now being used as a prognostic marker and targets for the disease management [90]. Evidence also shows higher expression of anti-mesothelin antibodies. The potential advantages of anti-mesothelin treatment is currently under investigation in clinical trials [29, 60]. Since most TILs express immune checkpoint markers [90], several immune checkpoint inhibitors have been investigated for their potential anti-tumour response. Anti PD-L1/PD-1 (Pembrolizumab) based therapy has been shown to improve patient survival in those who score positive for PD-L1 positive tumours [55, 91]. Pembrolizumab in Phase I trials has shown positive response in 24% patients and 52% showed disease control [66]. Cytotoxic T-lymphocyte Antigen 4 (CTLA-4), an immune suppressive receptor on CD-4 T-lymphocytes, represses a positive immune response when activated and has been detected in MPM immune infiltrates [55]. The MESOT-TREM-2012 Phase II clinical trial used Tremelimumab (Anti-CTLA-4) and showed long lasting response in 4 patients and 52% achieved stable disease post cisplatin as first-line therapy [66]. Another study conducted by Victor et al., showed that combination treatment with Anti-CTLA-4, Anti-PD-L1 and radiation can potentially reverse the immune suppression of T-regulatory cells, increase CD8 T-cell receptor repertoire diversity and increase CD8/T-reg ratio to activate the immune response [92].

Despite advances being made every day in the discovery of novel treatment opportunities, many clinical studies are yet to show convincing successes that can be implemented bedside.

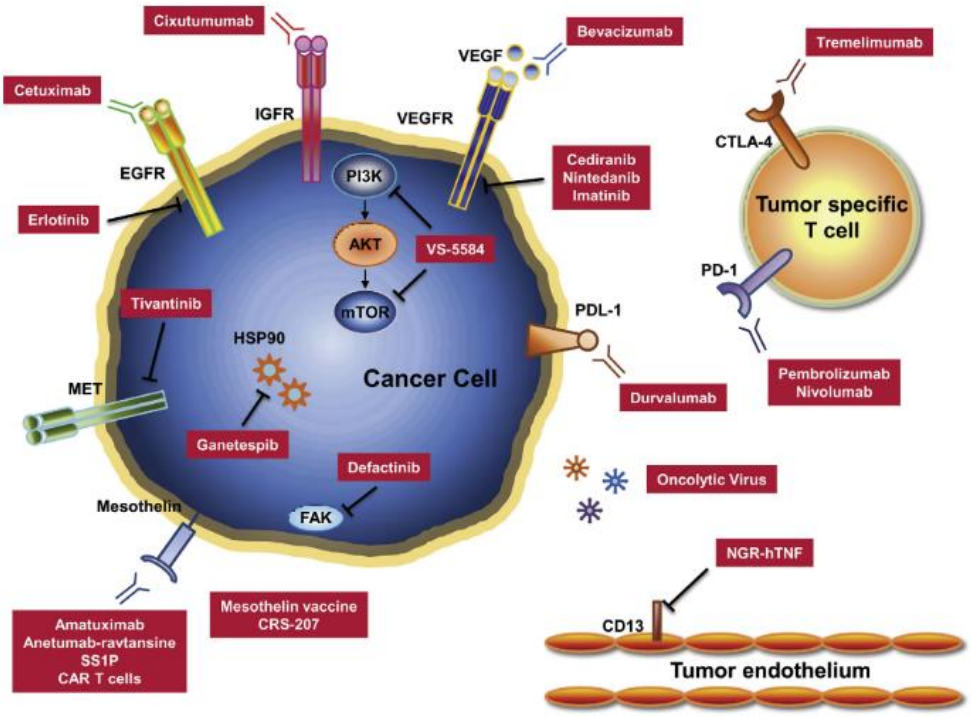

Figure XIII: Overview of different investigative treatments and their molecular targets in MPM. Source: Bonelli e al., 2017.

DRUG	MECHANISM	TRIAL STATUS	EFFICACY/RESULT
Bevacizumab	Anti-VEGF recombinant mAb	Phase II/III	Positive Overall survival increased by 2 months in combination with cisplatin and pemetrexed
Ranpirnase	Ribonuclease inhibitor targeting RET, c-Kit and Fit-3t	Phase II/Phase III (with doxorubicin)	5% response rate with overall survival at 6 months/no response
Alisertib	Aurora kinase inhibitor	Phase II	Ongoing study in patients irrespective of molecular signature
Tazemetostat	EZH2 inhibitor against BAP1 null MPM	Phase II	Ongoing study demonstrates positive disease control rate
Pembrolizumab	Anti-PD-L1	Phase I	Positive response in 24% patients and 52% showed disease control
Amatuximab	Anti-mesothelin	Phase I	Disease control rate of 90%
ADI-PEG 20	PEGylated arginine deiminase acting as an arginine depleting agent	Phase II/III	Proven safe and currently recruiting with positive overall survival rate
Gefitinib/Erlotinib	Anti EGFR	Phase II	Poorly 4% response rate and PFS 2.6 months – Negative
Imatinib	Anti PDGFR	Phase II	Non-responsive/Negative
Sunitinib	Targets VEGFR 1/2/3	Phase II	Response rate of 15 % with a median PFS of 3.5 months
Tivantinib	Anti-MET inhibitor	Phase I/II	Ongoing
Tremelimumab	Anti-CTLA-4	Phase II	52% disease control and positive long-term response in 4 patients

Table I: Table showing the list of novel treatments, targets and current status of the study.

8 TUMOUR MICROENVIRONMENT AND RESISTANCE

The MPM microenvironment is highly complex and multiple players systematically promote tumour progression and immune evasion [93] and consists of cancer cells, stromal cells, immune cells, extracellular matrix, and microvasculature [94]. The construction of this complex system commonly dictates how the tumour will respond to therapy and plays a crucial role in its prognosis. For instance, there is a very strong presence of immune suppressive cells surrounding MPM, in addition to surrounding supportive stromal tissues [93].

8.1 IMMUNE COMPONENT

From the initial exposure to asbestos, as discussed in the previous chapters, MPM is uniquely able to trigger a chronic inflammatory response that ultimately results in progression of the cancer. Chronic autocrine activation of leucocytes, release of inflammatory cytokines and VEGF which in turn trigger release of mitogenic factors, cause transformation of mesothelial cells. Asbestos also induces necrosis of the cells through mitochondrial and cellular stress, which triggers the release of HMGB1 – an inflammatory marker that promotes tumour growth and progression, activates tissue repair, macrophage M1 to M2 polarisation, proliferation of stem cells, EMT and neo-angiogenesis [35, 93].

The MPM microenvironment primarily consists of certain immune cells including M2 polarized TAMs, which are known to increase VEGF secretions, myeloid derived suppressor cells (MDSCs) and T-lymphocytes secreting TGF-β with increased PD-1 expression and decreased T-lymphocyte activation markers.

Additionally, MDSCs are highly plastic in their ability to trigger or supress an immune response, together with mesothelial cell transformation, proliferation invasion, angiogenesis, survival and immune escape [94]. Myeloid cells lean towards immunosuppressive phenotype by expressing PD-L1 on their surfaces, thereby inhibiting cytotoxic CD8+ T cell activity and triggering ROS production. Hypoxia can induce the MDSCs to secrete pro-inflammatory cytokines IL-6, IL-10 and TGF-β, which promotes immune cell recruitment and prolonged survival [93]. There has been also evidence of MPM presenting with “immune deserts” i.e., with little or no immune infiltrates where the cellular stroma acts as a barrier supressing normal immune responses and contributes to creating a hypoxic environment prompting the radio-resistive and chemo-resistive behaviour of MPM patients [68, 95] (Figure XIV).

TAMs are present in 26-42% of the MPM immune infiltrate and are typically monocyte-derived M2-polarised suppressor cells. Chemokines such as CCL2/4/5 and CXCL12 secreted by mesothelial cells recruit peripheral blood monocytes [35]. Activated TAMs express CD14, CD16, CD163, CXCR4, CCR2/5 and are responsible for triggering an immunosuppressive effect on T-cells following secretion of IL-10 and prostaglandin E2 [93].

In addition, the tumour infiltrating macrophages (TIMs), although present in large numbers, lack MHC-II expression and demonstrate increased production of cytokines TGF-β, IL-6, IL-1 and TNF-α possibly contributing to the resistive nature of MPM [35, 96]. There is evidence of a percentage of CD4+/FoxP3+ Treg cells secreting TGF-β along with 'exhaustion' CD8+ T-cells [97]. They show increased expression of PD-1, T-cell Immunoglobulin and Mucin Domain-containing Protein 3 (TIM-3) and Lymphocyte-Activation Gene 3 (Lag3) which is triggered by hypoxia, hypoglycaemia and ROS production resulting in immune suppressive effect and radio-resistance [35, 82, 93].

8.2 STROMAL COMPONENT

The extracellular matrix in MPM promotes tumour growth and invasion. Tumour cells secrete various components like collagen type IV, laminin, fibronectin that facilitate cell-cell communication and chemotaxis [93]. Additional stromal players include α-SMA expressing cancer associated fibroblasts (CAFs), which secrete fibrin, collagen, matrix metalloproteases (MMPs), VEGF and PDGF, facilitating tumour invasion and metastasis [68, 93, 98]. The CAFs and the fibrocytes develop a positive feedback loop where TGF-β, IL-6, Fibroblast Growth Factor 2 (FGF-2), C-X-C Motif Chemokine 12 (CXCL12) secreted by the tumour cells recruit CAFs which in turn secrete PDGF-A and Hepatocyte Growth Factor (HGF) that trigger growth and migration of the mesothelial cell [35, 99–101].

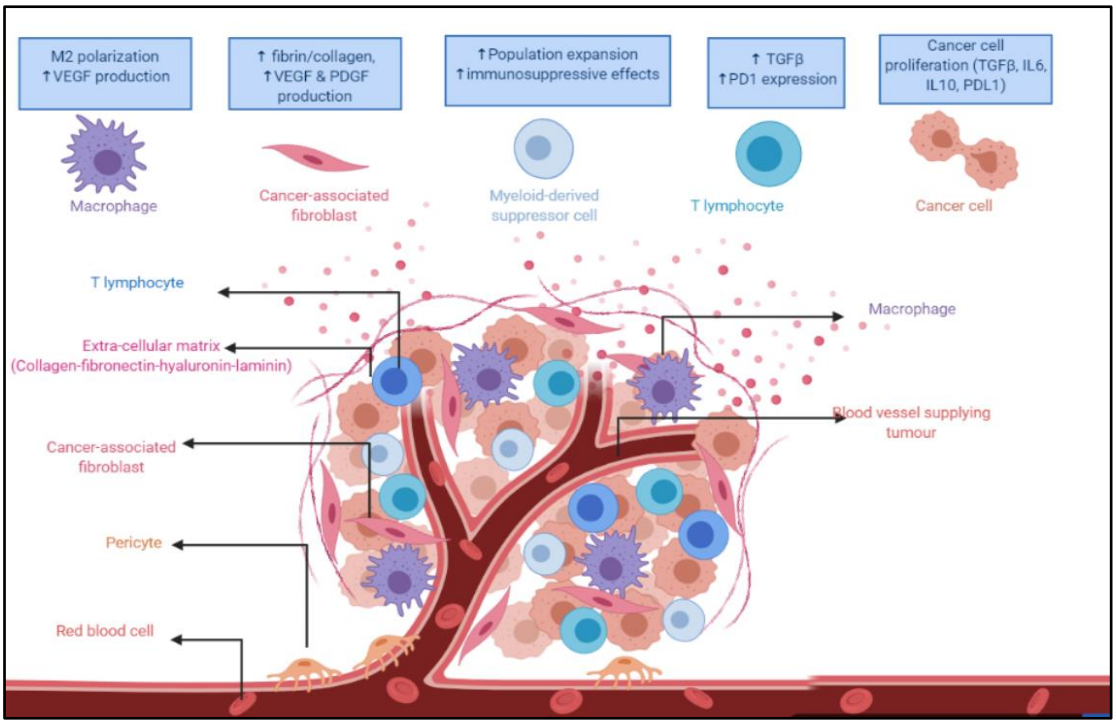

Figure XIV: Overview of Malignant Pleural Mesothelioma microenvironment facilitating tumour invasion and radio- and chemo-resistance.

8.3 TUMOUR HYPOXIA

A vital factor in MPM resistance to chemotherapy and radiotherapy is the highly hypoxic microenvironment, confirmed by PET-CT, characterized by a pO_2 <10mmHg [95]. Under hypoxic conditions, the activation of Hypoxia-Induced Factors HIF-1/HIF-2 (α and β subunits) induces activation of downstream HIF-target genes where most of them are implicated in metabolism, angiogenesis and survival thereby sustaining the cancer [102]. Hypoxia triggers the glucose uptake by increasing GLUT1, glycolytic genes and Mammalian Target of Rapamycin (MTOR) facilitating a metabolic switch to anaerobic glycolysis: these parameters correlate with poor patient prognosis [93, 102, 103]. Moreover, the HIF- downstream activated genes play a role in tiggering angiogenesis (VEGF), proliferation (PI3K/AKT/MTOR pathway), DNA damage repair [MutL Homolog 1 (MLH1), MutS Homolog 2 (MSH2), RAD50, Ataxia Telangiectasia Mutated (ATM) and Ataxia Telangiectasia and Rad3-related protein (ATR)] and unfolded protein response (UPR) directed cell survival (Cullin4A, Ubiquitin ligase E3, ubiquitin activating enzyme E1). Hypoxic environments have also strongly been associated with stemness, resistance to chemotherapy and EMT [93, 102, 104]. The hypoxic environment can be targeted by using hypoxia related markers such as GLUT-1 and carbonic anhydrase (CA)-IX to deliver polymeric and magnetic nanoparticles loaded with

chemotherapeutics [1, 105]. Over 90% of MPM has clear CA-IX expression but various small molecule and monoclonal antibody-based therapeutics have shown limited success as first line treatment in clinical trials [95].

9 3D IN-VITRO TECHNOLOGY AND DRUG DISCOVERY

9.1 EVOLVING FROM 2D TO ADVANCED CULTURE SYSTEMS

Since the introduction of mammalian cell culture almost 40 years ago, research and development has strongly depended on a plethora of techniques stemmed from the original two dimensional (2D) culture for numerous *in-vitro* assays and applications [106]. However, it has been well established that the tumour microenvironment is highly heterogenous and there is a strong cross-link and interplay between all the individual components resulting in a more proliferative, malignant, and elusive MPM. While we have learnt so much from research conducted with the help of 2D culture for drug discovery and understanding tumour pathology, there remain missing links in developing a complete and robust story that can accelerate the hunt for novel treatments [107]. Added model system complexity in *in-vitro* models can help augment our knowledge of MPM pathophysiology and novel drug efficacy [108]. Novel 3D culture systems that include all relevant cellular components need to be scalable for high throughput screening (HTS), user-friendly, time-efficient, standardizable and reproducible in different settings to speed up drug discovery and personalized medicine [109, 110]. Existing systems typically include 2D models with cells cultured on flat petri dishes and flasks and *in-vivo* rodent cancer models are generally used for translating this information to human tumour behaviors [107, 111]. However, 2D models are far from recapitulating the *in-vivo* cancer microenvironment due to their lack of spatial complexity and absence of typical biochemical and biophysical cues of the surrounding microenvironment [100, 108, 109]. Moreover, some compounds that were active in 2D cultures failed during development because of their lack of efficiency in co-culture conditions, due to the pro-tumour function of stromal cells [108]. Also, animal testing shows a lack of reproducibility, occasional poor correlation with humans and raises important ethical issues [100]. 3D cancer models are more physiologically relevant than the 2D models and represent an alternative to minimize animal testing, in accordance with the 3Rs principle. Nonetheless, application of 3D models in HTS remains a challenge due to low scalability to multi-well plates, reproducibility, labor intensiveness, material costs, and difficulties in the incorporation into automated screening setups. Thus, it is of paramount

importance to design and develop advanced 3D cell models for HTS systems in order to identify new diagnostic/predictive biomarkers, produce new and safe compounds applicable to personalized treatments, particularly in resistant tumours [107, 109, 112]. Different 2D and 3D culture techniques have been illustrated in Figure XV.

9.2 CURRENT 2D TECHNIQUES

In attempts to create a more organotypic models, modifications to the classical 2D system include cell co-culture techniques where different cell types are cultured together as a monolayer [113]. Such co-culture systems often have many variations depending on their applications with the introduction of biomaterials and the use of membrane trans-well inserts to facilitate cross-talk between different cell types [113, 114].

Other techniques include 'sandwich' culture where cells are cultured as bilayers within an ECM comprised of polyacrylamide or collagen to reproduce *in-vivo* behavior for evaluating pharmacokinetics. Sometimes, classical 2D surfaces are modified by micropatterning to alter the topography of the attachment surfaces that can influence cell adhesion, differentiation and behavior [107]. Stem cells have been shown to differentiate faster in 2D compared to 3D culture systems and can alter gene expression. Some advantages and disadvantages associated with 2D and 3D techniques for studying tumour growth and invasion have been described in the table below (Table II).

9.3 3D CULTURE COMPONENTS

9.3.1 ORGANOIDS

Organoids can be used to substitute patient derived xenograft models *in-vitro*. Organoids are 3D multicellular constructs that are self-assembled to create more relevant disease models for prostate, colorectal and pancreatic cancer models [112, 115]. These systems typically include cells cultured from embryonic stem cells (ESCs), induced pluripotent stem cells (iPSCs) and tissue fragments [112]. Such systems are able to recapitulate clonal heterogeneity of the original patient tumours, have self-renewal capacities and stable long-term expansion. While these systems are closer to patient xenografts, they sometimes lack structure of tumour microenvironments which limits their applications [115].

Criteria for relevant and translatable *in vitro* models		Scratch or exclusion zone	Transwell invasion	3D spheroid invasion	3D tumor-tissue invasion model
Relevance to metastasis	Tumor architecture and geometry	Cell monolayer on 2D tissue-culture plastic	Cell monolayer on 2D transwell insert	Self-aggregated multicellular spheroid embedded in 3D gel/matrix	User-defined tumor compartment embedded in 3D matrix
	ECM microstructure	thin layer or coating	thin layer or coating	3D hydrogel or fibrillar collagen (monomer)	3D fibrillar collagen (Oligomer)
	Accommodates heterogenous cell interactions	no	yes	yes	yes
	Aspect of metastasis being modeled	migration	migration or invasion	invasion	invasion
Reproducible and standardizable setup	Setup time	minutes	minutes	hours to days	minutes
	Reproducible setup	yes	yes	no	yes
	User control of biophysical properties	none	limited tunablity of surroundings	moderate tunablity of surroundings	high tunability of tumor and surroundings
Potential for HT-HC screening	Accommodates automated imaging and analysis	yes	no	no	yes
	Measures multiple phenotypic readouts	no	no	no	yes

Table II: Comparison of different 3D models for tumour invasion. Source: Puls et al., 2018.

9.3.2 SPHEROIDS

Cell spheroids can be generated by many innovative techniques including the hanging drop method or ultra-low adhesion modified tissue culture vessels that allow the cells to self-assemble, paper supported scaffolds, and magnetic levitation of cells [113–115]. Culturing spheroids allows for a high throughput and reproducible system which can be applied to drug discovery processes and in the study of genetic diseases [116]. Some systems also involve co-culture of spheroids with other cellular components such as vasculature [115]. These systems have the advantage of being highly controllable and multiplexed with as much as three different cell types with the addition of a scaffold or matrix to mimic the ECM better. The unique 3D geometry causes spheroids to develop a necrotic core and highly proliferative exterior that decreases chemosensitivity and provides quiescent cells within the core. Also, fibroblasts have been shown to migrate 1.3 times faster in 3D compared to 2D systems [107]. One study of pancreatic adenocarcinoma involved triple co-culture of pancreatic cells, fibroblasts and endothelial cells to form a fibroblast core with uniformly dispersed endothelial cells in type I collagen matrix with the help of a customized fabrication support. This tripartite culture has been used to measure tumour migration, invasion and drug dose response [108].

9.4 3D CULTURE TECHNOLOGY

9.4.1 DYNAMIC CULTURE IN BIOREACTORS

Cells can be cultured within a bioreactor with dynamic loading of cells, microfluidic actuation of media and other matrix components. They are used to understand cell behaviour in a larger scale such as micro-tissues and organs to study clinical applications. Cells are cultured in spinner flasks or rotating wall bioreactors in case of cells in suspension [115]. The microfluidic systems are incorporated within the systems to perfuse gas and nutrients using perfusion pumps or dynamic stress-loading actuators. Presently, these bioreactors are being scaled down in micro-dimensions to study bioactivity and drug screening in stem cells and tissue specific cells [107, 114].

9.4.2 3D BIOPRINTING

Construction of 3D structures are most often done with the help of three-dimensional scaffolds that are used to encapsulate cells to decipher cell-cell communication and extracellular factor (ECF) effects to recapitulate *in-vivo* replicative environments [111, 113]. Most polymers that are engineered are derived either from animal tissues (collagen, fibrin, gelatine, hyaluronic acid and chondroitin sulphate) for a more 'native' structure and non-mammalian biopolymers (alginate, chitosan) or synthetic hydrogels (Matrigel, RGD peptide) [107, 112, 113, 115]. 3D printing allows different cell types to be incorporated within a scaffold in a predefined spatial manner [117]. One study has shown that tumour cell-based bio-ink printed along with surrounding stromal cell-based bio-ink still form a compact tissue where the scaffold was subsequently dissolved during culture. This system has been used to evaluate drug efficacy, create distinct microenvironments and tumour subtypes [109, 114]. Often, some scaffolds can be prefabricated in different ways using 3D printing stereo-lithography, 3D printing electrospinning, polymer phase separation, gas foaming, lyophilisation and porogen leaching [115, 116]. However, most of these techniques are physical processes that are harsh for cells to survive, and require cells to be diffused and grown slowly into the scaffold following its construction [117]. Other studies have directly inserted printed cells forming spheroids into established microvascular networks to study cancer dynamics in lung cancer [118]. Another technique is bioprinting cell sheets without the need for scaffolds and then arranging the sheets

over one another to form a tissue: this approach has been applied for corneal replacement, myocardial, liver and kidney reconstruction [107, 112].

9.4.3 MICROFLUIDIC DEVICES

Microfluidics is defined as the science of manipulating fluids in 10^{-9} L to 10^{-18} L volumes. As we transition from macro-systems to micro-systems, micro- and nano-scale devices are up and coming in the field of cell studies. Most microfluidic systems are made of poly(dimethylsiloxane) (PDMS) scaffolds which has anti-corrosive properties when exposed to aqueous media, pressure and temperature changes. Here, cells are cultured within the micro dimension of the fluid chambers embedded in a suitable matrix. The nutrients and growth factors are perfused via microfabricated channels [111]. Microfluidics is now being widely used for cancer diagnostics, embryology and studies on vascularised systems [114, 115]. Different organ-on-chip (intestine, liver, lung, heart) and tumour-on-chip devices have been investigated for drug discovery and organ biology, thanks to their ease of multiplexing and high resolution imaging that allows the analysis of *in-vitro* biochemical, genetic and metabolic changes [114, 116]. Droplet microfluidic systems have been utilised to evaluate efficacy of single and combinatorial drugs through HT drug screening by utilising very low volumes of agents. This technique has also been successfully applied to the study of drug metabolism and drug toxicity by coupling the device with a MS and LC-MS system for metabolomics and secretomics [119]. Even though these systems show a lot of growing potential, they are limited by the need of careful planning and execution as they are much more fragile and complex and cannot function for long-term studies.

9.4.4 VIBRATION AND SOUND INDUCED MORPHOGENESIS

Among the technologies for the fabrication of 3D cell models, surface acoustic wave (SAW) systems enable the generation of spatially orchestrated cellular and multicellular constructs [120, 121]. Patterns shape can be tuned on demand by varying a set of parameters, such as sound frequency, amplitude, chamber shape [122]. Vibrations have been shown to have beneficial effects on differentiation and proliferation of cells when induced. Such dynamic simulations have similarities with *in-vivo* conditions with improved cell adhesions and are directly dependent on sound frequency and amplitude [117]. The 3D-SIM (3D – Sound Induced

Morphogenesis) method represents an innovative technology to develop 3D tumour-vascularized models, being smaller, portable, faster (i.e., realized within seconds), user-friendly, and more affordable than 3D-bioprinters. 3D-SIM allows to create large intricate 3D patterns of different kind of cells or pre-formed spheroids. These are often custom models based on loudspeaker vibratory, mechanical stimulatory, ultrasonic vibrations, 3D micro vibration stage and mechanical micro-vibrator systems that are used to generate vibrations for the study [117].

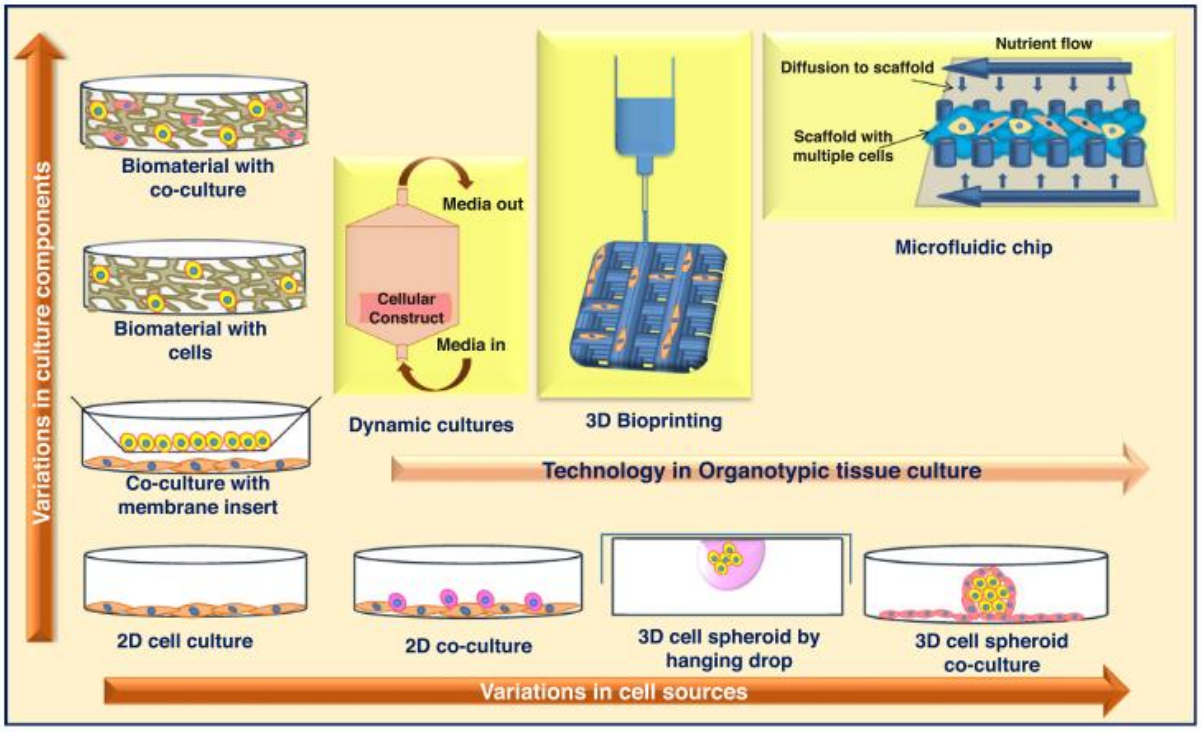

Figure XV: Overview of different 3D culture systems and their growing complexity with components and cell types. Source: Radhakrishnan et al., 2020.

AIMS

The general aim of this PhD Thesis is to discover new druggable targets for MPM, using an *in-vitro* system that allows to reproduce the 3D architecture of MPM and its environment, and to perform HTS of the novel identified drugs.

In the first year of PhD, following the previous findings of our group indicating that MPM cells are characterized by a higher activity of ubiquitination systems and protein turnover than non-transformed mesothelial cells [123], I investigated the effect of the inhibitor of neddylation and ubiqtination activating enzymes MLN4924/Pevonedistat on primary MPM cells, alone and in combination with the first-line chemtherapeutic drug cisplatin. Cytotoxicity and immunogenic cell death (ICD)-mechanisms induced by the compound were analysed on different phenotypic MPM cells and in murine syngenic models, to elucidate the sensitivity or resistance that various MPMs pose to treatments. Methods, results and data discussion are included in Chapter 1.

Between the second and the fourth year of PhD, I worked on identifying novel targets for the treatment of MPM using bioinformatics tools. After analysing the sequencing data of primary MPM cells to identify non-synonymous variants, I performed a big data analysis on these variants to isolate the significant variants and determine suitable targeting options. Using this information, I planned to translate this information *in-vitro* and *in-vivo*. I investigated the effect of the three drugs that emerged from the in-silico screening – Olaparib, Panobinostat and Bexarotene, on primary MPM cells of different histotypes, alone and in combination with the first-line chemotherapeutic drug cisplatin. Next, I validated the efficacy of the different treatments as single agents or as combination in syngenic murine MPM models. Tumour growth and immunohistochemical analyses was performed to study the anti-tumour efficacy and signs of eventual organ toxicity. To clarify the mechanisms of the efficacy of such novel drug combinations, additional transcriptomic studies were performed: an effect on genes controlling epigenetic modifications was found in the three histotypes following combinatorial treatments. Methods, results and data discussion are included in Chapter 2.

In the last part of my PhD, I developed a novel 3D-SIM as a new *in-vitro* system that can be used to study tumour progression and facilitate drug discovery. I propose the use of a proprietary SAW-based technology, developed at AO Foundation, Davos, Switzerland, where I spent six months of the last year, to build highly complex cancer models with precise spatial organization of cancer cells, stromal cells, immune cells, extracellular matrices, and microvasculature. My aim was to develop a 3D model of MPM mimicking the tumour microenvironment that can be used to evaluate the response to novel combinations of chemotherapeutic drugs and small molecule drugs. Methods, results and data discussion are included in Chapter 3.

.

CHAPTER 1

Proteasomal Inhibitors and Their Potential Role in Reversing Chemoresistance and Immune Resistance in Malignant Pleural Mesothelioma

1 MATERIALS AND METHODS:

1.1 CHEMICALS:

The plasticware for cell cultures was obtained from Falcon (Becton Dickinson, Franklin Lakes, NJ). The electrophoresis reagents were obtained from Bio-Rad Laboratories (Hercules, CA). The protein content of cell lysates was assessed with the Bicinchoninic Acid (BCA) kit from Sigma Chemicals Co. (St. Louis, MO). MLN4924 was from Sellekchem (Aurogene, Roma). Unless specified otherwise, all reagents were purchased from Sigma Chemicals Co.

1.2 CELLS:

Six primary human MPM cells [2 epithelioid (#646, #404), 2 biphasic (#487, #672), 2 sarcomatous (#720, #570)] were obtained from the Biologic Bank of Malignant Mesothelioma, S. Antonio e Biagio Hospital (Alessandria, Italy). Murine AB1 cells were purchased from Sigma Chemicals Co. (#10092305). Cells were grown in Ham's F12 nutrient mixture medium (primary MPM cells) or DMEM (AB1 cells), supplemented with 10% v/v fetal bovine serum (FBS), 1% v/v penicillin-streptomycin. Cells were checked for Mycoplasma spp. contamination by PCR every three weeks; contaminated cells were discharged. All cells were treated for 24 hrs and 48 hrs individually with 50 µM Cisplatin (Sigma-Aldrich, St. Louis, MO,) and 0.2 µM MLN4924 (Cayman Chemicals, Ann Arbor, MI, USA), alone or in combination.

1.3 CELL CYCLE ANALYSIS:

300,000 cells/well were rinsed with 1X Phosphate Buffer Saline (PBS) and harvested with Cell Dissociation Solution Non-Enzymatic 1X (Sigma Aldrich, C5789). The cells were fixed with 70% (v/v) ethanol for 15 min at 4°C and resuspended in 400µL Citrate Buffer Solution (50mM Na_2HPO_4, 25mM sodium citrate, 0.1% v/v Triton X-100) containing 1µg/mL Bovine Pancreatic RNase and 1µg/mL Propidium Iodide. The samples were incubated in the dark for 10 min and analysed using EasyCyte Guava™ flow cytometer (Millipore, Bedford, MA). 10,000 events were collected using the FL2 channel and analysed with the InCyte software (Millipore).

1.4 IN-VITRO CYTOTOXICITY ASSAY:

1.4.1 Lactate Dehydrogenase Assay (LDH):

300,000 cells/well in a 6 well plate was treated as afore mentioned in duplicates. Extracellular and intracellular LDH was measured using aliquots of extracellular culture medium and of cell lysates as previously described [124]. LDH activity was measured using a Synergy™ HT Multi-Detection Microplate Reader (BioTek, Winooski, USA), and expressed as percentage extracellular over total LDH activity/mg cellular proteins.

1.4.2 Crystal Violet Assay:

50,000 cells/well in 24 well plate was treated with 0.5% (w/v) crystal violet in 25% v/v methanol for 20 minutes. The crystal violet solution was discarded, and the plate was rinsed with water. The viability of cells was measured as a function of absorbance of crystal violet at 570nm using the Synergy™ HT Multi-Detection Microplate Reader. Results were expressed as percentage of viable cells vs. untreated cells, considered 100% viable.

1.5 IMMUNOGENIC CELL DEATH RESPONSE:

1.5.1 Calreticulin Exposure:

300,000 cells were rinsed with 1X PBS and harvested with Cell Dissociation Solution Non Enzymatic 1X (Sigma-Aldrich). The cells were collected and washed with 1mL PBS-BSA 0.25%, and the pellet resuspended in 100µL PBS-BSA 3% w/v containing Anti-Calreticulin mouse monoclonal antibody [FMC 75] Phycoerythrin (PE)-conjugated (ab83220, Abcam, Cambridge, UK), diluted 1:200, and incubated for 45 minutes at 4°C in the dark. 10,000 events were acquired on the FL2 channel using EasyCyte Guava™ flow cytometer. Analysis was carried out with the InCyte software.

1.5.2 Detection of ATP release:

500µL of the supernatant from 300,000 cells/well were collected at desired time points and spun at 500 x g, 5 min at 4 °C to remove cells or debris. 100µL of collected supernatant was subjected to ATP bioluminescent assay using the ATP Bioluminescent Assay Kit (Sigma-Aldrich) using 100µL of a 25-fold dilution of ATP Assay Mix stock solution with ATP Assay Mix Dilution Buffer. The amount of ATP was detected using Synergy™ HT Multi-Detection

Microplate Reader and calculated using a calibration curve of standard ATP. Results were expressed as relative luminescence units (RLUs)/mg cellular proteins.

1.5.3 Detection of HMGB1 release:

The supernatants of 300,000 cells/well were used to quantify HMGB1 release using the ELISA Kit for High Mobility Group Protein 1 (HMG1) (Cloud-Clone Corp. (Houston, TX, USA) according to manufacturer's instructions. Results were expressed as ng/ml.

1.6 GENERATION OF DENDRITIC CELLS (DC) FROM PERIPHERAL BLOOD MONOCYTES (PBMC):

Immature DC (iDC) were generated as described [125, 126]. PBMC were isolated from heparinized blood of voluntary healthy donors by standard density gradient centrifugation (Histopaque-1077), washed with RPMI-1640 medium supplemented with 5 mM EDTA and 2% heat-inactivated FBS, and suspended at 5×10^6/ml in RPMI-1640 medium supplemented with 10% FBS. After 2 h incubation at 37°C in a humidified 5% CO_2 incubator, non-adherent cells were removed, whereas adherent cells (monocytes) were cultured in the above complete medium supplemented with GM-CSF (1000 U/ml) and IL-4 (1000 U/ml). Cytokines were replaced on day 3 and iDC were collected on day 6.

1.7 PHAGOCYTOSIS AND IMMUNE ACTIVATION:

The tumour cells were green-stained with PKH2-fluorescein isothiocyanate (FITC) (Sigma Chemical Co.) according to the manufacturer's instructions. After 4 h the cells were washed and incubated for 20 h at 37°C with 1×10^5 iDC at a 1:1 ratio, and the mixed culture was stained with the PE-conjugated anti-CD80 antibody (BD Bioscience) for 20 min at 4°C. Phagocytosis of tumour cells by iDC was assessed by flow cytometric analysis as the percentage of double-stained (FITC plus PE) versus red (PE) stained cells on a total of 10,000 events, using the FACSCanto flow cytometer equipped with the DIVA software (BD). In parallel a phagocytosis assay was performed by co-incubating iDC and tumour cells at 4°C, instead of 37°C. The percentage of double-stained cells obtained after the incubation at 4°C was subtracted from that obtained after a 37°C incubation. The phagocytosis rate was expressed as phagocytic index, calculated as reported by Obeid et al., [127].

After tumour cell phagocytosis, DCs were washed and cocultured with autologous T cells, isolated from PBMC by immunomagnetic sorting with the Pan T Cell Isolation Kit (Miltenyi Biotec). DCs and T-cells were co-cultured for 10 days at a ratio of 1:5 in complete medium supplemented with IL-2 (10 U/mL). On day 10, CD107a and PD-1 expression on $CD8^+$ and $CD4^+$ T cells was determined by flow cytometry to assess the activation of tumour-specific cytotoxic T cells ($CD107a^+$-cells) or the T cells-anergy ($PD\text{-}1^+$-cells), using the following antibodies in combinations (all diluted 1:10, incubated 30 min at 4°C, from Miltenyi Biotec., Tieltow, Germany): CD8 (REA734, IgG1), anti CD107a/LAMP-1 (REA792, IgG1), anti-PD-1/CD279 (PD1.3.1.3, IgG2bk). At least 100,000 events in the lymphocyte gate were acquired and analysed by two-color flow cytometry using a FACSCanto flow cytometer equipped with the DIVA software.

1.8 IMMUNOBLOTTING:

Cells were rinsed with ice-cold lysis RIPA buffer (50 mM Tris-HCl, 150mM NaCl, 1mM EDTA, 1mM EGTA, 1% v/v Triton-X100; pH 7.5), supplemented with the protease inhibitor cocktail set III (80 μM aprotinin, 5 mM bestatin, 1.5 mM leupeptin, 1 mM pepstatin), 2 mM phenylmethanesulfonyl fluoride (PMSF) and 1 mM Na_3VO_4, and sonicated. Proteins were extracted after centrifugation at 13,000 × g, for 10 min at 4°C. Protein extracts (20 μg) were subjected to 4-15% gradient SDS-PAGE and probed with the following antibodies: PRKR-like Endoplasmic Reticulum Kinase/PERK H-300 #sc-13073 (rabbit polyclonal IgG, 1:1000, Santa Cruz Biotechnology Inc., Santa Cruz, CA), Inositol-requiring Enzyme 1/IRE1 H-190 #sc-20790 (rabbit polyclonal IgG, 1:1000, Santa Cruz Biotechnology Inc.), Activating Transcription Factor 6/ATF6 H-280 #sc-22799 (rabbit polyclonal IgG, 1:1000, Santa Cruz Biotechnology Inc.), CAAT-enhancer Binding Protein-β/C/EBP-β C-19 #sc-150 (rabbit polyclonal IgG,1:500, Santa Cruz Biotechnology Inc.), C/EBP-Homologous Protein/CHOP B-3 #sc-7351 (mouse monoclonal, 1:500, Santa Cruz Biotechnology Inc.), Eukaryotic Initiating Factor 2α/EIF2α FL-315, #sc-11386 (rabbit polyclonal IgG, 1:1000, Santa Cruz Biotechnology Inc.), phospho(Ser50)EIF2α #ab-3257 (rabbit monoclonal IgG, 1:1000, Abcam), , X-box Binding Protein 1/XBP1 #ab-37152 (rabbit polyclonal IgG, 1:1000, Abcam, Cambridge, CA), Glucose Regulated Protein 78/GRP78 H-129 #sc-13968 (rabbit polyclonal IgG, 1:1000, Santa Cruz Biotechnology Inc.), β-Actin C-4 #sc-47778 (mouse monoclonal IgG, 1:500, Santa Cruz Biotechnology Inc.). Blotting was followed by the peroxidase-conjugated secondary antibody (Bio-Rad). The membranes were washed with Tris-buffered saline (TBS)/Tween 0.01% v/v

and proteins were detected by enhanced chemiluminescence (Bio-Rad Laboratories). Blot images were acquired with a ChemiDoc™ 316 Touch Imaging System device (Bio-Rad Laboratories).

1.9 PCR ARRAY:

Total RNA was extracted using RiboZol RNA/DNA/Protein Extraction Kit (Amresco, VWR, Solon, OH, USA) and reverse-transcribed using the iScriptTM 350 cDNA Synthesis Kit (Bio-Rad Laboratories). qRT-PCR was performed using IQ™ SYBR Green Supermix (Bio-Rad Laboratories) using the pre-designed plates (Bio-Rad Laboratories): Prime PCR™ Unfolded Protein Response, (Bio-Rad Laboratories) and Prime PCR™ Innate and Adaptive Immune Response. Relative gene expression levels were calculated using Gene Expression Quantitation software (Bio-Rad Laboratories).

1.10 *IN-VIVO* TUMOR TOXICITY STUDY:

70,000 AB1 cells, mixed with 100 µl Matrigel (ECM Gel from Engelbreth-Holm-Swarm murine Sarcoma, #E1270, Sigma-Aldrich), were injected subcutaneously (s.c.) in 6-week-old female immunocompetent balb/C mice (Charles River Laboratories Italia, Calco), housed (4 per cage) under 12 h light/dark cycle, with food and water provided *ad libitum*. Tumour growth was measured every 3 days using Vernier Calipers and tumour volume was calculated using the equation $(LxW^2)/2$, where L= tumour length and W= tumour width. When tumour reached the volume of $50mm^3$ mice were randomized and treated as follows (n=4 animals/group): 1) control group, treated with 200 µl saline solution intraperitoneally (i.p.), once a week for 3 weeks; 2) cisplatin group, treated with cisplatin 5mg/kg i.p. once a week for 3 weeks; 3) MLN4924 group, treated with MLN4924 60mg/kg subcutaneously (s.c.) 4 times a week (4 days on/3 days off) for 3 weeks; 4) combo group, treated with cisplatin and MLN4924 as reported above. Tumour volumes were monitored daily, and animals were euthanized at day 21 after randomization with zolazepam (0.2 ml/kg) and xylazine (16 mg/kg). Tumours were resected and fixed in 4% v/v paraformaldehyde.

1.11 STATISTICAL ANALYSIS:

All data in the text and figures are provided as means ± SEM. The results were analyzed by a two-way analysis of variance (ANOVA) with $P<0.05$ as the significance cut-off over a 95% confidence interval.

2 RESULTS AND DISCUSSIONS:

2.1 CELL CYCLE ANAYSIS:

Cell cycle analysis of the 6 MPM primary cell cultures analysed showed slight changes in the percentage distribution of cells in the different phases of the cell cycle following treatments with cisplatin (PT) and MLN4924 (MLN) alone. After 24 hrs treatments, all cell lines showed increased percentage of cells in the S phase following PT, MLN and combined treatments compared to untreated cells. An increase in the percentage of cells in S phase owing to the effects of MLN on cell cycle has been documented [128–131]. However, there were no statistically significant changes in cell cycle distribution in our conditions, suggesting that it did not affect proteins involved in cell cycle progression (Figure 1-1). The increase in S-phase arrested cells is expected also in PT-sensitive cells, as an indication of DNA platination [132]. In our experimental setup, PT increased S-phase arrested cells in epithelioid cells that are known to be the most PT-sensitive MPM cells, less in biphasic and sarcomatous, with the exception of sarcomatous 720 cell line. The combination treatment increased the percentage of S-phase cells following this rank order: epithelioid MPM cells > biphasic MPM cells > sarcomatous MPM cells. This trend mimics the effect of PT suggesting that minor additional benefit may derive from the presence of MLN on cell cycle arrest.

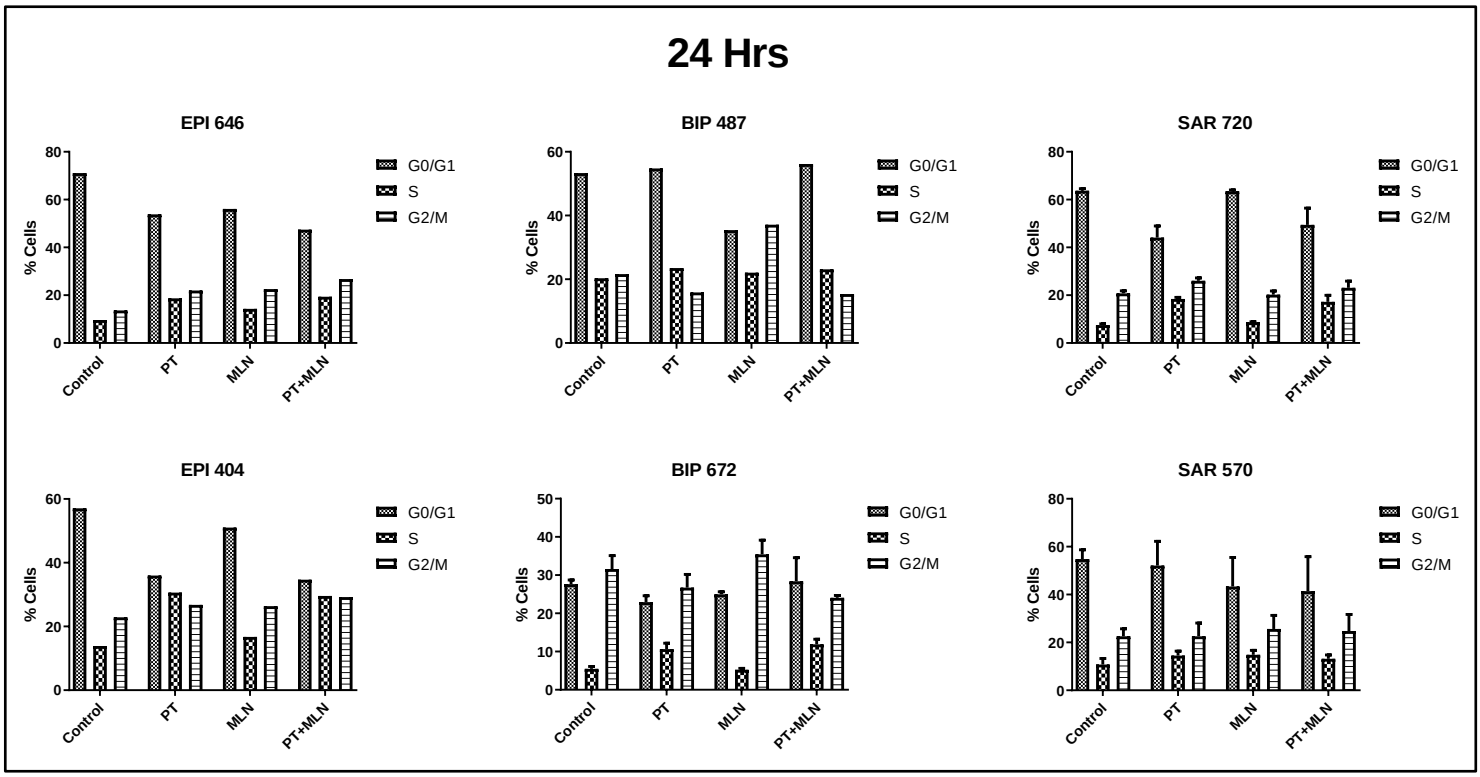

Figure 1-1: Cell cycle analysis of epithelioid, sarcomatous and biphasic human primary cell lines showing cell distribution in the three phases (G0/G1, S and G2/M) of the cell cycle following standard treatments with PT, MLN and PT+MLN at 24 hrs.

2.2 CYTOTOXICITY ASSAYS:

After 24 hrs, the MPM cells analysed differed for their sensitivity to PT: indeed, only in 720 – i.e., the MPM sarcomatous cell line that showed the highest sensitivity to the effect of PT on cell cycle - and EPI 646 cells, PT treatment increased the release of LDH, whereas the other cell lines did not. MLN alone did not induce any significant increase of LDH, suggesting that it was not cytotoxic as single agent in MPM. Combination treatment of PT and MLN after 24 hrs significantly increased the release of LDH activity in all cells compared to untreated cells, although with different behaviours among each MPM cell line (Figure 1-2).

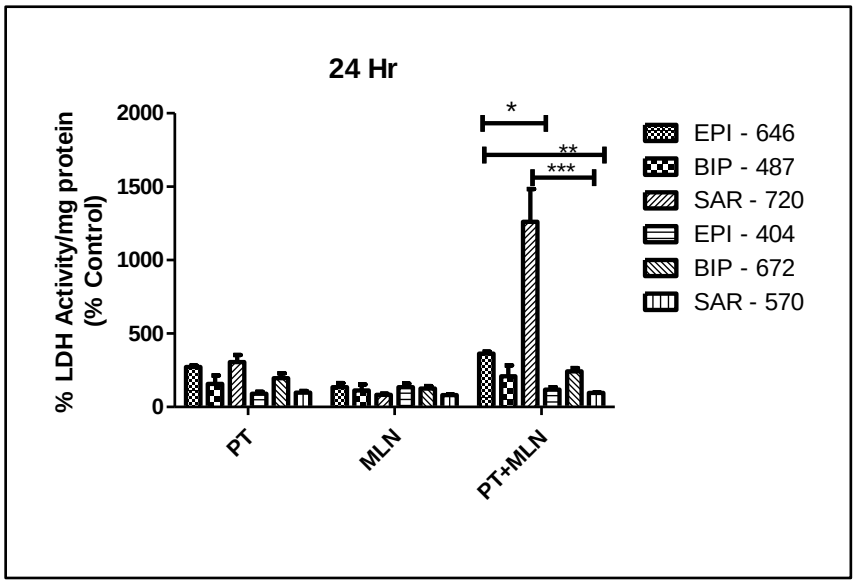

*Figure 1-2: LDH Assay of epithelioid, sarcomatous and biphasic human primary cell lines showing % LDH activity/mg of protein following standard treatments with PT, MLN and PT+MLN at 24 hrs. (*P <0.05, **P<0.01, ***P<0.001, accordingly to the significance values higher than 0.05 CI 95%).*

Based on the enhancement in terms of cytotoxicity produced by the combination treatment PT+MLN compared to PT or MLN alone, cells were classified as responders (646, 487 and 720; R) and non-responders (404, 672 and 570; NR) to the combo. This sensitivity does not reflect differences in histotype: indeed, either in responder or not-responder category, one epithelioid, one sarcomatous and one biphasic histotype was included. The sensitivity may reflect the sensitivity to PT alone: indeed 646, 487 and 720 cells showed increase of LDH release in response to PT alone and this effect was further increased by MLN, suggesting that the latter amplified a cell death mechanism somehow partially induced by PT alone.

2.3 IMMUNOGENIC CELL DEATH RESPONSE (ICD):

ICD is characterised by translocation of intracellular calreticulin to the cell surface, ATP and HMGB1 release into the extracellular matrix [125, 126].

For long time, cisplatin was not thought to trigger anti-tumour immune response [133, 134]. However, a recent report revealed that in non-small cell lung cancer, cisplatin increased intratumour DC recruitment, resulting in elevated phagocytosis and subsequent expansion of

anti-tumour CD8+ T-lymphocytes [135]. Intra-tumour recruitment of DC and their activation is mediated by cell surface expression of calreticulin [136].

MPM cells were highly refractory to expose calreticulin [125]. We investigated whether MLN+PT may act as an ICD-inducer, overcoming the refractoriness of MPM to this type of cell death. We first analysed calreticulin exposure, where the responder 487 and 720 cell line increased the exposure of calreticulin upon PT treatment and even more upon PT+MLN treatment, while the NR 404, 672 and 570 cell lines did not. Unexpectedly, R 646 cells treated with PT+MLN did not increase surface calreticulin. We are now investigating the reasons of this discrepancy (Figure 1-3).

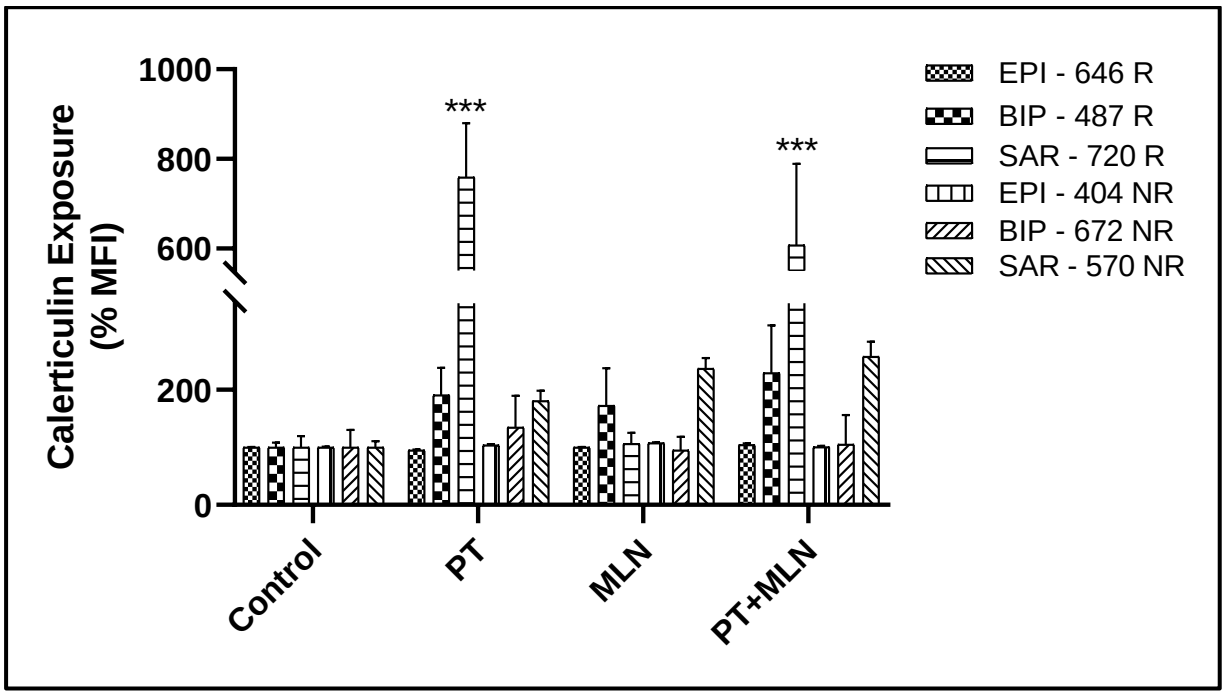

Figure 1-3: Calreticulin exposure of epithelioid, sarcomatous and biphasic human primary cell lines performed using flow cytometry. Results are expressed as a percentage control of Mean Fluorescence Intensity (MFI) following standard treatments with PT, MLN and PT+MLN after 24hrs. (p<0.05, ** p<0.01, *** p<0.001, 2-way ANNOVA; CI 95%). (R – Responder, NR - Non-responder).*

As for ATP release, a huge inter-patient variability – independent on the MPM histotype - was observed upon PT or MLN treatment alone. Two out of three R cell lines (i.e., 646 and 487) significantly increased the release of ATP upon PT+MLN treatment, while all the not-responder cell lines did not (Figure 1-4A). The differences between responders and not-responders cell lines were amplified after 48 hrs of treatment: at this time point, the combination PT+MLN was more effective than the single agents in releasing ATP in the responder cell lines (Figure 1-4B).

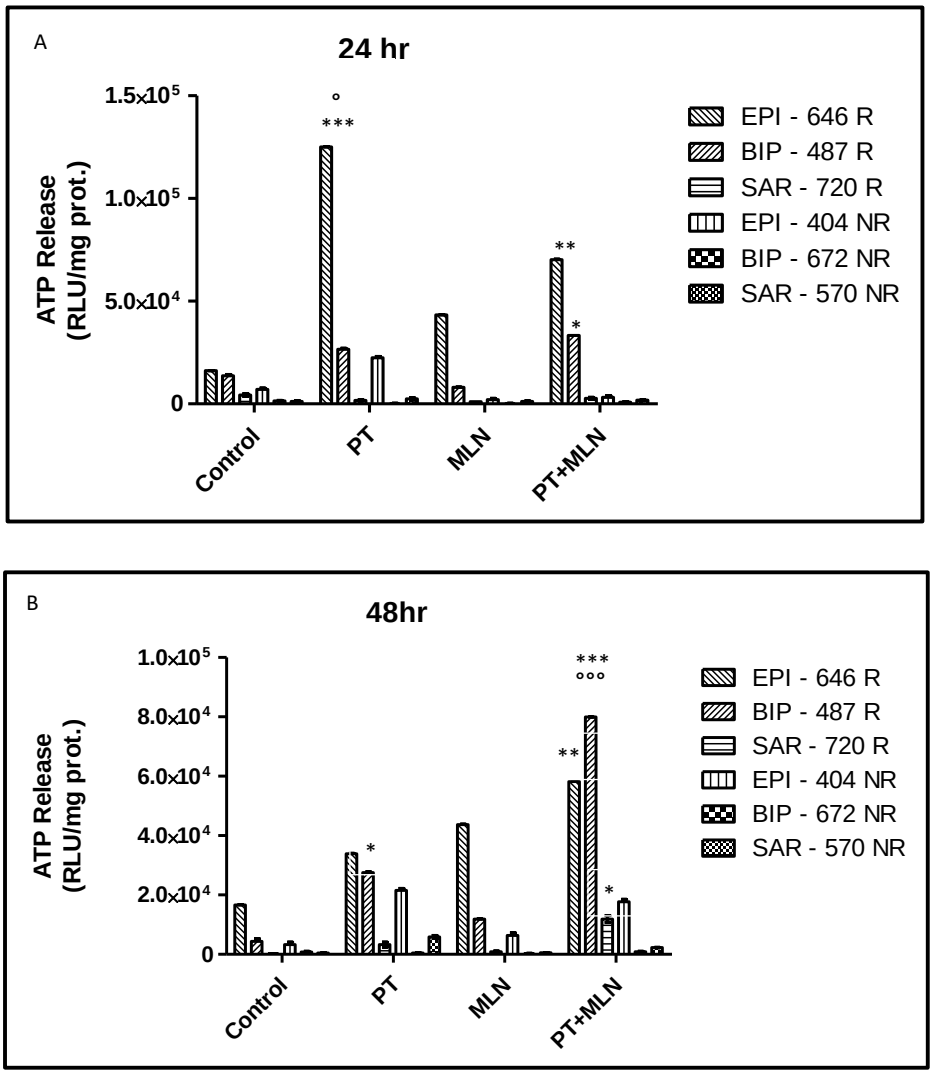

Figure 1-4: ATP release into extracellular spaces of epithelioid, sarcomatous and biphasic human primary cell lines. Results are expressed as Luminescence/Protein concentration following standard treatments with PT, MLN and PT+MLN. A) 24hrs and B) 48 hrs (/º P <0.05, **/ºº P<0.01, ***/ººº P<0.001, CI 95% accordingly to the significance values higher than 0.05 where * treatment vs. Control, º PT/MLN vs. PT+MLN). (R – Responder, NR - Non-responder).*

PT and MLN alone or in combination did not significantly increase the release of HMGB1 compared to untreated cells after 24 hrs, except for SAR – 570 NR cell line, which unexpectedly showed a significant increase with both single-agent or combination treatment (Figure 1-5A). For the other cell lines, no increase in HMGB1 was detected. By contrast after 48 hrs, all the R cell lines increased HMGB1 release upon PT+MLN treatment, the NR cell lines, with the only exception of SAR – 570 NR cell line, did not (Figure 1-5B).

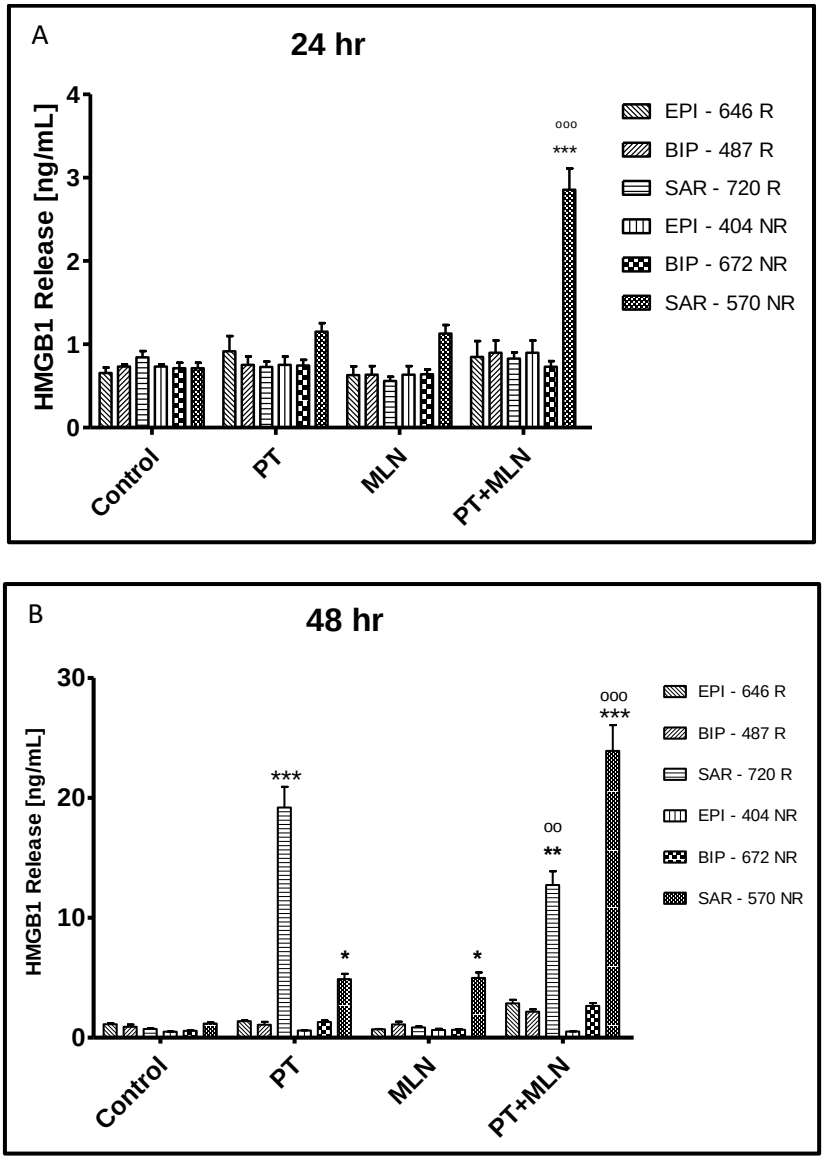

Figure 1-5: HMGB1 release into extracellular spaces of epithelioid, sarcomatous and biphasic human primary cell lines performed using ELISA. Results are expressed as protein concentration (ng/mL) following standard treatments with PT, MLN and PT+MLN. (/º P <0.05, **/ºº P<0.01, ***/ººº P<0.001, CI 95% accordingly to the significance values higher than 0.05 where * treatment vs. Control, º PT/MLN vs. PT+MLN). (R – Responder, NR - Non-responder).*

These results may be compatible with the different kinetics of ICD-related events: calreticulin is usually an early event, ATP and HMGB1 release occur later, when a greater cell damage is produced [133]. Indeed, R cell lines showed an increase of calreticulin after 24 hrs but a strong increase in ATP and HMGB1 release was detectable only after 48 hrs. Notwithstanding a certain degree of inter-patient variability, (e.g., the unexpected increase in HMGB1 in the NR 570 cell line, uncoupled however from the increased release of ATP and indicative of an ICD-independent toxicity) the NR cell lines did not show a global increase in ICD-parameters after the PT+MLN treatment, while the R cell lines did.

2.4 TUMOR PHAGOCYTOSIS AND IMMUNE ACTIVATION:

To further validate if the cytotoxic effect of PT+MLN could be due to ICD induction, we next measured the rate of phagocytosis and the activation of T-lymphocytes endorsed with anti-tumour activity, i.e. the key steps to produce a durable anti-tumour immune-response [133].

Increased MPM cell phagocytosis by DC was observed for the three R cell lines (646, 487, 720) treated with PT+MLN, although such increase was not significant toward untreated cells or cells treated with PT or MLN alone (Figure 1-6). The absence of significance may be due to the physiological variability of activity of DC that all derived from different healthy donors. Of note, all the NR cell lines were not more phagocytized than untreated cells upon PT+MLN exposure. Moreover, there was a significant difference between the phagocytosis rate of R 646 cells (top R) and NR 672 cells (worst NR) (p value <0.05, CI 95%). We are further increasing the number of experiments to reduce the inter-experiment variability and verify if significant differences occur between R and NR cells in their phagocytosis rate.

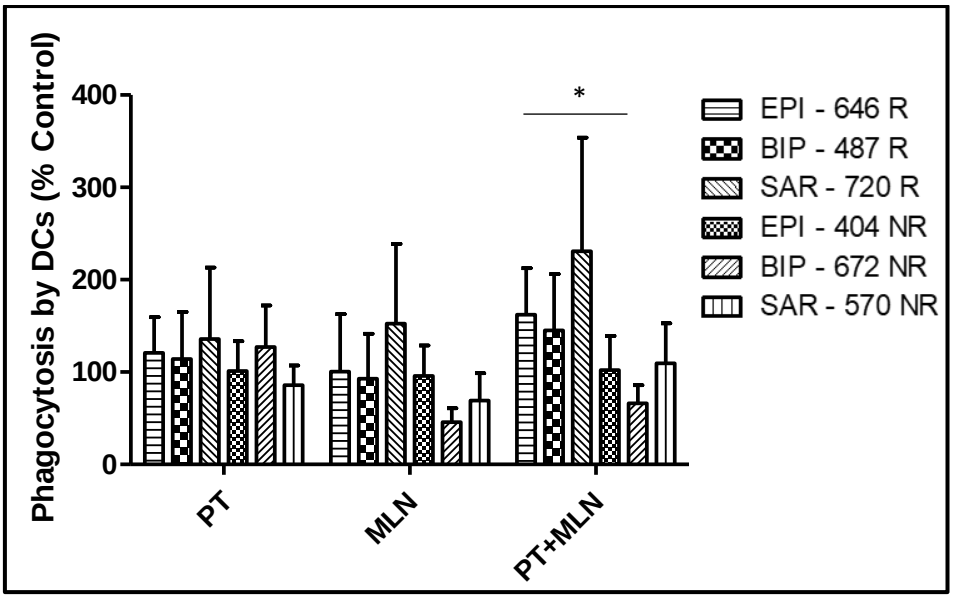

Figure 1-6: Phagocytosis of epithelioid, sarcomatous and biphasic human primary cell lines by iDCs on co-incubation. Results are expressed as percentage of phagocytic index of PT, MLN and PT+MLN vs. control (untreated) cells. (p<0.05, ** p<0.01, *** p<0.001, 2-way ANNOVA; CI 95%).*

Next, we investigated whether the phagocytosis of PT+MLN-treated cells increased the immunostimulatory capacity of DCs. This was done by evaluating the ability of DCs, after phagocytosis, to expand anti-tumour rather than immune-tolerant T-lymphocytes clones after co-culture with DCs.

Two out of three R cells (646 and 487) had a huge increase (> 50%) in $CD8^+CD107a^+$ cells upon PT+MLN treatment, while the increase in NR cells was low or absent (Figure 1-7A). While PT did not produce effects in $CD8^+CD107a^+$ cells, MLN alone increased the percentage of positive cells. Collectively, these data may suggest that PT+MLN treatment increased the DC-induced phagocytosis and expanded activated $CD8^+$cells with anti-tumour activity. Since this effect was produced also by MLN alone, this may provide a hypothetical mechanism explaining why MLN increased the cytotoxicity of PT in R cells.

The expression of the immune checkpoints, in particular PD-1, on $CD8^+$ T-lymphocytes, plays a key role in MPM-induced immune suppression [137]. MPM patients with a huge number of PD-1 positive-infiltrating T-lymphocytes have a poorer prognosis [137]. The effects of MLN were apparently independent on the expansion of $CD8^+PD\text{-}1^+$ T-lymphocytes: two out of three R, but also the NR cells treated with MLN, alone or in combination with PT, had a reduction

of $CD8^+PD\text{-}1^+$ cells (Figure 1-7B). The common trend between R and NR cells may suggest that such decrease is not dependent on MLN.

On the other hand, we worked with DC and T-lymphocytes obtained by healthy donors and not with the cells of each MPM patient, that are well-known to be positive for immune-checkpoints. This can represent an experimental bias. We plan to clarify this point by repeating these experimental set with autologous DC and T-lymphocytes.

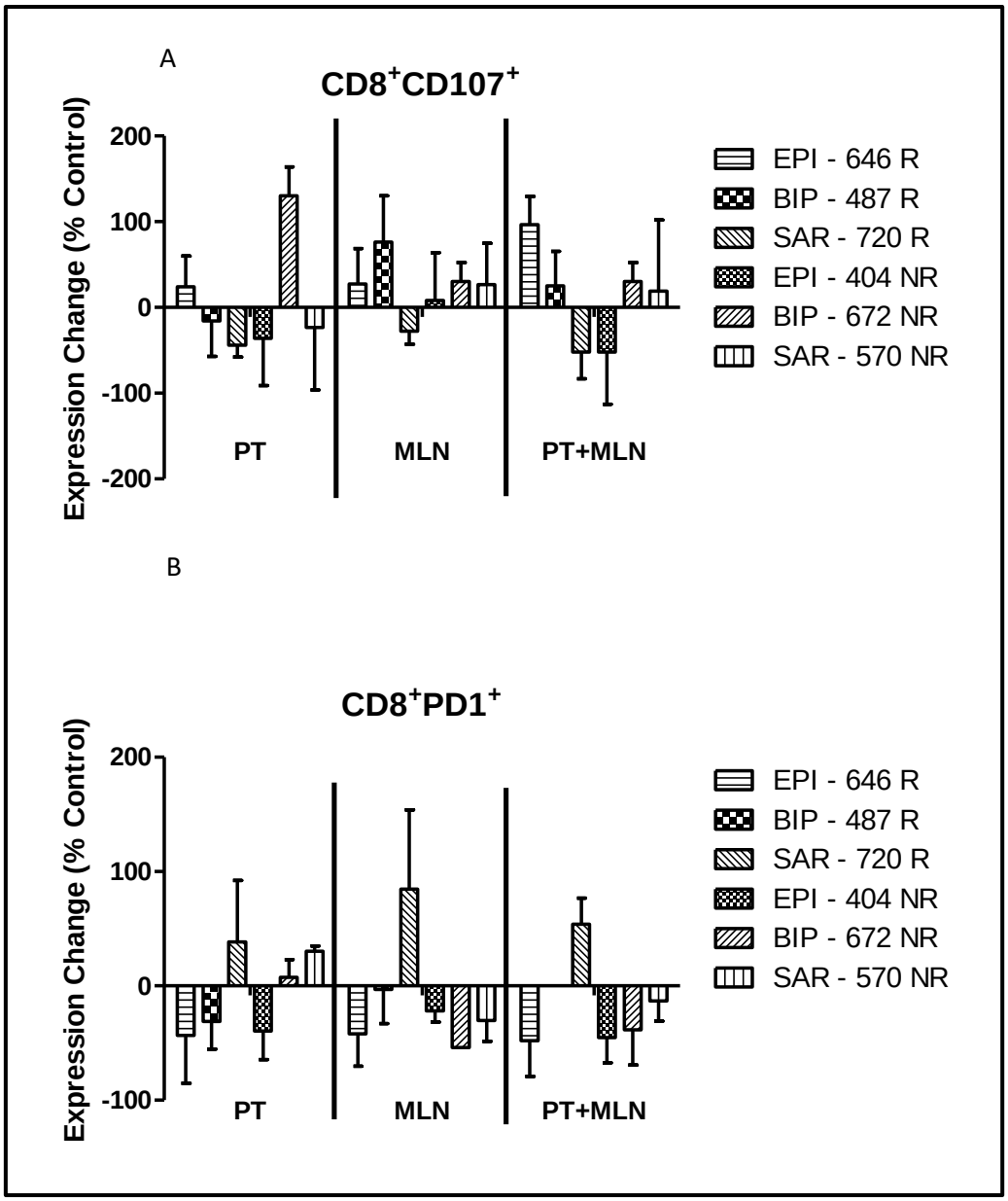

Figure 1-7: Immune activation $CD8^+$ T lymphocytes, co-cultured with iDC after phagocytosis of epithelioid, sarcomatous and biphasic human primary cell lines. Results are expressed as a percentage of change in expression of markers vs Control (untreated) cells. A) $CD8^+CD107a^+$ cells, B) $CD8^+PD1^+$ cells following treatments with PT, MLN and PT+MLN.

To get a deeper insight into the immune-phenotype of T-lymphocytes expanded, we next performed a high-throughput analysis of the genes related to innate and adaptive immunity in T-lymphocytes co-cultured with DC that have phagocytized R (720) and NR (570) MPM cells.

In NR 570 cells, PT+MLN modulated very few genes in $CD8^+$ T cells: compared to untreated cells. Down-regulated genes were CCL5 (10.5-fold), GUSB (5.1-fold), LY96 (4.5-fold), LYZ (5.0-fold) and upregulated genes were CCR5 (4.7-fold), IRF7 (4.4-fold). By contrast, the number of significantly modulated genes in $CD8^+$ T cells derived from DC after phagocytosis of R cells was higher: CCL2 (12.2-fold), CCL5 (4.8-fold), CCR4 (61.2-fold), CCR6 (4.8-fold), CD80 (15.8-fold), CSF2 (4.3-fold), ICAM1 (10.2-fold), IL17A (108.4-fold), IL18 (14.2-fold), IL2 (53.8-fold), IL6 (22.5-fold), IRF7 (4.1-fold), MAPK1 (5.4-fold), MYD88 (12.3-fold), NFKB1 (7.9-fold), TLR5 (55.9-fold) and TLR9 (4.5-fold) were significantly downregulated; CD14 was the only gene found to be upregulated 5.8 fold compared to control (Figure 1-8).

570

720

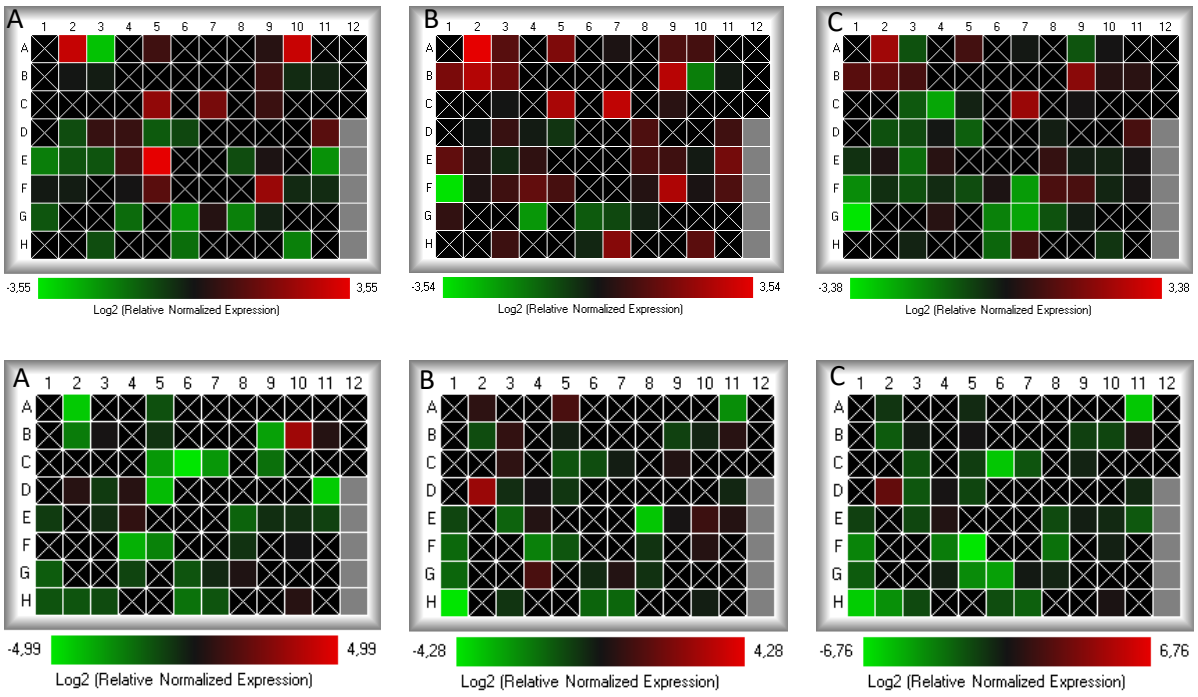

Figure 1-8: PCR Array heatmaps for innate and adaptive immune response pathways for two cell lines (570, 720) following treatments. [A - PT; B - MLN; C - PT+MLN] compared to sample controls.

By bio-informatic analysis, we are currently investigating the biological meaning of these changes. Although preliminary, these data suggest that targeting the ubiquitination/neddylation system of MPM cell may induce remarkable changes in the immune environment. We may speculate that altering protein degradation may change the pattern of surface proteins expressed on MPM. Besides calreticulin, other proteins may represent "eat-me" signals, triggering MPM cell phagocytosis by DC and affecting anti-tumour vs. tumour-tolerant phenotype of CD8+ cells. This feature is particularly critical in MPM that is known for its low antigenicity [90]. We will explore this mechanism by surfaceome analysis of R vs. NR MPM cells.

2.5 EFFECTS ON UNFOLDED PROTEIN RESPONSE:

As parallel mechanism of ICD induction, we focused on endoplasmic reticulum (ER) stress. Indeed, MLN alters protein ubiquitination and degradation, and an altered protein ubiquitination and degradation may increase the burden of unfolded proteins within ER, inducing ER stress and ER-dependent ICD [138]. The R 646 (epithelioid) and 487 (biphasic) cell lines and the NR 404 (epithelioid) cell line were subjected to a PCR Array for Unfolded Protein Response. 646 R cells showed no changes in gene expression except upregulation for two genes HSPA4L (5.8-fold) and INHBE (4.9-fold). 487 R cells showed overexpression in BEX2 (10.8-fold), CREB3L3 (5.7-fold), DDIT3 (6.0-fold), DNAJB9 (4.0-fold), INHBE (4.8-fold), PP1R15A (5.5-fold), while GINS2 was downregulated 9.1-fold, RRM2 (10.7-fold) and UHRF1 (8.8-fold). 404 NR cells showed overexpression in ADM2 (13.7-fold), BAX (4.2-fold), CREB3L3 (6.5-fold), DDIT3 (4.1-fold), HSPA4L (6.7-fold), INHBE (4.7-fold), PCNA (4.4-fold), PP1R15A (4.3-fold) (Figure 1-9).

404 646 487

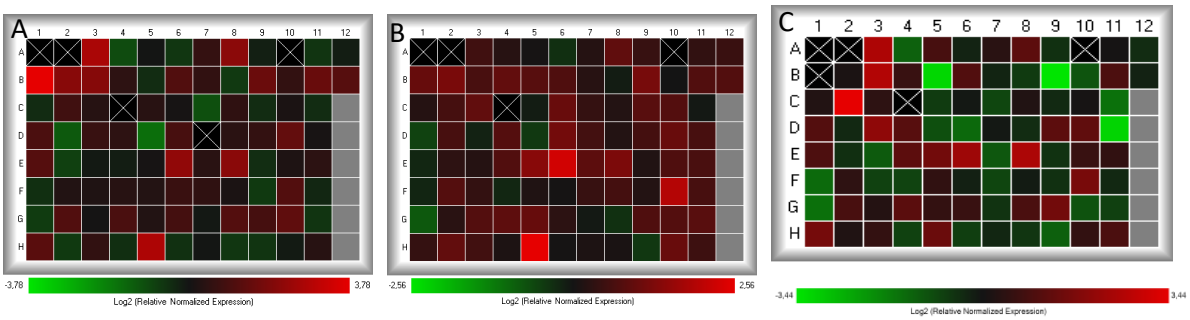

Figure 1-9: PCR Array heatmaps for unfolded protein response for three cell lines (A-404, B-646, C-487) following combined treatments compared to sample controls.

We will expand the analysis to a broader spectrum of R vs. NR cells. At present, the up-regulation of ER stress cell death executers like cAMP Responsive Element Binding Protein 3 Like 3 (CREB3L3) and DNA Damage Inducible Transcript 3 (DDIT3), which encodes for CHOP, both belong to the C/EBP-β pathway which is a driver of ICD in MPM [123]. Further, upregulation of INHBE, an ER stress dependent pro-apoptotic protein, may suggest that PT+MLN combination induces cell death by triggering ER stress, which results in ICD and apoptosis. The differences between R and NR can be explained by the fact that NR cells unlike R cells, have a significant induction of the anti-apoptotic gene Bcl2-Associated protein X (BAX) and of the proliferating cell nuclear antigen (PCNA), that may partially compensate the ER stress induced cell death elicited by PT+MLN.

2.6 EFFECT OF MLN TREATMENT ON MOUSE MESOTHELIAL CELL LINE AB1:

2.6.1 CELL CYCLE ANALYSIS:

We next repeated the key experiments in the murine MPM AB1 cell to characterize a cell line of MPM syngenic with Balb/C mice, with the purpose of testing PT+MLN efficacy in immunocompetent mice bearing AB1 tumours.

A slight increase in the percentage of cells in S phase treated with 1.0 µM MLN was observed compared to control, while PT was ineffective at both dosages tested. No changes occurred between single agent-treatment and combined treatment, suggesting that cell cycle analysis again was not significantly affected (Figure 1-10).

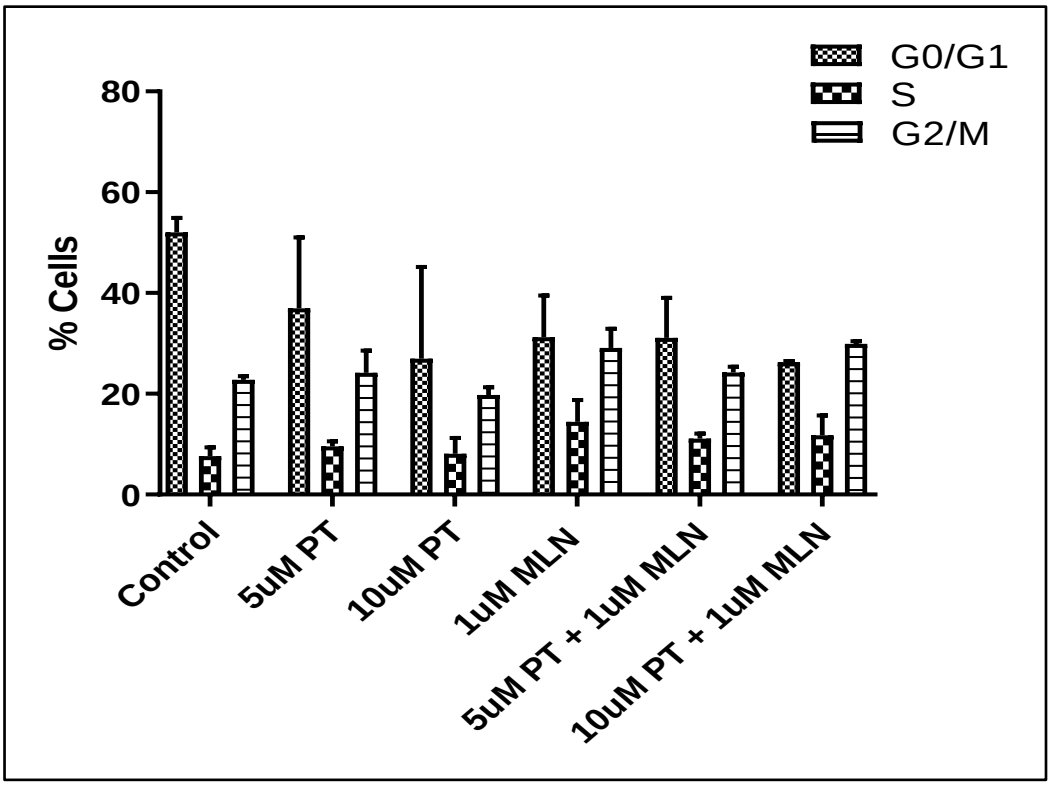

Figure 1-10: Cell cycle analysis of AB1 showing cell distribution in the three phases (G0/G1, S and G2/M) of the cell cycle following standard treatments with PT, MLN and PT+MLN at various concentrations after 24 hrs.

2.6.2 LDH ASSAY:

After 24 hr, 10 µM PT increased the release of LDH, while no significant increase was observed with MLN alone. However, MLN combined with 10 µM PT increased the release of LDH more than single agent treatment (Figure 1-11), reproducing the situation of "R" human MPM cells.

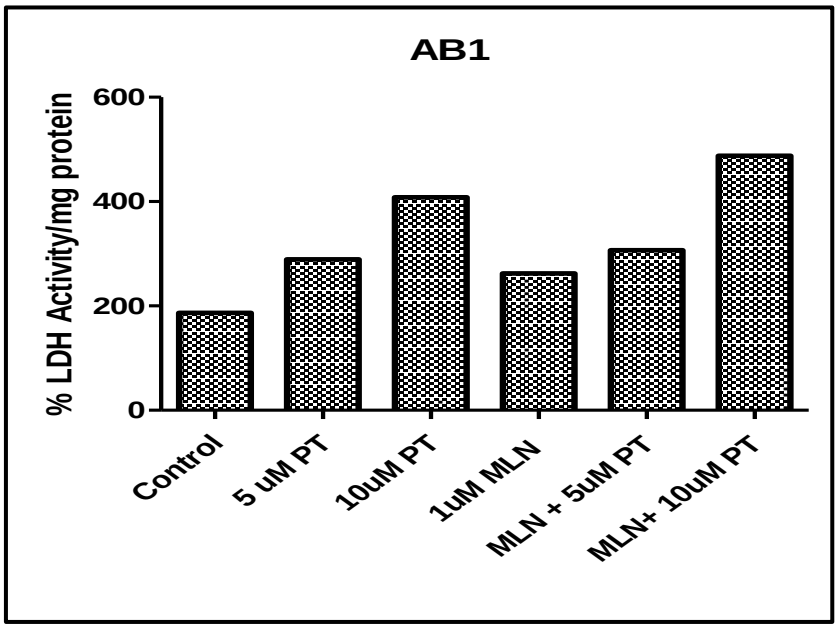

Figure 1-11: LDH activity expressed as enzyme activity/mg of protein for cellular cytotoxicity following treatment with PT, MLN and PT+MLN with concentrations mentioned above in the legend after 24hrs.

2.6.3 CRYSTAL VIOLET:

To further evaluate the enhancement benefits of MLN on PT effects, we tested its effects on proliferation with a second assay, using crystal violet staining. PT did not reduce cell viability below 10-20 µM concentration. By contrast, the presence of 0.1 µM MLN was sufficient to significantly reduce cell proliferation in crystal violet staining in combination with 10 or 20 µM PT ($p<0.05$, CI 95%) (Figure 1-12). No further increase was observed with higher concentrations of MLN, suggesting that 0.1 µM was sufficient to obtain a maximal effect.

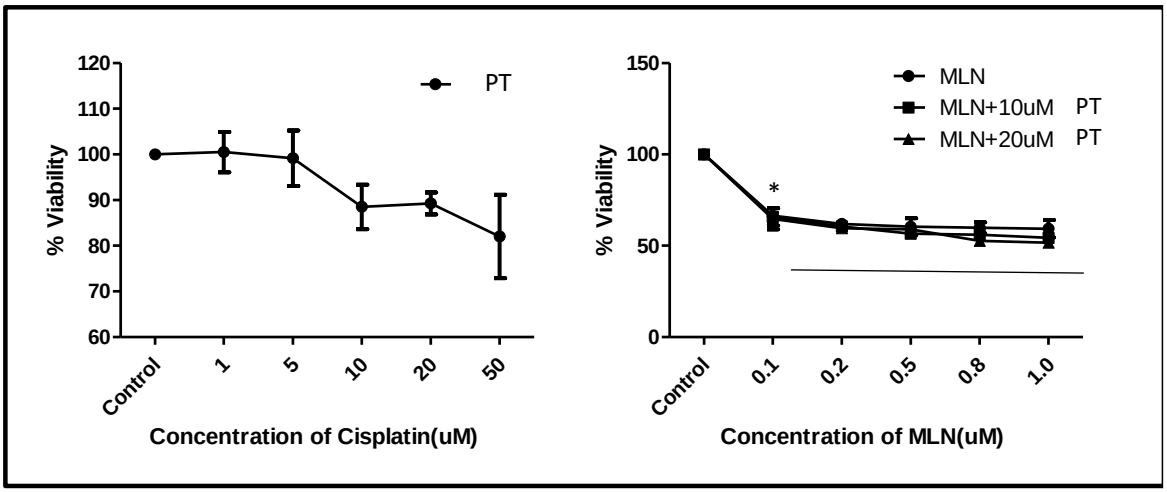

Figure 1-12: Crystal violet assay for cellular cytotoxicity following treatment with PT, MLN and PT+MLN with concentrations mentioned above in the legend after 24hrs. ($p<0.05$, CI 95%, for all MLN concentrations 0.1-1μM).*

2.7 IMMUNOBLOTTING TO STUDY ER STRESS RESPONSE:

Since in human cells we observed a higher induction of ICD and the activation of ER stress genes as possible inducers of ICD [133], we measured the expression of ER stress sensors and effectors EIF2α and phospho(Ser51)eIF2α that are downstream PERK; CEBPβ and CHOP that are downstream ATF6; XBP-1 which is regulated by IRE1 and GRP78 which aggregates in case of ER stress [137].

PT reduced IRE1, but not its downstream effector XBP-1, indicating that a univocal targeting of this arm of UPR is unlikely. PT also reduced phospho(Ser51)eIF2α: this response is known to limit protein translation and attenuate ER stress [137]. Moreover, it also reduced the amount of the pro-apoptotic protein CHOP (Figure 1-13). This result suggests that PT likely does not induce any ER stress-dependent pro-apoptotic response in AB1 cell. MLN reduced the pro-survival IRE1/XBP-1 axis [138], and increased CHOP and GRP78. It also prevented the PT-induced decrease of CHOP. These data point out that MLN triggers ER stress (suggested by GRP78 aggregation), characterized by the prevalence of cell death pathways (suggested by activated CHOP) and reduced pro-survival pathways (suggested by the decrease of IRE1/XBP1). This pattern that mimics the scenario of a human MPM R cell line, indicates that also in AB1, the ER stress induced by MLN alone or combined with PT, may elicit ICD.

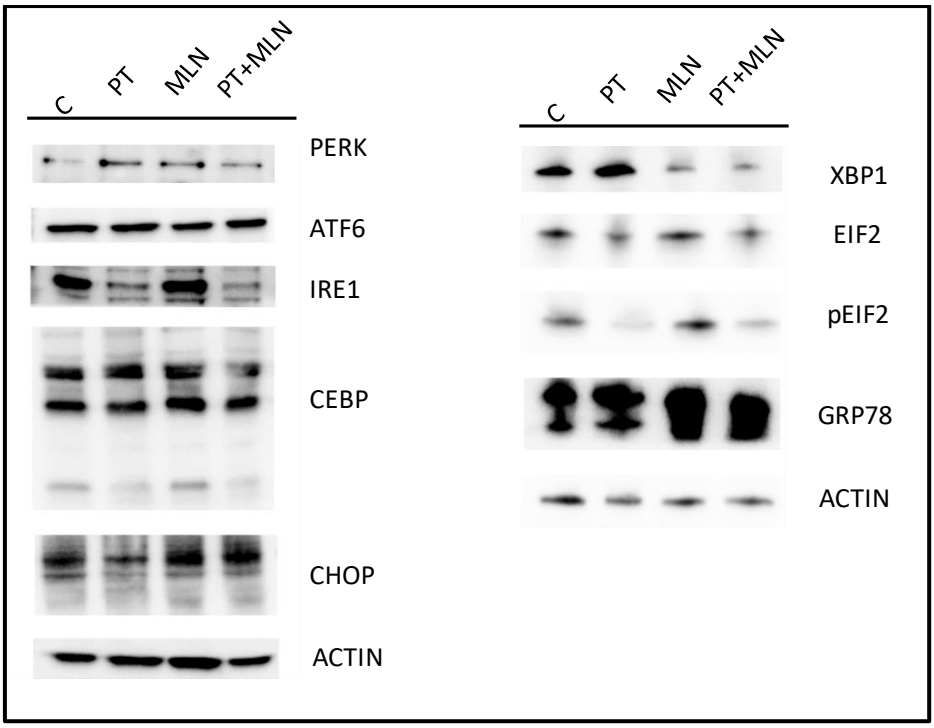

Figure 1-13: Immunoblots of AB1 following treatment with PT, MLN and PT+MLN after 24hrs. Actin (20µg) was used as control of equal protein loading.

2.8 *IN-VIVO* TUMOR TOXICITY STUDY:

We next set up in vivo experiments with AB1 treated cells, subcutaneously injected in female syngeneic immunocompetent balb/C mice, to evaluate if MLN was effective in a preclinical model with an active immune system. PT and MLN alone receiving animals did not show any decrease in tumour growth rate while only the combination treatment showed a significant reduction in the tumour volume ($p<0.001$) compared to control and individual treatments (Figure 1-14 and 1-15).

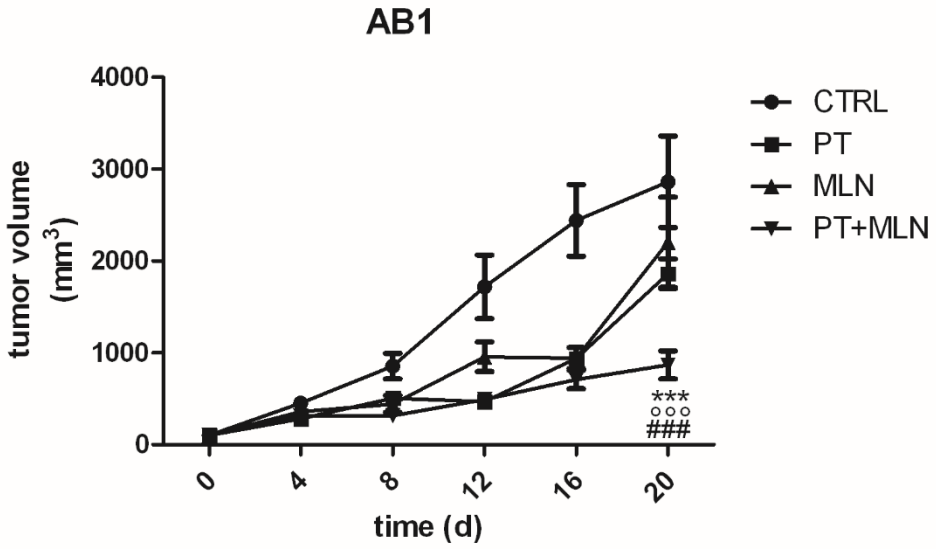

*Figure 1-14: In-vivo tumour growth of AB1 cells in Balb/C mice over 21 days treated with vehicle (Control), PT and MLN as reported in the Method section. (ANNOVA */°/# p < 0.5, **/°°/## p < 0.01, ***/°°°/### p < 0.001; CI 95%).*

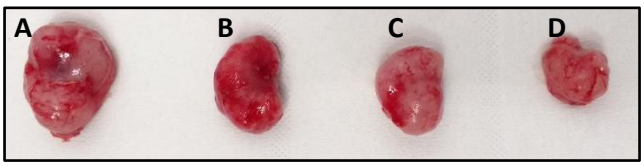

Figure 1-15: Representative image of resected tumours from Balb/C at day 21.

Preliminary experiments from the immune-infiltrating $CD8^+$ T cells indicate an increase of $CD8^+CD107a^+$ cells in the tumours of animals treated with PT+MLN, but not in the other treatment groups (data not shown). These results indicate that this combination therapy likely achieves a control of MPM growth by expanding immune-active $CD8^+$T cells with anti-tumour activity.

3 PRELIMINARY CONCLUSIONS AND FUTURE PERSPECTIVES:

Aim of this work was to propose the ubiquitination/neddylation inhibitor MLN4924 as a novel single agent or adjuvant agent for MPM treatments. The data obtained suggested that at the time and concentration used against human primary MPM cells and murine MPM cells, MLN was not effective as a single-agent, but it enhanced the effect of the first-line chemotherapy cisplatin in a subset of MPM samples, which was independent of the MPM histotype. The sensitivity to PT+MLN combination was independent from changes in cell cycle, but it was rather due to increased necrosis and immunogenic cell death. Furthermore, based on the ability of mesothelial cells to respond to MLN treatment, the different cell lines were grouped into responders and non-responders. Accordingly, following co-culture experiments, MPM responder cells induced a stronger activation of DC-mediated phagocytosis along with expansion of antitumour $CD8^+$ T-lymphocytes. Activated T-cell gene expression studies revealed several modifications in T-lymphocytes pathways corresponding to upregulation of adaptive immunity and proinflammatory markers such as CCL2, CCL5, CCR4, CCR6, IL17, IL18. The basis of the increased ICD may reside in the altered ubiquitination of proteins, that triggers ER stress, with a prevalence of pro-apoptotic and ICD inducers (e.g., CREB3L3 and CHOP) over the pro-survival mediators in responder cells.

Further, this combinatorial PT+MLN treatment efficacy was confirmed in preclinical immunocompetent model of MPM completely resistant to PT. The induction of a necrotic cell death and ER stress-dependent pro-apoptotic pathways, together with the increase in active CD8+ T-cells infiltrating the tumours, confirmed that the main mechanism of PT+MLN efficacy is based on the induction of an ICD.

Since the efficacy of PT+MLN combination is independent of the MPM histotype but seems to rather rely on the activation of specific ER stress mediators at transcriptional levels, this study opens the way to a targeted transcriptomic analysis, focused on ER stress related genes, of MPM patients, in order to identify patients who may benefit most from MLN as adjuvant agent of PT.

CHAPTER 2

Identification of Novel Therapeutic Targets in Malignant Pleural Mesothelioma – A Genome Study

1 MATERIALS AND METHODS:

1.1 CELLS:

Five primary human MPM cells [2 epithelioid (#317, #432), 1 biphasic (#487), 2 sarcomatous (#353, #359)] were obtained from the Biologic Bank of Malignant Mesothelioma, S. Antonio e Biagio Hospital (Alessandria, Italy). Cells were grown in Ham's F12 nutrient mixture medium, supplemented with 10% v/v fetal bovine serum (FBS), 1% v/v penicillin-streptomycin. Cells were checked for Mycoplasma spp. contamination by PCR every three weeks; contaminated cells were discharged.

1.2 TARGETED SEQUENCING:

DNA was first extracted from the 5 different MPM samples and targeted exon sequences were enriched using a custom made HaloPlexHS 501kb - 2.5Mb, ILM, 48 target enrichment system (G9941C) (Agilent Technologies, Santa Clara, USA) following the manufacturer's instruction [139]. The HaloPlex Enrichment technique is used to detect low allelic frequency somatic variants in heterogenous populations with a high sensitivity. The enriched DNA fragments were amplified by PCR followed by deep sequencing on an Illumina HiSeq2000 platform (Genergy Biotechnology Co Ltd, Shanghai, China). All samples were co-sequenced together. Paired-end sequencing was carried out for 100 bases from each end of around 200-bp insert fragment libraries using standard Illumina protocols.

1.3 SEQUENCE ANALYSIS:

Trimmed FASTQ files were generated by MiSeq reporter from Illumina. The sequencing outputs of the 5 samples obtained were uploaded and analysed on the StrandNGS software Version 3.1.1, Build 230243. © (Strand Life Sciences, Bangalore, India). A new DNA Variant Analysis experiment was created where the read sequencing was aligned to the reference whole human genome build (UCSC hg 19) (http://hgdownload.cse.ucsc.edu/) and genes were annotated to RefSeq Genes. The samples were aligned and filtered by Read Metric parameters: samples with base quality scores < 20 were removed. These were then saved as paired end reads and exported as BAM files using the proprietary algorithm (COBWeb). These files were filtered to remove duplicates, recalibrated and realigned. This process was followed by variant calling.

1.4 VARIANT CALLING:

The five filtered samples underwent a SNP Pre-processing step prior to SNP detection to avoid errors and to increase the support for low frequency Structural Variants (SV). This preprocessing was performed using two different pipelines called "Manual SNP Detection Pipeline" and "Inbuilt SNP Pipeline" provided by the software. The manual pipeline included first a Split Read Realignment (SRR) to split and realign to remove any split alignment artefacts. This was followed by a Local Realignment to realign the output clusters from the SRR to the human reference (UCSC hg19), eliminate alignment artifacts and to exclude indels annotated with 'dbSNP 138 indels'. Finally, the Base Quality Recalibration (BQR) was conducted to remove any errors in base calling, increasing the confidence score using the empirical method of the inbuilt GATK algorithm. Results were recalibrated with excluding variant locations with dbSNP 147 annotation. Since the Inbuilt SNP Pipeline performed the same steps as mentioned above, the BQR was not performed.

Following SNP Pre-processing, the SNPs were detected with a cutoff confidence score of 50 using the inbuilt Bayesian SNP Calling algorithm. The 2 output files obtained consisted of a Single Base Variant (SBV) List and a Multi Base Variant (MBV) List for all 5 samples.

1.5 SNP ANALYSIS:

Similarly, the SNP Analysis was performed using a multi-level and multi-step approach. First the analysis was carried out on the SNP Multi Sample Report output files by performing a SNP Effect Analysis which generates a report indicating the effect that these SNPs have on the genes in each annotation. Next, using the "Find Damaging Non-Synonymous Variants" tool, all deleterious SNPs were identified. This was followed by using the "Identify Common Variants" tool to identify all the variants within the samples. Subsequently, the SNP Effect Analysis was performed on individual SBV list of each sample. This was followed by determining Damaging Non-Synonymous Variants on two sets of output files – the SBV list obtained from the Manual Pipeline and the MBV from the Inbuilt SNP Pipeline. Using the Utilities tool to "Convert Variant List to Genes", the complete list of genes associated with the detected SNPs were annotated, using the reference genes from UCSC Browser hg19 (https://genome.ucsc.edu/), RefSeq (https://www.ncbi.nlm.nih.gov/assembly/GCF_000001405.13/) and Ensembl (http://grch37.ensembl.org/index.html).

Finally, all Protein Effect Genes were identified, and all Non-Protein Effect genes were excluded from each sample.

1.6 NETWORK ANALYSIS:

Using the list of genes obtained from the analysis, a set of networks were created on the open source software Cytoscape (Version 3.6.1) [140]. The App GeneMania (Version 3.5) [141] was used to create a network of all the associated genes to obtain an overview of the types of interactions between each gene. The gene list inputted was weighted using the Gen List Linear Regression model. Next, a Functional Interaction Network was generated for each sample using the Reactome FI App. Then, each network was annotated with the FI Database and subsequently annotated with various Cancer Pathways in the network. Finally, each network was annotated with Cancer Drugs from NCBI (https://www.ncbi.nlm.nih.gov/) having IC50, EC50, KD and KI <= 1µM. Additionally, the BiNGO App (Version 3.0.3) was used to identify any Biological Process and Molecular Functions using the Hypergeometric Statistical testing with a p value <= 0.05 and multiple testing correction using the Benjamin & Hotchberg False Discovery Rate (FDR) Correction using the ontology file GoSlim_GOA,

The entire workflow for the experiment has been discussed in Figure 2-1.

1.7 *IN-VITRO* CYTOTOXICITY ASSAY:

Cultured cells (10,000 cells/well in 96 well plate) were treated for 24 and 48hrs with increasing concentrations of Panobinostat, Olaparib and Bexarotene, i.e., the drug candidates who emerged as the most effective from the bioinformatic analysis. After treatment, the media was discarded, and the cells were treated with 0.5% (w/v) crystal violet in 25% v/v methanol for 20 minutes. The crystal violet solution was discarded, and the plate was rinsed with water. The viability of cells was measured as a function of absorbance of crystal violet at 570nm using the Synergy™ HT Multi-Detection Microplate Reader (BioTek).

1.8 CELL CYCLE ANALYSIS:

Cultured cells (300,000 cells/well) were treated for 24 and 48hrs with Panobinostat (0.3µM), Bexarotene (20µM) and Olaparib (20µM), alone and in combination. Cells were then rinsed with 1X PBS and harvested with Cell Dissociation Solution Non-Enzymatic 1X (Sigma

Aldrich, C5789). The cells were fixed with 70% v/v ethanol for 15 min at 4°C and resuspended in 400µL Citrate Buffer Solution (50mM Na_2HPO_4, 25mM sodium citrate, 0.1% v/v Triton X-100) containing 1µg/mL Bovine Pancreatic RNase and 1µg/mL Propidium Iodide. The samples were incubated in the dark for 10 min and analysed using EasyCyte Guava™ flow cytometer (Millipore). 10,000 events were collected using the FL2 channel and analysed with the InCyte software (Millipore).

1.9 IMMUNOBLOTTING:

Cells were rinsed with ice-cold lysis RIPA buffer (50 mM Tris-HCl, 150mM NaCl, 1mM EDTA, 1mM EGTA, 1% v/v Triton-X100; pH 7.5), supplemented with the protease inhibitor cocktail set III (80 µM aprotinin, 5 mM bestatin, 1.5 mM leupeptin, 1 mM pepstatin), 2 mM PMSF and 1 mM Na_3VO_4, then sonicated. Proteins were extracted after centrifugation at 13,000 × g, for 10 min at 4°C. Protein extracts (20 µg) were subjected to 4-15% gradient SDS-PAGE and probed with the following antibodies: cleaved PARP1 (194C1439) #sc-56196 (mouse monoclonal IgG, 1:1000, Santa Cruz Biotechnology Inc.), p21 (F-5) # sc-6246 (mouse monoclonal IgG, 1:1000, Santa Cruz Biotechnology Inc.), Bcl-2 (10C4) #sc-23960 (mouse monoclonal IgG, 1:1000, Santa Cruz Biotechnology Inc.), p15/p16 (C-7) #sc-377412 (mouse monoclonal IgG, 1:500, Santa Cruz Biotechnology Inc.), phosphor(Thr890)PERK (G.305.4) #MA5-15033 (mouse monoclonal IgG, 1:500, ThermoFischer Scientific, Waltham, MA), GAPDH (FL-335) #sc-23960 (rabbit polyclonal IgG, 1:1000, Santa Cruz Biotechnology Inc.). Blotting was followed by the peroxidase-conjugated secondary antibody (Bio-Rad). The membranes were washed with Tris-buffered saline (TBS)/Tween 0.01% v/v and proteins were detected by enhanced chemiluminescence (Bio-Rad Laboratories). Blot images were acquired with a ChemiDoc™ 316 Touch Imaging System device (Bio-Rad Laboratories).

1.10 PCR ARRAY:

Total RNA was extracted using RiboZol RNA/DNA/Protein Extraction Kit (Amresco, VWR) and reverse-transcribed using the iScript™ 350 cDNA Synthesis Kit (Bio-Rad Laboratories). qRT-PCR was performed using IQ™ SYBR Green Supermix (Bio-Rad Laboratories) on the Prime PCR™ Sin3 and NuRD Pathway in Transcription Regulation array (Bio-Rad Laboratories). Relative gene expression levels were calculated using Gene Expression Quantitation software (Bio-Rad Laboratories).

1.11 *IN-VIVO* TUMOR TOXICITY STUDY:

70,000 AB1 cells, mixed with 100µl Matrigel (ECM Gel), were injected subcutaneously (s.c.) in 6-week-old female immunocompetent balb/C mice (Charles River Laboratories Italia, Calco), housed (4 per cage) under 12 h light/dark cycle, with food and water provided *ad libitum*. Tumour growth was measured every 3 days using Vernier Callipers and tumour volume was calculated using the equation $(LxW^2)/2$, where L= tumour length and W= tumour width. When tumour reached the volume of $50mm^3$ mice were randomized and treated as follows (n=5 animals/group): 1) Control group, treated with 200µl saline solution intraperitoneally (i.p.), once a week for 3 weeks; 2) Cisplatin group, treated with Cisplatin 5mg/kg (i.p.) once a week for 3 weeks; 3) Olaparib group, treated with Olaparib 50mg/kg (i.p.) daily (5 days on/2 days off) for 3 weeks; 4) Panobinostat group, treated with Panobinostat 2mg/kg (i.p.) daily (5 days on/2 days off); 5) Bexarotene group, treated with 50mg/kg by oral gavage daily (5 days on/ 2 days off); 6) Olaparib + Panobinostat combination as reported above; 7) Olaparib + Bexarotene combination as reported above; 8) Panobinostat + Bexarotene combination as reported above. Tumour volumes were monitored daily and animals were euthanized at day 21 after randomization with zolazepam (0.2 ml/kg) and xylazine (16 mg/kg). Tumours were resected and fixed in 4% v/v paraformaldehyde.

1.12 IMMUNOHISTOCHEMISTRY:

Previously resected tumours were embedded in paraffin wax molds and sectioned. Sections of tumour samples, liver, kidney and spleen of all treatment groups were then transferred to glass slides and dried for further analysis. Organ tissue samples were stained using hematoxylin and eosin (H&E) to study the gross histological changes. For immunohistochemical analysis, slides were warmed to 60°C for 15 minutes to loosen the paraffin. Deparaffinisation steps were carried out using xylene washes and subsequent hydration steps in 100%, 90%, 70%, 50% and distilled water respectively. Heat induced Epitope Retrieval was performed according to manufacturer's instructions using the APTUM 2100 Retriever™ in APTUM R-Universal recovery buffer solution (#AP0530, Sigma Aldrich). Slides were washed in TBS 0.025%/Triton X-100 and blocked in 10% FBS with 1% BSA in TBS. The slides were then stained with the primary antibody for Ki-67 (1:100; ab9260, Millipore) and incubated overnight. Slides were washed and incubated in 1% H_2O_2 to remove endogenous peroxidases before the addition of the secondary anti-Rabbit-HRP for 1 hour. Slides are washed again and treated with the DAB (3,3′-Diaminobendizine buffered) (SigmaFast D9292, Sigma-Aldrich)

substrate, then counter stained with hematoxylin and the bluing agent Scott's Tap Water (S5134, Sigma-Aldrich). The slides were finally dehydrated again in ethanol and xylene before being mounted using the mounting solution (S25608 Eukitt® Quick Hardening Mounting Medium, Fluka, Sigma-Aldrich). Slides were imaged using light microscope (Leica) and analysed using the open-source QuPath 0.2.3 software.

1.13 STATISTICAL ANALYSIS:

All data in the text and figures are provided as means $\pm$ SEM. The results were analyzed by a two-way analysis of variance (ANOVA) with $P<0.05$ as the significance cut-off over a 95% confidence interval.

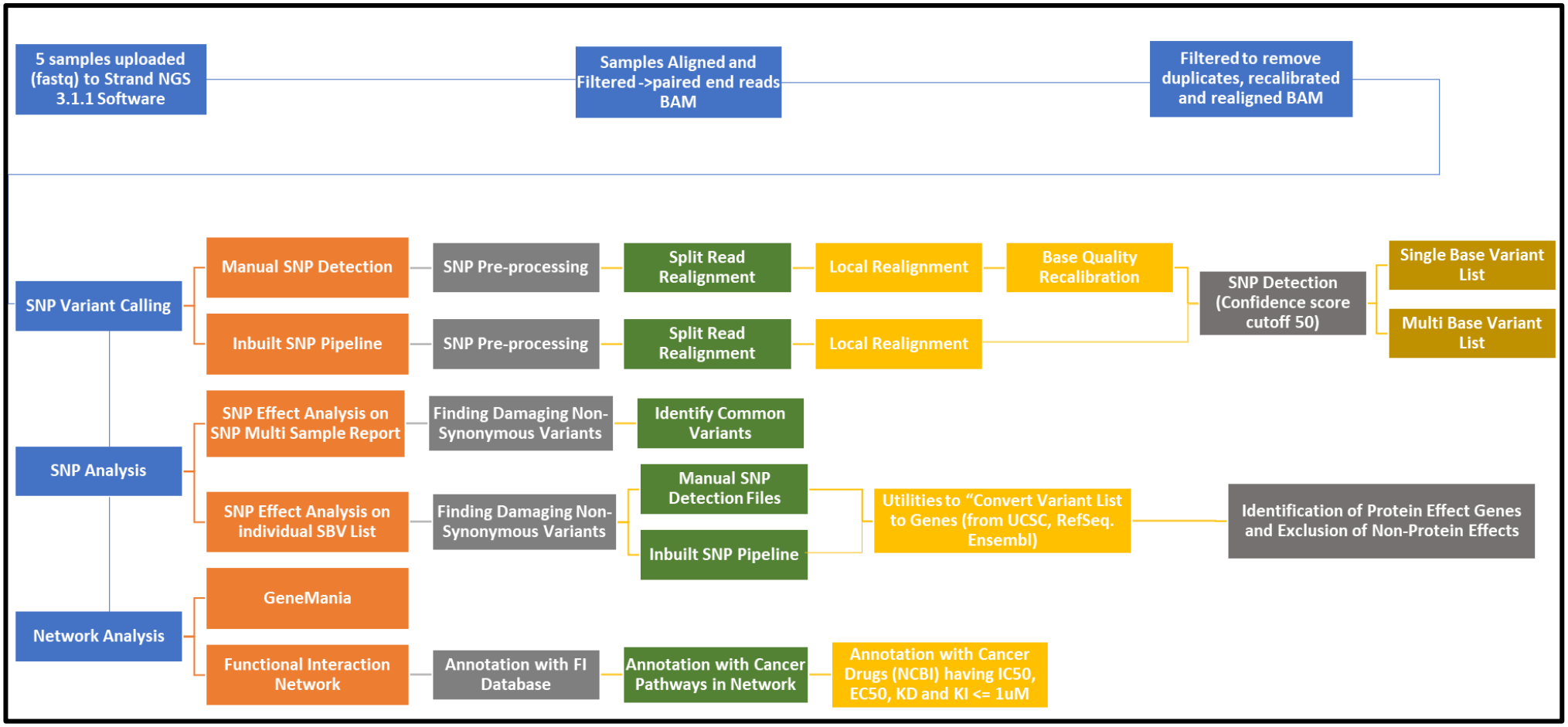

Figure 2-1: Workflow for determining deleterious mutations in protein effect genes in given mesothelioma samples.

2 RESULTS & DISCUSSIONS:

2.1 SEQUENCE ANALYSIS:

The BAM files of all 5 samples of cell lines (317, 353, 359,432, 487) were filtered to exclude all reads with an average base quality below 20. This filtered read list was used for the downstream processing. Figure 2-2 is a representative Quality Control (QC) chart of cell line 353 which shows the comparison of Pre-Alignment QC Plots between prefiltered (Figure 2-2A) and filtered (Figure 2-2B).

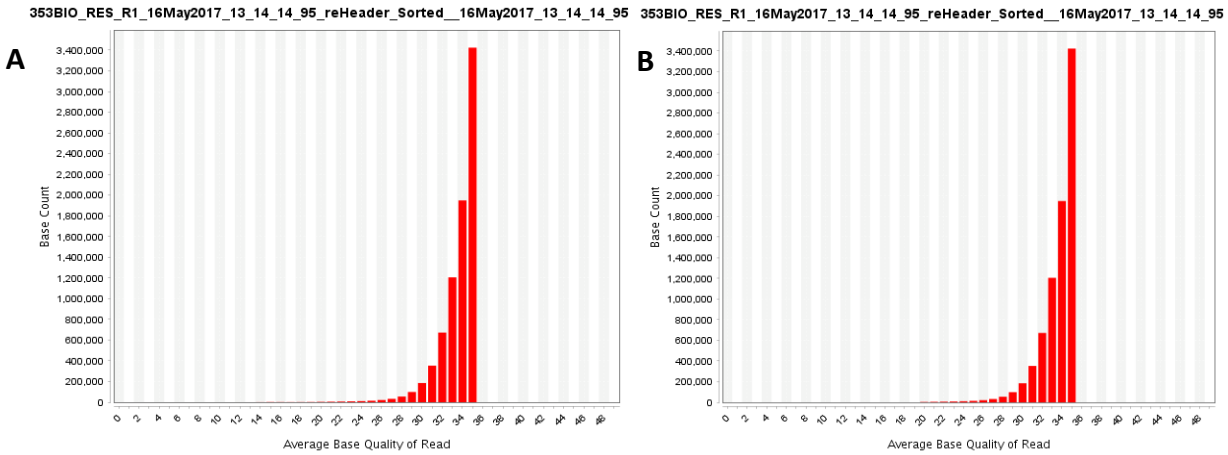

Figure 2-2: Representative Pre-Alignment Quality Control (QC) plot of cell line 353 showing prefiltered (Figure 2A) and filtered (Figure 2B) samples.

2.2 VARIANT CALLING:

Comparing the two pipelines, the data generated manually had lower artefacts and false positives compared to the Inbuilt Pipeline for variant calling. The subsequent downstream analysis was carried out individually for each cell line manually. The filtered samples underwent a SNP Pre-Processing step. First, the Split Read Realignment tool was used to remove any split alignment artefacts before a local realignment. Split read realignment (SRR) aims to increase support for low frequency structural variants (SV) by splitting and realigning poorly aligned reads. Since alignment algorithms map each read independently to the reference genome, it may result in some alignment artefacts. This means that SNPs or indels can be improperly placed with respect to their true location. This could be because of 1) sequencing errors; 2) several equally likely positions of the variant; and 3) adjacent variants or nearby errors. These misalignments can lead to false positive SNP calls as well as skewed recalibrated

base quality scores and thereby have critical impact on the downstream results. [142]. The Local Realignment Tool was used to remove such artefacts.

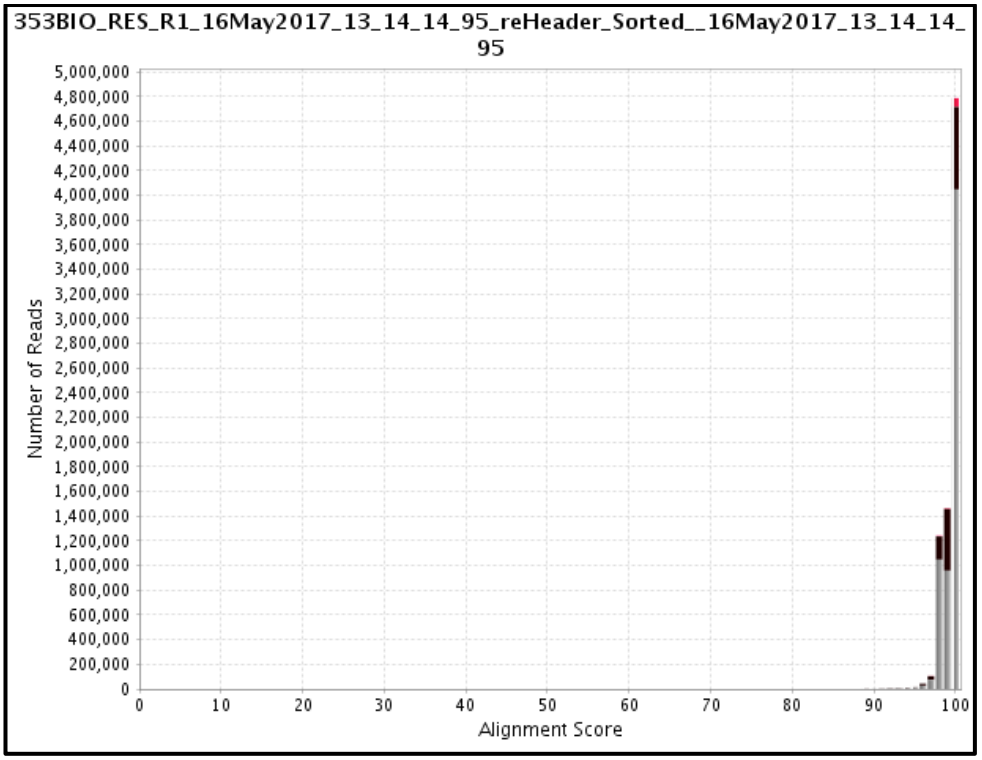

Figure 2-3: Representative post alignment Quality Control Alignment score of sample cell line 353.

The above figure shows 353 having all reads with an alignment score of 90% or higher with the most reads being aligned 100%.

Base quality score is the confidence of the sequencer in calling a base which reflects the probability of a sequencer making an error and calling incorrect base due to random sequences noise or other systematic biases (machine-, run- or sample-specific). The recalibration was performed to remove spurious false positive or false negative calls. The Base Quality Recalibration Plots obtained below (Figure 2-4) describe the effectiveness of the recalibration performed. The Reported Quality vs. Empirical Quality (Figure 2-4A) graph shows the recalibrated qualities close to the x=y line as the reported qualities is matching with the empirical qualities. The Original vs. Recalibrated Quality Score Distribution (Figure 2-4B) gives the quality score distribution over the number of bases. A slight shift in the score is observed towards lower base qualities. Additionally, Original vs. Recalibrated Residual Error by Context (Figure 2-4C) and by Machine Cycle (Figure 2-4D) both show a slight decrease in the difference between the reported and empirical quality which illustrates a successful recalibration as they tend to shift towards y=0.

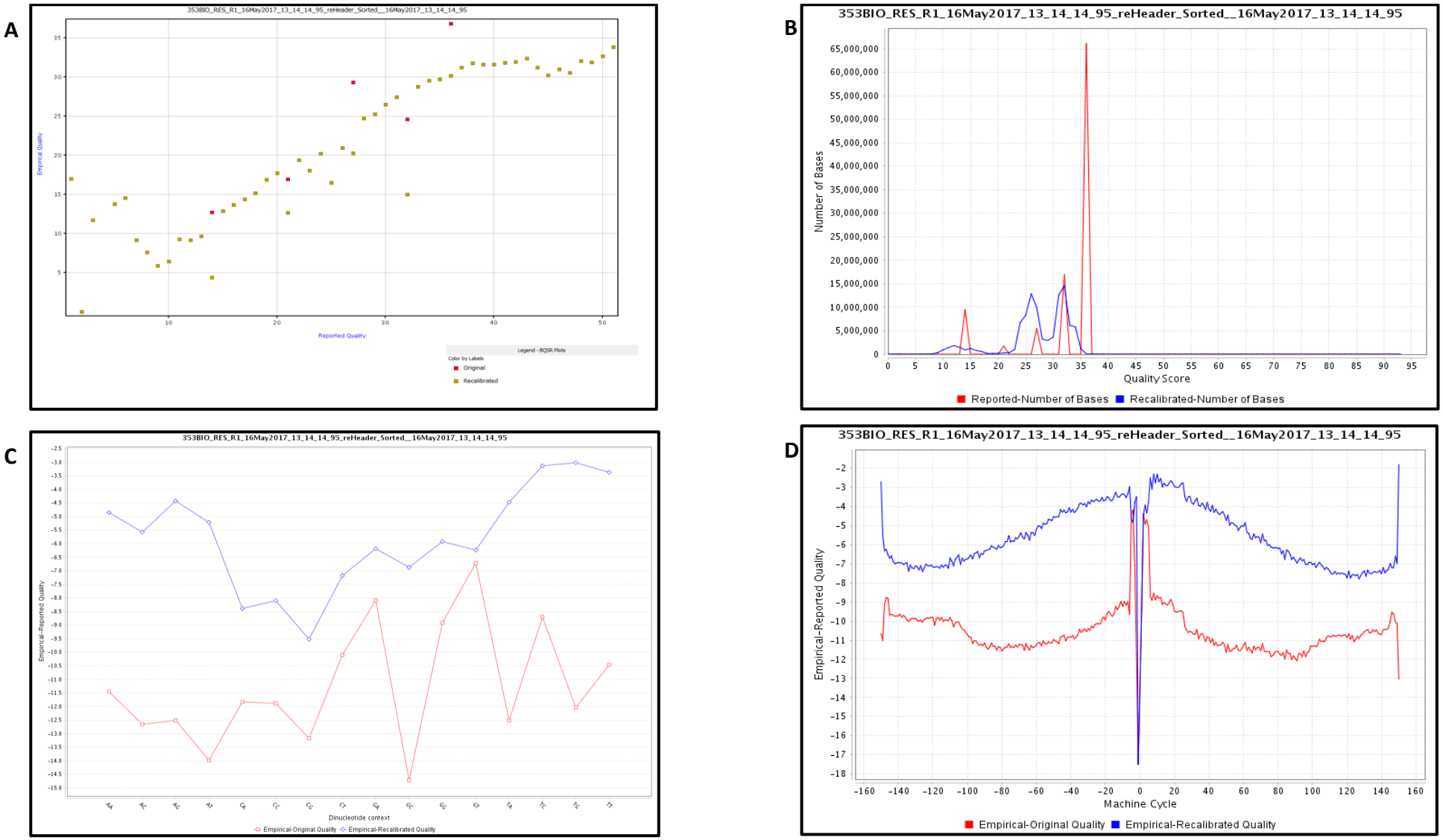

Figure 2-4: Representative Base Quality Score Recalibration (BQSR) Plots – A) Reported vs. empirical Base Quality B) Original vs. Recalibrated Score Quality Distribution C) Original vs. Recalibrated Residual Error by Machine Cycle D) Original vs. Recalibrated Residual Error by Context for cell line 353.

Subsequently, the SNPs were detected by comparing the reads from the sample genome against the reference genome using the propriety SNP calling algorithm. The mutations detected were categorised into mutations (substitutions), insertions, deletions and complex variations. SNP identification was only performed at sites determined by pre-processing to be likely SNP locations. The Decibel Confidence score cut-off was set at 50. This is proportional to the probability that the underlying genotype is the one declared, given the observed reads and associated quality scores. The high score implies greater confidence in the calling. The detected average Ti/Tv ratio (Transitions/ transversion) was 2.154 which is comparable to the ratio 2.8 observed in literature [143]. Furthermore, the ratio observed in non-pre-processed read list was lower (1.85). This improves Ti/Tv ratio suggests that the recalibration reduces any false positive variant calls.

2.3 SNP ANALYSIS:

Primarily, the Significant SNP list was generated using the read list obtained from the SNP Multi Sample Report. From the total of 6630 SNPs, 491 were low frequency allelic variants (Figure 2-5A) having a supporting reads percentage ranging from 5 – 10%. Additionally, 4678 genes were identified as high confidence common variant alleles (Figure 2-5B) and 4678 as high confidence rare variant alleles (Figure 2-5C) in all 5 samples with supporting reads percentage >= 35%.

Subsequently, the SNP Effect Analysis was performed to determine the effect of detected SNPs had on a nearby gene or transcript for a given annotation. To identify only protein effect mutations, each sample was annotated to the dbSNP 147 database and only non-synonymous mutations such as START_LOST, STOP_GAINED, STOP_LOST, FRAMESHIFT_CODING, NON-SYNONYMOUS_CODING, SPLICE_SITE, ESSENTIAL SPLICE_SITE, EXONIC, GENIC and COMPLEX_VARIATION was included. All synonymous variants (INTRONIC, 5_PRIME and 3_PRIME UTR, UPSTREAM, DOWNSTREAM, INTERGENIC and NEAR_GENE) were excluded from the list to obtain 938 total events from all the 5 samples.

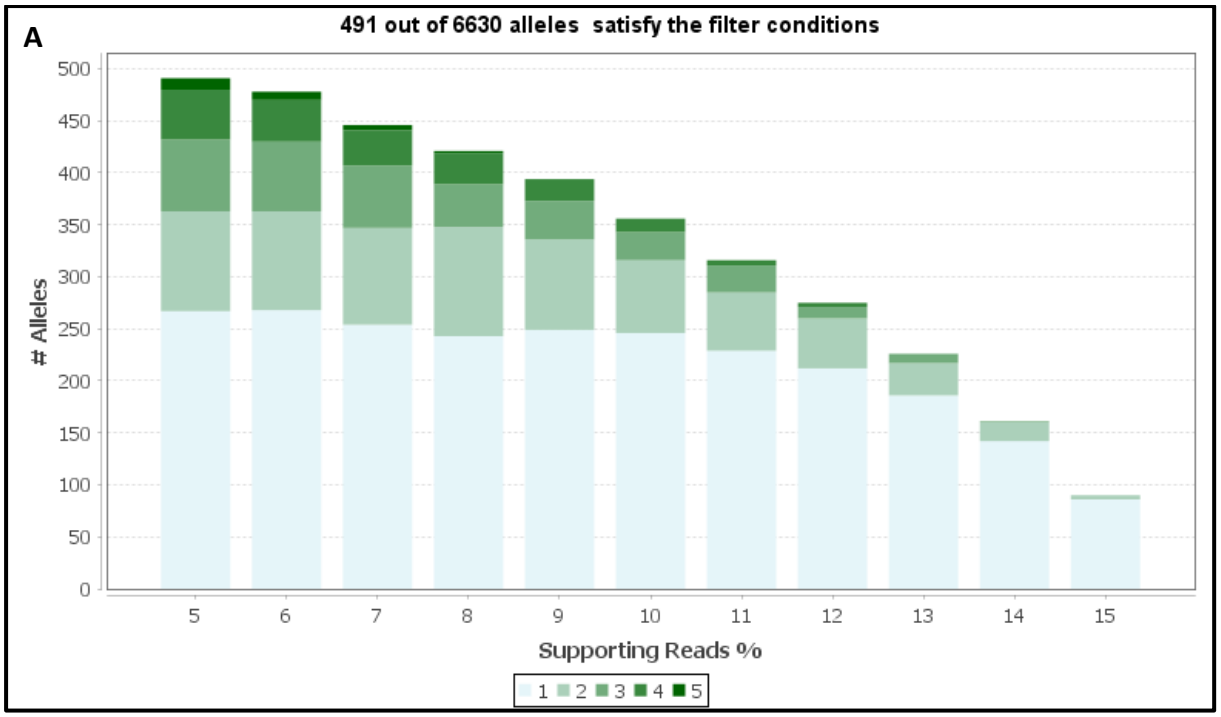
A
491 out of 6630 alleles satisfy the filter conditions
Alleles
500
450
400
350
300
250
200
150
100
50
0
5
6
7
8
9
10
11
12
13
14
15
Supporting Reads %
1 2 3 4 5

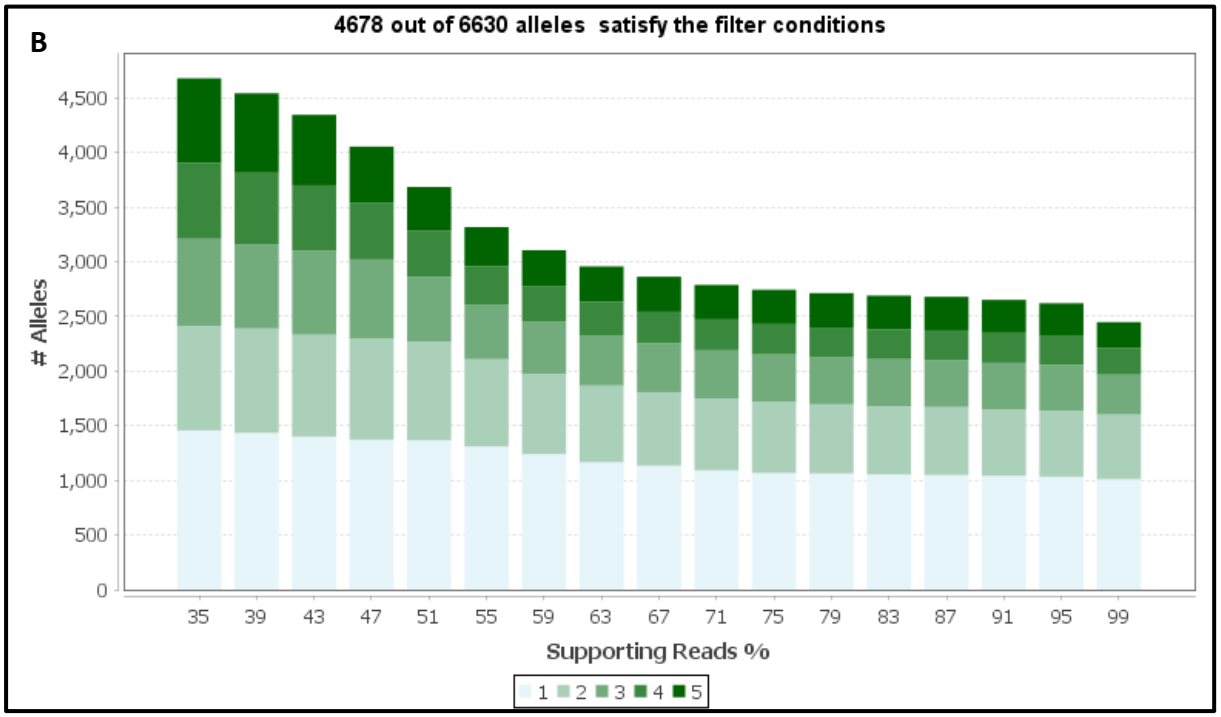
B
4678 out of 6630 alleles satisfy the filter conditions
Alleles
4,500
4,000
3,500
3,000
2,500
2,000
1,500
1,000
500
0
35
39
43
47
51
55
59
63
67
71
75
79
83
87
91
95
99
Supporting Reads %
1 2 3 4 5

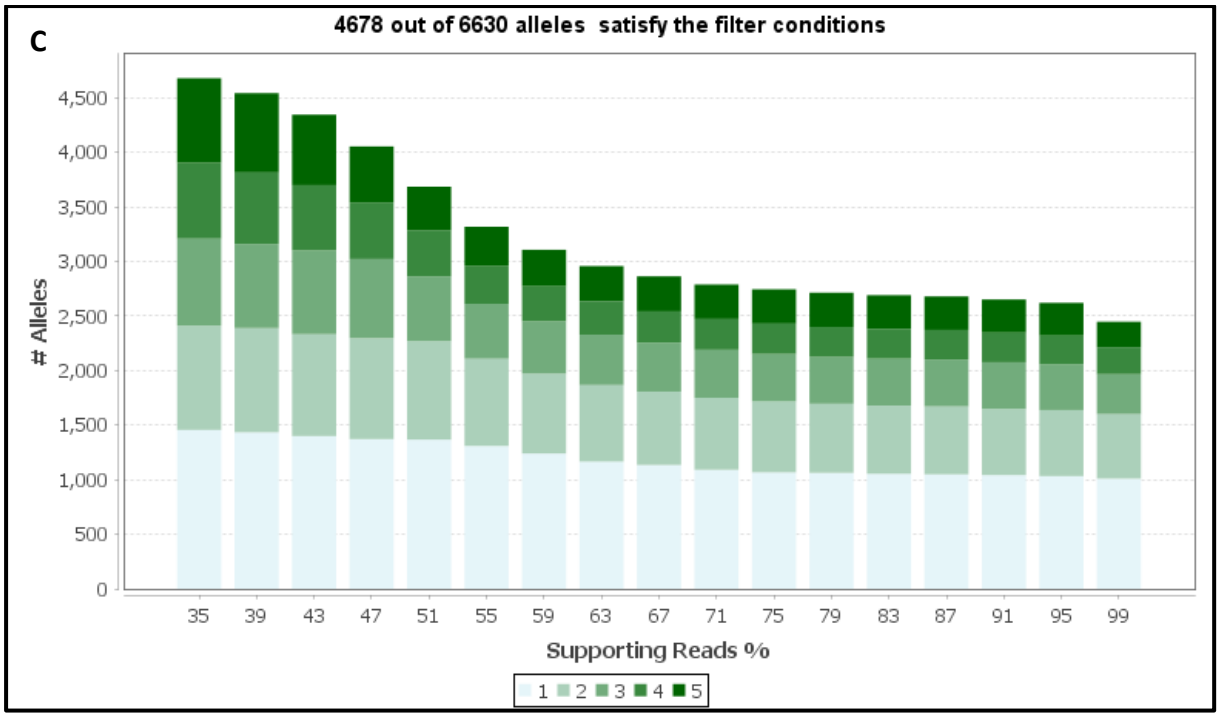

Figure 2-5: A – Low frequency mutations in all 5 samples; B - High confidence common variant alleles; C – High confidence rare variant alleles for representative cell line 353.

To further narrow the pool list of possible common and low frequency mutations that could be characteristic of malignancy, a "Damaging Non-Synonymous Variant" list was generated for each sample list. Here, any non-synonymous variant previously detected were passed through a functional prediction algorithm which determines if the variation is highly damaging or tolerable. This information was provided by annotating with dbNSFP v2b3. Here, the variations were filtered based on the deleterious nature of the variation, conservation status of the affected amino acid and variant allele frequency in the population. The identity of any unknown variant locations was obtained by employing the Utilities tool "Translate Regions to Genes" to obtain gene information from RefSeq annotations. Finally, the affected gene list which were most probably deleterious are listed below (Table 2-1) showing a total of 171 genes in all five samples.

Furthermore, all the above analysis was repeated for the In-Built SNP Pipeline and a total of 87 genes were identified in all five samples put together.

	317	353	359	432	487
# DETECTED REGIONS	140	99	103	169	149
Gene List	PIK3CD TP63 KDR TET2 IL7R NOTCH4 ARID1B KMT2C GALNT12 KLF4 PTEN RPS6KA4 MEN1 POLE RAD51B SMAD3 BLM CREBBP CDH1 ALOX12B FLCN CDK12 RARA BRCA1 RNF43 SETBP1 SMAD2 DOT1L SMARCA4 BRD4 CEBPA RUNX1 ERG SMARCB1 GPC3	FUBP1 VTCN1 ERBB4 VHL KDR PRDM1 PARK2 YAP1 KDM5A CCND2 KMT2D RAD51B CREBBP CDH1 FLCN ERBB2 RARA FLJ37644 SOX9 SMAD2 DOT1L BRD4 MEF2B CEBPA CIC RUNX1 ERG SMARCB1 EP300 KDM5C GPC3	PIK3CD AKT3 TP63 TET2 FBXW7 FAT1 IL7R NOTCH4 ARID1B KMT2C GALNT12 FGF4 YAP1 KMT2D POLE RAD51B SMAD3 CREBBP ALOX12B CDK12 BRCA1 RNF43 SETBP1 SMAD2 DOT1L SMARCA4 NOTCH3 BRD4 MEF2B CEBPA RUNX1 EP300	FUBP1 NOTCH2 AKT3 MLH1 FOXP1 GATA2 PDGFRA TET2 SDHA NOTCH4 EZH2 PAX5 FGF4 YAP1 KDM5A RAD52 KMT2D POLE RAD51B CREBBP ALOX12B NCOR1 FLCN BRCA1 RNF43 SMAD2 DOT1L BRD4 MEF2B CEBPA RUNX1 ERG SMARCB1 GPC3	FUBP1 AKT3 MSH2 PMS1 ERBB4 BAP1 GATA2 NPM1 EZH2 KMT2C MYC TSC1 FGF4 YAP1 ATM KDM5A PIK3C2G KMT2D PTPN11 POLE RAD51B CREBBP ABR ALOX12B NCOR1 FLCN SUZ12 RARA BRCA1 SMAD2 PMAIP1 DOT1L BRD4 JAK3 MEF2B CEBPA PTPRT RUNX1 SMARCB1
Total # variants	**35**	**31**	**32**	**34**	**39**

Table 2-1: List of all damaging non-synonymous variants obtained for all five cell lines 317, 353, 359, 432 and 487.

2.4 NETWORK ANALYSIS:

The network analysis was performed on all 5 cell lines. The GeneMANIA plug-in application was used to finds other genes that are related to the gene list in Table 1 as input genes, using a very large set of functional association data. Association data that was curated was - protein and genetic interactions, pathways, co-expression, co-localization and protein domain similarity. This information was obtained from GeneMANIA database of genomics and proteomics data and molecular interaction networks such as GEO, BioGRID, EMBL-EBI, Pfam, Ensembl, NCBI, MGI, I2D, InParanoid and Pathway Commons. This data was useful in understanding the kind of interactions the genes had with each other as well as with missing associated genes. From the network in Figure 2-6, it is observed that 62.17% were co-expression interactions, 13% physical interactions, 10.46% shared protein domains, 9.46% co-localisation, 3.53% genetic interactions, 0.95% pathway and 0.43% predicted interactions obtained from published data.

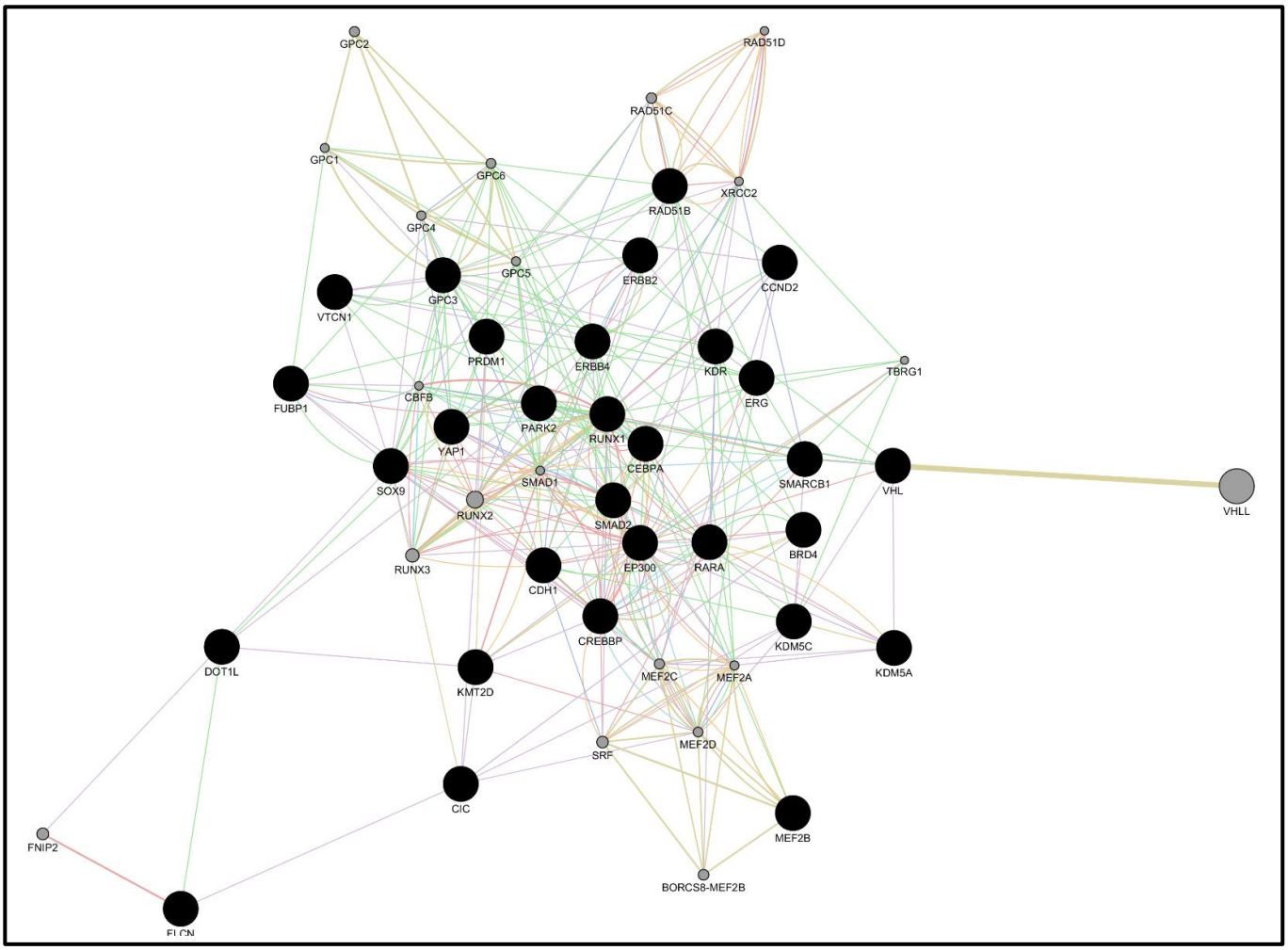

Figure 2-6: GeneMANIA force directed layout of 353 showing all functional interactions.

(% interactions)	317	353	358	432	487
Co-expression	38.16	62.17	27.26	63.42	39.41
Physical interactions	31.16	13	29.35	22.10	34.86
Shared protein domains	3.25	10.46	15.78	3.46	0.74
Co-localisation	10.84	9.46	6.76	3.60	6.70
Genetic Interactions	3.67	3.53	13.12	2.06	4.87
Pathway	3.20	0.95	3.78	2.98	7.15
Predicted	7.73	0.43	3.96	2.37	6.27

Table 2-2: Functional association table of all cell lines showing percentages of all interactions.

From the data in Table 2-2, all cell lines showed greater co-expression and physical interactions. Also, a few recorded interactions showed proteins exhibiting shared domains. From this, we can infer that mutations in these associated genes could possibly have a lot of downstream implications due to extensive protein co-expression and physical interactions. This could have a negative impact on the protein transport and localisation which results in malignancies.

The ReactomeFI app was used to find pathways and network patterns related to cancer by performing a pathway enrichment in the set of inputted genes for every cell line. This Functional Interaction Network is highly reliable as the network is developed from manually curated pathway-based protein functional interactions covering over 60% of human proteins. Furthermore, the network was annotated to determine the type of interactions vs. activations, inhibitions and indirect interactions. Closely interacting nodes were grouped into 3 or more related groups and the network was overlaid with a variety of information sources such as Cancer Gene Index annotations. Finally, all FDA-approved cancer drugs in the contexts of the FI network and Reactome pathways were visualised to investigate potential functional impacts of displayed cancer drugs as seen in Figure 2-7 for cell line 353 [144].

Subsequently, each individual gene set was subjected to a Gene Ontology Analysis using the BiNGO App function [145] showing a number of biological processes, molecular functions and cellular localisations listed in Table 2-3. Figure 2-8 shows all the processes involved with increasing degrees of significance. A majority of the proteins were found to be localised within the nucleus and are involved in regulation of various biological process, cell differentiation and organismal development. Functionally, these genes are involved in protein and nucleic acid binding and transcription regulation (Figure 2-8).

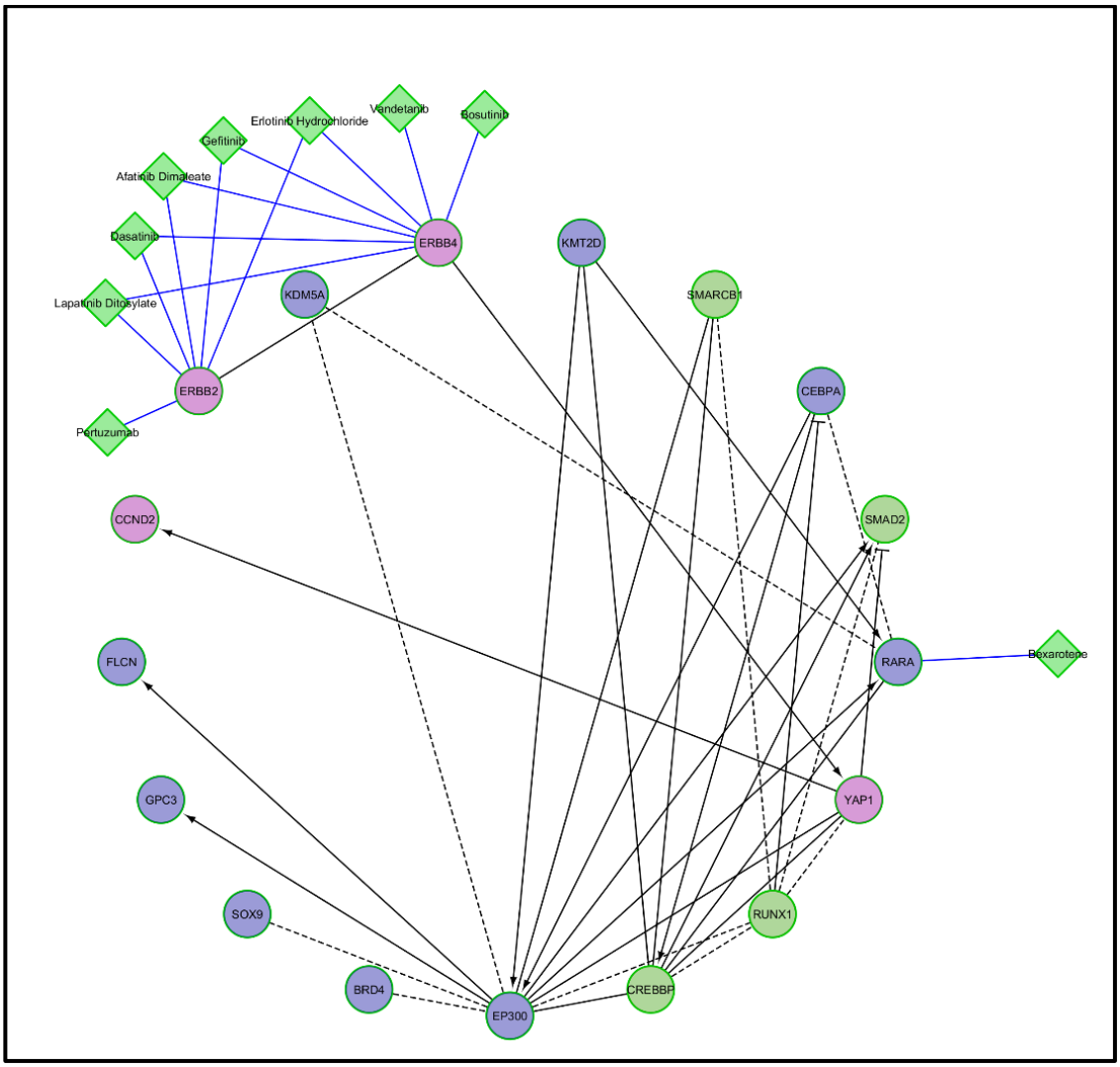

Figure 2-7: Functional Interaction Network annotated with the Cancer Gene Index and NCBI FDA Approved Cancer Drugs of 353.

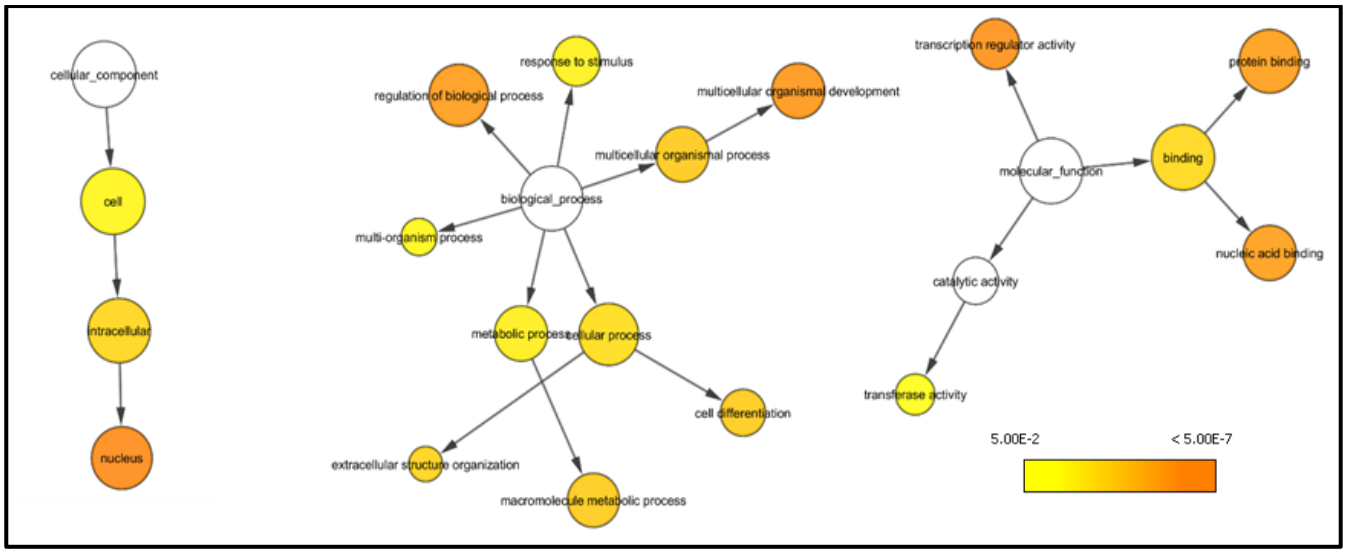

Figure 2-8: BiNGO GOSlim_GOA Analysis of 353 showing levels of significance in the three expanded compartments (cellular component, biological processes and molecular function.

In comparing all five cell lines obtained from the manual pipeline, all common genes in at least 3 cell lines were identified and further analysed as described above (Figure 2-9).

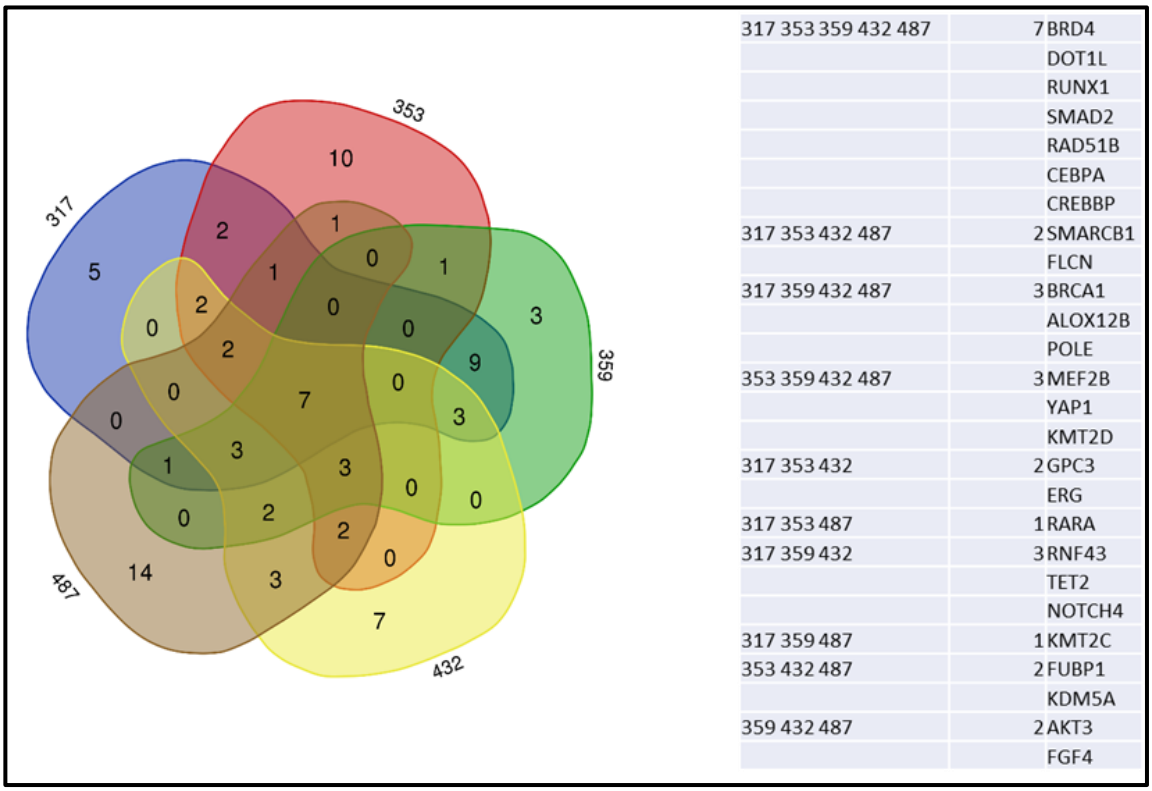

317 353 359 432 487	7	BRD4
		DOT1L
		RUNX1
		SMAD2
		RAD51B
		CEBPA
		CREBBP
317 353 432 487	2	SMARCB1
		FLCN
317 359 432 487	3	BRCA1
		ALOX12B
		POLE
353 359 432 487	3	MEF2B
		YAP1
		KMT2D
317 353 432	2	GPC3
		ERG
317 353 487	1	RARA
317 359 432	3	RNF43
		TET2
		NOTCH4
317 359 487	1	KMT2C
353 432 487	2	FUBP1
		KDM5A
359 432 487	2	AKT3
		FGF4

Figure 2-9: Venn diagram identifying intersecting genes in 5 cell lines 317, 353, 359, 432, 487.

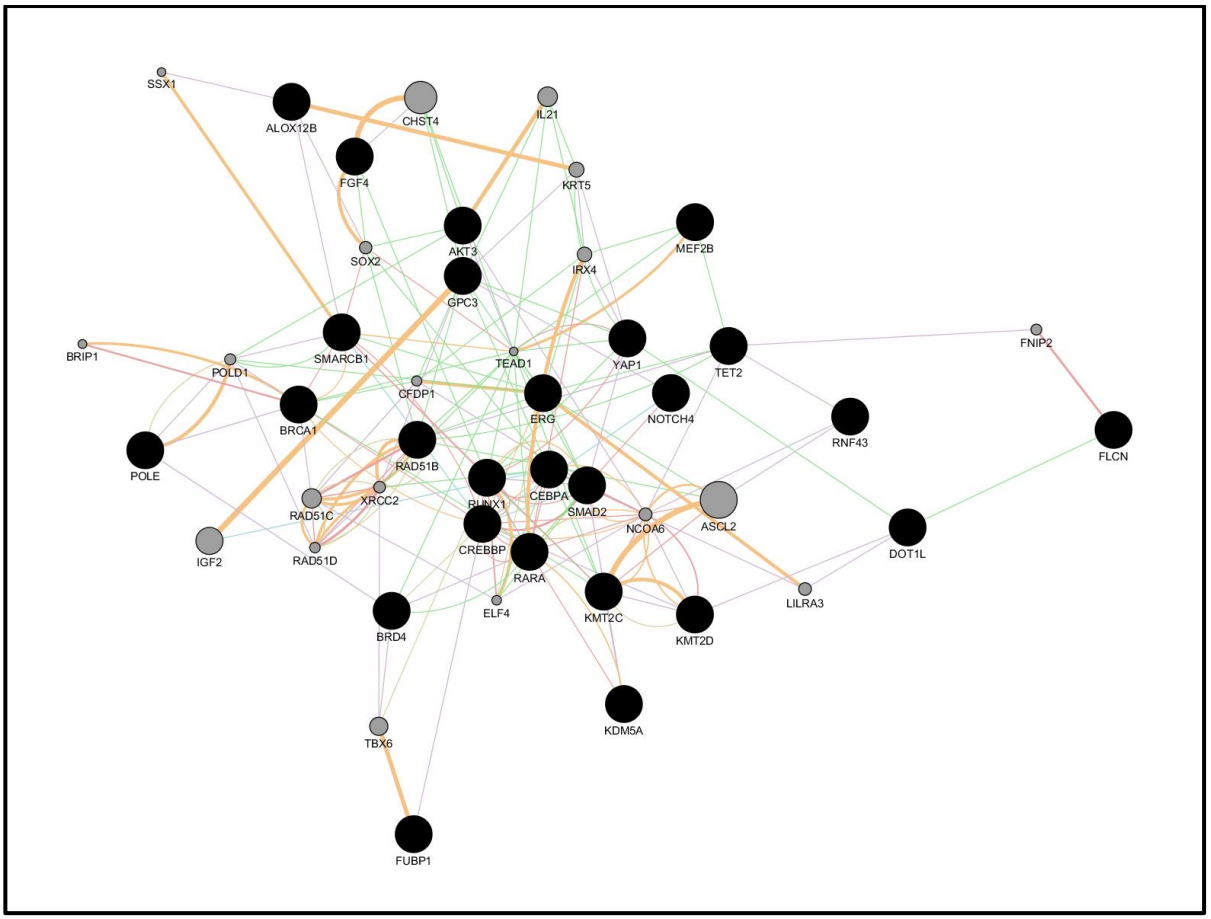

Figure 2-10: GeneMANIA force directed layout of genes common to at least 3 cell lines along with linker genes.

Figure 2-10 shows all the 26 interacting genes obtained from various GeneMANIA molecular interaction databases discussed above. Here, 54.79% of all interactions were co-expressed proteins, 23.3% of the proteins showed physical interaction within the cytoplasm and nucleus. Although significantly 13.37% showed predicted interactions between genes, 1.89% showed direct genetic interactions with 1.44% involved in activating proliferation and cancer pathways (Figure 2-11). It was observed that most of the mutant genes were evidently linked having direct and indirect interactions downstream.

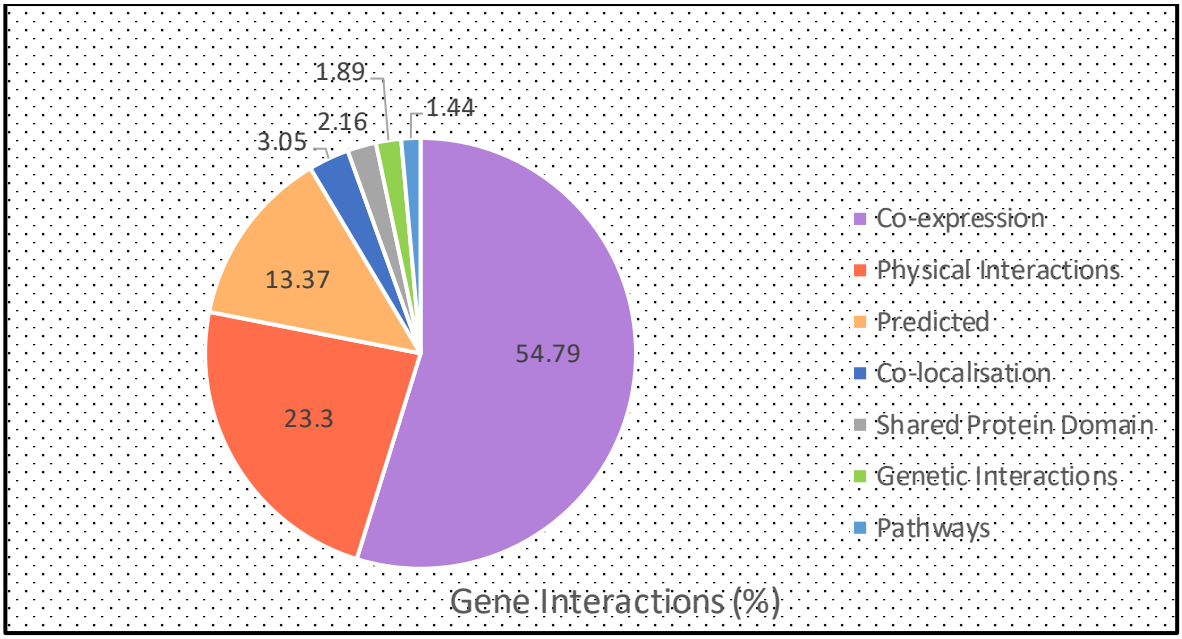

Figure 2-11: Percentage distribution of gene interactions on all cell lines.

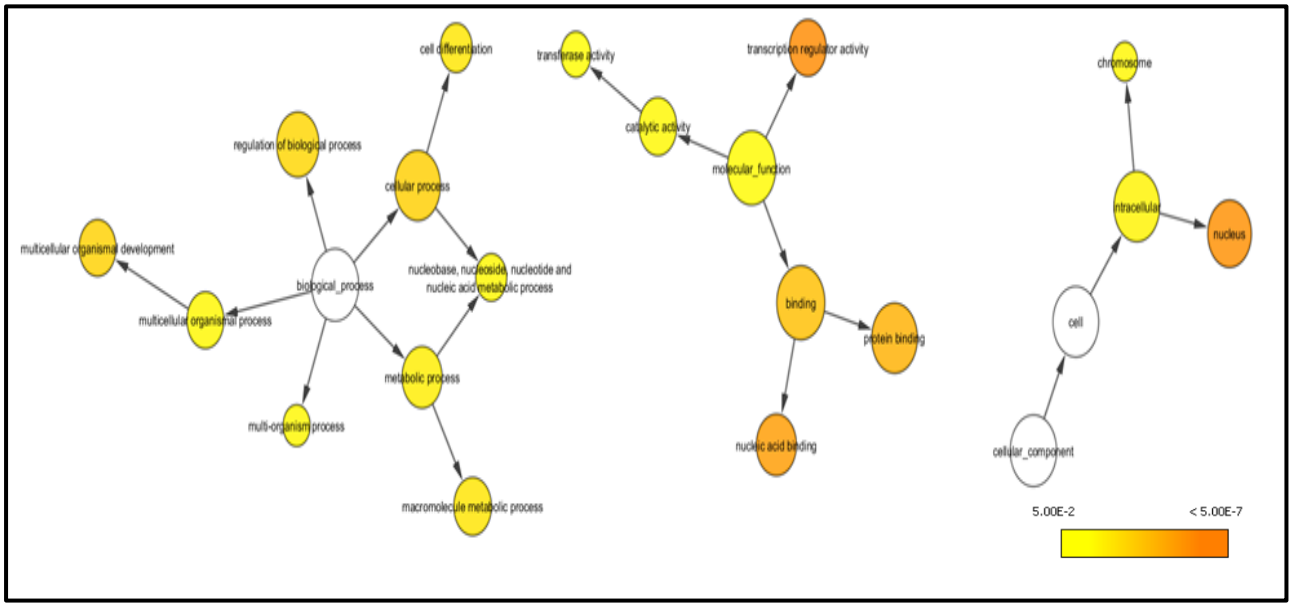

Figure 2-12: BiNGO GOSlim_GOA Analysis of intersecting genes.

A Gene Ontology Study was performed with BiNGO (Java based tool) which can be used directly or indirectly on molecular interaction graphs to identify overrepresented GO categories. In Figure 2-12, most of the significant overrepresented genes were involved in cellular development which is expected behaviour in MPM. Cellular GO processes showed the largest node with a few of these genes participating in cellular differentiation while a smaller percentage was involved in nucleic acid metabolism. Functionally, these genes were involved in direct nucleic acid binding and

transcriptional regulation which justifies the strong localisation of all overrepresented nodes within the nucleus (Table 2-3). This information facilitated the identification of possible targets using the functional interaction networks.

The functional interaction network was constructed and annotated with all interactions (activations and inhibitions) and displayed in a Circular Edge Directed Layout. All genes were annotated with cancer drugs having a Kd, Ki, IC50 and EC50 <=1µM. Satisfying all the conditions, Bexarotene was identified to act on Retinoic Acid Receptor α (RARA), Panobinostat, Romidepsin, Vorinostat and Belinostat and Rucaparib on Histone Deacetylase 2 (HDAC2) and Olaparib on Poly-ADP-ribose Polymerase (PARP1/2) and RAD51 Paralog B (RAD51B) (Figure 2-13).

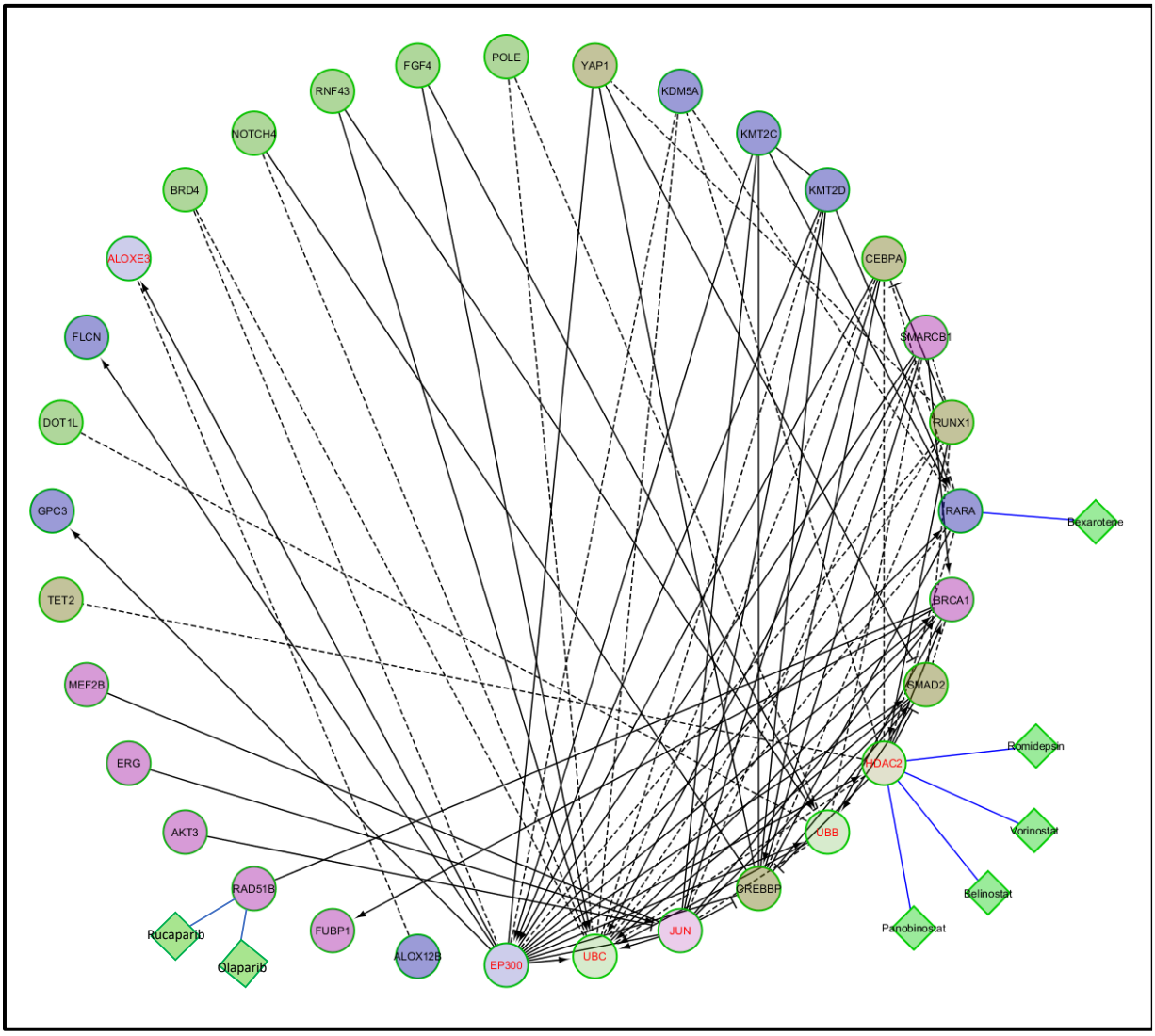

Figure 2-13: Functional Interaction Network annotated with the Cancer Gene Index and NCBI FDA Approved Cancer Drugs of intersecting genes.

GO-ID	CORR P-VALUE	DESCRIPTION	GENES IN TEST SET
3677	9.99E-05	DNA binding	KDM5A|SMAD2|CEBPA|KMT2D|CREBBP|MEF2B|KMT2C|DOT1L|BRCA1|RUNX1|RAD51B|FUBP1|RARA|ERG|POLE
16563	3.03E-04	transcription activator activity	YAP1|KDM5A|SMAD2|CREBBP|RARA|BRCA1|RUNX1
3682	3.03E-04	chromatin binding	KDM5A|SMAD2|CREBBP|RARA|POLE
30528	3.03E-04	transcription regulator activity	YAP1|KDM5A|SMAD2|CEBPA|CREBBP|MEF2B|FUBP1|RARA|BRCA1|ERG|RUNX1
3700	3.03E-04	transcription factor activity	KDM5A|SMAD2|CEBPA|CREBBP|MEF2B|FUBP1|RARA|ERG|RUNX1
18024	3.03E-04	histone-lysine N-methyltransferase activity	KMT2D|KMT2C|DOT1L
16278	3.03E-04	lysine N-methyltransferase activity	KMT2D|KMT2C|DOT1L
16279	3.03E-04	protein-lysine N-methyltransferase activity	KMT2D|KMT2C|DOT1L
8134	3.03E-04	transcription factor binding	YAP1|SMAD2|CEBPA|CREBBP|RARA|BRCA1|RUNX1
42054	4.75E-04	histone methyltransferase activity	KMT2D|KMT2C|DOT1L
10843	4.89E-04	promoter binding	SMAD2|CEBPA|KMT2D|RARA
44212	5.14E-04	DNA regulatory region binding	SMAD2|CEBPA|KMT2D|RARA
3676	5.61E-04	nucleic acid binding	KDM5A|SMAD2|CEBPA|KMT2D|CREBBP|MEF2B|KMT2C|DOT1L|BRCA1|RUNX1|RAD51B|FUBP1|RARA|ERG|POLE
8276	8.36E-04	protein methyltransferase activity	KMT2D|KMT2C|DOT1L
8170	8.36E-04	N-methyltransferase activity	KMT2D|KMT2C|DOT1L
5515	1.13E-03	protein binding	YAP1|KDM5A|SMAD2|CEBPA|KMT2D|RNF43|CREBBP|SMARCB1|MEF2B|NOTCH4|KMT2C|DOT1L|BRCA1|FGF4|RUNX1|FLCN|FUBP1|AKT3|GPC3|RARA|ERG|POLE|BRD4
51213	2.34E-03	dioxygenase activity	KDM5A|TET2|ALOX12B
16702	2.34E-03	oxidoreductase activity, acting on single donors with incorporation of molecular oxygen, incorporation of two atoms of oxygen	KDM5A|TET2|ALOX12B
16701	2.34E-03	oxidoreductase activity, acting on single donors with incorporation of molecular oxygen	KDM5A|TET2|ALOX12B
8757	2.58E-03	S-adenosylmethionine-dependent methyltransferase activity	KMT2D|KMT2C|DOT1L

3713	2.93E-03	transcription coactivator activity	YAP1|CREBBP|RARA|BRCA1
46982	2.93E-03	protein heterodimerization activity	CEBPA|NOTCH4|RARA|RUNX1
43565	3.44E-03	sequence-specific DNA binding	SMAD2|CEBPA|KMT2D|MEF2B|RARA|ERG
2039	4.22E-03	p53 binding	CREBBP|SMARCB1
60422	9.35E-03	peptidyl-dipeptidase inhibitor activity	GPC3
51577	9.35E-03	MyoD binding	CREBBP
43426	9.35E-03	MRF binding	CREBBP
43566	9.45E-03	structure-specific DNA binding	SMAD2|FUBP1|RARA
8168	1.39E-02	methyltransferase activity	KMT2D|KMT2C|DOT1L
46332	1.39E-02	SMAD binding	SMAD2|CREBBP
16741	1.39E-02	transferase activity, transferring one-carbon groups	KMT2D|KMT2C|DOT1L
3712	1.40E-02	transcription cofactor activity	YAP1|CREBBP|RARA|BRCA1
5488	1.40E-02	binding	YAP1|KDM5A|CEBPA|KMT2D|SMARCB1|NOTCH4|KMT2C|DOT1L|ALOX12B|BRCA1|FGF4|FLCN|AKT3|GPC3|POLE|BRD4|SMAD2|RNF43|CREBBP|MEF2B|TET2|RUNX1|RAD51B|FUBP1|RARA|ERG
4052	2.22E-02	arachidonate 12-lipoxygenase activity	ALOX12B
31625	2.49E-02	ubiquitin protein ligase binding	SMAD2|BRCA1
42975	2.80E-02	peroxisome proliferator activated receptor binding	CREBBP
30618	3.40E-02	transforming growth factor beta receptor, pathway-specific cytoplasmic mediator activity	SMAD2
46914	3.76E-02	transition metal ion binding	KDM5A|KMT2D|RNF43|CREBBP|KMT2C|RARA|ALOX12B|BRCA1|POLE
16165	3.77E-02	lipoxygenase activity	ALOX12B
3708	3.77E-02	retinoic acid receptor activity	RARA
34713	4.29E-02	type I transforming growth factor beta receptor binding	SMAD2
46872	4.46E-02	metal ion binding	KDM5A|KMT2D|RNF43|CREBBP|NOTCH4|KMT2C|TET2|RARA|ALOX12B|BRCA1|POLE|RUNX1
31490	4.46E-02	chromatin DNA binding	RARA
70410	4.46E-02	co-SMAD binding	SMAD2
43425	4.46E-02	bHLH transcription factor binding	CREBBP

43169	4.50E-02	cation binding	KDM5A|KMT2D|RNF43|CREBBP|NOTCH4|KMT2C|TET2|RARA|ALOX12B|BRCA1|POLE|RUNX1
43167	4.50E-02	ion binding	KDM5A|KMT2D|RNF43|CREBBP|NOTCH4|KMT2C|TET2|RARA|ALOX12B|BRCA1|POLE|RUNX1
8270	4.50E-02	zinc ion binding	KDM5A|KMT2D|RNF43|CREBBP|KMT2C|RARA|BRCA1|POLE
46983	4.62E-02	protein dimerization activity	CEBPA|NOTCH4|RARA|RUNX1
70411	4.82E-02	I-SMAD binding	SMAD2
43395	4.82E-02	heparan sulfate proteoglycan binding	GPC3
5072	4.82E-02	transforming growth factor beta receptor, cytoplasmic mediator activity	SMAD2
5102	4.89E-02	receptor binding	SMAD2|CREBBP|RARA|BRCA1|FGF4

Table 2-3: List of significant molecular processes and pathways affected in at least three cell lines.

2.5 *IN-VITRO* CYTOTOXICITY ASSAY:

To evaluate the cytotoxic effects of the drugs at 24hrs, 48hrs and 72hrs, the three different cell lines were exposed to all three drugs singly and in combination along with PT. At 24 hrs, no cell death was induced. No difference was observed between 48hr and 72hr for concentrations of Panobinostat (PAN), Olaparib (OLA) and Bexarotene (BEX). The average IC_{50} for PAN was 0.70µM, for OLA was 28.77µM and for BEX was 42.0µM in all 3 histotypes. For the combinations, the cells were treated with 50µM of PT and half of IC_{50} concentrations of 0.3µM of PAN, 20µM of OLA and 20µM of Bexarotene. The combinations of PAN+BEX and PAN+OLA showed a significantly minimum IC_{50} of 49.27µM ($p<0.05$) and 52.36µM respectively compared to all other combinations (Figure 2-14). In our experimental setup, the viability of the three cell lines was reduced after the exposure to individual treatment following this rank order: PAN>OLA>BEX. Interestingly, these cells were less sensitive to first-line PT therapy than to the combination PAN+OLA and PAN+BEX ($p<0.01$, in all histotypes). These combinations were further analysed for the biological effects triggered.

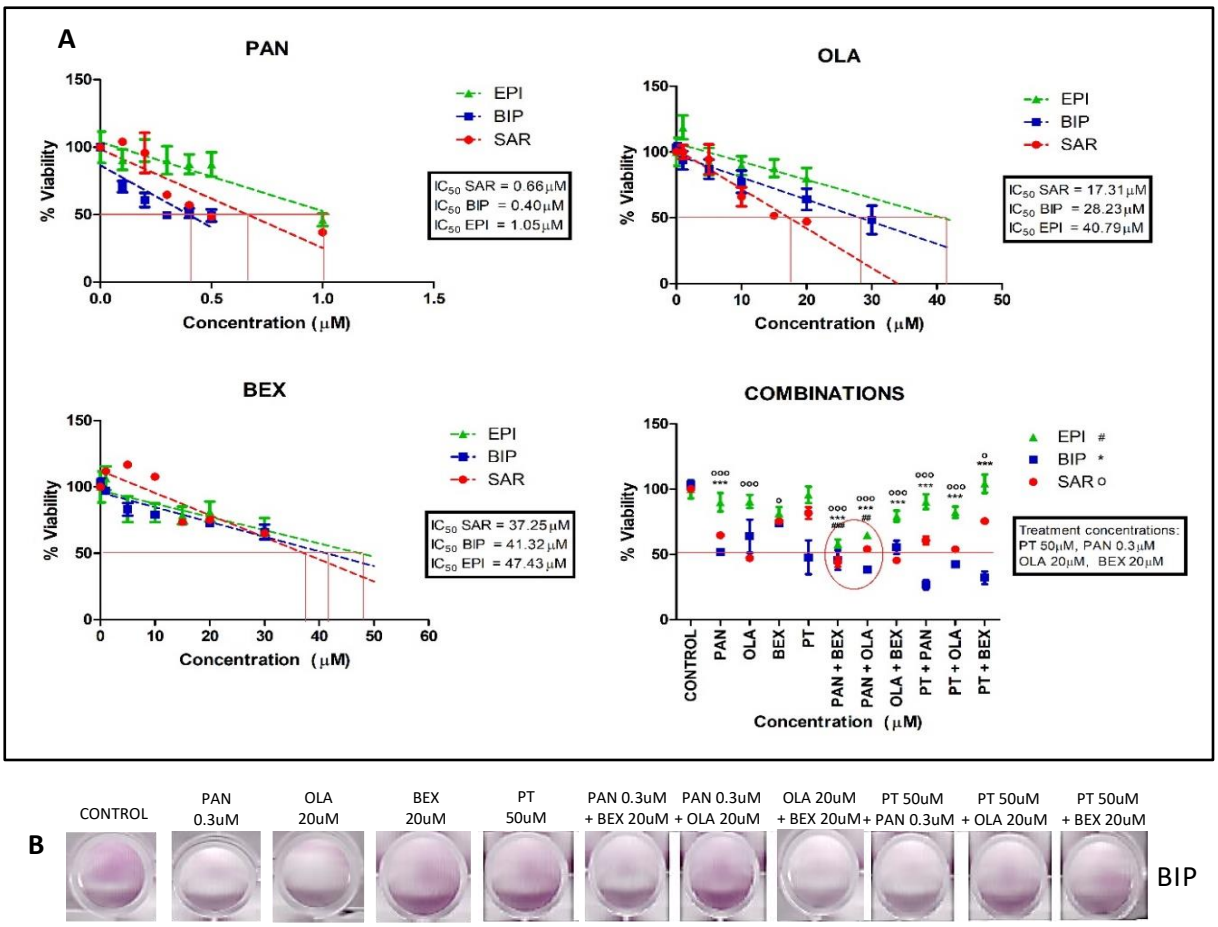

*Figure 2-14: A) Crystal Violet Assay showing IC50 after 48hr treatments with PAN, OLA, BEX and combinations: PAN+BEX, PAN+OLA, OLA+BEX, PT+PAN, PT+OLA and PT+BEX; (ANNOVA */°/# $p < 0.5$, **/°°/## $p < 0.01$, ***/°°°/### $p < 0.001$; CI95%). B) Representative image showing all treatment conditions after 48hrs in biphasic MPM.*

2.6 CELL CYCLE ANALYSIS:

Cell cycle analysis of the 3 MPM primary cell lines analysed showed changes in the percentage distribution of cells in the different phases of the cell cycle following treatments with single treatments with OLA, PAN, BEX and with the combination of PAN+OLA and PAN+BEX. After 24 hr treatments, all cell lines showed increased percentage of cells in the G2/M phase following all treatment conditions with the maximum increase seen in the combined treatment of PAN+OLA compared to untreated cells. Following 48 hr treatments, similar increase in G2/M phase was observed with a significant increase particularly seen in the combination (PAN+OLA) in epithelioid (70.13% increase) and sarcomatous (127% increase) cell lines and a 43.4% increase in the biphasic cell line. An additive effect of the combined treatments was seen in PAN+BEX treatment, with increased proportions of S and G2/M phase arrest compared to control in sarcomatous (216% and 61.5%), biphasic (88.9% and 59.5%) and epithelioid (81.2% and 40.1%) MPM cells. A significant increase was seen in S and G2/M phase following treatment with PAN+OLA in epithelioid (23.5% and 70.13%; $p<0.01$) and in sarcomatous (82.9% and 27.3%; $p<0.001$) cells. A similar pattern was observed in biphasic cells (99.1% and 43.4%) (Figure 2-15).

This increase in G2/M-phase arrested cells is suggestive of replicative stress and possible reduction of cellular DNA damage response [146, 147] triggering subsequent apoptosis and necrosis [148]. Additionally, greater S phase arrest was also observed in the cells treated with PAN and BEX and in the combinations, again indicating replicative stress [149, 150].

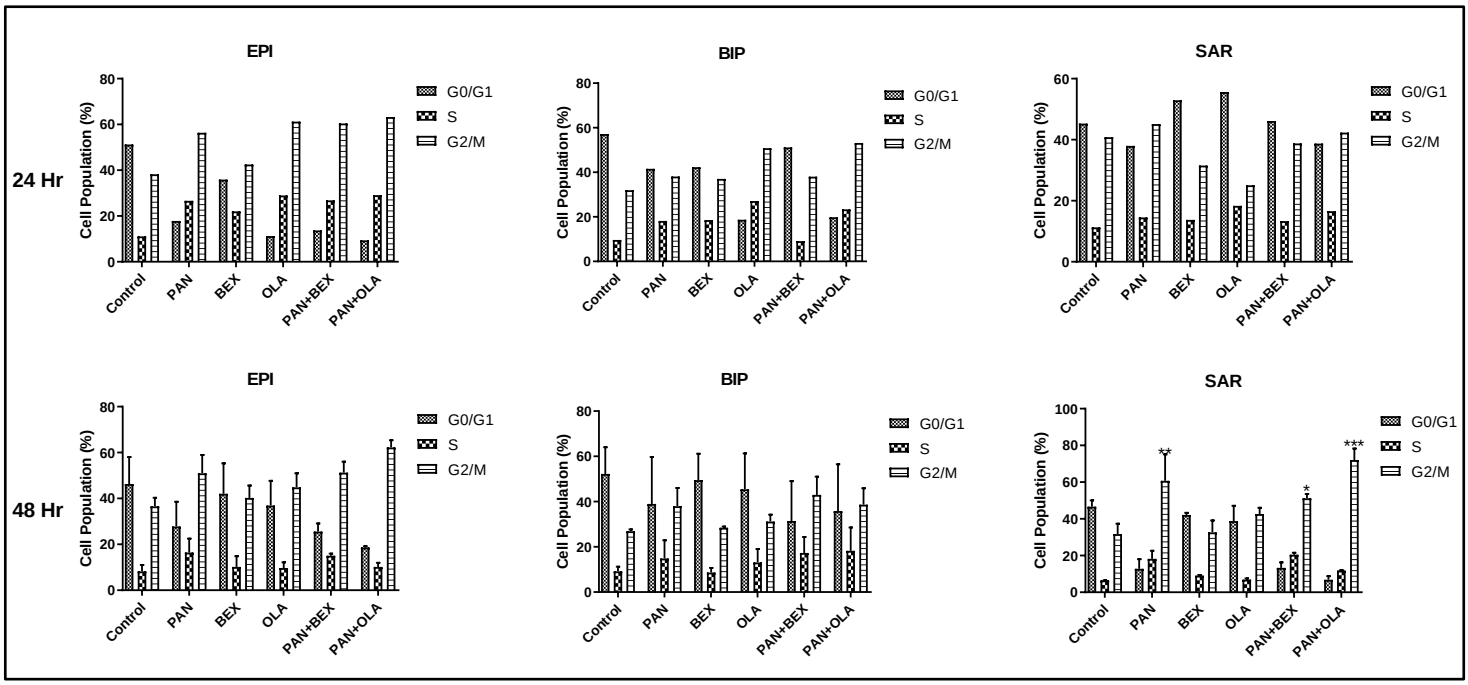

*Figure 2-15: Cell cycle population percentage in G0/G1, S and G2/M phase in epithelioid, biphasic and sarcomatous cell lines after 24hrs and 48hrs with single and combinatorial treatments showing significant increase in G2/M phase arrest on PAN+OLA treatment (Two-way ANNOVA test of significance; p <0.01 *, p<0.05 **, p<0.001 ***)*

2.7 IMMUNOBLOTTING:

Variations in the proportions of S and G2/M phase of the cell cycle is suggestive of cellular replicative stress which results in the cell progression either towards apoptosis or DNA repair pathway activations [146–152]. As an increase in S and G2/M phase populations was observed following 48hrs of treatment with PAN, OLA, BEX alone and in combination, different replicative, apoptotic and cell-cycle checkpoint protein expressions were investigated (Figure 2-16).

Interestingly, BEX alone and the combinations of PAN+OLA and OLA+BEX resulted in a lowered expression of cleaved PARP.

p21 expression was decreased by 77.2% in PAN, 75% in BEX and almost negligible in PAN+OLA treated samples showing a synergistic effect. The anti-apoptotic factor was decreased by 34.4% in PAN, 27.6% in BEX and 42.1% in PAN+OLA treated cells, while the onco-suppressive protein p15/16 was dramatically increased in all treatment conditions with the maximum levels (700%) observed in OLA+BEX. In contrast, no increases were observed

in the levels of phosphorylated PERK, suggesting that ER stress mediated apoptosis was not the result of UPR. All these suggest that treatment induced cellular apoptosis as a result of nuclear events that alter or damage DNA, preventing MPM progression in the cell cycle.

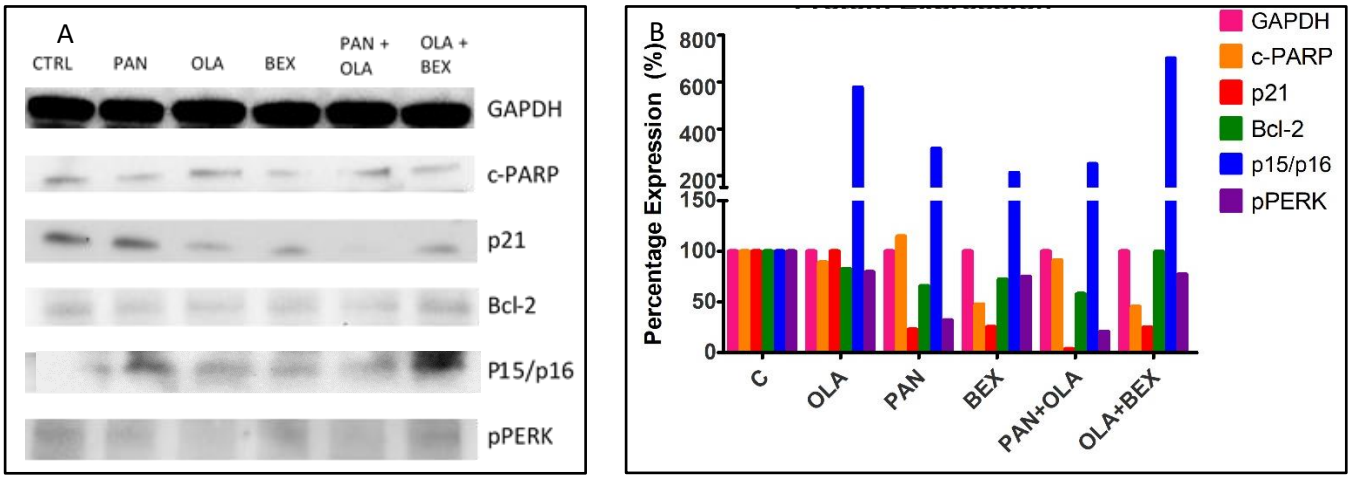

Figure 2-16: A) Immunoblots showing protein expression levels of apoptosis, cell cycle checkpoint and ER stress proteins: c-PARP, p21, Bcl-2, p15/p16 and pPERK with internal control GAPDH; B) Graph showing Percentage expression of proteins treated with PAN, OLA, BEX, PAN+OLA and OLA+BEX relative to control in biphasic cell line.

2.8 REAL TIME PCR ARRAY:

Since a vast majority of the 26 genes identified by the enrichment analysis on genome wide SNPs were directly involved in epigenetic functions and the most promising drug candidates seemed to affect DNA integrity, the expression of various epigenetic factors was studied using a targeted PCR array of Sin3/NuRD pathway (Figure 2-17). This pathway plays an important role in regulating gene transcription, genome integrity and cell cycle progression, by modulating chromatic remodelling [153–155].

With the significant fold increase threshold of 2.0 and p value threshold <1.0 various genes (listed in Table 2-4) were found to be upregulated and downregulated following treatment differentially in all histotypes with the maximum upregulated variations observed in the epithelioid cell line. This change could be attributed to its greater sensitivity of epithelioid MPM to combined treatment. Treatment with PAN, PAN+OLA and OLA+BEX saw a

considerable change in the expression profiles compared to control (Figure 2-18). The main molecular changes with functional significance are detailed below.

Histone H4 (encoded by HIST1H4I) and Retinoic X Acid Receptor β (RARB) were greatly upregulated in most conditions and has been shown to reverse chemoresistance and enhance apoptotic downstream pathways [156]. The upregulation of HIST1H4I on treatment with PAN+OLA could be the result of hyperacetylation of H4 histone, potentially inhibiting tumour proliferation and viability [157]. Further, a downregulation of Chromodomain Helicase DNA binding protein (CHD3), which is responsible for the acetylation of ATM and the activity of DNA double-strand break repair pathway genes. Such decrease could lead to the possible accumulation of double strand breaks in the DNA and induce apoptosis [158], decrease tumorigeneses, EMT and metastasis [159]. Additionally, a downregulation of 2.44 fold in CREBBP can result in decreased proliferation and cell cycle arrest in the G0/G1 phase [146, 160] (Figure 2-18). While a high upregulation (2.3 and 13.13) of Metastasis Associated Protein 1 and 2 (MTA1 and MTA2) implicated in tumour metastasis and progression via NuRD complex [161, 162] was observed on treatment with PT, the combined treatment with PAN+OLA observed no change and downregulation (-2.5) respectively suggesting a switching-off of the metastasis processes. A trend of higher significant responsiveness to all treatments was observed in the epithelioid type followed by biphasic and sarcomatous types which showed downregulation of all regulatory genes.

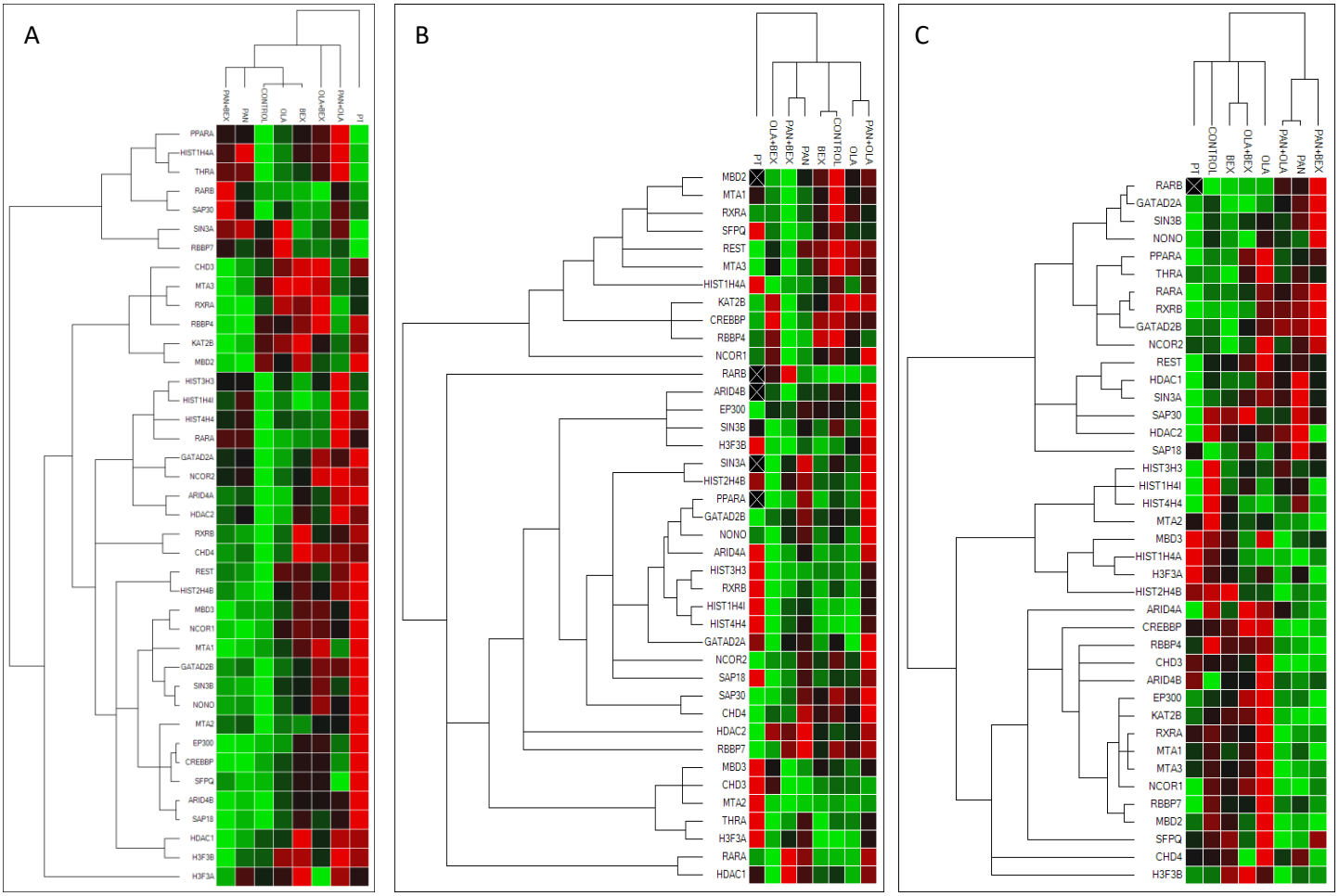

Figure 2-17: Sin3/NurD Pathway gene expression levels in a heatmap showing treatment with single PT, PAN, OLA, BEX and combinations of PAN+OLA, OLA+BEX and PAN+BEX relative to control in A) epithelioid, B)biphasic and C)sarcomatous cell lines (n=3).

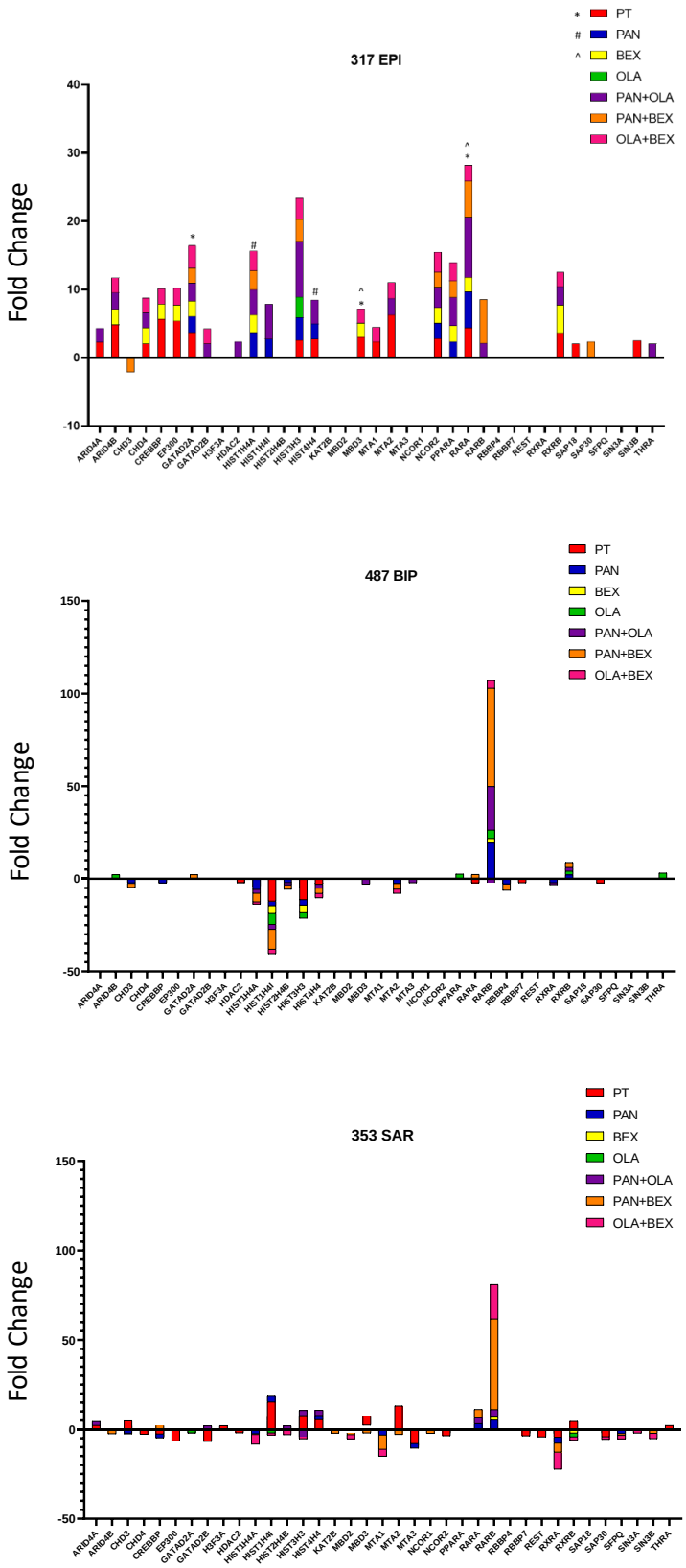

*Figure 2-18: Sin3/NurD Pathway gene expression fold-change on all three histotypes on treatment with PT, PAN, OLA, BEX, PAN+OLA and OLA+BEX and PAN+BEX combinations compared to control. (2-way ANNOVA, multivariate Bonferroni's post-test across columns * p-value <0.05, ** p-value <0.01, *** p-value <0.001, 95% confidence interval)*

EPI		BIP		SAR	
↑	↓	↑	↓	↑	↓
ARID4A (2.07)		RARB (23.53)	CHD3(-2.51)	ARID4A (2.13)	RXRA (-2.56)
ARID4B (2.42)		RXRB (2.01)	CREBBP (-2.09)	GATAD2B (2.02)	
CHD4 (2.15)			HIST1H4A (-3.86)	HIST1H4I (5.04)	
GATAD2A (2.68)			HIST1H4I (-2.6)	HIST2H4B (2.04)	
GATAD2B (2.08)			HIST2H4B (-3.30)	HIST3H3 (2.92)	
HDAC2 (2.35)			HIST4H4 (-2.25)	HIST4H4 (2.91)	
HIST1H4A (3.69)			MBD3 (-2.96)	RARA (3.60)	
HIST1H4I (5.15)			MTA2 (-2.52)	RARB (3.67)	
HIST3H3 (8.14)			MTA3 (-2.17)		
HIST4H4 (3.45)			RBBP4 (-2.453)		
MTA2 (2.36)			RXRA (-3.26)		
NCOR2 (2.98)					
PPARA(4.14)					
RARA (8.80)					
RARB (2.16)					
RXRB (2.66)					
THRA (2.06)					

Table 2-4: List of modulated genes on combined treatment with PAN+OLA in all 3 cell lines (Upregulation - ↑, Downregulation - ↓) (Significant threshold 2, p-value <1.0, n=3).

2.9 IN-VIVO TUMOUR STUDY:

2.9.1 IN-VITRO CYTOTOXICITY EVALUATION:

First, to determine the cytotoxic effects of the three drugs and the combinations on the mouse mesothelial cell line AB1, cell viability was evaluated at 24hrs, 48hrs and 72hrs. No significant toxic effects were observed at 24 hrs at high doses. Further, no difference except for the highest doses of PAN and OLA were observed following 48hrs and 72hrs of treatment. Subsequently, the IC_{50} of the drugs were determined at 48hrs to be 0.32µM for PAN, 30.8µM for OLA and 55.2µM for BEX. Combinatorial treatment for AB1 was performed as earlier. As expected, single treatments did not significantly decrease cell survival except for PAN and all the combination treatments, except PT+BEX (Figure 2-19).

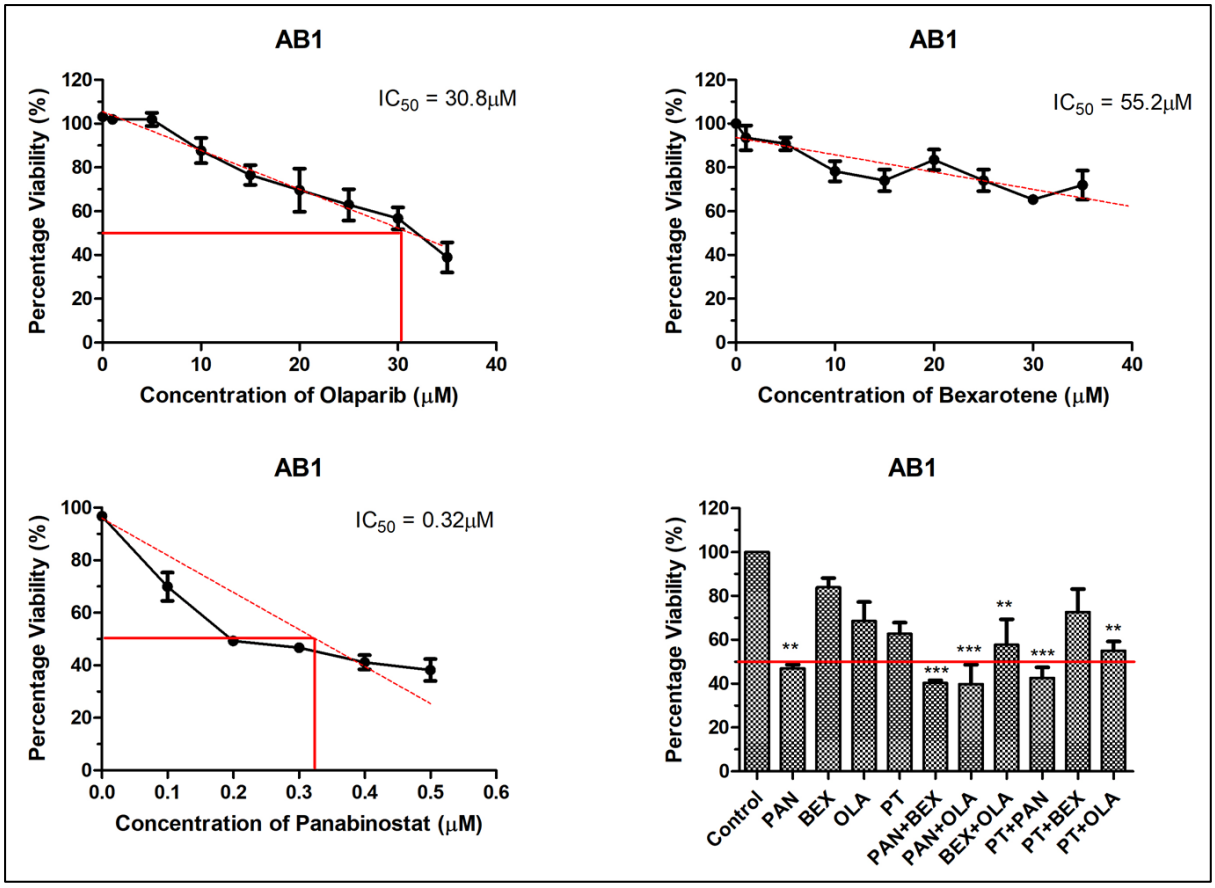

*Figure 2-19: AB1 cytotoxicity study following single and combination treatments at 48hrs with Panobinostat, Olaparib, Bexarotene and Cisplatin (2-way ANNOVA, * p-value <0.05, ** p-value <0.01, *** p-value <0.001, 95% confidence interval).*

2.9.2 *IN-VIVO* EVALUATION:

We finally set up an *in-vivo* experiment with AB1 mouse mesothelial cells, subcutaneously injected in female syngenic immunocompetent balb/C mice. At the end of treatment, while the tumour volume of the control animals increased alarmingly, PT treatment did not slow down tumour growth. Each single treatment (PAN, OLA and BEX) reduced tumour growth; and combinations had significant lower growth rates. Particularly, the combination of PAN+OLA showed the highest significant synergistic effect up to the third week of treatment with very little change in the tumour volume. The animals were observed for one week after the end of treatment (Figure 2-20A). All the groups had a similar 50% mortality (Figure 2-20B).

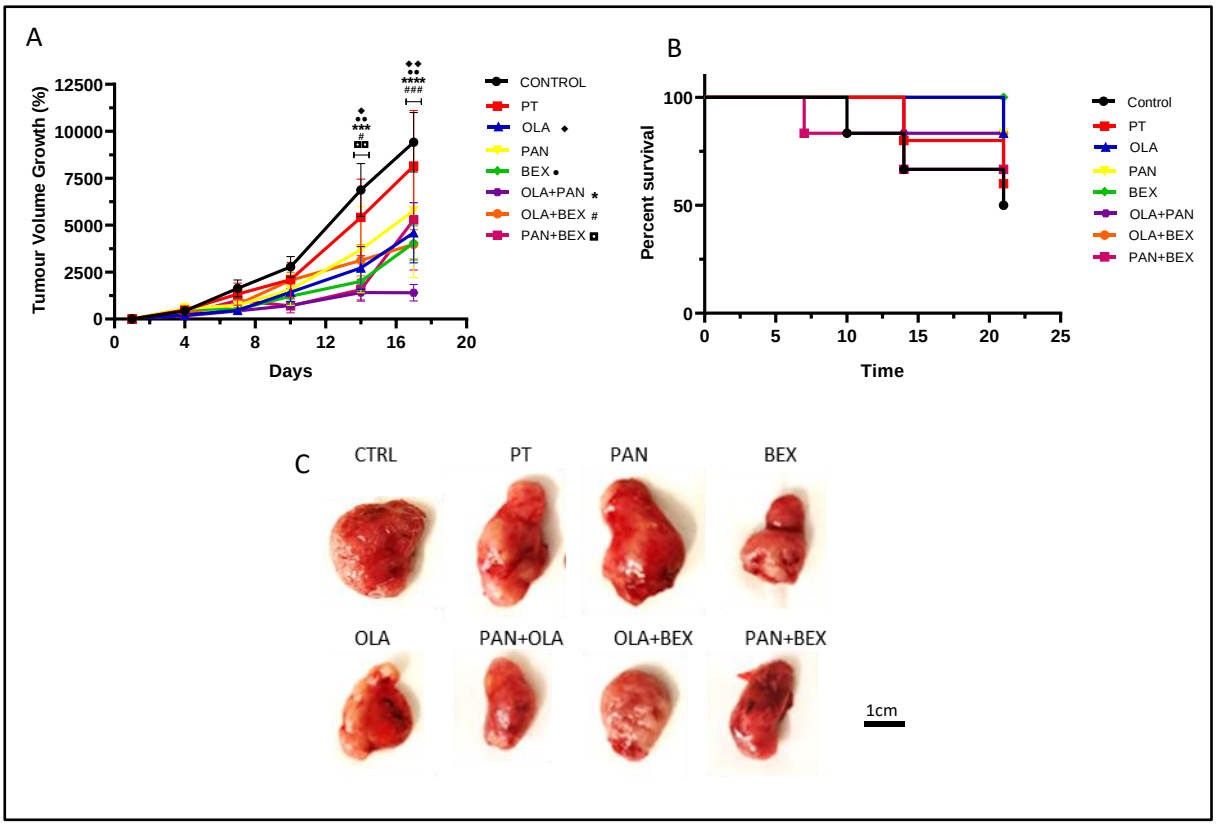

Figure 2-20: A) Graph showing percentage of tumour volume growth inhibition following various treatments (single and combination) with PAN, OLA, BEX and PT over a period of 3 weeks in AB1 xenograft Balb/C female mouse models ($p<0.5$, ** $p<0.01$, *** $p< 0.001$, **** $p< 0.0001$). B) Percent survival of treated animals over a 21-day period; C) Resected tumours at Day 21.*

2.9.3 SYSTEMIC RESPONSE TO TREATMENT AND TUMOUR PROLIFERATION:

The histological analysis of the kidney, liver and spleen tissue samples using H&E staining revealed a few interesting points following the treatment with all the single and combinatorial drugs (Figure 2-21).

In the liver, all hepatocytes showed signs of cytoplasmic glycogen depletion while microvascular lipid storage suggestive of steatosis were seen in the combinatorial treatment with PAN+BEX (green arrows). Treatment with PT shows increased presence of immune infiltrates along with few granulomatous foci (white arrows). Surprisingly, treatment with OLA followed presence of cellular hyperplasia, multinucleate hepatocytes and karyomegaly (red arrows), which is a sign of mitochondrial stress, or of the presence of ROS and DNA damage, as a direct result of Olaparib effect's on PPAR-α [163]. Other treatment conditions did not change the liver histology. No apparent change was observed in the overall kidney

histopathology except for a single rare case of superior margin renal metastasis in one animal of the OLA+BEX treatment group. Almost all conditions presented with few increased cellularity in the glomerulus (black arrows) [164]. Looking into splenic changes, macro scale variations were observed in the PT treatment arm where there was complete loss of a well-organized red and white pulp (yellow arrows). Furthermore, abnormal presence of megakaryocytes was found suggestive of loss of proper B and T-cell clonal generation and immune dysfunctions [165].

Ki-67 is a well-known marker for cellular proliferation and is highly expressed in dividing cell of all phases except for quiescent G0 cells. It has also been used as a marker for poor prognosis in patients with late stage disease particularly of the epithelioid subtype of MPM [150, 166] The Ki-67 index was analysed for the expression of the proliferative marker in MPM through immunohistochemical analysis of the tumour slides following all the different treatment conditions (Figure 2-22). The combinatorial treatment of PAN+OLA had a highly significant reduction ($p<0.001$) on the expression of Ki-67 compared to other treatments (Figure 2-23). This directly corroborates the decrease in tumour volume in mice previously recorded. Although the other treatments and combinations showed a degree of success *in-vivo*, the Ki-67 expression was found to not significantly differ from untreated mice. This may be suggestive of a temporary response to chemotherapy that is cytostatic and that may not preclude a complete block of proliferation.

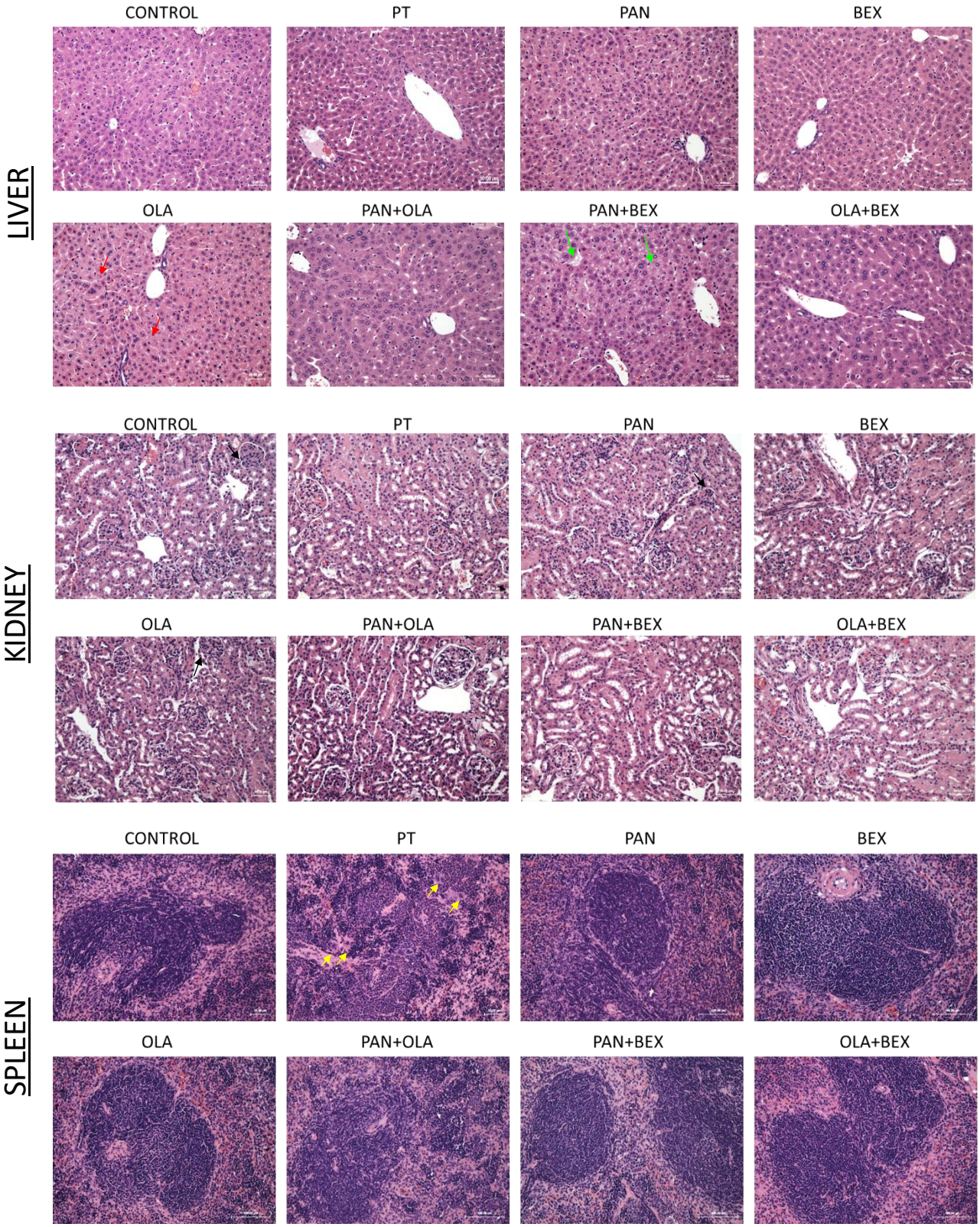

Figure 2-21: *HE representative images of liver (white/green/red arrows) kidney (black arrows) and spleen (yellow arrows) showing marked transformations of all treatment conditions including PT, PAN, BEX, OLA, PAN+BEX, PAN+OLA, OLA+BEX. Magnification 23X.*

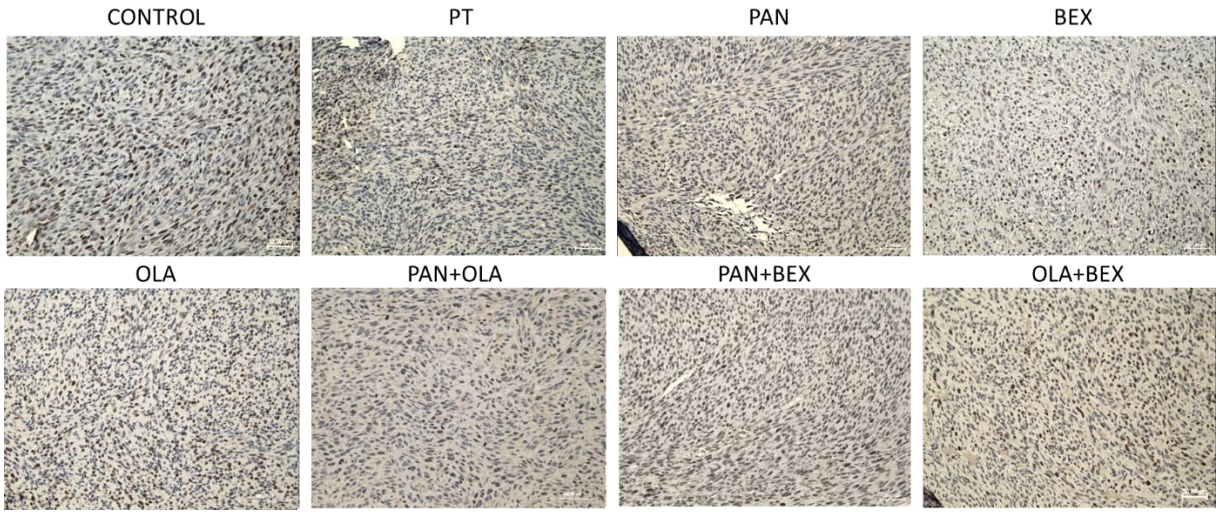

Figure 2-22: Representative images of immunohistochemical staining of tumour tissue samples against proliferative marker Ki-67 showing positive cells stained brown and negative cells visible using nuclear haematoxylin stain following treatment with single PT, PAN, BEX, OLA and combinatorial PAN+OLA, OLA+BEX and PAN+BEX observed at 23X magnification.

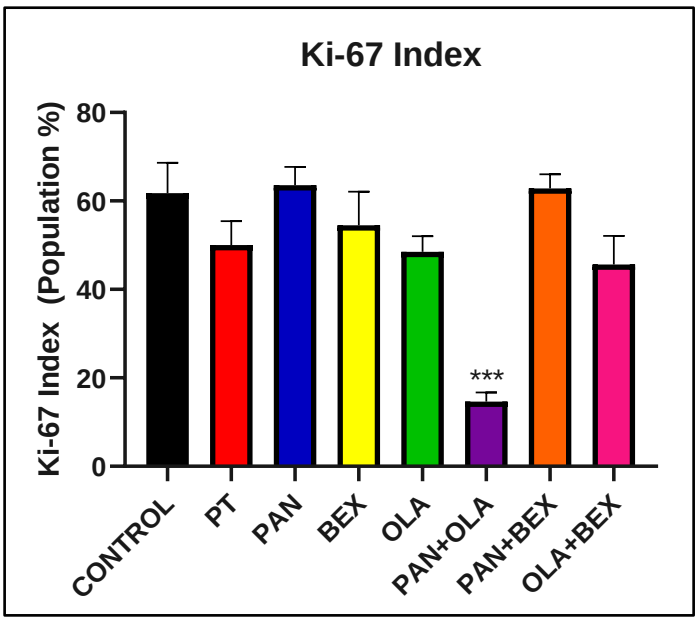

*Figure 2-23: Percentage population of cells marking positive for Ki-67 following treatments with single and combination small molecules determined using QuPATH software for IHC. PAN+OLA combinatorial treatment showed marked significant decrease in Ki-67 expression compared to control and other treatments. Significance: *** $p<0.001$, ** $p<0.01$, * $p<0.05$. ($n=6$).*

3 PRELIMINARY CONCLUSIONS AND FUTURE PERSPECTIVES:

Following the genome wide sequencing analysis of 5 primary MPM, we identified 26 candidate genes having more than one significant SNPs. 84% of these genes had direct interactions within the cell. Out of which, 3 genes were identified as possible targets: RARA, HDAC2 and PARP1/2 that can be targeted by bexarotene, by HDAC inhibitors Panobinostat, Romidepsin, Vorinostat and Belinostat and Rucaparib, and by Olaparib, respectively. Bexarotene, a retinoid specific for Retinoid X receptors, currently used in the treatment of T- cell lymphoma [149], induces apoptosis and alters the cell cycle by inducing a G2/M cell cycle arrest. RARA is found to be also implicated in development, differentiation, apoptosis, granulopoiesis, and transcription of clock genes [167, 168]. Panobinostat is a broad-spectrum HDAC inhibitor currently in Phase 3 clinical trials. It is also associated with histone H3K9 and H4K8 acetylation. It has also been found to reduce c-myc and increase p21 expression [169, 170], thereby explaining its anti-tumour activity. Olaparib acts directly on BRCA1/BRCA2 mutations and was found to directly impair PARP1 activity by increasing the number of double stranded DNA breaks [171].

In-vitro experiments on primary human and murine MPM cells indicated that all the cell lines were killed – although to different extents – by the single agents and even more so by the combinations. The combinations of PAN+BEX and PAN+OLA were the most sensitising with minimum IC_{50} for all cell types. The mechanism of cell death was likely due to an increase of S- phase and G2/M-phase arrested cells, which are suggestive of replicative stress and possible reduction of cellular DNA damage response [146, 147, 149, 150], and may trigger subsequent apoptosis and necrosis if the DNA damage is not repaired [146–152]. The expression pattern of replicative, apoptotic and cell-cycle checkpoint proteins (p21, Bcl-2, cleaved PARP, p15/p16) supported this hypothesis [172–174].

Interestingly, multiple candidate genes identified were primarily involved in transcription regulation and belonged to the Sin3/NuRD Pathway, an epigenetic controller of genome integrity and cell cycle progression [153–155]. Looking into changes in gene expression levels on single and combined treatments, we found key genes involved in chromatin remodelling, such as HIST1H4I, HDAC1, HIST3H3, upregulated. Changes in histone acetylation due to regulatory changes can potentially inhibit cellular proliferation. All three histotypes showed also significant increased level of RARB, which has been shown to reverse chemoresistance and enhance apoptosis [156]. By contrast, the treatment down-regulated CHD3, which is

responsible for the acetylation of ATM and the control of DNA double-strand break repair pathway genes. CHD3 downregulation could trigger the possible accumulation of double strand breaks in the DNA, increasing apoptosis [158] and decreasing tumorigenesis [159].

In AB1 tumours which are insensitive to PT, all treatments and particularly the combination treatments significantly reduced tumour growth. Particularly, the combination of PAN+OLA showed the highest significant synergistic effect, also confirmed by a durable decrease in Ki-67 intratumour expression. Only minor modifications with the combination treatments were observed in the gross pathology of liver, kidney and spleen. This part of the work is the first application in MPM of a drug discovery process based on a genome-wide analysis of SNP, which identified suitable druggable targets that support a novel drug discovery approach. The combination of Panobinostat and Olaparib emerged as a promising therapeutic modality for MPM.

CHAPTER 3

Novel 3D Vascularised Cancer Model for Drug Discovery – Tackling the Resistant Tumour

1 MATERIALS AND METHODS:

1.1 CHEMICALS:

The plasticware for cell cultures was obtained from Falcon (Becton Dickinson). The electrophoresis reagents were obtained from Bio-Rad Laboratories. Unless specified otherwise, all reagents were purchased from Sigma Chemicals Co.

1.2 CELL CULTURE:

The primary human epithelioid MPM cell line #317 was obtained from the Biologic Bank of Malignant Mesothelioma, S. Antonio e Biagio Hospital (Alessandria, Italy). Cells were grown in Ham's F12 nutrient mixture medium, supplemented with 10% v/v fetal bovine serum (FBS), 1% v/v penicillin-streptomycin. MRC-5 (ATCC® CCL-171™) human lung fibroblast and Calu-3 (ATCC® HTB-55™) non-small cell lung cancer cell lines were acquired from ATCC (Manassas, VA) and cultured in Eagle's Minimum Essential Medium, supplemented with 10% v/v FBS, 1% v/v penicillin-streptomycin. GFP-expressing human umbilical vein endothelial cells (HUVEC-GFP) (Angio-Proteomie®, Boston, MA) were cultured in EBM™-2 (Endothelial Cell Growth Basal Medium-2) supplemented with EGMTM-2 Endothelial SingleQuots™ Kit (Lonza, Switzerland). Cells were checked for Mycoplasma spp. contamination by PCR every three weeks; contaminated cells were discarded.

Mixed tumour spheroids were cultured in ultra-low attachment Nunclon™ Sphera™ 96-Well, Nunclon Sphera-Treated, U-Shaped-Bottom Microplate (ThermoFischer Scientific, Waltham, MA) in mixed media (1:1). Each cell line was stained with a live cell tracker shortly before seeding using the CellTrace™ Far Red Cell Proliferation Kit (ThermoFischer Scientific) for the MPM or Calu-3 cell line and the CellTrace™ Yellow Cell Proliferation Kit (ThermoFischer Scientific) for MRC-5 according to the kit instructions. Different concentrations of MPM 317 and Calu-3 cells were seeded along with MRC-5 in the ratio 5:1 and 10:1, allowed to self-assemble for 48hrs and tumour spheroids were subsequently characterized.

1.3 *IN-VITRO* CYTOTOXICITY ASSAY:

HUVEC-GFP cells (10,000 cells/well in 96 well plate) and previously cultured spheroids were treated for 48hrs with increasing concentrations of PT, Bevacizumab (BEV), Panobinostat (PAN) and Olaparib (OLA). After treatment, the media was discarded, and cell viability was determined using the CellTiter-Blue® Cell Viability Assay (Promega, USA) according to the kit. Spheroids were incubated with the reagent for additional 24hrs [175] to increase the sensitivity and reactivity. The viability of cells was measured as a function of absorbance of resazurin at 560/590nm using the TECAN Infinite® 200 PRO Microplate Reader (Tecan, Switzerland).

1.4 3D VASCULARISED MODEL OPTIMISATION:

1.4.1 SYSTEM LABWARE:

To create the optimal platform to conduct the patterning, different systems and labware were tested. The work involved identifying a suitable chamber using different commercial well plates – IBIDI™ 15 well Angiogenesis µ-slide, 96-well plates, 96-well plate covers, 24-well plates and 60mm petri dishes with polymeric inserts, agarose and silicone internal chambers having different dimensions, as well as custom-made systems that could be adapted for use on the custom 150mm vibrating plate of the SIM device.

1.4.2 PATTERNING PARAMETERS:

HUVEC–GFP endothelial cells were patterned within the inner well of the IBIDI 15-well microslide in such a way as to obtain a single ring that can form a proto-vessel around the tumour organoid. Various cell suspension volumes (ranging from 6µl-10µl), cell concentrations ($0.5x10^6$ cells/ml, $0.8x10^6$ cells/ml and $1x10^6$ cells/ml), amplitude and frequency were tested to obtain the most optimal pattern and orientation of cells in the shortest time frame possible. The cells were patterned by solely applying sound at 54Hz for 1-2 min at approximately 40% amplitude. Once patterning parameters were set, mixed cell populations (HUVEC-GFP: MRC-5) were patterned in the ration 5:1 and cultured for a period of 6 days to observe the stability of the pattern.

1.4.3 GELLING FABRICATION PARAMETERS:

Three different hydrogels were tested for their ability to pattern cells and provide a stable culturing environment. Collagen-I was tested at concentrations of 0.2mg/ml and 0.5mg/ml. Cells were patterned using the same parameters mentioned above with $1x10^6$ cells/mL of endothelial cells. Once a pattern was obtained, the gel was allowed to crosslink at 37°C for 1 hr. The well was filled 40µL EGM-2 media and the space surrounding the wells of the IBIDI well plate was filled with 1% agarose to reduce evaporation. GelMA (gelatin methacrylate) 5 % (w/v) was solubilised at 60°C and used to pattern cells ($1x10^6$ cells/ml). The gel was then crosslinked using UV for 10-15 min. Fibrin gels were synthesised using Fibrinogen 2.5mg/ml and thrombin 0.25 IU/ml (1:1). $1x10^6$ cells/ml of HUVECs were resuspended in thrombin and then quickly mixed with fibrinogen on ice shortly before applying sound as fibrin crosslinks at room temperature within 5 min. Wells were then filled with 40µl EGM-2 media.

1.4.4 VASCULARISED MODEL ASSEMBLY AND CO-CULTURE:

Once the endothelial cells were allowed to mature for 48hrs, the previously self-assembled tumour spheroids were individually picked and placed centrally in the upper well within each microwell at Day 0. The media was first aspirated from the 96-well culture plate and a spheroid was carefully aspirated using 20µl of collagen or fibrin hydrogel and placed in the centre of the well without disturbing the bottom layer. This was then allowed crosslink as described above and the remaining volume was filled with EGM-2 media.

1.5 3D VASCULARISED MODEL VALIDATION:

From the day of patterning (Day -2) the stability of the hydrogel and cell proliferation and vessel maturation was observed by imaging every 24hrs using Axiovert fluorescence microscopy (Zeiss). From Day 0 to Day 3, multi-channel Z-stack images of the complete system were taken every 24hrs using LSM 800 confocal microscopy systems (Zeiss). The images were processed using ImageJ Software V.1.53e. The cells were fixed using 4% paraformaldehyde at Day 3 and stained for E-cadherin, Phalloidin and DAPI to assess cellular crosstalk within the system and presence of proto-vessels.

1.6 APOPTOSIS ASSAY:

Once the system was optimised, the model was treated with 120µM PT and 0.3µg/ml BEV in EGM-2 media at Day 0 for 48hrs in single and combined treatments. Prior to fixation at Day 2, the media was aspirated, and apoptosis assay was performed according to manufacturer's instructions using the CellEvent™ Caspase-3/7 Green Flow Cytometry Assay Kit (Invitrogen, Milano, Italy). Percentage of cell death only within the spheroid was calculated based on maximum green fluorescence intensity.

1.7 STATISTICAL ANALYSIS:

All statistical analysis and graphs were conducted and generated using GraphPad Prism version 8.00 for Windows, (GraphPad Software, San Diego California USA, www.graphpad.com). For all grouped data, the test of significance was performed using Two-way ANOVA with Bonferroni's post-tests to compare all treatment conditions with reference to control ($p>0.05$ – non-significant; $p<0.05$ - *; $p<0.01$ - **; $p<0.001$-***).

2 RESULTS & DISCUSSION:

2.1 3D VASCULARISED TUMOUR MODEL FOR MALIGNANT PLEURAL MESOTHELIOMA:

2.1.1 MODEL OPTIMISATION:

To first develop the 3D design fabrication and organization, different culture systems like 96 well plate, 24 well plates and IBIDI™ 15 well Angiogenesis µ-slide were tested, since they could both be adapted to the custom 150mm vibrating plate of the SIM system (Figure 3-1A). Although cells could be patterned on 96 well plate covers and 24 well plate surfaces, the systems proved not ideal due to lack of sterility, modulation and ease of image acquisition. IBIDI™ µ-slide was the system chosen as it provided easy attachment and scalability while retaining sterility across the 3D culture fabrication and manipulation process.

2.1.2 PATTERNING PARAMETERS:

HUVEC–GFP endothelial cells were patterned in such a way as to obtain a single ring that can form a proto-vessel around the tumour organoid. The cells were patterned by solely applying sound at 54Hz for 1-2 min at approximately 40% amplitude. Cultured fabricated circular patterns approximately 2mm in diameter were observed to develop proto-vessels by 2 days within all 15 wells with a patterning efficiency of 80% (Figure 3-1B). Cells at concentration between 0.6 x 10^6 cells/mL and 1 x 10^6 cells/mL were patterned to enable visually discernible patterns as lower concentrations did not allow for easy visualization despite using an overhead camera. Further, patterned co-culture of HUVECs with CAFs (5:1 using 0.6 x 10^6 cells/mL cells in total) enhanced pattern stability and facilitated uniform growth over a period of 6 days. Ortho image analysis showed presence of early vessel and lumen formation after 48hrs.

2.1.3 GELLING FABRICATION PARAMETERS:

In the case of the collagen matrix, it was optimised at a low concentration (0.2mg/ml) to facilitate cellular patterning and prevent premature cross linking of the matrix at room temperature. Although, this resulted in the collagen being too weak to retain patterns for a long time which started showing signs of shrinking. This was most likely attributed to the specific

spatial organisation of the cells stressing the gel. GelMA tests failed to generate any pattern of cells within either system. Ultimately, HUVECs at two different concentrations of 1 x 10^6 cells/ml and 0.5 x 10^6 cells/ml were patterned successfully in fibrin gel composed of Fibrinogen 2.5mg/ml and thrombin 0.25 IU/ml (1:1 final concentrations) in the lower well. The fibrin gel showed greater stability with no sign of shrinkage but the HUVECs on prolonged culture beyond 6 days displayed a loss in pattern continuity.

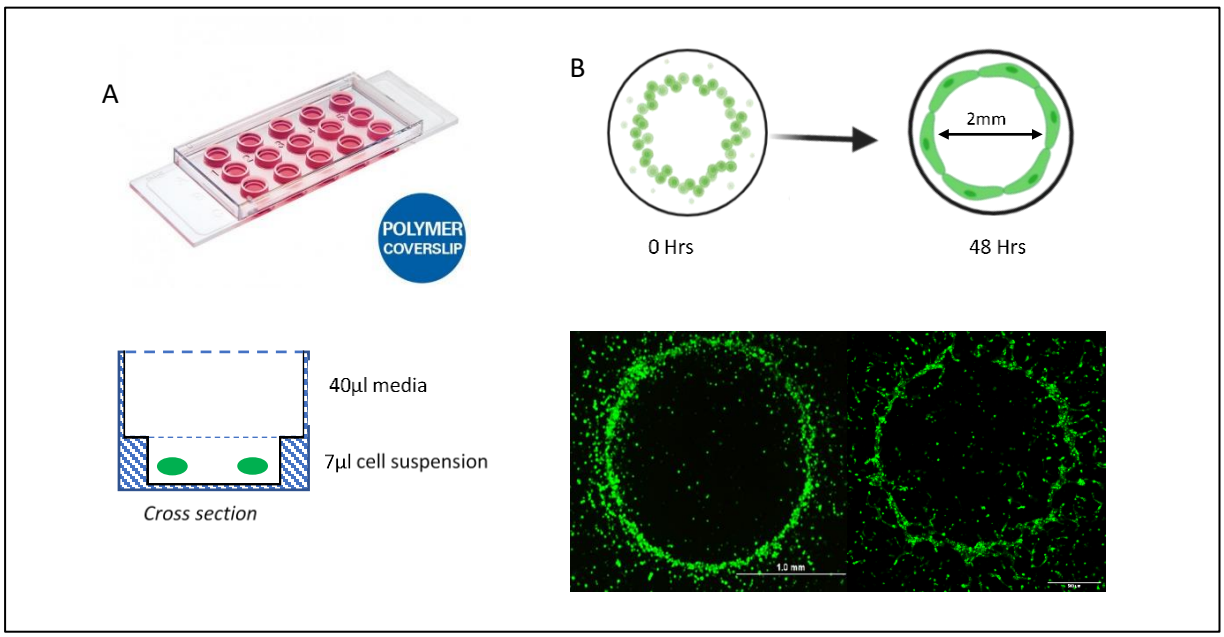

Figure 3-1: A) Outline showing the IBIDI 15-well Angiogenesis microslide and pattern construction; B) Pattern after 48hrs showing visible proto-vessel with internetworked branches.

2.1.4 PATTERN CHARACTERISATION AND APPROACH:

Once patterns were established successfully, rings of 2mm in diameter were uniformly reproduced in all wells. Using the Skeleton Analysis macro on ImageJ image analysis software, the branch distribution, branch length and branch number were studied as an evolution with time over 48 hrs (Figure 3-2A). Using the maximum integrated green fluorescence intensity, the thickness of the rings was found to be 100±50µm (n=15) (Figure 3-2B). The branched proto-vessel networks were shown to have lumens ranging from 20-50µm in diameter (Figures 3-2C/D).

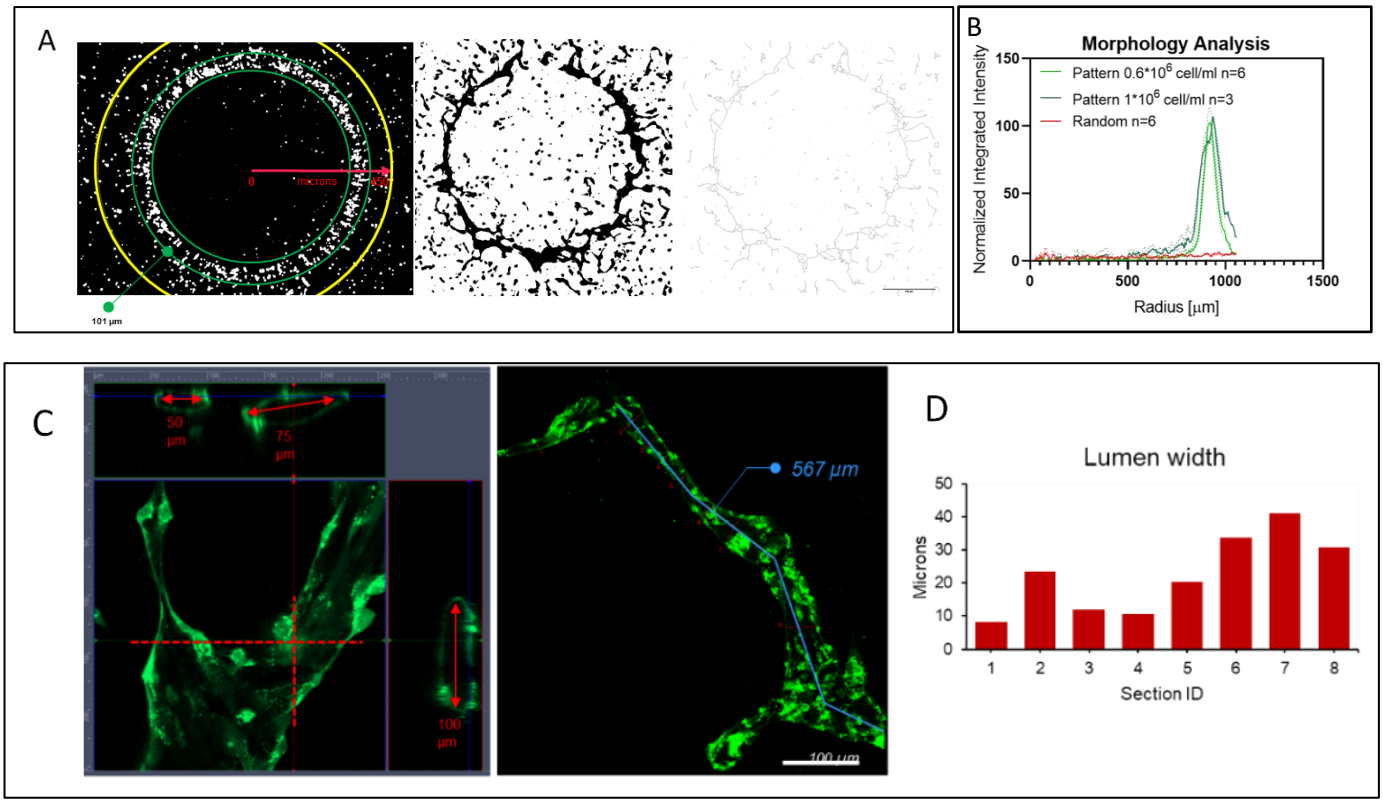

Figure 3-2: A) Representative Skeleton analysis on patterned HUVEC-GFP cells after 48hrs culture. B) Normalised Integrated green fluorescence intensity showing average thickness of constructed patterns (n=15). C) Confocal Ortho Analysis on a selected branched region 567µm in length having lumens with median diameter of 35.6µm within the constructed proto vessel (25X magnification). D) Binned lumen width distribution chart showing the range of lumen diameters within a single well.

2.1.5 SPHEROID CHARACTERISATION:

The main objective for spheroid culture was the ability to obtain uniformly sized single spheroids that can be easily isolated and transferred to the 3D system without compromising its integrity. This was achieved by culturing tumour cells of different concentrations in ULA U-well plates where ideal, self-assembled spheroids of 501.2µm and 582.3µm were obtained after 48 hrs after seeding 20000 and 10000 cells/well respectively of MPM 317, and 2000 and 1000 cells/well of MRC5 (Figure 3-3A/B). The size and uniformity of the spheroids were assessed using images taken both using light and confocal microscopy. Two different cell lines were used to validate the protocols for spheroid generation stability and live cell trace staining. Both tumour cell lines were able to self-assemble spheroids of uniform diameters that increased in size with increased seeding concentrations. Additionally, mixed population spheroids were obtained using MRC-5:MPM in the ratio of 1:10 and 1:5 to study the influence of CAFs on the

invasiveness of MPM and on vessel formation. The different ratios of MRC5 and tumour lines did not significantly alter the spheroid dimensions or growth. The live cell trace staining was stable for over 96hrs without any loss in signal (Figure 3-3C).

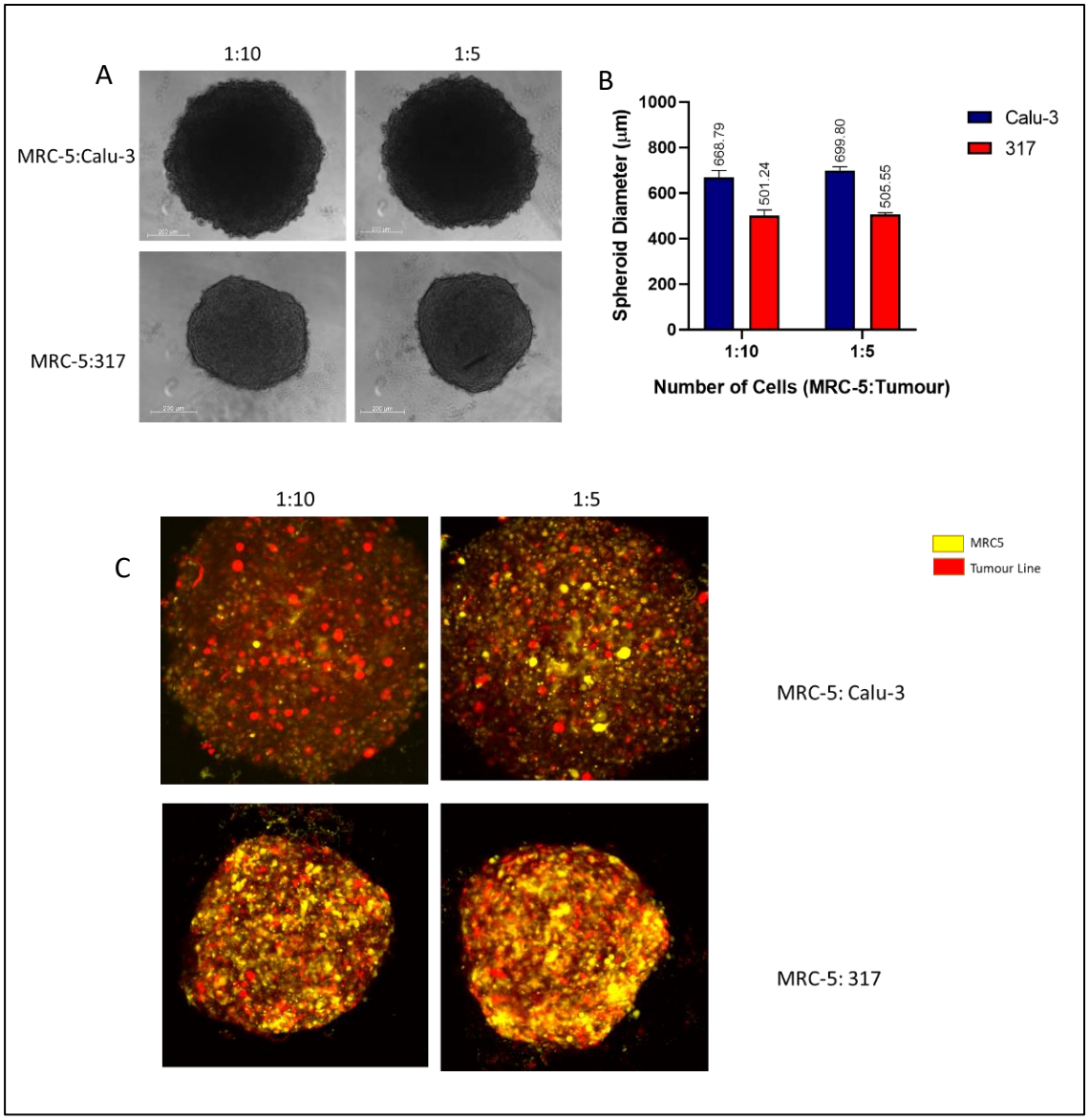

Figure 3-3: A) Mixed heterotypic tumour spheroids of Calu-3 and MPM 317 cell lines with MRC5 fibroblasts (5x magnification). B) Mixed spheroid size distribution (n=5). C) Representative Confocal Z projection multichannel image showing tumour cell line (Calu-3 and MRC5) stained with Far Red live Cell Trace and MRC5 stained with Yellow Cell Trace (5X magnification).

2.1.6 VASCULARISED MODEL SYSTEM VALIDATION:

Figure 3-4A describes the outline of the workflow used to set up the complete vascularised model from Day-2 to Day 0 (Figure 3-4C). Z-stack Ortho analysis of the complete setup at Day 0 shows the endothelial cells patterned in the lower well with the spheroid centrally placed in the upper well of the IBIDI. At the end of Day 4, tumour spheroid sprouting was seen with both MPM and MRC5 cells migrating towards the lower endothelial layer (Figure 3-4B).

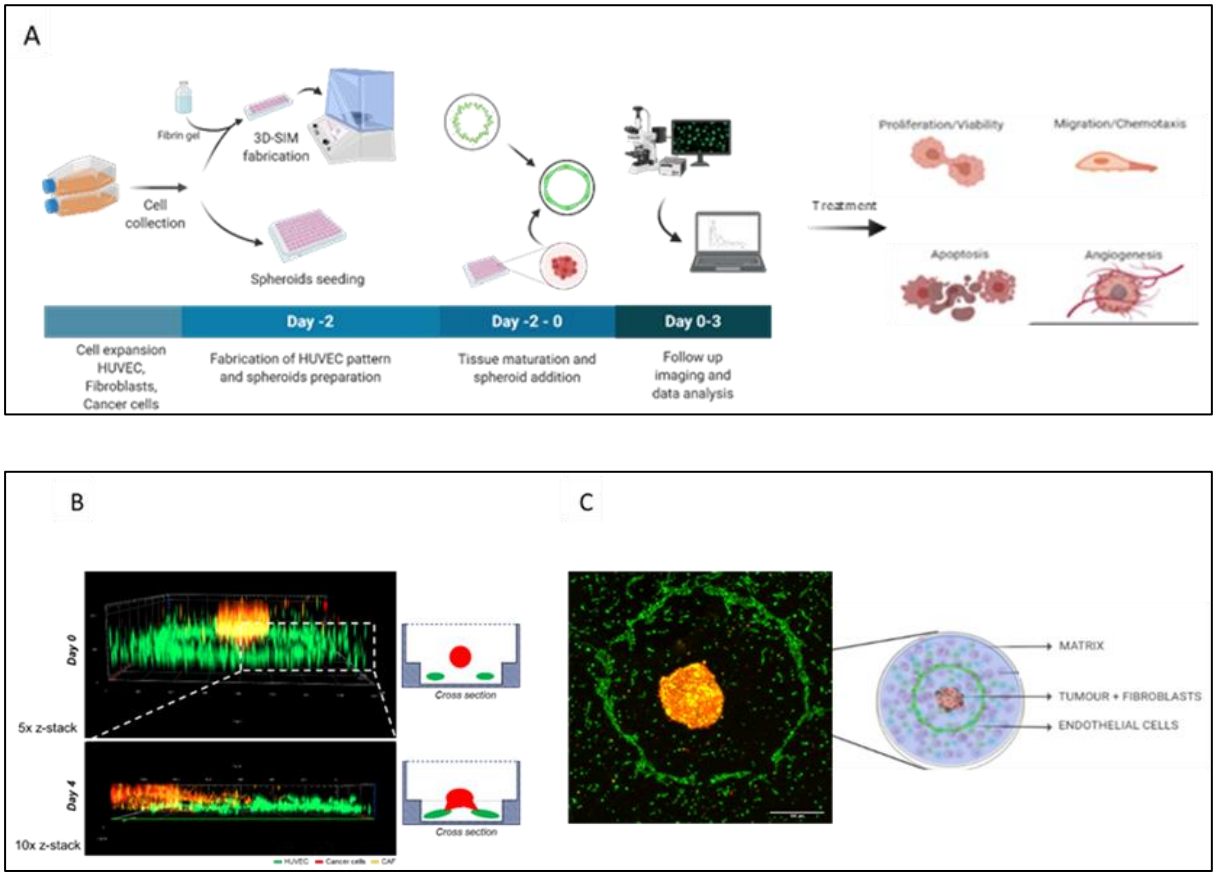

Figure 3-4: A) Outline of the workflow to set up the vascularised 3D model. B) 3D ortho analysis of the model at Day 0 and Day 4 showing spheroid migration. C) Z-projection of the model describing various heterogenous components of the system.

Five different conditions were analysed including spheroid only, HUVEC/MRC5 pattern + spheroid, HUVEC/MRC5 pattern only, HUVEC/MRC5 random and HUVEC/MRC5 random + spheroid. The random condition describes the system with non-patterned HUVECs and fibroblasts randomly dispersed within the Fibrin hydrogel; and the pattern indicates the controlled seeding condition of HUVECs and fibroblasts previously set up (Figure 3-5A). To

study the influence of the mixed population spheroids on vessel formation and tumour invasiveness, the spheroids were placed in fibrin into each microwell, cultured for 4 days and imaged every 24 hrs. The spheroids alone began sprouting within 24 hrs and observed a 34% area expansion after 72hrs while the extent of branches and sprouting of the spheroid in the presence of patterned circular HUVECs was 57% greater compared to Day 0 (Figure 3-5D). Additionally, the area expansion of the spheroid in the presence of randomly distributed HUVECs was 52% showing that the presence of patterned spatially organised cells increased the spheroid invasion. Preliminary evolution analysis of the vascular network with time showed that the branch number and length decreased accompanied by pattern loss in the condition of HUVEC alone, while the presence of the spheroid in both randomly oriented and patterned HUVECs increased branch length and stabilised the vascular network (Figure 3-5C/E). Further, a significant decrease in stability ($p<0.033$) of pattern alone compared to pattern + spheroid condition after 120 hrs was observed. A similar significant decrease ($p<0.002$) in HUVEC area and stability was seen in the case of random HUVEC and random HUVEC + spheroid condition proving that the system comprising of patterned HUVECs and spheroids showed greater stability (Figure 3-5B). Ultimately, mixed cell co-culture proved to co-interact and mutually influence each cell type within the system to possibly form a clinically relevant Vascularised Tumour Model (VTM).

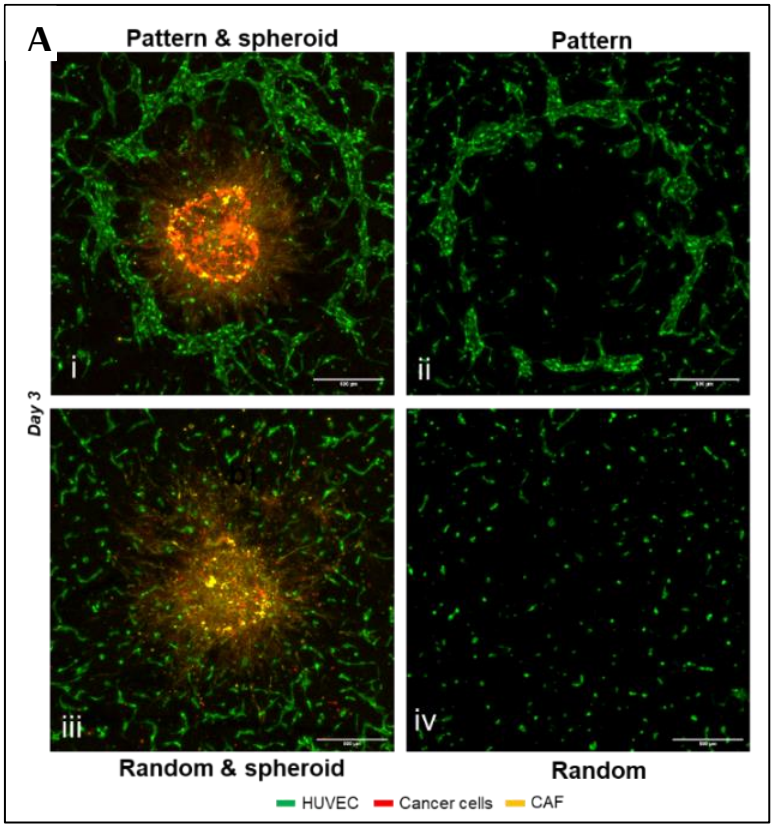

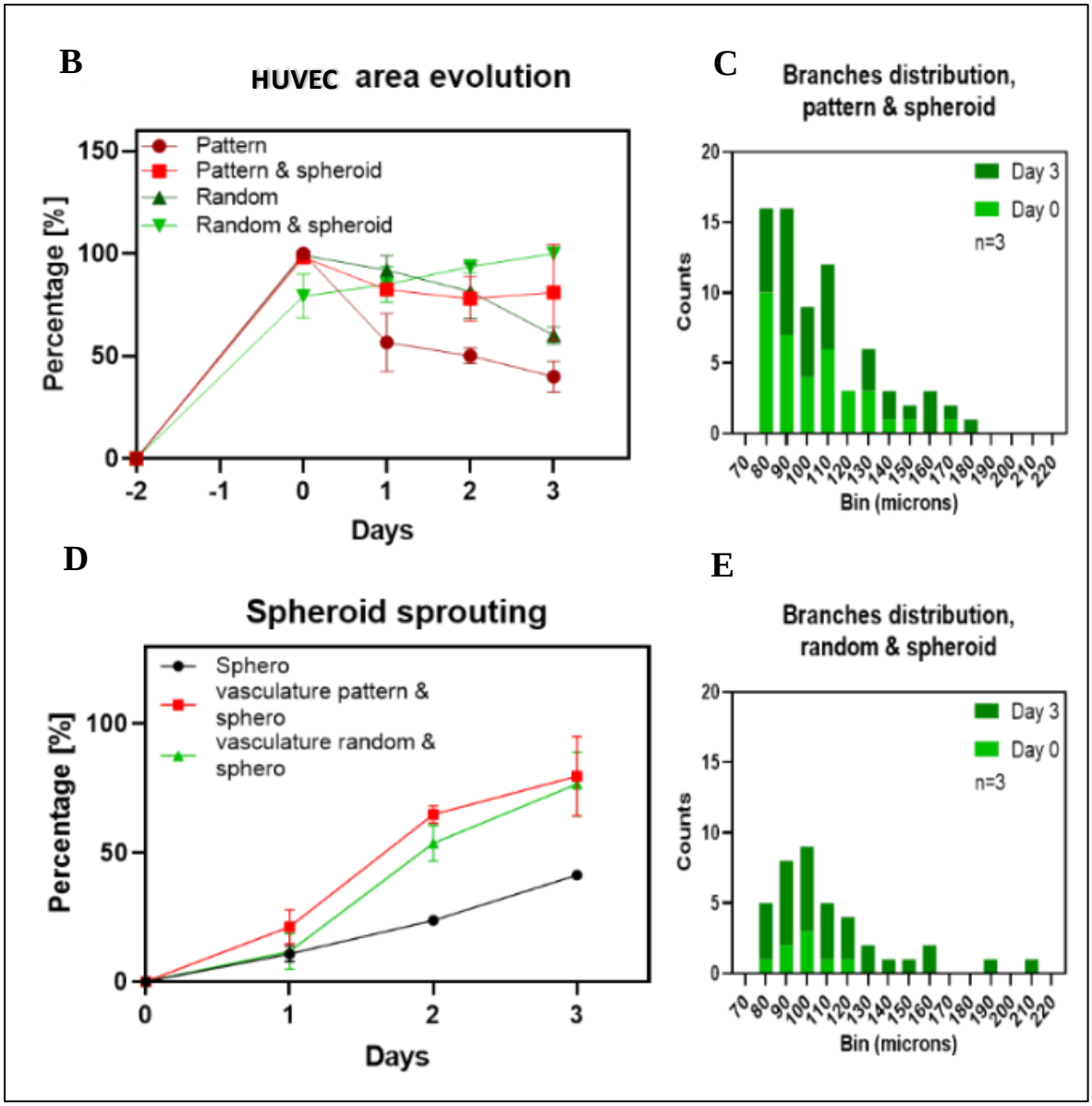

Figure 3-5: A) The four conditions pattern + spheroids, pattern only, random + spheroid and random only at Day 3. B) Sprouted area evolution of HUVEC-GFP vascular network as a function of time from Day -2 to Day 3. C)Branch distribution showing the number and length of endothelial branches from Day 0 to Day 3 in the system containing pattern+spheroid. D) Percentage of the tumour spheroid sprouting over time in different conditions. E) Branch distribution showing the number and length of endothelial branches from Day 0 to Day 3 in the system containing randomly dispersed HUVECs and a spheroid. All conditions were analysed in triplicates (n = 3).

2.2 *IN-VITRO* CYTOTOXICITY ASSAY:

Preliminary cytotoxicity test was performed on MPM mixed spheroids and HUVECs cultured in 2D to determine the IC50 of PT (as gold standard), the recently approved antiangiogenic drug BEV, two drugs identified as potentially effective novel drugs in the previous chapter, PAN and OLA. Figure 3-6A showed that the tumour spheroids were poorly sensitive to PT (IC50: 204.9µM), BEV and OLA (IC50: 374.9µM), while they displayed good sensitivity to PAN (IC50: 2µM). These IC50 were higher than those find in 2D cultures (Figure 2-14). As expected, HUVECs were sensitive to BEV, but not to the other drugs (Figure 3-6B). Following these observations, PT and BEV were selected for the following experiments on the established VTMs.

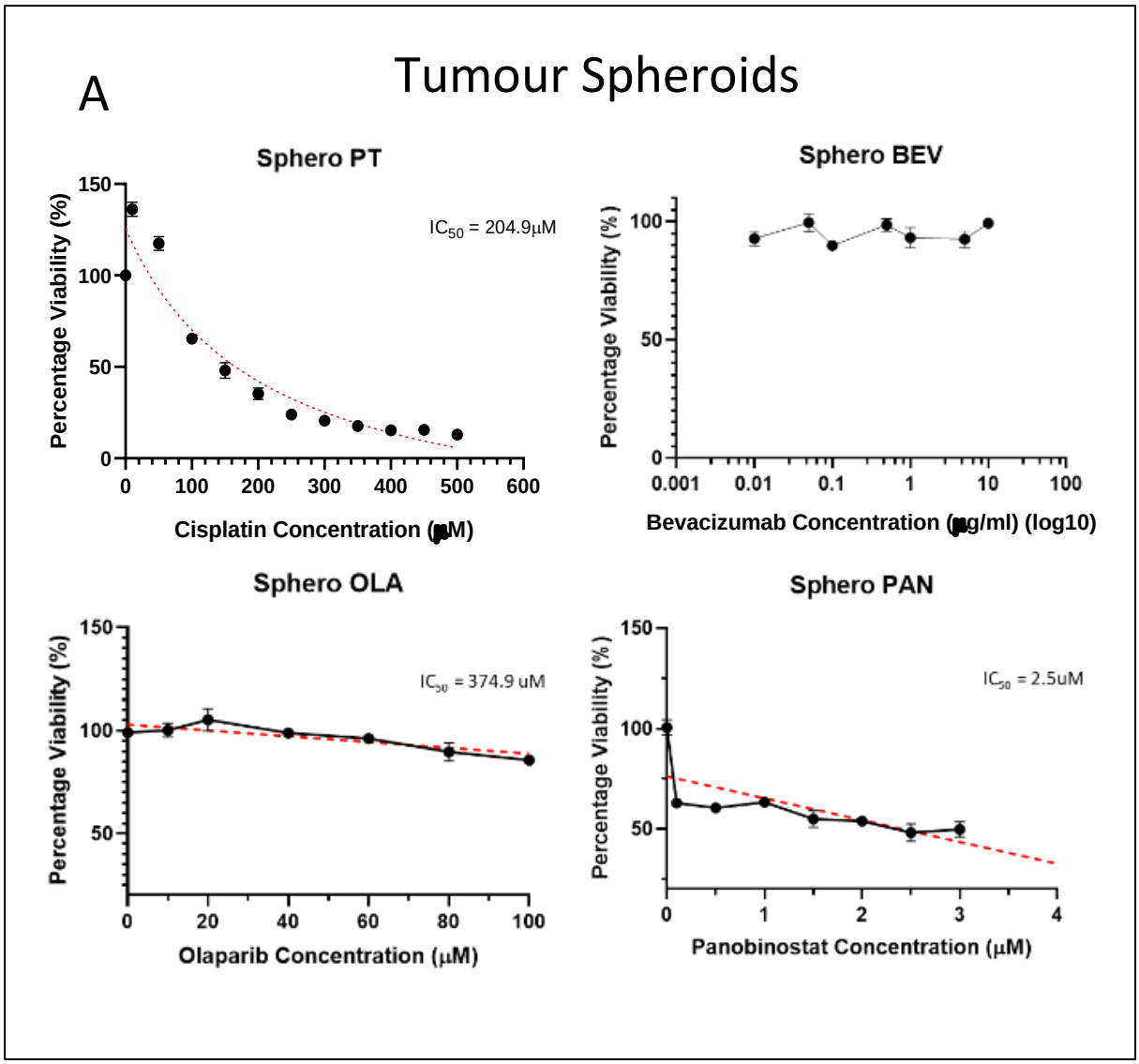

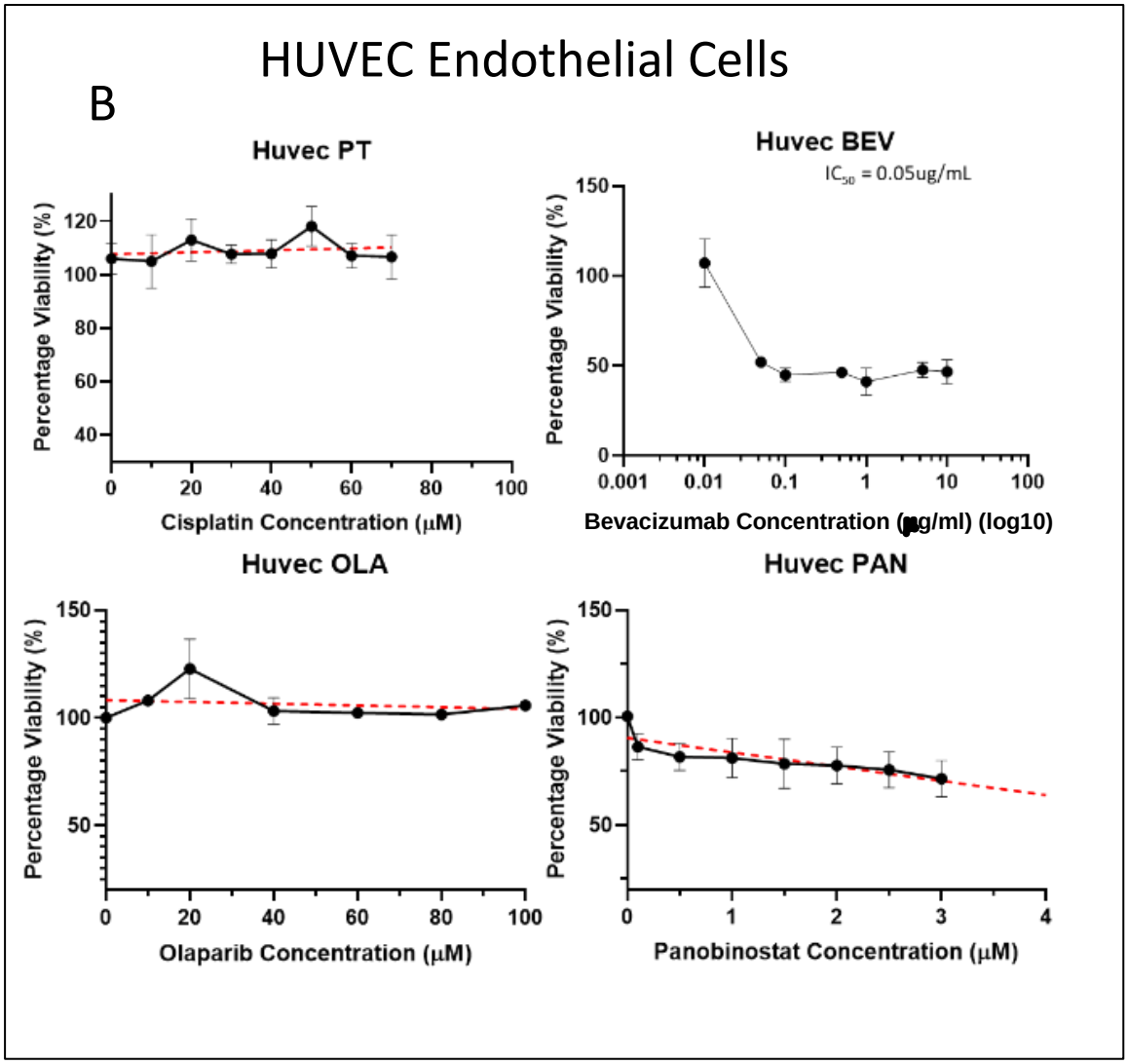

Figure 3-6: A) Percentage viability of the mixed tumour spheroids and B) percentage viability of HUVEC endothelial cells on treatment with Cisplatin, Bevacizumab, Olaparib and Panobinostat for 48hrs.

2.3 TREATMENT INDUCED APOPTOSIS AND REDUCED VASCULARISATION:

On VTMs, PT and BEV produced a 75% and 45% decrease in spheroid sprouting, respectively, after 48 hrs (Figure 3-7A/B). Additionally, a significant additive effect ($p<0.05$) on combined treatment was observed compared to control on preventing tumour sprouting by 87%. PT alone produced a 4-fold increase in apoptosis and the combinatorial treatment further produced a similar increase in apoptosis (Figure 3-7A/C). We are completing the experiments with PAN and OLA, alone or combined with PT, to evaluate possible synergisms.

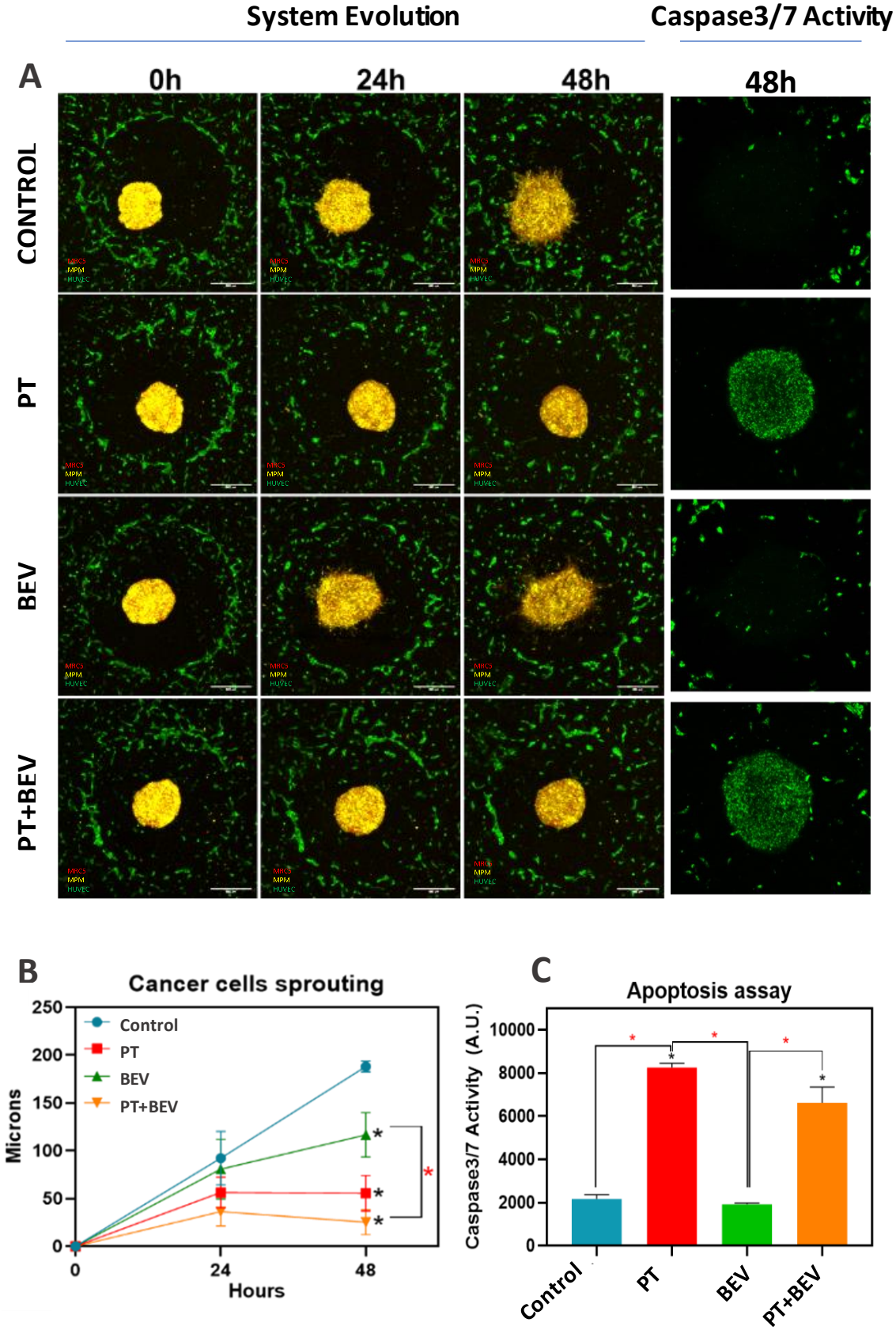

Figure 3-7: A) Representative Z-projection comparing the system evolution of control VCM with single (PT, BEV) and combination treatments over 48hrs.(n=3) and Caspase3/7 Activity at 48hrs (n=3). B) Spheroid Sprouting evolution over 48hrs following treatment; C) Caspase3/7 Activity as a function of maximum green fluorescence intensity detected within the spheroid.

3 PRELIMINARY CONCLUSIONS & FUTURE PERSPECTIVES:

In the attempt to shift from the traditional 2D and time consuming *in-vivo* validation for drug discovery, complex new 3D systems are being developed over the world. There is a growing need for advanced 3D models to overcome shortcomings of traditional 2D methods and animal testing. Creating such models simulating the whole tumour microenvironment (TME) is challenging and have mostly been developed using microfluidic techniques, with limited scalability, making drug discovery time-consuming and expensive. We exploited the Sound Induced Morphogenesis (SIM) technique to develop an advanced 3D *in-vitro* model that resembles *in-vivo* MPM. This tunable multicomponent model consisted of spatially organized cancer cells, cancer associated fibroblasts (CAFs) and microvasculature within a matrix, to reproduce the highly heterogenous TME and to investigate the response to conventional and novel chemotherapeutic drugs. Using SIM, HUVEC–GFP endothelial cells and CAFs were patterned in a fibrin hydrogel within 2 min to obtain a circular ring (diameter: 2mm; thickness: 100 ± 50µm) forming a microcapillary network in 48hrs. Patient derived heterotypic tumour spheroids (MPM:CAF) of around 582.3µm were co-cultured in fibrin matrix over the assembled endothelial cells and followed for 4 days. Using confocal microscopy, microcapillary area evolution, spheroid sprouting, and apoptosis was evaluated. Preliminary analysis of the vascular network over the time showed that the patterned HUVECs/spheroids system had great stability and allowed to monitor MPM migration. The vascularized model was treated with PT, the gold standard therapy, and BEV, a recently approved anti-angiogenic drug in MPM. Thanks to the system, we were able to detect the decrease in spheroid growth and the increase in apoptosis induced by the drugs alone, as well as the additive effects of combination treatments on spheroids sprouting.

After this proof-of-concept work, we believe that this platform may represent an excellent and innovative model in MPM research. Indeed, it offers an advanced vascularized *in-vitro* model to investigate tumour growth, invasion, and resistance, suitable for high-throughput drug screening and testing the previously validated combinations of chemotherapeutics. The model is robust, highly reproducible, and fast, having the potential to dramatically reduce the time of preclinical drug discovery studies.

DISCUSSION AND CONCLUSIONS

Malignant Pleural Mesothelioma (MPM) is a highly aggressive cancer having diverse pathologies and mechanistic origins [1]. The prognosis is generally poor with a reported median survival from presentation of 9–12 months in either untreated or treated (surgery, radiotherapy, or chemotherapy) patients [4]. The common consensus is that novel molecular targets must be identified by elucidating various molecular defects and pathways involved in MPM pathogenesis and progression, to achieve- better disease control and therapeutic options in the near future [1–4].

Various novel drug targets, including genetic and epigenetic ones, have been identified among multiple mechanisms that are responsible for the transformation of normal mesothelial cells into mesothelioma such as mitogenic and anti-apoptotic signalling, autocrine and paracrine cytokine pathways involved in cell plasticity, invasion and metastasis [1, 2, 137, 176, 177]. Due to the clinical successes and therapeutic potential of proteasome inhibitors for tumour treatment, targeting the protein degradation system shows promise [178]. However, proteasome inhibitors prevent the degradation of all intracellular proteins which could have detrimental effects on normal cellular functions. Targeting or inhibiting only a specific subset of proteins part of the ubiquitin-proteasome system that are overexpressed in cancers could dramatically reduce toxicity and adverse effects of such compounds.

Interestingly, *CUL*-family genes are deregulated in MPM also. The *CUL4A* gene has been found to be overexpressed in approximately 64% of primary MPM. Moreover, patients with high CUL4A expression have significantly shorter overall and disease-free survival [179]. CUL4A interacts with a variety of proteins involved in cell cycle and survival, such as Fbw5, Cdt2, PCNA, βTrCP, COP1 and DET1 [179]. NEDD8-activating enzyme (NAE) is an integral component of the NEDD8 conjugation pathway controlling the activity of CRLs: the neddylation of CRLs promotes cancer cell growth and survival pathways [180]. One such promising drug candidate, MLN4924, currently in Phase 1 clinical trials, acts specifically on the SKP1–CUL1–F-box protein (SCF) complex, a ubiquitination system containing the cullin-RING ubiquitin ligases (CRLs) that is often deregulated in many cancer types [172]. It has been found to disrupt the CRL-mediated protein turnover by inhbiting the neddylation of CRL contained in SCF complex: this results in the accumulation of substrates, such as p21, p27 and

Wee1 [131] that trigger cell-cycle arrest, apoptosis, autophagy and senescence in cancer [128, 130].

With this goal in mind, in the first part of my Thesis, I investigated the effects of MLN4924 one of the first-in-class inhibitor of ubiquitination/neddylation on human primary MPM cells. In primary human MPM, MLN4924 alone was not effective as an apoptosis inducer and a cell cycle arresting agent, but it shows a good synergy with the first line treatment cisplatin (PT) which was confirmed also *in-vivo*. Differently from non-selective 'pan-Cullin' inhibitors, MLN4924 targets a specific subset of CRLs (i.e., those contained in the SCF complex). This peculiarity represents an advantage in reducing off target effects [179]. The effects of MLN4924 and PT involved pleiotropic mechanisms. First, they both reduce cell cycle progression, likely as a consequence of the increased number of proteins repressing the cell cycle, spared from SCF-mediated ubiquitination. Second, they increase the immunogenic cell death (ICD): this could be attributed to an increased exposure of antigenic proteins spared from ubiquitination, that may overcome the low antigenicity typical of MPM, or to the induction of ER stress, which is a well-known inducer of ICD. The change from an immune-suppressive/tumour-tolerant behaviour towards an immune-activated/anti-tumour behaviour was confirmed by the $CD8^+$ T cells immune-phenotype after the treatment of MPM cells with MLN4924 and PT. After this preclinical validation, we aim at proposing such combination for future Phase I trials, in particular for those patients with low response to PT or having sarcomatous histotype, which is known to be the least chemo-sensitive type of MPM. Indeed, the efficacy of MLN4924 and PT combination was independent from the sensitiveness to PT or from the histotypes.

Although a multitude of research is being conducted on various tumour targets, using FDA approved and experimental drugs, most of the work is conducted based on trial and error [64]. In order to increase the probabilities of success and efficient use of resources, performing big data analysis and using information already available from well curated databases, represent a chance to better address the therapeutic treatments in MPM [144, 181, 182]. Traditional biological research approaches typically study one gene or a few genes at a time. As research progresses, high-throughput technologies usually generate larger gene lists that can be analysed collectively as their final outputs. Over the last few decades, bioinformatics methods, using the biological knowledge accumulated in public databases, make it possible to dissect large gene lists and assemble a summary of the most enriched and pertinent biology. Performing

enrichment analysis on genome wide SNPs can help shed light on the functional properties of SNPs [183]. The rationale of enrichment analysis is that in an abnormal biological process, the co-functioning genes are enriched together. Such a rationale can make the analysis of large gene lists move from an individual gene-oriented view to a relevant gene group-based analysis. Gene Ontology tools systematically map a large number of interesting genes in a list to the associated biological annotation terms (e.g. GO Terms or Pathways) and then statistically examine the enrichment of gene members for each of the annotations [182]. Following this approach, we performed an SNP enrichment analysis on 5 different patients affected by MPM, looking from unknown druggable targets, possibly common to at least 3 (i.e., 60%) patients. We are aware of the small size of our sample that is a problem common to the research in MPM, a rare tumour. Indeed, we have validated findings in a larger cohort of MPM, available by Genentech Inc. (EGAS00001001563, EGAD00001001913 datasets). The results of this analysis are not included in the present Thesis because they are currently being examined by Genentech Inc. From the analysis of our in-house samples, 3 target genes – RARA, HDAC2, PARP1 - were identified, using exome sequencing data and construction of functional interaction networks, as potentially druggable. We thus set up new single agent or combination treatments with Bexarotene (BEX, a RARA modulator), Panobinostat (PAN, a HDAC2 inhibitor) and Olaparib (OLA, a PARP1/2 antagonist).

Our work on these novel small molecule drugs and their targets shows the potential benefits of a new combinatorial treatments, in particular of the combination of PAN and OLA. *In-vitro* studies showed that combinatorial treatment increased replicative stress and triggered a cell cycle arrest at G2/M phase. Our analysis of replicative, apoptotic and cell cycle checkpoint protein expression demonstrated that the combinatorial treatment decreased the anti-apoptotic proteins p21 and Bcl-2 and increased the pro-apoptotic protein p15/p16 indicating that cells arrested at G2/M phase likely undergo apoptosis. Moreover, several genes involved in chromatin remodelling and epigenetic control of DNA replication were modulated by the PAN+OLA combination, providing a second mechanism for the cytotoxic efficacy observed in primary MPM cells. For instance, H2/3/4 histone acetylases like HIST1H4I, HIST4H4, HIT3H3 and HIST3H4B, which can increase the activation of downstream tumour suppressor genes, were strongly upregulated. In preclinical model of PT resistant MPM, the combinatorial treatment yielded positive outcomes in terms of reduced tumour growth, reduced cellular proliferation and a good safety profile, according to the number of deaths and the post-mortem immunohistochemical analysis of liver, kidney and spleen. Further Phase I clinical trials can

help us in better understanding the feasibility of the combinatorial treatment that we would like to propose as a second line treatment in patients unresponsive to PT.

One of the main issues that arises in studying a rare tumour is the low number of animal models and patient samples available. This issue slows down the possibility of identifying rapidly new molecular targets and discovering effective drugs. In order to overcome this obstacle, in MPM research there is a growing need to develop a new class of advanced *in-vitro* models that could resemble the *in-vivo* MPM microenvironment and that could possibly be scalable for high throughput screening (HTS) [109, 110]. The existing systems typically include 2D models with cells cultured on flat petri dishes and flasks and *in-vivo* rodent cancer models. However, 2D models are far from recapitulating the *in-vivo* cancer microenvironment due to their lack of complexity and absence of typical biochemical and biophysical cues of the surrounding microenvironment [100, 108, 109]. Moreover, some compounds that were active in 2D cultures failed during development because of their lack of efficiency in co-culture conditions, due to the pro-tumour function of stromal cells [108]. In the case of rare tumours, animal testing often shows a lack of reproducibility, poor correlation with humans and raises important ethical issues [100]. Nonetheless, application of 3D models in HTS remains a challenge due to scalability to multi-well plates, reproducibility, labor intensiveness, material costs, and difficulties in incorporation into automated screening setups. Thus, it is of paramount importance to design and develop advanced 3D cell models for HTS systems. Among the technologies for the fabrication of 3D cell models, surface acoustic wave (SAW) systems enable the generation of spatially orchestrated cellular and multicellular constructs [120, 121]. Patterns shape can be tuned on demand by varying a set of parameters, such as sound frequency, amplitude, chamber shape [122]. In this scenario, the 3D-SIM (3D - Sound Induced Morphogenesis) method represents an innovative technology to develop 3D tumour-vascularized models, being smaller, portable, faster (realised within seconds), user-friendly, and more affordable than 3D-bioprinters. 3D-SIM allow to create large intricate 3D patterns of different kind of cells or pre-formed spheroids. It can be easily tuned-on-demand to accommodate different types of extracellular-matrices commonly used in 3D *in-vitro* models. Adaptability to petri dishes makes the 3D models compatible with automated lab equipment and suitable for HTS systems.

We exploited the SIM technique to develop an advanced 3D *in-vitro* model that include MPM cells, cancer associated fibroblasts (CAFs) and microvasculature within a matrix, to reproduce the highly heterogenous microenvironment observed *in-vivo*. This system was used to test the gold standard therapy (cisplatin) and the recently approved drug Bevacizumab and proved to be suitable to verify the resistance on 3D tumours (far different form the data obtained in standard 2D cultures) and possible synergy between two drugs, that is useful in identifying new combinatorial treatments. After this proof-of-concept study, we will test the system with the newly discovered drug candidates and for future HTS in MPM biology.

Overall, this Thesis presents three different tools – a selective inhibition of a specific target, a big data analysis that uncovered new druggable targets in an unbiased manner, a new 3D technique that is functional to implement the drug discovery and testing process – that will be useful in speeding up the biological and pharmacological research in resistant cancers like MPM. The combined use of these complementary tools will help in the identification of new, effective and safe agents against MPM, moving towards a personalized treatment despite being a rare tumour.

4 REFERENCES:

1. Thellung S, Favoni RE, Würth R, Nizzari M, Pattarozzi A, Daga A, et al. Molecular Pharmacology of Malignant Pleural Mesothelioma: Challenges and Perspectives From Preclinical and Clinical Studies. Curr Drug Targets. 2016;17:824–49. http://www.ncbi.nlm.nih.gov/pubmed/26240051.

2. Sekido Y. Molecular pathogenesis of malignant mesothelioma. Carcinogenesis. 2013;34:1413–9.

3. D'Amato-Brito C, Cipriano D, Colin DJ, Germain S, Seimbille Y, Robert JH, et al. Role of MIF/CD74 signaling pathway in the development of pleural mesothelioma. Oncotarget. 2016;7:11512–25.

4. Spugnini EP, Bosari S, Citro G, Lorenzon I, Cognetti F, Baldi A. Human malignant mesothelioma : Molecular mechanisms of pathogenesis and progression. Int J Biochem Cell Biol. 2006;38:2000–4.

5. Røe OD, Stella GM. Malignant Pleural Mesothelioma: History, Controversy, and Future of a Man-Made Epidemic. In: Testa JR, editor. Asbestos and Mesothelioma. Cham: Springer International Publishing; 2017. p. 73–101. doi:10.1007/978-3-319-53560-9_4.

6. Tossavainen A. Global use of asbestos and the incidence of mesothelioma. Int J Occup Environ Health. 2004;10:22–5.

7. Wylie AG. Asbestos and Fibrous Erionite. In: Testa JR, editor. Asbestos and Mesothelioma. Cham: Springer International Publishing; 2017. p. 11–41. doi:10.1007/978-3-319-53560-9_2.

8. Baumann F, Ambrosi JP, Carbone M. Asbestos is not just asbestos: An unrecognised health hazard. Lancet Oncol. 2013;14:576–8. doi:10.1016/S1470-2045(13)70257-2.

9. Alleman JE, Mossman BT. Asbestos Revisited. Scientific American. 1997;:70–5.

10. Acheson ED, Gardner MJ, Pippard EC, Grime LP. Mortality of two groups of women who manufactured gas masks from chrysotile and crocidolite asbestos: A 40-year follow up. Br J Ind Med. 1982;39:344–8.

11. Godwin MC, Jagatic J. Asbestos and mesotheliomas. First. Cham: Springer Nature; 1970.

12. Gibbs GW, Berry G. Mesothelioma and asbestos. Regul Toxicol Pharmacol. 2008;52 1 SUPPL.:S223–31.

13. Testa JR. Malignant Mesothelioma: An Asbestos Legacy. In: Testa JR, editor. Asbestos and Mesothelioma. Cham: Springer International Publishing; 2017. p. 1–9. doi:10.1007/978-3-319-53560-9_1.

14. Carbone M, Baris YI, Bertino P, Brass B, Comertpay S, Dogan AU, et al. Erionite exposure in North Dakota and Turkish villages with mesothelioma. Proc Natl Acad Sci U S A. 2011;108:13618–23. doi:10.1073/pnas.1105887108.

15. LaDou J, Castleman B, Frank A, Gochfeld M, Greenberg M, Huff J, et al. The case for a global ban on asbestos. Environmental Health Perspectives. 2010;118:897–900. doi:10.1289/ehp.1002285.

16. Baumann F, Maurizot P, Mangeas M, Ambrosi J-P, Douwes J, Robineau B. Pleural Mesothelioma in New Caledonia: Associations with Environmental Risk Factors. Environ Health Perspect. 2011;119:695–700. doi:10.1289/ehp.1002862.

17. Harington JS, Mcglashan ND. South African asbestos: Production, exports, and destinations, 1959-1993. Am J Ind Med. 1998;33:321–6. doi:10.1002/(SICI)1097-0274(199804)33:4<321::AID-AJIM2>3.0.CO;2-X.

18. Commission extends ban on asbestos products in EU | News | CORDIS | European Commission. https://cordis.europa.eu/article/id/13445-commission-extends-ban-on-asbestos-products-in-eu. Accessed 28 Dec 2020.

19. Wagner JC, Sleggs CA, Marchand P. Diffuse Pleural Mesothelioma and Asbestos Exposure in the North Western Cape Province. Brit J Ind Med. 1960;17:260–71.

20. Stayner L, Welch LS, Lemen R. The Worldwide Pandemic of Asbestos-Related Diseases. Annu Rev Public Health. 2013;34:205–16. doi:10.1146/annurev-publhealth-031811-124704.

21. Britton M. The epidemiology of mesothelioma. Semin Oncol. 2002;29:18–25.

22. Suzuki Y. Pathology of Human Malignant Mesothelioma-Preliminary Analysis of 1,517 Mesothelioma Cases. Ind Health. 2001;39:183–5.

23. Pavlisko EN, Carney JM, Sporn TA, Roggli VL. Mesothelioma Pathology. In: Testa JR, editor. Asbestos and Mesothelioma. Cham: Springer International Publishing; 2017. p. 131–60. doi:10.1007/978-3-319-53560-9_6.

24. Butnor KJ, Pavlisko EN, Sporn TA, Roggli VL. Malignant peritoneal mesothelioma and

Crohn disease. J Clin Pathol. 2017;70:228–32.

25. Liu B, van Gerwen M, Bonassi S, Taioli E. Epidemiology of Environmental Exposure and Malignant Mesothelioma. Journal of Thoracic Oncology. 2017;12:1031–45. doi:10.1016/j.jtho.2017.04.002.

26. Nuyts V, Nawrot T, Nemery B, Nackaerts K. Hotspots of malignant pleural mesothelioma in Western Europe. Transl Lung Cancer Res. 2018;7:516–9.

27. Mutsaers SE. The mesothelial cell. Int J Biochem Cell Biol. 2004;36:9–16.

28. Mutsaers SE. Mesothelial cells: Their structure, function and role in serosal repair. Respirology. 2002;7:171–91. doi:10.1046/j.1440-1843.2002.00404.x.

29. van Zandwijk N, Clarke C, Henderson D, Musk AW, Fong K, Nowak A, et al. Guidelines for the diagnosis and treatment of malignant pleural mesothelioma. J Thorac Dis. 2013;5:E254. doi:10.3978/j.issn.2072-1439.2013.11.28.

30. Yang H, Testa JR, Carbone M. Mesothelioma epidemiology, carcinogenesis, and pathogenesis. Curr Treat Options Oncol. 2008;9:147–57.

31. Hume LA, Rimstidt JD. The biodurability of chrysotile asbestos. Am Mineral. 1992;77:1125–8.

32. Bocchetta M, Di Resta I, Powers A, Fresco R, Tosolini A, Testa JR, et al. Human mesothelial cells are unusually susceptible to simian virus 40-mediated transformation and asbestos cocarcinogenicity. Proc Natl Acad Sci U S A. 2000;97:10214–9. doi:10.1073/pnas.170207097.

33. Mutsaers SE, Prele CM-A, Pengelly S, Herrick SE. Mesothelial cells and peritoneal homeostasis. Fertil Steril. 2016;106:1018–24.

34. Spugnini EP, Bosari S, Citro G, Lorenzon I, Cognetti F, Baldi A. Human malignant mesothelioma: Molecular mechanisms of pathogenesis and progression. International Journal of Biochemistry and Cell Biology. 2006;38:2000–4. doi:10.1016/j.biocel.2006.07.002.

35. Abbott DM, Bortolotto C, Benvenuti S, Lancia A, Filippi AR, Stella GM. Malignant pleural mesothelioma: Genetic and microenviromental heterogeneity as an unexpected reading frame and therapeutic challenge. Cancers. 2020;12:1186. doi:10.3390/cancers12051186.

36. Yap TA, Aerts JG, Popat S, Fennell DA. Novel insights into mesothelioma biology and

implications for therapy. Nature Reviews Cancer. 2017;17:475–88.

37. Maki-Nevala S, Sarhadi VK, Knuuttila A, Scheinin I, Ellonen P, Langstrom S, et al. Driver Gene and Novel Mutations in Asbestos-Exposed Lung Adenocarcinoma and Malignant Mesothelioma Detected by Exome Sequencing. Lung. 2015;194:125–35.

38. Cregan S, McDonagh L, Gao Y, Barr MP, O'Byrne KJ, Finn SP, et al. KAT5 (Tip60) is a potential therapeutic target in malignant pleural mesothelioma. Int J Oncol. 2016;48:1290–6.

39. Rynne-Vidal A, Jimenez-Heffernan JA, Fernandez-Chacon C, Lopez-Cabrera M, Sandoval P. The Mesothelial Origin of Carcinoma Associated-Fibroblasts in Peritoneal Metastasis. Cancers (Basel). 2015;7:1994–2011.

40. Carbone M, Kratzke RA, Testa JR. The pathogenesis of mesothelioma. Semin Oncol. 2002;29:2–17.

41. Robinson C, Bruggen I Van, Segal A, Dunham M, Sherwood A, Koentgen F, et al. A Novel SV40 TAg Transgenic Model of Asbestos-Induced Mesothelioma : Malignant Transformation Is Dose Dependent. Cancer Res. 2006;66:10786–95.

42. Pistolesi M, Rusthoven J. Malignant pleural mesothelioma: Update, current management, and newer therapeutic strategies. Chest. 2004;126:1318–29.

43. Andersson M, Wallin H, Jönsson M, Nielsen LL, Visfeldt J, Vyberg M, et al. Lung carcinoma and malignant mesothelioma in patients exposed to thorotrast: Incidence, histology and p53 status. Int J Cancer. 1995;63:330–6. doi:10.1002/ijc.2910630304.

44. Farioli A, Ottone M, Morganti AG, Compagnone G, Romani F, Cammelli S, et al. Radiation-induced mesothelioma among long-term solid cancer survivors: A longitudinal analysis of SEER database. Cancer Med. 2016;5:950–9. doi:10.1002/cam4.656.

45. Teta MJ, Lau E, Sceurman BK, Wagner ME. Therapeutic radiation for lymphoma: Risk of malignant mesothelioma. Cancer. 2007;109:1432–8. doi:10.1002/cncr.22526.

46. Ordõez NG. Pleomorphic mesothelioma: Report of 10 cases. Mod Pathol. 2012;25:1011–22.

47. Meyerhoff RR, Yang C-FJ, Speicher PJ, Gulack BC, Hartwig MG, D'Amico TA, et al. Impact of mesothelioma histologic subtype on outcomes in the Surveillance, Epidemiology, and End Results database. J Surg Res. 2015;196:23–32.

48. Kojima M, Kajino K, Momose S, Wali N, Hlaing MT, Han B, et al. Possible reversibility between epithelioid and sarcomatoid types of mesothelioma is independent of ERC/mesothelin expression. Respir Res. 2020;21:1–11.

49. Ali G, Bruno R, Fontanini G. Practical Approach to mesothelioma Diagnosis. J Thorac Dis. 2018;10 Suppl 2:S276–87. doi:10.21037/jtd.2017.10.125.

50. Brcic L, Kern I. Clinical significance of histologic subtyping of malignant pleural mesothelioma. Transl Lung Cancer Res. 2020;9:924. doi:10.21037/TLCR.2020.03.38.

51. Bibby AC, Tsim S, Kanellakis N, Ball H, Talbot DC, Blyth KG, et al. Malignant pleural mesothelioma: An update on investigation, diagnosis and treatment. Eur Respir Rev. 2016;25:472–86. doi:10.1183/16000617.0063-2016.

52. Van Ruth S, Baas P, Zoetmulder FAN. Surgical treatment of malignant pleural mesothelioma: A review. Chest. 2003;123:551–61.

53. Zellos LS, Sugarbaker DJ. Multimodality treatment of diffuse malignant pleural mesothelioma. Semin Oncol. 2002;29:41–50. doi:10.1053/sonc.2002.30230.

54. Ismail-Khan R, Robinson LA, Williams CC, Garrett CR, Bepler G, Simon GR. Malignant pleural mesothelioma: A comprehensive review. Cancer Control. 2006;13:255–63.

55. Kondola S, Manners D, Nowak AK. Malignant pleural mesothelioma: An update on diagnosis and treatment options. Therapeutic Advances in Respiratory Disease. 2016;10:275–88. doi:10.1177/1753465816628800.

56. Saito R, Kasajima A, Taniuchi S, Fujishima F, Ishida K, Nakamura Y, et al. Case reports of primary pulmonary adenocarcinoma with pleural spread: So-called pseudomesotheliomatous adenocarcinoma. Pathol Int. 2012;62:709–15. doi:10.1111/j.1440-1827.2012.02860.x.

57. He X, Wang L, Riedel H, Wang K, Yang Y, Dinu CZ, et al. Mesothelin promotes epithelial-to-mesenchymal transition and tumorigenicity of human lung cancer and mesothelioma cells. Mol Cancer. 2017;16:63.

58. Ae Ri An, Kim KM, Kim JH, Jin GY, Choe YH, Chung MJ. Pseudomesotheliomatous carcinoma of the lung in the parietal pleura. J Pathol Transl Med. 2020;54:192–5. doi:10.4132/jptm.2019.11.14.

59. Attanoos RL, Gibbs AR. “Pseudomesotheliomatous” carcinomas of the pleura: A 10-year analysis of cases from the Environmental Lung Disease Research Group, Cardiff. Histopathology. 2003;43:444–52. doi:10.1046/j.1365-2559.2003.01674.x.

60. Panou V, Vyberg M, Weinreich UM, Meristoudis C, Falkmer UG, Røe OD. The established and future biomarkers of malignant pleural mesothelioma. Cancer Treatment Reviews. 2015;41:486–95.

61. Panou V, Vyberg M, Weinreich UM, Meristoudis C, Falkmer UG, Røe OD. The established and future biomarkers of malignant pleural mesothelioma. Cancer Treat Rev. 2015;41:486–95. doi:10.1016/j.ctrv.2015.05.001.

62. Ray M, Kindler HL. Malignant pleural mesothelioma: An update on biomarkers and treatment. Chest. 2009;136:888–96.

63. Kato T, Lee D, Wu L, Patel P, Young AJ, Wada H, et al. SORORIN and PLK1 as potential therapeutic targets in malignant pleural mesothelioma. Int J Oncol. 2016;49:2411–20.

64. Carbone M, Adusumilli PS, Alexander HR, Baas P, Bardelli F, Bononi A, et al. Mesothelioma: Scientific clues for prevention, diagnosis, and therapy. CA Cancer J Clin. 2019;69:402–29.

65. Hmeljak J, Sanchez-Vega F, Hoadley KA, Shih J, Stewart C, Heiman D, et al. Integrative Molecular Characterization of Malignant Pleural Mesothelioma. Cancer Discov. 2018;8:1548–65. doi:10.1158/2159-8290.CD-18-0804.

66. Bonelli MA, Fumarola C, La Monica S, Alfieri R. New therapeutic strategies for malignant pleural mesothelioma. Biochemical Pharmacology. 2017;123:8–18.

67. Cheung M, Menges CW, Testa JR. Germline and Somatic Mutations in Human Mesothelioma and Lessons from Asbestos-Exposed Genetically Engineered Mouse Models. In: Testa JR, editor. Asbestos and Mesothelioma. Cham: Springer International Publishing; 2017. p. 175–95. doi:10.1007/978-3-319-53560-9_8.

68. Patil NS, Righi L, Koeppen H, Zou W, Izzo S, Grosso F, et al. Molecular and Histopathological Characterization of the Tumor Immune Microenvironment in Advanced Stage of Malignant Pleural Mesothelioma. J Thorac Oncol. 2018;13:124–33. doi:10.1016/j.jtho.2017.09.1968.

69. Parrotta R, Okonska A, Ronner M, Weder W, Stahel R, Penengo L, et al. A Novel BRCA1-

Associated Protein-1 Isoform Affects Response of Mesothelioma Cells to Drugs Impairing BRCA1-Mediated DNA Repair. J Thorac Oncol. 2017;12:1309–19. doi:10.1016/j.jtho.2017.03.023.

70. Bott M, Brevet M, Taylor BS, Shimizu S, Ito T, Wang L, et al. The nuclear deubiquitinase BAP1 is commonly inactivated by somatic mutations and 3p21.1 losses in malignant pleural mesothelioma. Nat Genet. 2015;43:668–72.

71. Guo G, Chmielecki J, Goparaju C, Heguy A, Dolgalev I, Carbone M, et al. Whole-Exome Sequencing Reveals Frequent Genetic Alterations in BAP1 , NF2 , CDKN2A , and CUL1 in Malignant Pleural Mesothelioma. Cancer Res. 2015;75:8–14.

72. Kadariya Y, Menges CW, Talarchek J, Cai KQ, Klein-Szanto AJ, Pietrofesa RA, et al. Inflammation-Related IL1beta/IL1R Signaling Promotes the Development of Asbestos-Induced Malignant Mesothelioma. Cancer Prev Res (Phila). 2016;9:406–14.

73. Li J, Poi MJ, Tsai MD. Regulatory mechanisms of tumor suppressor P16INK4A and their relevance to cancer. Biochemistry. 2011;50:5566–82.

74. Cooper J, Xu Q, Zhou L, Pavlovic M, Ojeda V, Moulick K, et al. Combined Inhibition of NEDD8-Activating Enzyme and mTOR Suppresses NF2 Loss-Driven Tumorigenesis. Mol Cancer Ther. 2017;16:1693–704.

75. De Rienzo A, Richards WG, Bueno R. Gene Signature of Malignant Pleural Mesothelioma. In: Testa JR, editor. Asbestos and Mesothelioma. Cham: Springer International Publishing; 2017. p. 197–209. doi:10.1007/978-3-319-53560-9_9.

76. Duruisseaux M, Rouquette I, Adam J, Cortot A, Cazes A, Gibault L, et al. Efficacy of PD-1/PD-L1 immune checkpoint inhibitors and PD-L1 testing in thoracic cancers. Ann Pathol. 2017;37:61–78.

77. Black M, Barsoum IB, Truesdell P, Cotechini T, Macdonald-goodfellow SK, Petroff M, et al. Activation of the PD-1 / PD-L1 immune checkpoint confers tumor cell chemoresistance associated with increased metastasis. Oncotarget. 2016;7:10557–67.

78. Sugarbaker DJ, Wolf AS. Surgery for malignant pleural mesothelioma. Expert Rev Respir Med. 2010;4:363–72. doi:10.1586/ers.10.35.

79. Tsao AS, Wistuba I, Roth JA, Kindler HL. Malignant pleural mesothelioma. Journal of Clinical Oncology. 2009;27:2081–90. doi:10.1200/JCO.2008.19.8523.

80. Sterman DH, Kaiser LR, Albelda SM. Advances in the treatment of malignant pleural mesothelioma. Chest. 1999;116:504–20.

81. Neumann V, Löseke S, Nowak D, Herth FJF, Tannapfel A. Malignant pleural mesothelioma: incidence, etiology, diagnosis, treatment, and occupational health. Dtsch Arztebl Int. 2013;110:319–26. doi:10.3238/arztebl.2013.0319.

82. Illidge T. Turning Radiotherapy into an Effective Systemic Anti-cancer Treatment in Combination with Immunotherapy. Clin Oncol. 2015;27:696–9. doi:10.1016/j.clon.2015.09.001.

83. Perrot M de, Wu L, Wu M, Cho BCJ. Radiotherapy for the treatment of malignant pleural mesothelioma. The Lancet Oncology. 2017;18:e532–42.

84. Fennell DA, Gaudino G, O'Byrne KJ, Mutti L, van Meerbeeck J. Advances in the systemic therapy of malignant pleural mesothelioma. Nat Clin Pract Oncol. 2008;5:136–47.

85. Ong ST, Vogelzang NJ. Chemotherapy in malignant pleural mesothelioma: A review. J Clin Oncol. 1996;14:1007–17.

86. Pasello G, Favaretto A. Molecular Targets in Malignant Pleural Mesothelioma Treatment. Curr Drug Targets. 2009;10:1235–44.

87. Nowak AK, Brosseau S, Cook A, Zalcman G. Antiangiogeneic Strategies in Mesothelioma. Front Oncol. 2020;10:1–13.

88. Cantini L, Hassan R, Sterman DH, Aerts JGJV. Emerging Treatments for Malignant Pleural Mesothelioma: Where Are We Heading? Frontiers in Oncology. 2020;10:343. doi:10.3389/fonc.2020.00343.

89. Scherpereel A, Wallyn F, Albelda SM, Munck C. Novel therapies for malignant pleural mesothelioma. The Lancet Oncology. 2018;19:e161–72.

90. Aerts JG, Lievense LA, Hoogsteden HC, Hegmans JP. Immunotherapy prospects in the treatment of lung cancer and mesothelioma. Transl lung cancer Res. 2014;3:34–45. doi:10.3978/j.issn.2218-6751.2013.11.04.

91. Vanneman M, Dranoff G. Combining Immunotherapy and Targeted Therapies in Cancer Treatment. Nat Rev Cancer. 2014;12:237–51.

92. Victor CT, Rech AJ, Maity A, Rengan R, Pauken KE, Stelekati E, et al. Radiation and dual

checkpoint blockade activate non-redundant immune mechanisms in cancer. Nature. 2015;520:373–7. doi:10.1038/nature14292.

93. Chu GJ, Zandwijk N Van, Rasko JEJ. The Immune Microenvironment in Mesothelioma: Mechanisms of Resistance to Immunotherapy. Front Oncol. 2019;9:1–12.

94. Yap TA, Aerts JG, Popat S, Fennell DA. Novel insights into mesothelioma biology and implications for therapy. Nat Rev Cancer. 2017;17:475–88. doi:10.1038/nrc.2017.42.

95. Nabavi N, Bennewith KL, Churg A, Wang Y, Collins CC, Mutti L. Switching off malignant mesothelioma: Exploiting the hypoxic microenvironment. Genes and Cancer. 2016;7:340–54. doi:10.18632/genesandcancer.124.

96. Bielefeldt-Ohmann H, Fitzpatrick DR, Marzo AL, Jarnicki AG, Himbeck RP, Davis MR, et al. Patho- and immunobiology of malignant mesothelioma: characterisation of tumour infiltrating leucocytes and cytokine production in a murine model. Cancer Immunol Immunother. 1994;39:347–59.

97. Hegmans JPJJ, Hemmes A, Hammad H, Boon L, Hoogsteden HC, Lambrecht BN. Mesothelioma environment comprises cytokines and T-regulatory cells that suppress immune responses. Eur Respir J. 2006;27:1086–95.

98. Lee SS, Bindokas VP, Kron SJ. Multiplex three-dimensional optical mapping of tumor immune microenvironment. Sci Rep. 2017;7:1–11. doi:10.1038/s41598-017-16987-x.

99. Campia I, Buondonno I, Castella B, Rolando B. An Autocrine Cytokine / JAK / STAT-Signaling Induces Kynurenine Synthesis in Multidrug Resistant Human Cancer Cells. PLoS One. 2015;10:1–20.

100. Nguyen M, Ninno A De, Mencattini A, Martinelli E, Businaro L, Parrini MC. Dissecting Effects of Anti-cancer Drugs and Cancer- Associated Fibroblasts by On-Chip Reconstitution of Immunocompetent Tumor Microenvironments. Cell Rep. 2018;25:3884–93.

101. Li Q, Wang W, Yamada T, Matsumoto K, Sakai K, Bando Y, et al. Pleural mesothelioma instigates tumor-associated fibroblasts to promote progression via a malignant cytokine network. Am J Pathol. 2011;179:1483–93.

102. Morishita Y, Ookawara S, Hirahara I, Muto S, Nagata D. HIF-1alpha mediates Hypoxia-induced epithelial-mesenchymal transition in peritoneal mesothelial cells. Ren Fail. 2016;38:282–9.

103. Rozpedek W, Pytel D, Mucha B, Leszczynska H, Diehl JA, Majsterek I. The Role of the PERK/eIF2α/ATF4/CHOP Signaling Pathway in Tumor Progression During Endoplasmic Reticulum Stress. Curr Mol Med. 2016;16:533–44. http://www.ncbi.nlm.nih.gov/pubmed/27211800. Accessed 20 Sep 2019.

104. Dong H, Guo H, Xie L, Wang G, Zhong X, Khoury T, et al. The Metastasis-Associated Gene MTA3, a Component of the Mi-2/NuRD Transcriptional Repression Complex, Predicts Prognosis of Gastroesophageal Junction Adenocarcinoma. PLoS One. 2013;8. doi:10.1371/journal.pone.0062986.

105. Kopecka J, Campia I, Jacobs A, Frei AP, Ghigo D, Wollscheid B, et al. Carbonic anhydrase XII is a new therapeutic target to overcome chemoresistance in cancer cells. Oncotarget. 2015;6:6776–93.

106. Haycock JW. 3D Cell Culture: A Review of Current Approaches and Techniques. In: Haycock JW, editor. 3D Cell Culture: Methods and Protocols. Totowa, NJ: Humana Press; 2011. p. 1–15. doi:10.1007/978-1-60761-984-0_1.

107. Duval K, Grover H, Han LH, Mou Y, Pegoraro AF, Fredberg J, et al. Modeling physiological events in 2D vs. 3D cell culture. Physiology. 2017;32:266–77. doi:10.1152/physiol.00036.2016.

108. Puls TJ, Tan X, Husain M, Whittington CF, Fishel ML, Voytik-Harbin SL. Development of a Novel 3D Tumor-tissue Invasion Model for High-throughput, High-content Phenotypic Drug Screening OPEN. Sci Rep. 2018;8:1–14. doi:10.1038/s41598-018-31138-6.

109. Langer EM, Allen-Petersen BL, King SM, Kendsersky ND, Turnidge MA, Kuziel GM, et al. Modeling Tumor Phenotypes In Vitro with Three-Dimensional Bioprinting. Cell Rep. 2019;26:608–23.

110. Singh A, Pruett N, Hoang CD. In vitro experimental models of mesothelioma revisited. Transl lung cancer Res. 2017;6:248–58. doi:10.21037/tlcr.2017.04.12.

111. Huh D, Hamilton GA, Ingber DE. From 3D cell culture to organs-on-chips. Trends in Cell Biology. 2011;21:745–54.

112. Kaushik G, Ponnusamy MP, Batra SK. Concise Review: Current Status of Three-Dimensional Organoids as Preclinical Models. Stem Cells. 2018;36:1329–40. doi:10.1002/stem.2852.

113. Justice BA, Badr NA, Felder RA. 3D cell culture opens new dimensions in cell-based assays. Drug Discovery Today. 2009;14:102–7.

114. Radhakrishnan J, Varadaraj S, Dash SK, Sharma A, Verma RS. Organotypic cancer tissue models for drug screening: 3D constructs, bioprinting and microfluidic chips. Drug Discovery Today. 2020;25:879–90.

115. Fong ELS, Toh TB, Yu H, Chow EKH. 3D Culture as a Clinically Relevant Model for Personalized Medicine. SLAS Technology. 2017;22:245–53. doi:10.1177/2472630317697251.

116. Jensen C, Teng Y. Is It Time to Start Transitioning From 2D to 3D Cell Culture? Front Mol Biosci. 2020;7:1–15.

117. Yuan H, Xing K, Hsu H-Y. Trinity of Three-Dimensional (3D) Scaffold, Vibration, and 3D Printing on Cell Culture Application: A Systematic Review and Indicating Future Direction. Bioengineering. 2018;5:1–21. doi:10.3390/bioengineering5030057.

118. Mazzocchi AR, Rajan SAP, Votanopoulos KI, Hall AR, Skardal A. In vitro patient-derived 3D mesothelioma tumor organoids facilitate patient-centric therapeutic screening. Sci Rep. 2018;8:1–12. doi:10.1038/s41598-018-21200-8.

119. Cui P, Wang S. Application of microfluidic chip technology in pharmaceutical analysis: A review. J Pharm Anal. 2019;9:238–47.

120. Lata JP, Guo F, Guo J, Huang PH, Yang J, Huang TJ. Surface Acoustic Waves Grant Superior Spatial Control of Cells Embedded in Hydrogel Fibers. Adv Mater. 2016;28:8632–8. doi:10.1002/adma.201602947.

121. Naseer SM, Manbachi A, Samandari M, Walch P, Gao Y, Zhang YS, et al. Surface acoustic waves induced micropatterning of cells in gelatin methacryloyl (GelMA) hydrogels. Biofabrication. 2017;9:015020. doi:10.1088/1758-5090/aa585e.

122. Guo F, Mao Z, Chen Y, Xie Z, Lata JP, Li P, et al. Three-dimensional manipulation of single cells using surface acoustic waves. PNAS. 2016;113:1522–7.

123. Kopecka J, Salaroglio IC, Righi L, Libener R, Orecchia S, Grosso F, et al. Loss of C/EBP-β LIP drives cisplatin resistance in malignant pleural mesothelioma. Lung Cancer. 2018;120:34–45. doi:10.1016/j.lungcan.2018.03.022.

124. Riganti C, Miraglia E, Viarisio D, Costamagna C, Pescarmona G, Ghigo D, et al. Nitric Oxide Reverts the Resistance to Doxorubicin in Human Colon Cancer Cells by Inhibiting the Drug Efflux. Cancer Res. 2005;65:516–26.

125. Riganti C, Castella B, Kopecka J, Campia I, Coscia M, Pescarmona G, et al. Zoledronic Acid Restores Doxorubicin Chemosensitivity and Immunogenic Cell Death in Multidrug-Resistant Human Cancer Cells. PLoS One. 2013;8:1–14.

126. Boo S De, Kopecka J, Brusa D, Gazzano E, Matera L, Ghigo D, et al. iNOS activity is necessary for the cytotoxic and immunogenic effects of doxorubicin in human colon cancer cells. Mol Cancer. 2009;8:1–18.

127. Obeid M, Tesniere A, Ghiringhelli F, Fimia GM, Apetoh L, Perfettini JL, et al. Calreticulin exposure dictates the immunogenicity of cancer cell death. Nat Med. 2007;13:54–61. doi:10.1038/nm1523.

128. Luo Z, Yu G, Lee HW, Li L, Wang L, Yang D, et al. The Nedd8-Activating Enzyme Inhibitor MLN4924 Induces Autophagy and Apoptosis to Suppress Liver Cancer Cell Growth. Cancer Res. 2012;72:3360–72.

129. Lan H, Tang Z, Jin H, Sun Y. Neddylation inhibitor MLN4924 suppresses growth and migration of human gastric cancer cells. Nat Sci Reports. 2016;6:1–12. doi:10.1038/srep24218.

130. Lin JJ, Milhollen MA, Smith PG, Narayanan U, Dutta A. NEDD8-Targeting Drug MLN4924 Elicits DNA Rereplication by Stabilizing Cdt1 in S Phase , Triggering Checkpoint Activation , Apoptosis , and Senescence in Cancer Cells. Cancer Res. 2010;70:10310–21.

131. Tong S, Si Y, Yu H, Zhang L, Xie P, Jiang W. MLN4924 (Pevonedistat), a protein neddylation inhibitor , suppresses proliferation and migration of human clear cell renal cell carcinoma. Sci Rep. 2017; June:1–9. doi:10.1038/s41598-017-06098-y.

132. Fishel ML, Newell DR, Griffin RJ, Davison R, Wang L, Curtin NJ, et al. Effect of Cell Cycle Inhibition on Cisplatin-Induced Cytotoxicity. J Pharmacol Exp Ther. 2005;312:206–13.

133. Galluzzi L, Buqué A, Kepp O, Zitvogel L, Kroemer G. Immunogenic cell death in cancer and infectious disease. Nat Rev Immunol. 2016;:1–15. doi:10.1038/nri.2016.107.

134. Tesniere A, Schlemmer F, Boige V, Kepp O, Martins I, Ghiringhelli F. Immunogenic death of colon cancer cells treated with oxaliplatin. Oncogene. 2009;29:482–91. doi:10.1038/onc.2009.356.

135. Nejad EB, Sluis TC Van Der, Duikeren S Van, Yagita H, Janssen GM, Veelen PA Van, et al. Tumor Eradication by Cisplatin Is Sustained by CD80/86 Mediated Costimulation of CD8+ T Cells. Cancer Res. 2016;76:1–14.

136. Blasio S Di, Wortel IMN, Bladel DAG Van, De LE, Boer TD, Worah K, et al. Human CD1c DCs are critical cellular mediators of immune responses induced by immunogenic cell death. Oncoimmunology. 2017;5:1–14. doi:10.1080/2162402X.2016.1192739.

137. Marcq E, Pauwels P, Meerbeeck JP Van, Smits ELJ. Targeting immune checkpoints : New opportunity for mesothelioma treatment ? Cancer Treat Rev. 2015;41:914–24. doi:10.1016/j.ctrv.2015.09.006.

138. Chevet E, Hetz C, Samali A. Endoplasmic reticulum stress–activated cell reprogramming in oncogenesis. Cancer Discov. 2016;5:586–97.

139. Liu Z-J, Li H-F, Tan G-H, Tao Q-Q, Ni W, Cheng X-W, et al. Identify mutation in amyotrophic lateral sclerosis cases using HaloPlex target enrichment system. Neurobiol Aging. 2014;35:2881.e11-2881.e15. doi:10.1016/J.NEUROBIOLAGING.2014.07.003.

140. Shannon P, Markiel A, Owen Ozier 2, Baliga NS, Wang JT, Ramage D, et al. Cytoscape: a software environment for integrated models of biomolecular interaction networks. Genome Res. 2003;:2498–504.

141. Warde-Farley D, Donaldson SL, Comes O, Zuberi K, Badrawi R, Chao P, et al. The GeneMANIA prediction server: biological network integration for gene prioritization and predicting gene function. Nucleic Acids Res. 2010;38:W214–20. doi:10.1093/nar/gkq537.

142. Homer N, Nelson SF. Improved variant discovery through local re-alignment of short-read next-generation sequencing data using SRMA. Genome Biol. 2010;11:R99. doi:10.1186/gb-2010-11-10-r99.

143. Wang J, Raskin L, Samuels DC, Shyr Y, Guo Y. Genome measures used for quality control are dependent on gene function and ancestry. Bioinformatics. 2015;31:318–23. doi:10.1093/bioinformatics/btu668.

144. Wu G, Feng X, Stein L. A human functional protein interaction network and its application to cancer data analysis. Genome Biol. 2010;11:1–23. doi:10.1186/gb-2010-11-5-r53.

145. Maere S, Heymans K, Kuiper M. BiNGO: a Cytoscape plugin to assess overrepresentation of Gene Ontology categories in Biological Networks. Bioinformatics. 2005;21:3448–9.

doi:10.1093/bioinformatics/bti551.

146. Jelinic P, Levine DA. New insights into PARP inhibitors' effect on cell cycle and homology-directed DNA damage repair. Mol Cancer Ther. 2014;13:1645–54.

147. Weston VJ, Oldreive CE, Skowronska A, Oscier DG, Pratt G, Dyer MJS, et al. The PARP inhibitor olaparib induces significant killing of ATM-deficientlymphoid tumor cells in vitro and in vivo. Blood. 2010;116:4578–87.

148. Rein ID, Landsverk KS, Micci F, Patzke S, Stokke T. Replication-induced DNA damage after PARP inhibition causes G2 delay, and cell line-dependent apoptosis, necrosis and multinucleation. Cell Cycle. 2015;14:3248–60.

149. Zhang C, Hazarika P, Ni X, Weidner DA, Duvic M. Induction of apoptosis by bexarotene in cutaneous T-cell lymphoma cells: relevance to mechanism of therapeutic action. Clin Cancer Res. 2002;8:1234–40.

150. Nieto-Rementería N, Pérez-Yarza G, Boyano MD, Apraiz A, Izu R, Díaz-Pérez JL, et al. Bexarotene activates the p53/p73 pathway in human cutaneous T-cell lymphoma. Br J Dermatol. 2009;160:519–26.

151. Visser S, Yang X, Visser S, Yang X. LATS tumor suppressor : A new governor of cellular homeostasis. Cell Cycle. 2015;9:3892–903.

152. Pettazzoni P, Pizzimenti S, Toaldo C, Sotomayor P, Tagliavacca L, Liu S, et al. Induction of cell cycle arrest and DNA damage by the HDAC inhibitor panobinostat (LBH589) and the lipid peroxidation end product 4-hydroxynonenal in prostate cancer cells. Free Radic Biol Med. 2011;50:313–22.

153. McDonel P, Costello I, Hendrich B. Keeping things quiet: Roles of NuRD and Sin3 co-repressor complexes during mammalian development. International Journal of Biochemistry and Cell Biology. 2009;41:108–16.

154. Lai AY, Wade PA. Cancer biology and NuRD: A multifaceted chromatin remodelling complex. Nature Reviews Cancer. 2011;11:588–96.

155. Basta J, Rauchman M. The nucleosome remodeling and deacetylase complex in development and disease. Transl Res. 2015;165:36–47. doi:10.1016/j.trsl.2014.05.003.

156. Ren HY, Chen B, Huang GL, Liu Y, Shen DY. Upregulation of retinoic acid receptor-β

reverses drug resistance in cholangiocarcinoma cells by enhancing susceptibility to apoptosis. Mol Med Rep. 2016;14:3602–8.

157. Martins MD, Castilho RM. Histones: Controlling Tumor Signaling Circuitry. J Carcinog Mutagen. 2013;5:1–12. doi:10.4172/2157-2518.S5-001.

158. Mills AA. The chromodomain helicase DNA-binding chromatin remodelers: Family traits that protect from and promote cancer. Cold Spring Harb Perspect Med. 2017;7:1–15.

159. Li W, Mills AA. Architects of the genome: CHD dysfunction in cancer, developmental disorders and neurological syndromes. Epigenomics. 2014;6:381–95.

160. Gao C, Liu S, Lu W, Yue Z, Zhao X, Xing T, et al. Downregulating CREBBP inhibits proliferation and cell cycle progression and induces daunorubicin resistance in leukemia cells. Mol Med Rep. 2020;22:2905. doi:10.3892/mmr.2020.11347.

161. Grzeskowiak CL, Kundu ST, Mo X, Ivanov AA, Zagorodna O, Lu H, et al. In vivo screening identifies GATAD2B as a metastasis driver in KRAS-driven lung cancer. Nat Commun. 2018;9.

162. Sen N, Gui B, Kumar R. Role of MTA1 in cancer progression and metastasis. Cancer Metastasis Rev. 2014;33:879–89. doi:10.1007/s10555-014-9515-3.

163. Thoolen B, Maronpot RR, Harada T, Nyska A, Rousseaux C, Nolte T, et al. Proliferative and nonproliferative lesions of the rat and mouse hepatobiliary system. Toxicol Pathol. 2010;38 7 SUPPL.:5–81.

164. Greaves P. Chapter 10 - Urinary Tract. In: Greaves P, editor. Histopathology of Preclinical Toxicity Studies (Fourth Edition). Fourth Edi. Boston: Academic Press; 2012. p. 537–614. doi:https://doi.org/10.1016/B978-0-444-53856-7.00010-5.

165. Greaves P. Chapter 4 - Hemopoietic and Lymphatic Systems. In: Greaves P, editor. Histopathology of Preclinical Toxicity Studies (Fourth Edition). Fourth Edi. Boston: Academic Press; 2012. p. 99–155. doi:https://doi.org/10.1016/B978-0-444-53856-7.00004-X.

166. Ghanim B, Klikovits T, Hoda MA, Lang G, Szirtes I, Setinek U, et al. Ki67 index is an independent prognostic factor in epithelioid but not in non-epithelioid malignant pleural mesothelioma: A multicenter study. Br J Cancer. 2015;112:783–92. doi:10.1038/bjc.2015.9.

167. Rao R, Balusu R, Fiskus W, Mudunuru U, Venkannagari S, Chauhan L, et al. Combination

of Pan-Histone Deacetylase Inhibitor and Autophagy Inhibitor Exerts Superior Efficacy against Triple-Negative Human Breast Cancer Cells. Mol Cancer Ther. 2012;11:973–83. doi:10.1158/1535-7163.MCT-11-0979.

168. Ellis L, Bots M, Lindemann RK, Bolden JE, Newbold A, Cluse LA, et al. The histone deacetylase inhibitors LAQ824 and LBH589 do not require death receptor signaling or a functional apoptosome to mediate tumor cell death or therapeutic efficacy. Blood. 2009;114:380–93.

169. Scuto A, Kirschbaum M, Kowolik C, Kretzner L, Juhasz A, Atadja P, et al. The novel histone deacetylase inhibitor, LBH589, induces expression of DNA damage response genes and apoptosis in Ph- acute lymphoblastic leukemia cells. Blood. 2008;111:5093–100. doi:10.1182/blood-2007-10-117762.

170. Wirries A, Jabari S, Jansen EP, Roth S, Figueroa-Juárez E, Wissniowski TT, et al. Panobinostat mediated cell death: a novel therapeutic approach for osteosarcoma. Oncotarget. 2018;9:32997–3010.

171. Menear KA, Adcock C, Boulter R, Cockcroft X, Copsey L, Cranston A, et al. 4-[3-(4-Cyclopropanecarbonylpiperazine-1-carbonyl)-4-fluorobenzyl]-2 *H* -phthalazin-1-one: A Novel Bioavailable Inhibitor of Poly(ADP-ribose) Polymerase-1. J Med Chem. 2008;51:6581–91. doi:10.1021/jm8001263.

172. Prystowsky MB, Adomako A, Smith R V., Kawachi N, McKimpson W, Atadja P, et al. The histone deacetylase inhibitor LBH589 inhibits expression of mitotic genes causing G2/M arrest and cell death in head and neck squamous cell carcinoma cell lines. J Pathol. 2009;218:467–77.

173. Dalby KN, Tekedereli I, Lopez-Berestein G, Ozpolat B. Targeting the prodeath and prosurvival functions of autophagy as novel therapeutic strategies in cancer. Autophagy. 2010;6:322–239.

174. Dziadkowiec KN, Gąsiorowska E, Nowak-Markwitz E, Jankowska A. PARP inhibitors: review of mechanisms of action and BRCA1/2 mutation targeting. Prz menopauzalny = Menopause Rev. 2016;15:215–9. doi:10.5114/pm.2016.65667.

175. Eilenberger C, Kratz SRA, Rothbauer M, Ehmoser EK, Ertl P, Küpcü S. Optimized alamarBlue assay protocol for drug dose-response determination of 3D tumor spheroids.

MethodsX. 2018;5:781–7. doi:10.1016/j.mex.2018.07.011.

176. Kopecka J, Salaroglio IC, Righi L, Libener R, Orecchia S, Grosso F, et al. Loss of C/EBP-β LIP drives cisplatin resistance in malignant pleural mesothelioma. Lung Cancer. 2018;120:34–45.

177. Rapisarda V, Salemi R, Marconi A, Loreto C, Graziano AC, Cardile V, et al. Fluoro-edenite induces fibulin-3 overexpression in non-malignant human mesothelial cells. Oncol Lett. 2016;12:3363–7.

178. Skaar JR, Pagan JK, Pagano M. SCF ubiquitin ligase-targeted therapies. Nat Publ Gr. 2014;13:889–903. doi:10.1038/nrd4432.

179. Lee J, Zhou P. Cullins and Cancer. Genes Cancer. 2010;1:690–9.

180. Soucy TA, Smith PG, Milhollen MA, Berger AJ, Gavin JM, Adhikari S, et al. An inhibitor of NEDD8-activating enzyme as a new approach to treat cancer. Nature. 2009;458:732–6. doi:10.1038/nature07884.

181. Bakir-Gungor B, Sezerman OU. A New Methodology to Associate SNPs with Human Diseases According to Their Pathway Related Context. PLoS One. 2011;6:e26277. doi:10.1371/journal.pone.0026277.

182. Huang DW, Sherman BT, Lempicki RA. Bioinformatics enrichment tools: paths toward the comprehensive functional analysis of large gene lists. Nucleic Acids Res. 2009;37:1–13. doi:10.1093/nar/gkn923.

183. Sivadas E, Bruvold NT, Nelson MR. A reduced version of the horizontal and vertical individualism and collectivism scale: A four-country assessment. J Bus Res. 2008;61:201–10. doi:10.1016/J.JBUSRES.2007.06.016.

5 ADDENDUM:

PUBLICATIONS

1. Godel, M., Morena, D., Ananthanarayanan, P., Buondonno, I., Ferrero, G., Hattinger, C. M., Di Nicolantonio, F., Serra, M., Taulli, R., Cordero, F., Riganti, C., Kopecka, J. 2020. Small Nucleolar RNAs Determine Resistance to Doxorubicin in Human Osteosarcoma. International Journal of Molecular Sciences. 21(12):4500. https://doi.org/10.3390/ijms21124500

2. Salaroglio, I.C., Kopecka, J., Napoli, F., Pradotto, M., Maletta, F., Costardi, L., Gagliasso, M., Milosevic, V., Ananthanarayanan, P., Bironzo, P., Tabbò, F., Cartia, C.F., Passone, E., Comunanza, V., Ardissone, F., Ruffini, E., Bussolino, F., Righi, L., Novello, S., Di Maio, M., Papotti, M., Scagliotti, G. V, Riganti, C., 2019. Potential Diagnostic and Prognostic Role of Microenvironment in Malignant Pleural Mesothelioma. J. Thorac. Oncol. 14, 1458–1471. https://doi.org/10.1016/j.jtho.2019.03.0294)

3. Milosevic, V., Kopecka, J., Salaroglio, I.C., Libener, R., Napoli, F., Izzo, S., Orecchia, S., Ananthanarayanan, P., Bironzo, P., Grosso, F., Tabbò, F., Comunanza, V., Alexa-Stratulat, T., Bussolino, F., Righi, L., Novello, S., Scagliotti, G. V, Riganti, C., 2019. Wnt/IL-1β/IL-8 autocrine circuitries control chemoresistance in mesothelioma initiating cells by inducing ABCB5. Int. J. Cancer. https://doi.org/10.1002/ijc.32419

4. Kopecka, J., Salaroglio, I.C., Righi, L., Libener, R., Orecchia, S., Grosso, F., Milosevic, V., Ananthanarayanan, P., Ricci, L., Capelletto, E., Pradotto, M., Napoli, F., Di Maio, M., Novello, S., Rubinstein, M., Scagliotti, G. V, Riganti, C., 2018. Loss of C/EBP-β LIP drives cisplatin resistance in malignant pleural mesothelioma. Lung Cancer 120, 34–45. https://doi.org/10.1016/j.lungcan.2018.03.022

5. Ananthanarayanan, P.,* Godel, M.,* Ricci, L., Righi, L., Novello, S., Riganti, C., Scagliotti, G.V.,* Kopecka, J.* Targeting SCF complex: a new approach to reverse chemo- and immune-resistance in malignant pleural mesothelioma. *Manuscript in preparation.*

6. Di Marzio, N., Ananthanarayanan, P., Guex, A.G., Alini, M., Riganti, C., Scagliotti, G.V., Serra, T. New 3D Vascularized *in-vitro* Model of Malignant Pleural Mesothelioma via SIM. *Manuscript in preparation*.

7. Ananthanarayanan, P., Lingua, M., Kopecka, J., Mohr, T., Taulli, R., Scagliotti, G.V.*, Riganti, C.* A Bioinformatic Approach to Discover New Druggable Targets In Malignant Pleural Mesothelioma. *Manuscript in preparation.*

ORAL COMMUNICATIONS AND POSTERS

1. Oral Presentation on "Novel Acoustic Wave Programmed 3D Vascularised Cancer Model in Malignant Pleural Mesothelioma: A Platform for drug screening". STRATAGEM International Online Symposium on "*New diagnostic and therapeutic tools against multidrug resistant tumours".* November 4, 2020.

2. Oral and Poster Presentation titled "Identifying Unique Molecular Targets and Using Novel Gene Group Based Shotgun Treatments In Malignant Pleural Mesothelioma". 1st international conference *"From Single Gene Analysis to Single Cell Profiling: A New Era for Genomic Medicine" organised by AICC, Magna Graecia University Campus in Catanzaro.* October 1-2, 2019.

3. Poster presentation titled "Targeting Protein Metabolism to overcome chemoresistance and trigger anti-tumour immune response in Malignant Pleural Mesothelioma". 2nd MS-based International Proteomics & Metabolomics Conference and Advanced School on "*Ms-Based Untargeted Proteomics and Metabolomics: Cancer Metabolism, Therapeutic Targets and Biomarkers*", AICC, University of Verona, Verona, July 1-2, 2019.

4. Poster presentation titled "Targeting Protein Metabolism to overcome chemoresistance and trigger anti-tumour immune response in Malignant Pleural Mesothelioma". 5th Annual Meeting of the International Society of Cancer Metabolism on "*Metabolic Adaptations and Targets in Cancer*", Biomedical Research Center, Slovak Academy of Sciences, Bratislava, Slovakia. October 17-20, 2018.

5. Business pitch on project titled "Smart Vivopatch For Emergency Rapid Diagnosis". Summer School on Safer NanoDesign by European Scientific Institution, Bio-Health Computing Schools, Archamps Geneva. June 13-19, 2017.

MEETINGS AND SEMINARS ATTENDANCE

1. STRATAGEM International Online Symposium on "*New diagnostic and therapeutic tools against multidrug resistant tumours".* November 4, 2020.

2. 1st international conference *"From Single Gene Analysis to Single Cell Profiling: A New Era for Genomic Medicine" organised by AICC, Magna Graecia University Campus in Catanzaro,* 1st-2nd October 2019.

3. 2nd MS-based International Proteomics & Metabolomics Conference and Advanced School on "*Ms-Based Untargeted Proteomics and Metabolomics: Cancer Metabolism, Therapeutic Targets and Biomarkers*", AICC, University of Verona, Verona, July 1-2, 2019.

4. 5th Annual Meeting of the International Society of Cancer Metabolism on "*Metabolic Adaptations and Targets in Cancer*", Biomedical Research Center, Slovak Academy of Sciences, Bratislava, Slovakia. October 17-20, 2018.

5. D-Day, Molecular Biotechnology Center, University of Turin. September 13,2018.

6. D-Day, Molecular Biotechnology Center, University of Turin. September 19,2017.

7. 28a Riunione Nazionale "A. Castellani" dei Dottorandi di Ricerca in Discipline Biochimiche, Brallo, University of Pavia. June 5-9, 2017.

TRAINING SCHOOLS ATTENDANCE

1. International Research period conducted at AO Research Institute, Davos-Platz, Switzerland as part of a grant awarded COST-ACTION "CA17104" on "New diagnostic and therapeutic tools against multidrug resistant tumours". January 10 – July 31, 2020.

2. Workshop on "Open Science and FAIR Data". University of Turin. 23-24 September 2019.

3. Advanced School "Bioinformatics tools for mass mass-spectrometry based omic data: from pathways reconstruction to multi-omic data integration". Verona. July 2,2019.

4. Summer School on Safer NanoDesign by European Scientific Institution, Bio-Health Computing Schools, Archamps Geneva. June 13-19, 2017.

5. Mini Neurosciences Course, Molecular Biotechnology Center, University of Turin. May 29-31, 2017.

6. Training Bibliography Course by University of Turin. May 5-12, 2017.

AWARDS

1. Awarded 1st Prize for the best oral presentation on ""Novel Acoustic Wave Programmed 3D Vascularised Cancer Model in Malignant Pleural Mesothelioma: A Platform for drug screening". At STRATAGEM International Online Symposium. November 4, 2020.

2. Received two Short Term Scientific Mission grants from the COST-ACTION "CA17104" on "New diagnostic and therapeutic tools against multidrug resistant tumours" for the period of January 10, 2020 to April 10,2020 and May 15, 2020 to July 31, 2020.

3. Awarded the Mass Spectrometry Division Prize for Best Presentation for project titled "*Targeting SCF Complex and Protein Turnover to Overcome Chemoresistance and Trigger Innate Anti-Tumour Immune Response in Malignant Pleural Mesothelioma*". 2nd MS-based International Proteomics & Metabolomics Conference, Verona. July 1, 2019.

4. Winner of the Travel Grant Award for ""Targeting Protein Metabolism to overcome chemoresistance and trigger anti-tumour immune response in Malignant Pleural Mesothelioma" for 5th Annual Meeting of the International Society of Cancer Metabolism. Bratislava, Slovakia. October 17-20, 2018.